Electric Vehicles
Design, Modelling and Simulation

Edited by Nicolae Tudoroiu

Electric Vehicles - Design, Modelling and Simulation

Edited by Nicolae Tudoroiu

Notice

Statements and opinions expressed in the chapters are these of the individual contributors and not
necessarily those of the editors or publisher. No responsibility is accepted for the accuracy of
information contained in the published chapters. The publisher assumes no responsibility for any
damage or injury to persons or property arising out of the use of any materials, instructions, methods
or ideas contained in the book.

We are IntechOpen,
the world's leading publisher of Open Access books
Built by scientists, for scientists

6,700+
Open access books available

181,000+
International authors and editors

195M+
Downloads

156
Countries delivered to

Our authors are among the
Top 1%
most cited scientists

12.2%
Contributors from top 500 universities

Interested in publishing with us?
Contact book.department@intechopen.com

Numbers displayed above are based on latest data collected.
For more information visit www.intechopen.com

Meet the editor

Nicolae Tudoroiu holds a BS and MS in Automation and Computers, a BS in Mathematics, and a Ph.D. in Automation and Electrical and Computer Engineering. From 1979 to 1993 he was a professor in the Department of Automation and Control, University of Craiova and the Technical University of Timisoara, Romania. Since 2001 he has held the positions of postdoctoral fellow and research associate at Concordia University, Canada, and professor at John Abbott College, Canada, and Spiru Haret University, Romania. His research interests are in automation and control, including process identification, modeling, state and parameter estimation, fault detection and isolation, battery management systems for electric and hybrid electric vehicles, simulation and control of HVACs, aircraft systems, intelligent control strategies using artificial intelligence, and control and processes optimization.

Contents

Preface

This book provides a comprehensive overview of hybrid and electric vehicles. It explores various aspects of current research in the field, such as design, modeling of Li-ion battery management systems, state-of-charge (SOC) estimation algorithms, and the most used electric motors. It also discusses new trends in electric vehicle automation as well as different control strategies. Almost all simulations presented were performed in the MATLAB and Simulink environment or other specialized software.

The book begins with Chapter 1, which presents a case study of investigations of different approaches to nonlinear speed control methods and SOC estimation techniques applied to a rechargeable Li-ion battery adapted to power the electrical motor of an electric vehicle. The investigations use the most suitable design approaches for the real-time implementation of the most advanced state estimators based on intelligent neural networks and neural control strategies.

Chapter 2 proposes an intelligent controller for a hydrogen-powered, plug-in fuel cell hybrid electric vehicle that integrates a fuel cell with two energy storage systems (ultracapacitor and battery), resulting in a high dynamic response while maintaining efficient use of resources for energy storage.

Chapter 3 introduces a battery SOC management technique designed for an electric vehicle traction system that incorporates an indirect field-oriented induction motor drive. The primary goal of this technique is to restrict the change in battery SOC from exceeding a maximum limit by compensating the motor speed tracking performance, dealing with a fuzzy-tuned model predictive controller.

Chapter 4 proposes a nonlinear robust H-infinity control approach to enhance the trajectory-following capabilities of autonomous ground electric vehicles. Given the inherent influence of driving maneuvers and road conditions on vehicle trajectory dynamics, the primary objective is to address the control challenges associated with trajectory following, including parametric uncertainties, system nonlinearities, and external disturbance.

Chapter 5 discusses vehicle system dynamics, torque vector control, and stability performance analysis.

Finally, Chapter 6 presents the main typical topologies of hybrid energy storage systems for electric vehicles and reviews different electrochemical energy storage technologies by highlighting their pros and cons.

It is my great pleasure to acknowledge the contributing authors and the staff at IntechOpen, especially Publishing Process Manager Mr. Dominik Samardzija, for their tremendous efforts, excellent collaboration, support, and guidance. I would

Nicolae Tudoroiu
Engineering Technologies Department,
John Abbott College,
Sainte-Anne-de-Bellevue, Montreal, Quebec, Canada

Investigations of Different Approaches for Controlling the Speed of an Electric Motor with Nonlinear Dynamics Powered by a Li-ion Battery – Case Study

Roxana-Elena Tudoroiu, Mohammed Zaheeruddin,

Nicolae Tudoroiu, Sorin Mihai Radu and Hana Chammas

Abstract

This research investigated different nonlinear models, state estimation techniques and control strategies applied to rechargeable Li-ion batteries and electric motors powered and adapted to these batteries. The finality of these investigations was achieved by finding the most suitable design approach for the real-time implementation of the most advanced state estimators based on intelligent neural networks and neural control strategies. For performance comparison purposes, was chosen as case study an accurate and robust EKF state of charge (SOC) estimator built on a simple second-order RC equivalent circuit model (2RC ECM) accurate enough to accomplish the main goal. An intelligent nonlinear autoregressive with exogenous input (NARX) Shallow Neural Network (SSN) estimator was developed to estimate the battery SOC, predict the terminal voltage, and map the nonlinear open circuit voltage (OCV) battery characteristic curve as a function of SOC. Focusing on nonlinear modeling and linearization techniques, such as partial state feedback linearization, for "proof concept" and simulations purposes in the case study, a third order nonlinear model for a DC motor (DCM) drive was selected. It is a valuable research support suitable to analyze the performance of state feedback linearization, system singularities, internal and zero dynamics, and solving reference tracking problems.

Keywords: Li-ion battery, SOC, Simscape generic model, PID control, state feedback linearization, NARX shallow neural network, NARMA-L2 neuro controller

1. Introduction

Clean and efficient transportation across the planet is only possible if governments and scientists focus on stimulating and sustaining the automotive industry of electric vehicles (EVs) by developing and deploying the most advanced battery technologies. Nowadays, Li-ion battery technologies have made significant progress and have

undoubtedly proven to have a promising future and great potential for development. These are recommended for their excellent features, such as lightweight, high-energy density, low memory effect and relatively low self-discharge, outperforming almost all other competing batteries of different chemistries on the market [1, 2]. Thanks to several improvements in Li-ion battery technologies recently, they have become safer, eliminating explosion hazards as much as possible and their chemistry is less toxic, both to nature and to humans. Battery state of charge (SOC) is an essential internal parameter that plays a vital role in utilizing battery energy efficiency, operating safely under various realistic conditions and environments, and extending battery life [3, 4]. The SOC is a piece of valuable information on the remaining capacity available during the operation of EV car. As the central internal state of the battery, the SOC is continuously supervised by a battery management system (BMS), which is integrated into the EV energy storage system (ESS) structure to power the traction powertrain [1–6]. The SOC can be calculated directly by a simple open-loop integration operation, known as the coulomb counting method or the ampere method since it accumulates the charge transferred between the battery and the environment over time. However, this measurement method is prone to the initial value of SOC and accuracy of the current profile data set measurement. The ampere method accumulates significant errors caused by the integration operation that accumulates errors over time [7]. The battery SOC estimation is one of the main tasks of a BMS. An extensive critical review of Lithium-ion battery SOC, and a smarter BMS description for EV applications are made in [8]. Being interpreted as a remaining capacity of the battery, the SOC is also an important support for energy management (EM) and control strategies. An interesting comprehensive review on Energy Management Strategies (EMS) for EVs taking into consideration the realistic conditions of Li-ion battery degradation based on aging models is found in HAL Open Science that includes the most representatives research papers from 2021 IEEE Access, with a new release version in 2023 [9]. The accuracy of Li-ion battery SOC estimation has a significant impact on the efficient operation and EMS of the battery. Many of studies are dedicated to advancing the BMS functions, such as intelligent cell balancing and charging control strategies for lithium-ion battery packs [10], SOC and state of health (SOH) monitoring [11–13], and thermal battery control temperature [14].

Nowadays, an impressive amount of work has been done in the research field to investigate and study large-scale new developments and implementations of SOC estimation algorithms to be applied to an extensive range of applications in the EV automotive industry. The main flaw of coulomb counting method is that it is not suitable in real time online SOC estimation. Also, it is noteworthy to know that the battery model accuracy significantly impacts SOC estimation. The well-known equivalent circuit model (ECM) is suitable for online estimation due to its simplicity and mastering well the relationship between parameters [1], [3–6]. The traditional methods include the most popular Kalman filter (KF) algorithms, among them linear KF and linearized extended KF (EKF) [5, 6, 15, 16], and nonlinear unscented KF (UKF) [7], ensemble KF (EnKF) [17], particles filter (PF) [18], which are commonly used as a nonlinear filter estimation methods. Only the linear KF is an optimal state estimator compared to the EKF, a suboptimal estimation algorithm. Still, it is an appropriate state estimator for complex working conditions with severe current fluctuations [7]. Compared to EKF, the UKF method uses an unscented transform to obtain the statistics of the process noise covariance and reaches a fast convergence speed and high estimation accuracy [7]. Also, its robustness is better when estimating

the SOC of different chemistry batteries. To achieve higher accuracy of state estimation, various intelligent algorithms based on Machine Learning (ML) and Deep Learning (DL) Artificial Intelligence (AI) models are applied to the SOC estimation and terminal voltage prediction, as those developed in [7, 12, 13, 17, 19–38] easily to be adapted to all types of batteries and chemistries. The neural networks (NNs) learning techniques have a wide range of applications and are suitable for all types of batteries chemistry. Well, these learning techniques such as machine learning (ML) and deep learning (DL) models require large amounts of accurate training data [27–30]. The estimation accuracy and the convergence speed of the Li-ion battery SOC depend on the chosen training method, architecture structures, number of hidden layers and hidden neurons, learning rate, gradient value and on number of samples and epochs [29, 30]. The flow of this research paper is organized into four sections, as follows. For "proof concept" and simulation purposes, in Section 2 a generic Simulink Simscape model, simple and accurate is adopted to power a particular small EV car. The model parameters are extracted from a Simulink Simscape battery block set up for a preset model of the Li-ion battery. Additionally, the battery Simscape model is used for performance comparison with the adopted second-order ECM battery model (2RC ECM) used as support in Section 3 to build an accurate and robust EKF SOC estimator. In Section 3 is developed and implemented a NARX SNN intelligent SOC estimator. Section 4 is chosen as a case study of a DCM Drive nonlinear model of the high complexity of applying the state feedback linearization as a powerful tool for nonlinear control systems in a closed loop. Also, the model singularities, internal and zero dynamics stabilizability and reference tracking problems to solve represent some issues /challenges that merit being studied. Additionally, the traditional PID control strategy is a valuable tool used in this last section for performance comparison. At the end of Section 4, a learning NARMA-L2 controller intelligent strategy is applied to learn and linearize the DCM Drive nonlinear model. Therefore, this research work opens other directions of research to explore the application of clever neuro-control strategies on a large scale in future developments in the EV automotive industry.

2. Li-ion battery: model selection, accuracy, robustness, SOC estimation and terminal voltage prediction

In this research, we try to develop new approaches for identification, modeling, state estimation, and linear and nonlinear speed control strategies for a typical choice of DC or AC electric motor powered by a Li-ion battery and suitable for possible cars' mid-size EVs applications. Nowadays, we have a great opportunity to take advantage of the significant advances in modeling, identification and control systems inspired by the latest achievements in artificial intelligence, statistics and machine learning, deep learning, signal process analysis. Therefore, our research objectives are expanded with new approaches.

2.1 Li-ion battery model selection

In the case study, for "proof-of-concept" and simulation reasons, our selection strategy is to adopt a Li-ion battery model that meets the following requirements:

simple, accurate, easy to implement and suitable for online real-time simulations for a wide range of applications in the automotive industry of EVs.

The experience gained so far in process identification, modeling, design, and implementation confirms the existence of such a Li-ion battery model; depending on the complexity of the proposed research objectives, this could be an ECM, i.e., an electrical circuit consisting of a Thevenin-type voltage source OCV connected to the internal resistance Rint of the battery in series with one, two or three RC polarization cells. The number of RC cells substantially increases the accuracy of the model, which undoubtedly fulfills the above-mentioned characteristics, thus becoming valuable support for achieving research goals [3]. In our research, a second order ECM Li-ion battery model (abbreviated 2RC ECM) with a nominal voltage of 3.7 V and a rated capacity of 7.5 Ah was adopted, and the model was validated for different operating conditions in [3]. The electrical circuit diagram is shown in **Figure 1**, where the first polarization cell R1C1 captures the fast dynamics of the battery. In contrast, the second R2C2 polarization cell captures the slow dynamics of the Li-Ion battery. From the systemic perspective, it is a single-input, single-output (SISO) system with the input u = i indicating the charge (i < 0) or discharge (i > 0) current, and y = Vbat denoting the voltage at the output terminal of the battery. The voltages across the bias cells, Vc1 and Vc2, and the internal SOC state of the battery represent the internal states of the system. In addition, the proposed Li-ion battery SOC estimator based on the adopted model is expected to perform much better in terms of accuracy and robustness of battery SOC estimates for different operating conditions [3, 5, 7].

The adopted Li-ion battery (LIB) ECM model plays an important role in our research since it is valuable to support building a model-based EKF SOC and terminal voltage estimator, whose accuracy and robustness depended on the accuracy and robustness of the battery model. In addition, the ECM battery model is used for training data set generation to develop a data-driven intelligent neural network learning technique for SOC estimation and terminal voltage prediction, as a viable alternative to the traditional EKF estimator. The new modeling and estimation approach has proven its use for all battery types and different chemistries, outperforming traditional model-based state estimators. Their convergence does not depend on the complexity of model nonlinearity, unmodelled parts or model uncertainties. Also, intelligent learning techniques are much more suitable for real time online applications in the EVs industry. Model selection is also suggested due to its simplicity and ability to accurately describe the static and dynamic behavior of Li-ion battery.

The new modeling approaches use a specialized Simulink Simscape battery block to preset a specific Li-ion battery operating for different temperature ranges that
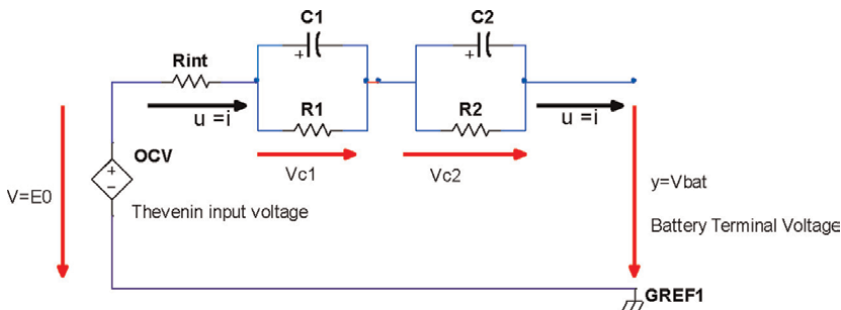
Figure 1.
2RC ECM wiring diagram.

significantly affect battery internal resistance $R_\int$, SOC, and RC components of the bias cells. Therefore, depending on user settings, Simscape multi-object models, built by a kind of specific object-oriented programming language, become valuable tools for generating different measurement input-output data sets for physical systems or subsystems. Then, these data sets are trained to develop and implement in MATLAB Simulink intelligent neural networks (NNs) learning techniques or to extract the model parameter values of a particular Li-ion battery, as well as to adjust and obtain the optimal values of them. For interested readers, such a Simscape block is shown in **Figure 2**.

Figure 3a and **b** show the discharge characteristics curves of rated current at 0.9, 5.4, 10.8, and 27 A versus battery capacity (Ah) as in **Figure 3a**, and time (h) in **Figure 3b**. The parameter values of a generic preset Li-ion battery model are also disclosed.

2.2 Li-ion 2RC ECM analytical model state space representation and continuous time domain

The analytical model of the Li-Ion battery is described in the continuous time domain by three first-order linear differential state equations and a highly nonlinear static output-state-input equation:

$$\frac{dx_1}{dt} = \frac{-\eta}{Q_{nom}} u(t) \tag{1}$$

$$\frac{dx_2}{dt} = \frac{-1}{R_1 C_1} x_2 + \frac{1}{C_1} = \frac{-1}{T_1} x_2 + \frac{1}{C_1}, T_1 = R_1 C_1 [s] \tag{2}$$

$$\frac{dx_3}{dt} = \frac{-1}{R_2 C_2} x_3 + \frac{1}{C_2} = \frac{-1}{T_2} x_3 + \frac{1}{C_2}, T_2 = R_2 C_2 [s] \tag{3}$$
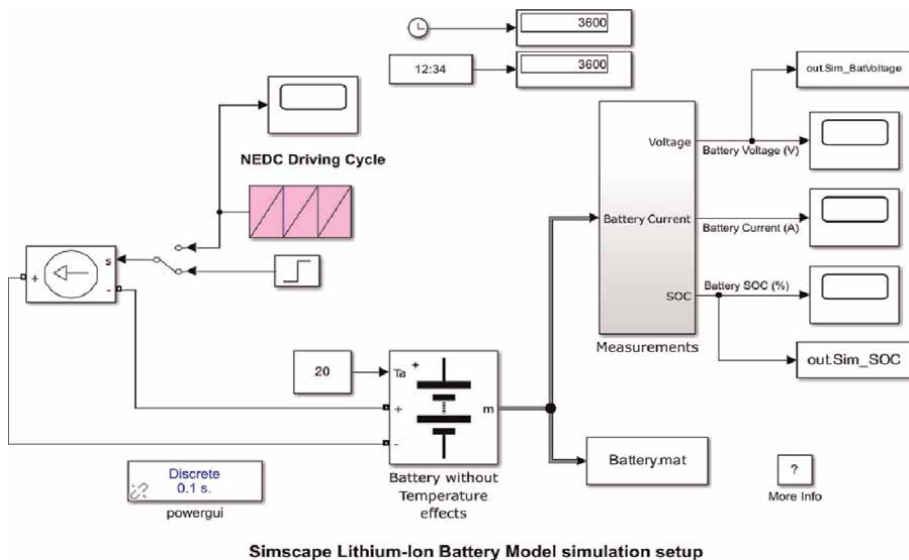
Figure 2.
Simulink Simscape block configured for Li-ion battery and NEDC driving cycle current profile test.
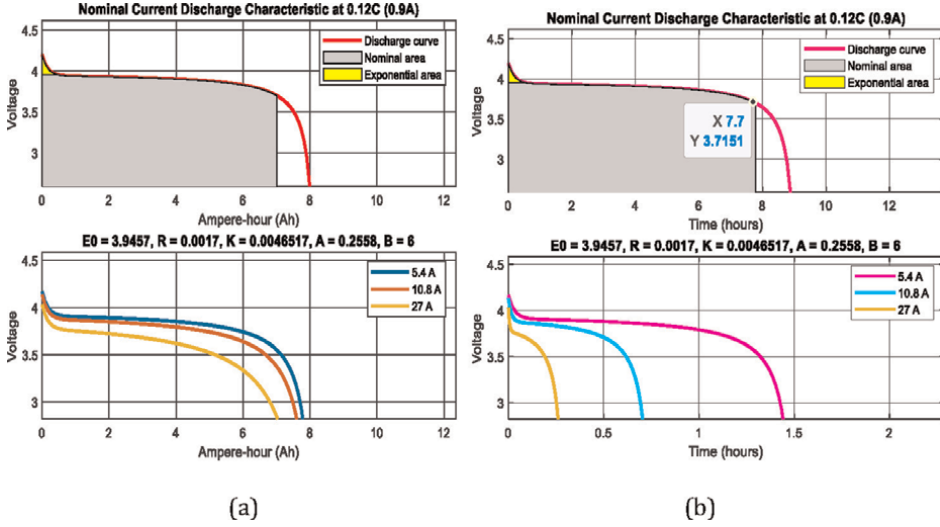
Figure 3.
Li-ion battery-rated current discharge characteristics and battery terminal voltage curves: (a) battery voltage-rated capacity curve (V-Ah); (b) battery voltage-time curve (V-h).

$$y = h(x_1) - x_2 - x_3 - R \int u(t) \tag{4}$$

where,

$$h(x_1) = OCV(x_1) = k_0 - k_1 \frac{1}{x_1} - k_2 x_1 + k_3 \ln(x_1) + k_4 \ln(1 - x_1) \tag{5}$$

is a nonlinear static function that represents the dependence of OCV on SOC, that is, OCV(SOC), and SOC = x_1, the first component of the state vector x, given by

$$x = \begin{bmatrix} x_1 \\ x_2 \\ x_3 \end{bmatrix} \begin{bmatrix} \ \end{bmatrix} \tag{6}$$

Both, T_1 and T_2, denote the time constant of the first and second polarization cells, respectively. Also, the constants η, and Q_{nom} designate the coulombic efficiency (η) for both, charging and discharging cycles, and the nominal capacity of the battery (Q_{nom}) respectively.

It is worth noting that, Eqs. (5) and (6) represent a combination of three separate models, namely Shepherd, Unnewehr and Nernst, reported in [3, 5] to predict terminal voltage based on SOC measurements. The combined model performs better than using either model separately. The constants $k_0, k_1, k_2, k_3, , k_4$ can be estimated using a least square estimation (LSE) procedure provided in the MATLAB System Identification Toolbox. To understand how LSE technique works, a simple offline (batch) processing method that calculates all these unknown parameters is well described in [3, 5]. For tuning these parameters and finding their optimal values, a Global Pattern Search (GPS) genetic algorithm from MATLAB Optimization Toolbox is a valuable tool to use [3].

2.3 Analytical model of Li-ion 2RC ECM in state space and discrete time domain representation

The Li-ion battery model described in the continuous-time state space representation can be discretized using a Taylor series expansion and then keeping only the first linear term, obtained by using the following approximation

$$\frac{dx_i}{dt} = x_i \qquad (7)$$

where,

T_s is the sampling time, $t_k = k \times T_s, k \; Z^+$ denotes the time instance, and k is a sample index

A matrix representation describes a compact Li-ion battery model of the following form:

$$x(k+1) = Ax(k) + Bu(k), y(k) = Cx(k) + Du(k) + h_1(x(k)) \qquad (8)$$

where

$$A = \begin{bmatrix} 1 & 0 & 0 \\ 0 & 1 - \dfrac{T_s}{T_1} & 0 \\ 0 & 0 & 1 - \dfrac{T_s}{T_2} \end{bmatrix}, B = \begin{bmatrix} \dfrac{-\eta T_s}{Q_{nom}} \\ \dfrac{T_s}{C_1} \\ \dfrac{T_s}{C_2} \end{bmatrix}, C = [-k_2 \;\; -1 \;\; -1], D = \qquad (9)$$

and,

$$h_1(x(k)) = k_0 - k_1 \frac{1}{x_1} + k_3 \ln(x_1) + k_4 \ln(1 - x_1) \qquad (10)$$

The MATLAB simulation results obtained by iteratively solving the discrete-time Eqs. (8)–(10) describing the dynamics of the battery model over a finite time horizon defined by the number of samples are shown in **Figure 4a–c**. **Figure 4a** shows the SOC evolution of the battery over a full one-hour discharge cycle for a discharge current of 1C (7.5A), decreasing from 100% (fully charged battery) to 0% (fully discharged battery). **Figure 4b** reveals one of the main characteristics of the proposed Li-ion battery, which can be found in any catalog specifications of battery manufacturers. This well-known non-linear OCV-SOC curve differs from battery to battery. The time evolution of the battery terminal voltage and its OCV are illustrated in **Figure 4c** (Vbat) and 4d (OCV), respectively. The development of OCV and the terminal voltage of the Li-Ion battery is studied over the same full discharge cycle of 1h @7.5A (1C rate) discharge current.

3. SOC estimation and terminal voltage prediction of Li-ion battery

Section 1 details the vital role of the SOC battery in energy efficiency, safe operation and life extension. Also, information on the best-known state estimators and
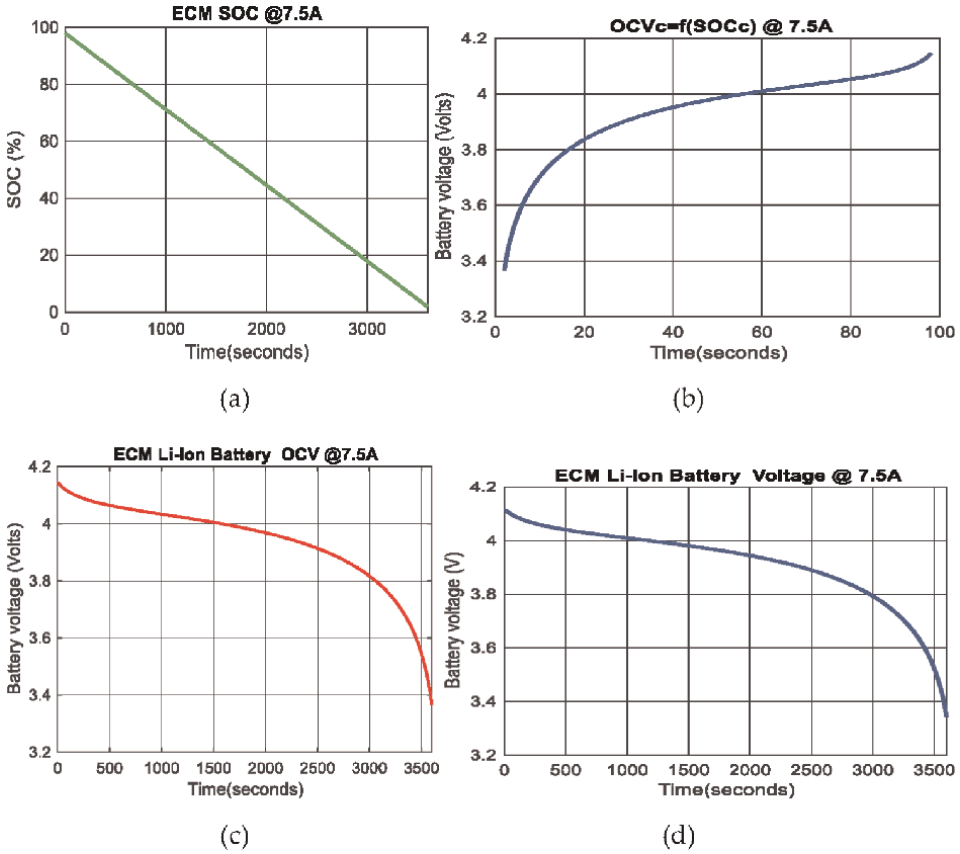
Figure 4.
MATLAB simulation results @ constant current = 7.5 A: (a) discharged battery SOC during one-hour discharge cycle; (b) OCV characteristics of the Li-ion battery; (c) Li-ion battery terminal voltage during one-hour discharge cycle; (d) OCV battery during a one-hour discharge cycle.

parameters reported in the literature is provided to interested readers and implementers. Among these estimators, the most popular is the Kalman filter estimator in various versions, such as KF, EKF, UKF, and EnKF, as mentioned in the Introduction section. This section briefly introduces the EKF state estimator, which is easily adapted to estimate the SOC of the Li-ion battery proposed in the case study.

3.1 EKF state estimator design and MATLAB implementation

The Kalman Filter is reported in the literature field since 1960. It is "an optimal recursive model-based data processing algorithm for linear filtering purposes" [3].
A new modified form of KF, abbreviated EKF, was adopted for nonlinear process dynamics, a non-optimal filter estimator based on the linearization of process dynamics. Only KF is the optimal filter that addresses Gaussian linear processes whose measurement and process noises are zero-mean and uncorrelated of covariance matrices, e.g., Q for process noise and R for measurement noise, respectively. The state estimation of a process minimizes the minimum mean squared error, abbreviated MMSE, between state estimate values and true state

model values given the measured input data set and the observed output data set [3, 5].

The EKF is a discrete-time recursive algorithm based on the LIB model whose states need to be estimated. For simplicity, the steps of the general iterative KF procedure when applied to linear systems are shown; it consists of the following two update phases [3–6, 15, 16]:

1. Prediction (forecasting) phase (time update) steps

    1.1 Predict the LIB state given in Eq. (8) one step ahead

$$\hat{x}_{k+1,k} = A\hat{x}_{k,k} + Bu(k) \tag{11}$$

    1.2 Predict one step ahead the error state covariance

$$\hat{P}_{k+1,k} = A\hat{P}_{k,k}A^T + Q_k \tag{12}$$

2. Correction phase (measurement update)

    2.1 Kalman gain computation

$$K_{k+1} = \hat{P}_{k+1,k}C^T \left(C\hat{P}_{k+1,k}C^T + R_{k+1}\right)^{-1} \tag{13}$$

    2.2 Update the state estimate with a new available measurement

$$\hat{x}_{k+1,k+1} = \hat{x}_{k+1,k} + K_{k+1}\left(y_{k+1} - C\hat{x}_{k+1,k}\right) \tag{14}$$

    2.3 Update error state covariance

$$\hat{P}_{k+1,k+1} = (I - K_{k+1}C)\hat{P}_{k+1,k} \tag{15}$$

Summarizing, in the prediction/forecast phase are predicted the LIB states $\hat{x}_{k+1,k}$ and the covariance of the states $\hat{P}_{k+1,k}$. The second is a correction phase that occurs only if a new output measurement y_{k+1} (terminal voltage) is available, as it must calculate the Kalman gain K_{k+1} and, based on it, are updated the estimated state $\hat{x}_{k+1,k+1}$ and its estimated covariance $\hat{P}_{k+1,k+1}$ [3, 5, 15, 16].

For general recursive EKF procedure, the matrices $A, B, C \wedge D$ are obtained by linearizing the following nonlinear functions around the last predicted estimate in each iteration:

$$x_{k+1} = f(x_k, u_k) + w_k \tag{16}$$

$$y_k = g(x_k, u_k) + v_k \tag{17}$$

where

f, g are nonlinear time-varying functions, w_k and are both zero-mean and uncorrelated Gaussian process and measurement noises, respectively, with the statistics represented by the covariance matrices $Q_k \wedge R_k$ given or calculated at iteratively at the time instance zero mean and uncorrelated, of covariance matrix The

matrices represent the so-called Jacobian matrices required in the Eqs. (11)–(15), defined as

$$A_k = \left(\frac{\partial f}{\partial x}\right) \hat{x}_{k,k}, C_k = \left(\frac{\partial f}{\partial x}\right) \hat{x}_{k,k} \tag{18}$$

This is just the unique difference between KF and EKF steps; the latter requires the calculation of the Jacobian matrices $A_k, \wedge C_k$ first and then the steps remain the same. It is worth noting that the matrices $A_k \wedge C_k$ are time-varying, compared to matrices (A, C) which have constant elements.

For a rigorous SOC performance analysis of the EKF algorithm in terms of accuracy and robustness, some of the MATLAB simulation results for the adopted 2RC ECM Li-Ion model, are shown below in **Figures 5**–**7** some of the MATLAB simulation results for the adopted 2RC ECM Li-Ion model. In **Figure 5**, the adopted Li-Ion model is tested with a New European Driving Cycle (NEDC) input current profile test, and the SOC of the battery is estimated following the steps of the EKF state estimation algorithm. For more details on the EKF state estimator, the reader can refer to [3–6, 29, 30]. **Figure 5a** shows the NEDC driving cycle current profile test, and **Figure 5b** show the SOC values generated by the 2RC ECM model versus the SOC EKF estimated values. **Figure 5b** reveals excellent SOC steady-state accuracy and robustness to changes in SOC initial value from 80% (in the model) to 30% in the initial SOC estimate value. Therefore, the EKF estimator performs very well with high SOC accuracy and robustness.

Instead, in **Figure 6a**–**d**, the EKF SOC estimator starts from the same initial SOC value that initializes the Li-Ion battery model; the MATLAB simulation results show now the battery model SOC versus its predicted EKF value, such as in **Figure 6a**, the model terminal voltage versus its predicted EKF value in **Figure 6b**, and, newly, both SOC and terminal voltage error residuals in **Figure 6c** and **d**, which provide valuable information on SOC accuracy and terminal voltage prediction. The lower values of both residuals (close to zero) indicate an excellent performance of the EKF SOC estimator and prove that the assumption regarding the accuracy of the proposed Li-ion battery model is correct; thus there is an accuracy transfer from the model to the EKF estimator.
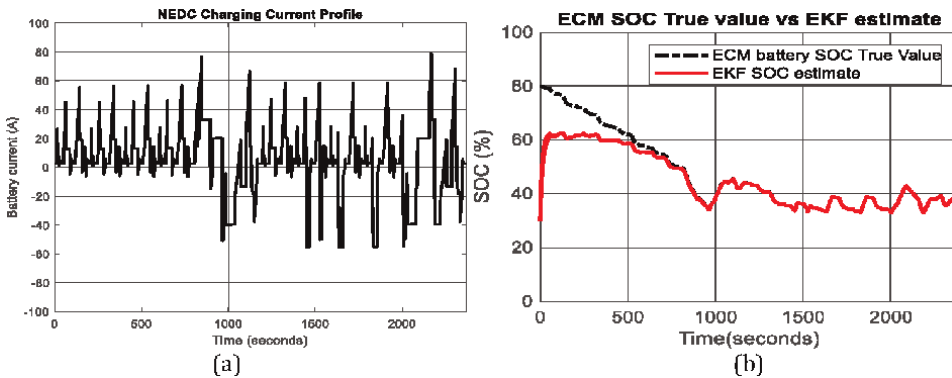
Figure 5.
MATLAB simulation results: (a) NEDC driving cycle current profile test; (b) Li-ion battery SOC ECM model versus EKF SOC estimator.
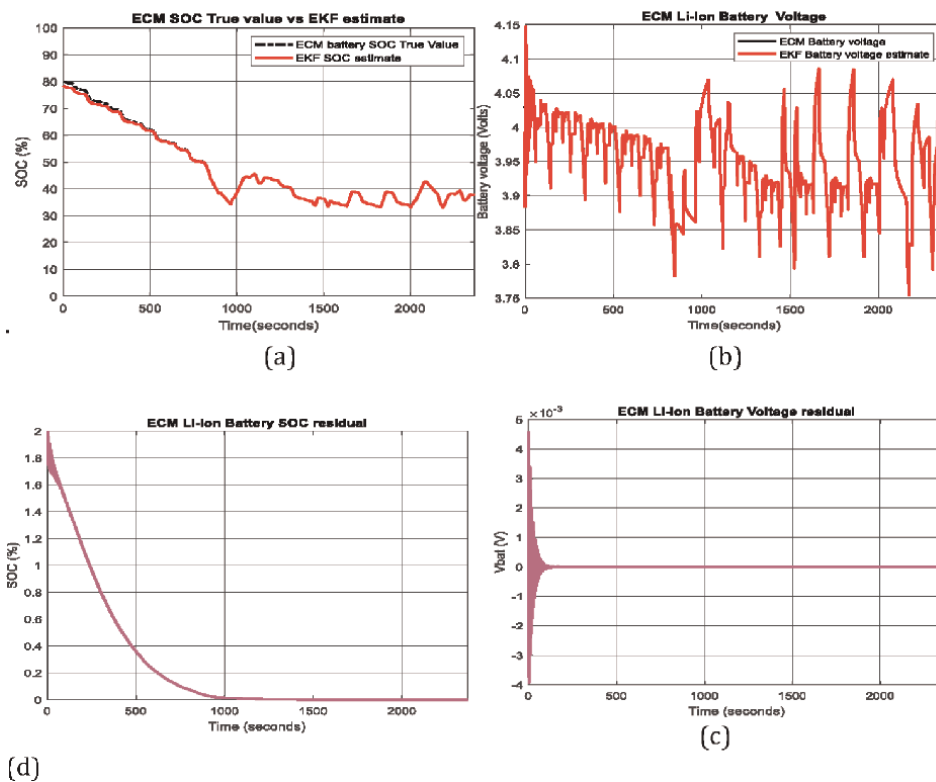
Figure 6.
MATLAB Simulation results: (a) Battery SOC ECM model vs. EKF SOC estimate (same initial conditions); (b) ECM terminal voltage vs. EKF predicted terminal voltage; (c) Battery SOC residual; (d) Battery terminal voltage residual.

Similarly, the MATLAB simulation results depicted in **Figure 7a–e** by changing the driving style, switching from a European NEDC cycle drive current profile test to an American Federative Transport Procedure FTP-75, shown in **Figure 7a**, and the response of the EV car is reflected in the high accuracy of the battery SOC shown in **Figure 7b**, an excellent prediction of the terminal voltage, as in **Figure 7c**. Again, the driving style is changed by moving from the American FTP-75 cycle drive current profile test to the latest European World Harmonized Light Transport Procedure (WLTP) with a more aggressive behavior, very close to the operating conditions of an environment realistic, shown in **Figure 7d**, and the impact reflected in **Figure 7e** by high SOC accuracy and excellent terminal voltage prediction is revealed in **Figure 7e**.

Summarizing this subsection, the EKF SOC estimator performs excellently in high SOC accuracy and terminal voltage prediction and with excellent robustness revealed by the MATLAB simulation results depicted in **Figures 5–7**. All these results are obtained for different operating conditions, mainly some changes in the initial battery SOC values and driving style by switching three driving cycles current profile tests, NEDC, FTP-75, and WLTP. In any of these scenarios the EKF SOC estimator performs excellently, with no significant impact from one driving scenario to another.
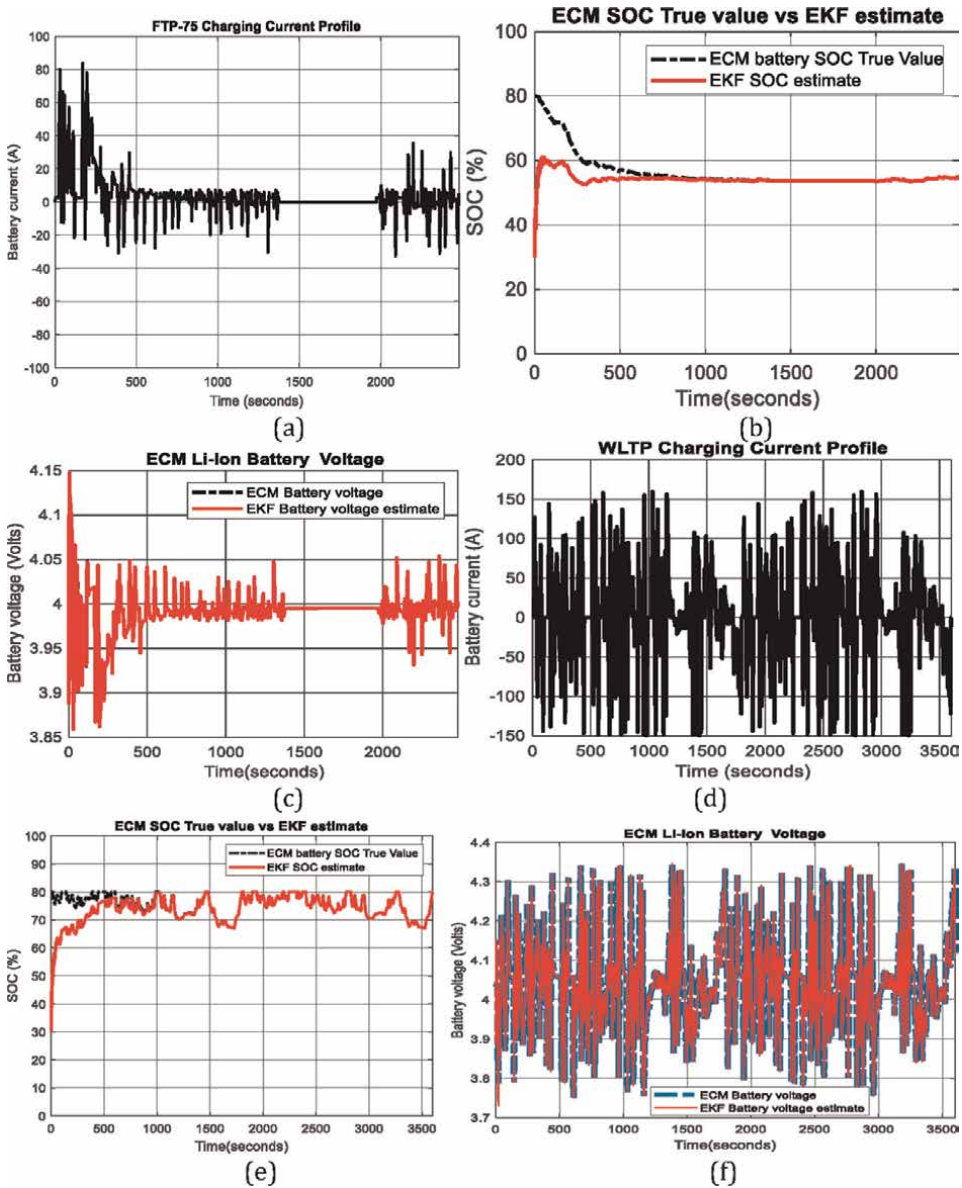
Figure 7.
MATLAB simulation results – Robustness of EKF estimator to change the driving style and initial SOC value from 80 to 30%. (a) FTP-75 driving cycle current profile test; (b) ECM SOC vs. ECM EKF SOC estimate for FTP-75; (c) ECM terminal voltage vs. ECM EKF prediction terminal voltage; (d) WLTP driving cycle current profile test; (e) ECM SOC vs. ECM EKF SOC estimate for WLTP; (f) ECM terminal voltage vs. ECM EKF prediction terminal voltage.

3.2 Li-ion battery neural network learning techniques for nonlinear OCV characteristic estimation, SOC and terminal voltage estimation

This subsection explores a new approach to designing and implementing data-driven intelligent learning structures using neural networks (NNs). The intention is to

use these smart structures for possible applications as state estimators. All these investigations aim to find a viable alternative to traditional model-based state estimators, such as the EKF used in the case study. This is why it is necessary to evaluate the capability and accuracy of their performance in a state estimation to see if they are suitable for mapping the non-linear characteristic OCV = f(SOC) characteristic of the battery and for estimating the battery SOC and terminal voltage. Therefore, three intelligent structures of nonlinear autoregressive neural networks with external input (NARX) are investigated. They are easily accessible from MATLAB Simulink Deep Learning Toolbox. Since they are data-driven structures, performance accuracy does not depend on battery model accuracy, modeling uncertainties, and the unmodeled part. In addition, they are suitable for real-time online applications and can be easily updated for all types of batteries and chemistries. NARX is a learning regression shallow neural network (SNN) estimator that consists of a single hidden layer with a certain number of hidden neurons, having a significant impact on the performance of neural structure. The input-output measurement data set is collected under the signals from the battery sensors using appropriate instruments provided by a specialized data acquisition (DAQ) system. Then the data set is processed for denoising, outliers removal, and data sharpness that significantly affect the performance accuracy. Essentially, these intelligent regressive neural network structures solve nonlinear time series problems using dynamic neural networks, including feedback networks [27–30]. They can be applied in open-loop, closed-loop, and open/closed-loop multistep prediction [27, 28]. Dynamic feedback networks can switch from open-loop to closed-loop to make multistep predictions, i.e. continue to predict when external feedback is missing using internal feedback [27, 30].

The design and implementation in MATLAB Simulink follow the steps inspired by [27–30] and are summarized in this subsection as follows:

1. Load the input (Predictors)-output (Target) data in the format required by the algorithm (e.g., sequences of cells, row or column vectors, matrices, tables, etc.)

2. Partition the data into training data XTrain and TTrain (in the case study the format is a sequence of cells), and data for prediction XPredict

3. Create a NARX network. Define the input delays, feedback delays, and size of the hidden layers, using the MATLAB

$$net = narxnet\,(1:5, 1:5, 65)$$

   i.e., 0.5 samples delay for input and output, and 65 hidden neurons.

   Prepare the time series data using a MATLAB-specific function 'preparets' and the MATLAB code line (the interpretation of the arguments Xs, Xi, Ai is given in step 6):

$$[Xs, Xi, Ai, Ts] = preparets\,(net, XTrain, \{\}, TTrain)$$

4. Train the NARX network, using the MATLAB-specific functions 'net' and 'train', writing the following code line (in open-loop)

$$net = train\ (net, Xs, Ts, Xi, Ai)$$

5. Display the trained network diagram, using the MATLAB code line

$$view\ (net)$$

6. Calculate the network output Y, final input states Xf and final layer states Af of the open-loop network from the network input Xs, initial input states Xi, and initial layer states Ai.

$$[Y, Xf, Af] = net\ (Xs, Xi, Ai)$$

7. Calculate the network performance using the specific MATLAB function 'perform' and the MATLAB code line:

$$perf = perform\ (net, Ts, Y)$$

8. Setup the closed-loop form of the NN architecture using the following MATLAB code line

$$[netc, Xic, Aic] = closeloop\ (net, Xf, Af)$$

Remark 1. The final input states Xf and layer states Af of the open-loop network net become the initial information states Xic and layer states Aic of the closed-loop network netc.

9. Display the closed-loop network diagram, using following MATLAB code line

$$[netc, Xic, Aic] = closeloop\ (net, Xf, Af)$$

10. Run the prediction for Ts-time steps ahead desired in closed-loop mode, using MATLAB code line

$$Yc = netc\ (XPredict, Xic, Aic)$$

$$Ycmatrix = cell2mat\ (Yc)$$

11. Plot Yc to visualize the simulation results

Following these steps, the MATLAB simulation results are presented below, followed by a performance analysis for all three NARX Shallow NN learning estimators.

3.2.1 The innovative NARX shallow neural network learning SOC estimator

The input-output data set is given by following sequence of cells, converted from a row vector format to a sequence of cells using the MATLAB line of code:

X = num2cell (u), u is the battery input sequence of current profile as Predictor.
T = num2cell (y), y is the battery terminal voltage output sequence as target.
XP = num2cell ([(u*]), u* is the Predicted input sequence proposed for test.

The MATLAB simulation results are depicted in **Figure 8a–d** with following interpretations:

a. Training phase progress;

b. NARX NN structure;

c. Battery SOC estimate versus the SOC ECM 2RC model (Target);

d. The best performance validation reached at epoch 242;

Performance analysis: The NN structure consists of a hidden layer with 60 hidden neurons and a 'sigmoid' activation function, an input layer with two input sequences, an output layer with one output sequence, and a linear 'pureline' activation function. The best validation performance is obtained at epoch 242. The learning rate is lr = 0.01, and a mean square error (MSE) accuracy performance of 2.79×10^{-11}*is*revealed in the **Figure 8a,c** and **d**.

In conclusion, with an MSE accuracy performance of 2.79×10^{-11} the NARX SOC estimator undoubtedly outperforms the EKF SOC estimator.

3.2.2 The innovative NARX shallow neural network learning OCV = f(SOC) estimation

X = num2cell (SOC), u is the input battery SOC as Predictor
T = num2cell (OCV), OCV is the battery OCV as Target
XP = num2cell ([(SOC*]), SOC* is the SOC Predicted input sequence for test
    purpose

The MATLAB simulation results are shown in **Figure 9a–c**, with the following interpretation for each subfigure

a. Li-Ion battery OCV estimate versus the OCV ECM 2RC model;

b. The best validation performance reached at epoch 45;

c. Training phase progress;

Performance analysis: The structure of the NN is identical to the first NN NARX. The best validation performance is achieved much faster than the first NARX estimator, i.e., at epoch 45. The learning rate is lr = 0.01, and a better mean square error (MSE) accuracy performance than the first NARX SOC estimator of 1.14×10^{-11} revealed in the **Figure 9a–c**.

In conclusion, with an MSE accuracy performance of 1.14×10^{-12}, the NARX OCV estimator also outperforms the EKF OCV estimator.

(a)

(b)

(c)

(d)
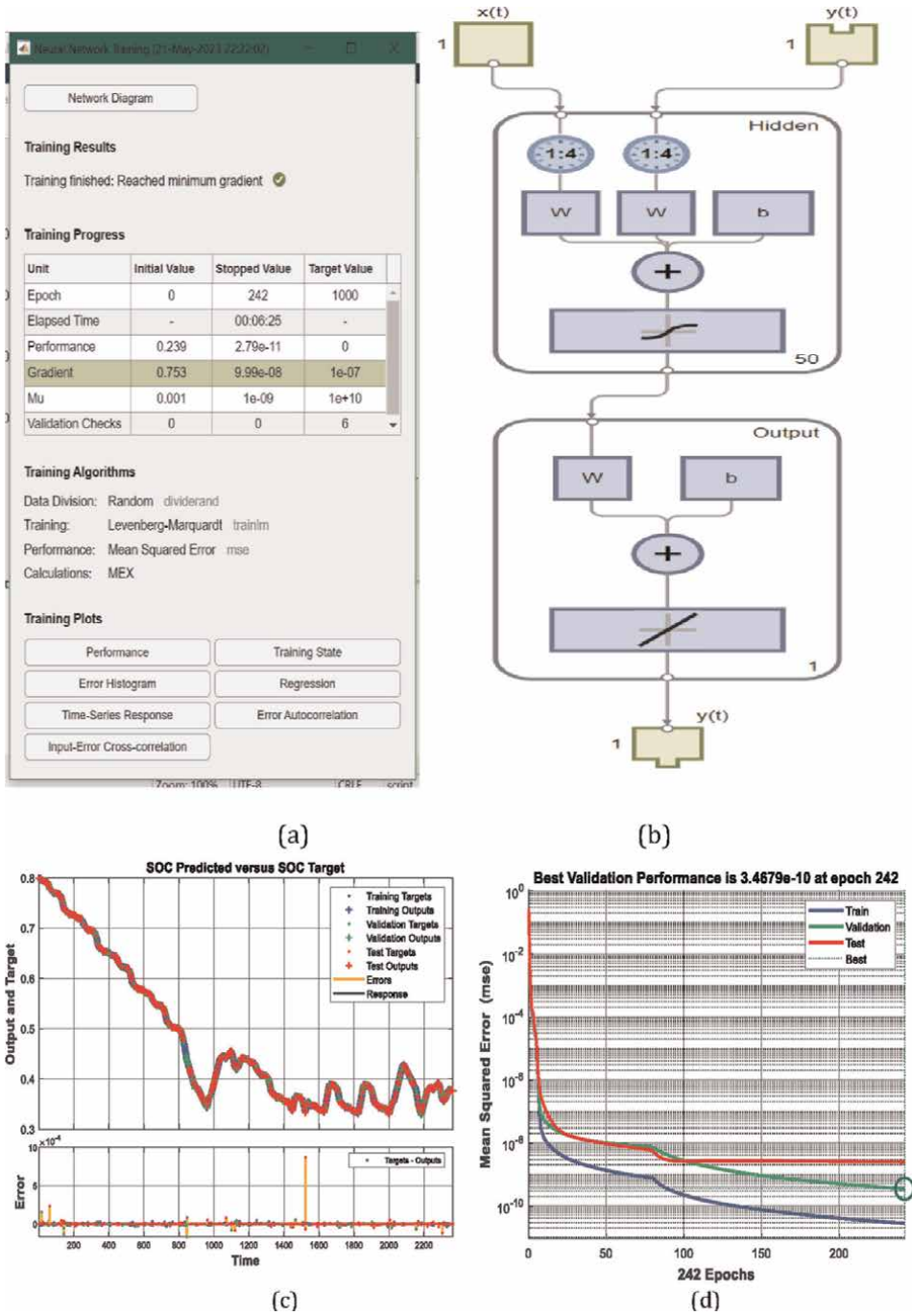
Figure 8.
NN NARX SOC estimator of Li-ion battery: (a) training phase progress; (b) NARX NN structure; (c) battery SOC estimate versus ECM 2RC SOC model (Target); (d) best performance validation achieved in epoch 242.
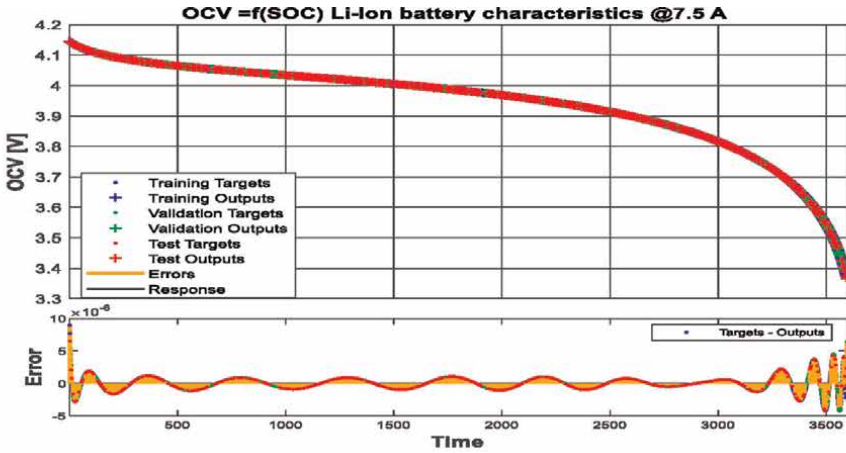
(a)
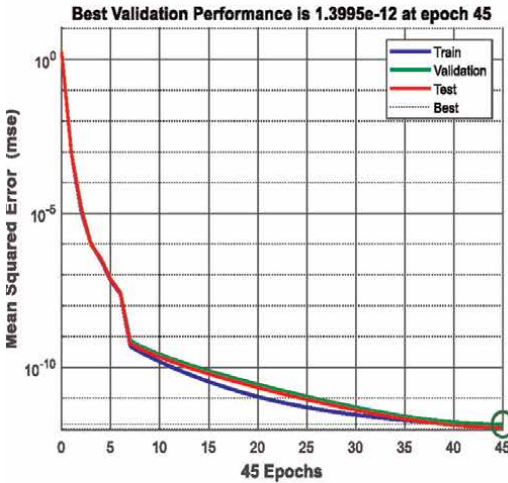
(b)   (c)

Figure 9.
NN NARX estimator of Li-ion battery OCV as a function of SOC: (a) Li-ion battery OCV estimate versus the ECM 2RC OCV model; (b) best validation performance achieved in epoch 45; (c) training phase progress.

3.2.3 NN NARX Li-ion battery terminal voltage predictor

The input-output data set is given by following sequence of cells, converted from a row vector format to a sequence of cells using the MATLAB line of code:

X = num2cell ([SOC; u]), u denotes the input current profile and SOC the input battery (Predictors)

T = num2cell (y), y signifies the output terminal voltage (Target)

XP = num2cell ([SOC*; u]), is the Predicted input sequence proposed for the test

The MATLAB simulation results are revealed in **Figure 10a–d**, each capture of the figure with following interpretations:

a. Li-Ion battery terminal voltage predicted versus ECM 2RC terminal voltage model;

(a)   (b)

(c)   (d)
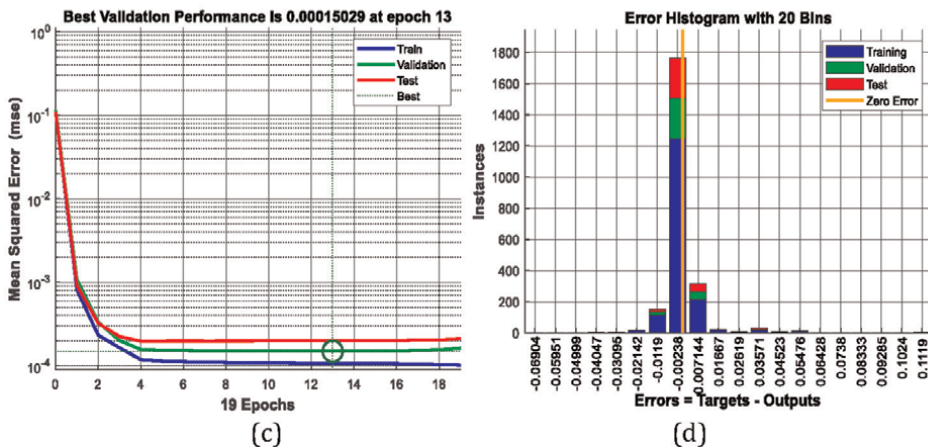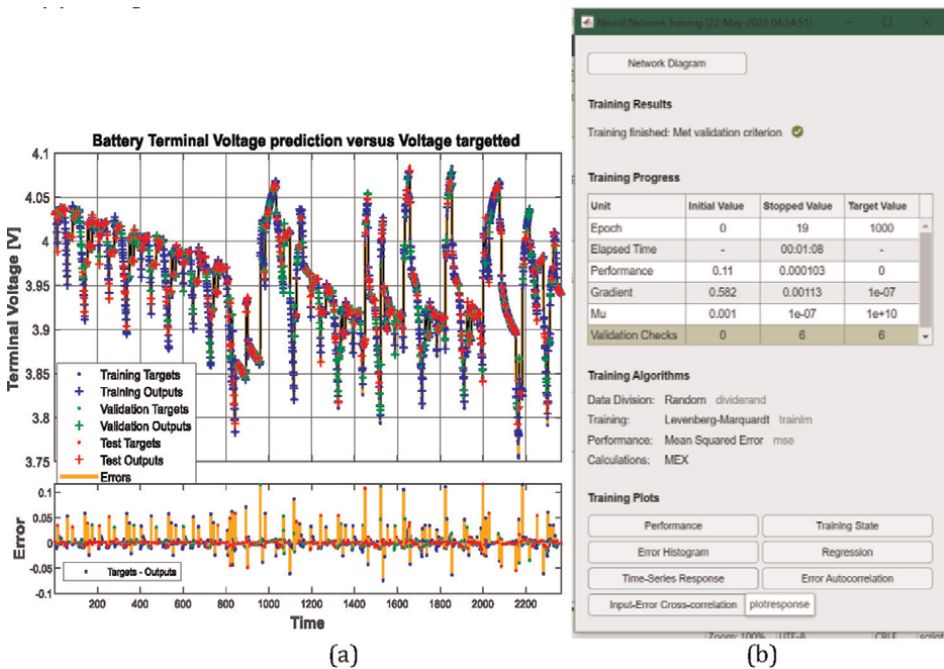
Figure 10.
NN NARX terminal voltage predictor: (a) Li-ion battery terminal voltage predicted versus ECM 2RC terminal voltage model; (b) training phase progress; (d) histogram error; (c) best validation performance achieved after 19 epochs.

b. Training phase progress;

c. The best validation performance reached at 19 epochs;

d. Histogram error;

Performance analysis: The NN structure consists of one hidden layer with 60 hidden neurons and a 'sigmoid' activation function, an input layer with two input sequences, an output layer with one output sequence, and a 'pureline' linear activation function. The best validation performance is achieved at epoch 19. The learning rate is lr = 0.01, and a mean square error (MSE) accuracy performance of 1.03×4 shown in **Figure 8a–c**.

In conclusion, for an MSE accuracy performance of 1.03×10^{-4}, it can say that the NARX SOC estimator outperforms the EKF SOC estimator.

Summarizing all the investigations made in subsection 3.2, the valuable information provided by MATLAB simulation results depicted in **Figures 8–10** demonstrate that all three NN NARX estimators perform better than the traditional model-based EKF, and are indeed a viable alternative to conventional estimators using an EKF algorithm.

4. Electrical drives: nonlinear DC model with singularities, feedback linearization and closed-loop speed control strategies

Electric propulsion is a central system integrated into the architectural structure of an EV. It consists of three main subsystems: an AC or DC electric motor, power converters, and electronic controllers. A Li-ion battery powers the electric motor, like the one proposed in the case study. It converts the electric energy received from the battery into mechanical energy to propel the vehicle or to generate electricity during regenerative braking periods for recharging the same battery [33].

The power converter is controlled by an electronic controller to supply a regulated voltage and current to the electric motor. The main task of the controller is to generate a suitable control law (PID, fuzzy, neuro, sliding mode, state feedback linearization, etc.) such that the electric motor can produce the appropriate torque and speed converted by sensors (transducers) into electric signals through an interface circuitry [33]. These signals are then conditioned to the appropriate level and fed to be processed by a processor. For a good insight into the electric propulsion system the reader can find details in [33]. Choosing an electric drive system for a particular EV depends on the driver's expectations, the vehicle's constraints, and the power source. About driver's expectations (driving style) were mentioned in the previous section, three driving cycles, FTP-75, NEDC and WLTP, for analyzing robustness performance analysis of the EKF SOC estimator. Vehicle constraints, including "volume and weight, depend on vehicle type, weight, and payload" [33]. In the case study, the power source refers to the selection of a Li-ion battery such that its terminal voltage, rated capacity, and rated power are adapted to the electric motor of certain EVs. A traditional DC motor drive typically needs a commutator and brushes to "feed current into the armature, making it less reliable and unsuitable for maintenance-free operation and high speed" [33]. Also, the "wound-excited DC motors have a low specific power density"; however, "because of their mature technology and simple control, DC motor drives have been prominent in electric propulsion systems" [33]. Five constructive configurations of DC motors are manufactured: series excited, shunt excited, and compound excited, separately excited

and permanent magnet (PM) excited motors, as mentioned in [33]. For "proof of concept" and simulation purposes, this section is limited to a specific nonlinear DC motor drive model, focusing on the main aspects, such as nonlinearities, feedback linearization, challenges/issues when faced with the presence of singularities, the design and implementation in MATLAB Simulink of suitable nonlinear control strategies to be applied in realistic environments for a large range of EVs. If the results obtained will satisfy the expectations, an extension of them to AC motor drives will be a big challenge. A nonlinear third-order separately excited DC motor drive model (i.e., three internal states: armature current, field current and rotor speed) is adopted for the case study.

4.1 Field controlled DC motor drive-nonlinear model

4.1.1 DC motor drive – physical model

Applying Kirchhoff's voltage law (KVL) for both armature circuit and the field circuit, the DC motor drive model is described in continuous time by the following equations [35]:

For the field circuit: i_f is the field current, v_f is the field voltage:

$$L_f \frac{di_f}{dt} = v_f - R_f i_f \tag{19}$$

For the armature circuit: i_a is the armature current, v_a means the armature voltage, and $e_f = c_1 \omega i_f$ represents the back electromotive force (emf) induced in the armature circuit:

$$L_a \frac{di_a}{dt} = v_a - R_a i_a - c_1 \omega i_f \tag{20}$$

For shaft motion: $T = c_2 i_a i_f$ is the torque due to the interaction of armature current with the field circuit flux:

$$J \frac{d\omega}{dt} = c_2 i_a i_f \tag{21}$$

State-output equation:

$$y = \omega \tag{22}$$

4.1.2 DC motor drive: State space representation

After some mathematical manipulations the DC motor drive is described in a simple form of state space representation [32, 33]:

$$\frac{dx_1}{dt} = -ax_1 + u \tag{23}$$

$$\frac{dx_2}{dt} = -bx_2 - cx_1 x_3 + q \tag{24}$$

$$\frac{dx_3}{dt} = \theta x_1 x_2, \tag{25}$$

$$y = x_3 \tag{26}$$

where

$$x_1 = i_f, x_2 = i_a, x_3 = \omega \tag{27}$$

and, the numerical values are set to the same values as in [35]:

$$a = \frac{R_f}{L_f} = 103.995, b = \frac{R_a}{L_a} = 35.4034, c = \frac{c_1}{L_a} = 1.45, q = \frac{v_a}{L_a} = 52.7588 \tag{28}$$

$$\theta = \frac{c_2}{J} = 230.769, \omega_0 = 10 \left[\frac{rad}{s}\right] \tag{29}$$

The DC motor drive model given by Eqs. (23)–(26) is nonlinear since the product $x_1 x_3$ appears in the second equation, and the product $x_1 x_2$ appears in the third equation.

4.1.3 DC motor drive: State feedback linearization

The DC motor drive model can be writing in a general vectorial field form:

$$\frac{dx}{dt} = f(x) + g(x)u \tag{30}$$

$$y = h(x) \tag{31}$$

where the field vectors f(x), g(x) and h(x) have the vectorial form:

$$f(x) = \begin{bmatrix} f_1(x) \\ f_2(x) \\ f_3(x) \end{bmatrix} = \begin{bmatrix} -ax_1 \\ -bx_2 - cx_1x_3 + q \\ \theta x_1 x_2 \end{bmatrix}, g(x) = \begin{bmatrix} 1 \\ 0 \\ 0 \end{bmatrix}, h(x) = \begin{bmatrix} 0 & 0 & 1 \end{bmatrix} \tag{32}$$

Preliminaries: Feedback Linearization, Lie derivative definition, Diffeomorphism – Definitions.

Definition 1. A nonlinear system described in a state space representation (30) and (31), where the nonlinear functions f: $D_0 \mapsto R^n, g : D_0 \mapsto R^n$ are sufficiently smooth on a domain $D_0 \subset R^n$ is said to be feedback linearizable (or input-state linearizable) if there exists a diffeomorphism, $T : D_0 \mapsto R^n$ such that $Dz = T(D_0)$ contains the origine and the change of variable $z = T(x)$ transforms the system given by Eqs. (30) and (31) into a linear system of the form

$$\frac{dz}{dt} = Az + B\gamma(x)[u - \alpha(x)] \tag{33}$$

that has the pair of the matrices (A, B) controllable and $\gamma(x)$ invertible (or nonsingular) for all $x \in D_0$,as is also mentioned in [34].

Remark 2. If linearizing the state equation does mean that at a same time is also linearized the output equation [34].

Remark 3. The state feedback control or partially feedback linearizable systems is an excellent control tool that can solve both system stabilization and reference tracking control [34].

Definition 2. If the DC motor drive described by Eqs. (30) and (31) can be put in the form given by Eq. (33) then it can be linearized via the state feedback, choosing for the input u the following control law [34]

$$u = \alpha(x) + \beta(x)v \tag{34}$$

and

$$\beta(x) = \gamma(x)^{-1} \tag{35}$$

To stabilize the DC motor drive model, the new control law v introduced in Eq. (34) is designed as

$$v = -Kx \tag{36}$$

such that the matrix $(A - BK)$ is Hurwitz, equivalent to say that the pair (A, B) is controllable (stabilizable).

The original nonlinear stabilizing state feedback control in closed-loop is given by

$$u = \alpha(x) - \beta(x)Kx \tag{37}$$

Remark 4. The DC motor drive state feedback linearized (FL) model is not unique and depends on the choice of the state variables.

Definition 3. (Lie derivative operator). Assuming that the vector field functions f(x), g(x) and h(x) are sufficiently smooth in a domain $D_0 \subset R^n$, then the mapping functions f and g on $D_0 \subset R^n$ and the first derivative of the output variable $\frac{dy}{dt}$ can be put in the following form [34–36]

$$\frac{dy}{dt} = \frac{dy}{dx}\frac{dx}{dt} = \frac{\partial h}{\partial x}[f(x) + g(x)u] \triangleq L_f h(x) + L_g h(x)u \tag{38}$$

were the Lie derivative operators $L_f h$ and $L_g h$ defined as

$$L_f h(x) = \frac{\partial h}{\partial x}f(x), L_g h(x) = \frac{\partial h}{\partial x}g(x) \tag{39}$$

are called the Lie derivatives of h to respect to f (or equivalent, along f), and of h to respect to g (along g), respectively.

In fact, the notation $L_f h(x) = \frac{\partial h}{\partial x}f(x)$ is an adapted concept of the derivative of h along the trajectories of the system $\frac{dx}{dt} = f(x)$. It is an appropriate formal procedure for repeating the calculation of the derivative with respect to the same vector field or a new one [34], such as

$$L_g L_f h(x) = \frac{\partial(L_f h)}{\partial x}g(x), L_f^0 h(x) = h(x), L_f^2 h(x) = L_f L_f h(x) \tag{40}$$

Or, in a general repetitive form given by

$$L_f^k h(x) = L_f L_f^{k-1} h(x) = \frac{\partial \left(L_f^{k-1} h \right)}{\partial x} f(x) \tag{41}$$

Remark 5. The repetitive notation (41) applied on DC motor drive output y, leads to the following main result of using the full state feedback linearization (FSFL):

If $L_g h(x) = 0$, it means that

$$\frac{dy}{dt} = L_f h(x), \tag{42}$$

and can be interpreted as independence of function $\frac{dy}{dt}$ with respect to the input u.

If $L_g L_f h(x) = 0$, then

$$y^{(2)} = \frac{d}{dt} \left(\frac{dy}{dt} \right) = \frac{d}{dt} \left(L_f h(x) \right) = \frac{\partial (L_f h)}{\partial x} \frac{dx}{dx} = \partial \frac{(L||fh)}{\partial x} [f(x) + g(x)u] \tag{43}$$

Then, the final result is

$$y^{(2)} = L_f^2 h(x) + L_g L_f h(x)u = L_f^2 h(x) \tag{44}$$

and it means that the second derivative of the output $y^{(2)}$, is also independent of input u.

Iteratively, by repeating the procedure, and

If $L_g L_f^{k-1} h(x) = 0$, for $k = 1, \rho - 1$, and $L_g L_f^{\rho-1} h(x) \neq 0$, therefore in the first $(\rho - 1)$ derivatives of the output y the input u does not appear, it only occurs in the last derivative $y^{(\rho)}$ [34]

$$y^{(\rho)} = L_f^\rho h(x) + L_g L_f^{\rho-1} h(x)u \tag{45}$$

The last equation (45) is showing without doubt that the model is input-output linearizable, of ρ the relative degree, and is in the required form given in Eqs. (30) and (31). The control law u, can be written in the following form

$$u = \frac{L_f^\rho h(x)}{L_g L_f^{\rho-1} h(x)} \left[-L_f^\rho h(x) + v \right] \tag{46}$$

that leads to a following form for the input-output map [34]

$$y^{(\rho)} = v \tag{47}$$

as the result of a chain of ρ integrators applied to the output y.

For the normal canonical form, the new control law v from Eq. (46) is chosen as

$$v = -Kx \tag{48}$$

where, the feedback gain K is calculated using a pole placement procedure, using the following MATLAB code line:

$$K = place \left(A, B, \left[p_1, p_2, ..., p_\rho \right] \right) \tag{49}$$

where $p_1, p_2, \ldots, p_\rho$ represent the poles' locations in the left-half plane of the complex domain, such as the matrix $(A - BK)$ is Hurwitz (the system in closed-loop and canonical form is stable).

If the relative degree $\rho = n = dim(x \in R^x)$, the state-space dimension, then the system is full-state linearizable (FSL) and stabilizable. Also, the transformation $T : D_0 \mapsto R^n$ with $z = T(x)$ that convert the system given by Eqs. (30)–(31) into the form defined in Eq. (33) is a diffeomorphism. The new variables z are defined as follows [34]:

$$z = T(x) = \begin{bmatrix} h(x) \\ L_f h(x) \\ . \\ . \\ L_f^{n-1} h(x) \end{bmatrix} \tag{50}$$

that converts the system into normal minimal form defined by [34]

$$\frac{dz}{dt} = A_c z + B_c \gamma(x)[u - \alpha(x)] \tag{51}$$

$$y = C_c z \tag{52}$$

The following choice of the input u [21, 22]

$$u = \alpha(x) + \gamma(x)^{-1} v \tag{53}$$

brings the system in a canonical form [34–36]

$$\frac{dz}{dt} = A_c z + B_c v, y = C_c z \tag{54}$$

Therefore, the state transformation defined in Eq. (50) is a full-state linearization, and in the same time also, is an input-output linearization [34].

In the case when the relative degree $\rho < n$ then the state feedback linearization problem is brining some complications (issues) such singularities and instability. In this case the transformation $z = T(x)$ converts the original system into following form [34]

$$z = T(x) = \begin{bmatrix} \eta \\ \ldots\ldots \\ \xi \end{bmatrix} = \begin{bmatrix} \phi_1(x) \\ . \\ . \\ \phi_{n-\rho}(x) \\ \ldots \ldots \ldots \ldots \\ h(x) \\ L_f h(x) \\ . \\ . \\ L_f^{\rho-1} h(x) \end{bmatrix} = \begin{bmatrix} \Phi(x) \\ \ldots \ldots \ldots \\ \Psi(x) \end{bmatrix} \tag{55}$$

where the functions $\phi_1(x)$, $\phi_2(x)$, $\ldots \ldots, \phi_{n-\rho}(x)$ are selected such that the transformation $T(x)$ still to remains a diffeomorphism. Additionally, in [34] is stated that

such of functions $\phi_i(x), i = 1, n - \rho$, do exist at least locally, satisfying the following conditions:

$$\frac{\partial \phi_i(x)}{\partial x} g(x) = 0, \forall i = 1, n - \rho \tag{56}$$

The transformation given by Eq. (55) converts the system into the following canonical form

$$\frac{d\eta}{dt} = f_0(\eta, \xi) \tag{57}$$

$$\frac{d\xi}{dt} = A_c \xi + B_c \gamma(x)[u - \alpha(x)] \tag{58}$$

$$y = C_c \xi \tag{59}$$

$$u = \alpha(x) + \gamma(x)^{-1} v \tag{60}$$

and,

$$f_0(\eta, \xi) = \frac{d\Phi(x)}{dx} = \frac{\partial\Phi(x)}{\partial x} f(x)_{x=T(x)^{-1}}, \gamma(x) = L_g L_f h(x), \alpha(x) = \frac{-L_f^\rho h(x)}{L_g L_f^{\rho-1} h(x)} \tag{61}$$

The following main valuable results can be extracted from this general modeling approach:

1. Internal dynamics of the system, described by the Eq. (57)

$$\frac{d\eta}{dt} = f_0(\eta, \xi)$$

It is noticeable that this dynamic is unobservable for the system output y, therefore it does not directly affect the other states ξ or the system output y since it does not appear in Eq. (58) or Eq. (59).

For the internal dynamics of the system is required to solve the **stabilization problem** around the origin of its zero dynamics

2. Zero dynamics of the internal dynamics of the system

It is obtained for $\xi = 0$, and first equation of the system dynamics in normal form becomes

$$f_0(\eta, 0) = 0$$

3. Input-output linearization of the system

The system defined by Eqs. (58) and (59) is a linear system for which two critical closed-loop problems can be solved:

   a. Stabilization problem

      b. Tracking problem to an input reference, constant or time varying, with zero steady-state error.

Interestingly, by solving the tracking problem for the linear part of the system dynamics described by Eqs. (58) and (59), the general tracking problem for the nonlinear system is also solved, but only if the internal dynamics of the same system is stable at the origin of zero dynamics of the internal dynamics of the system given by $f_0(\eta, 0) = 0$.

Repeating the Lie derivative operator in the Eq. (45) three times on DC motor drive output y, the following results are obtained

$$\frac{dy}{dt} = \frac{dx_3}{dt} = \theta x_1 x_2, \frac{d^2 y}{dt^2} = \theta \frac{dx_1}{dt} x_2 + \theta x_1 \frac{dx_2}{dt} = M(x_1, x_2, u) + N(x_1, x_2, x_3) \quad (62)$$

where
$M(x_1, u) = \theta(-ax_1 + u)x_2$, depends on u, instead.
$N(x_1, x_2, x_3) = \theta x_1(-bx_2 + q - cx_1 x_3)$ it is not dependent on u.
therefore,

if $x_2 \neq 0$, then $\frac{d^2 y}{dt^2} \neq 0$, and since u appears in the second derivative the relative degree of the DC motor drive model is $\rho = 2$. In conclusion, the DC motor drive model has $\rho = 2$ on the set $D = \{x \in R^3 | x_2 \neq 0\}$, so it is worth to notice a singularity of the DC motor drive model when the state $x_2 = 0$.

A transformation of state variables $z = T(x)$ such is defined in Eq. (55) has the form

$$z = T(x) = \begin{bmatrix} \phi_1(x) \\ h(x) \\ L_f h(x) \end{bmatrix} \quad (63)$$

By calculation,

$$L_f h(x) = \frac{\partial h}{\partial x} f(x) = [001] \begin{bmatrix} -ax_1 \\ -bx_2 - cx_1 x_3 + q \\ \theta x_1 x_2 \end{bmatrix} = \theta x_1 x_2$$

$$\frac{\partial \phi_1}{\partial x} g(x) = \begin{bmatrix} \frac{\partial \phi_1}{\partial x_1} & \frac{\partial \phi_1}{\partial x_2} & \frac{\partial \phi_1}{\partial x_3} \end{bmatrix} \begin{bmatrix} 1 \\ 0 \\ 0 \end{bmatrix} = \frac{\partial \phi_1}{\partial x_1} = 0, \text{ according to the constraint given in Eq. (56)}$$

to exist the function $\phi_1(x)$ and the transformation $z = T(x)$ to be diffeomorphism on the set $D = \{x \in R^3 | x_2 \neq 0\}$.

The equation $\frac{\partial \phi_1}{\partial x_1} = 0$ shows an independence of function $\phi_1(x)$ on x_1. A simpler solution for this equation is only $\phi_1(x) = x_2, \vee \phi_1(x) = x_3$, but the second solution is not good since the transformation $z = T(x)$ is not more a diffeomorphism.

One of the possible solutions can be chosen $\phi_1(x) = x_2$, even if exist other choices, but not simple than this last selection [34].

So, we can write that $z = T(x) = \begin{bmatrix} x_2 \\ x_3 \\ \theta x_1 x_2 \end{bmatrix} = \begin{bmatrix} \eta \\ \xi_1 \\ \xi_2 \end{bmatrix}$ and after some math manipu-

lations the dynamics in the new variables can be written as

a. The internal dynamics is given by:

$$\frac{d\eta}{dt} = -b\eta + q - c\frac{\xi_1\xi_2}{\theta\eta} = f_0(\eta, \xi), \xi = (\xi_1, \xi_2) \tag{64}$$

b. The normal form of the DC motor drive dynamics is given by:

$$\frac{d\xi_1}{dt} = \xi_2 \tag{65}$$

$$\frac{d\xi_2}{dt} = \theta x_2\left(u - (a+b)x_1 + q\frac{x_1}{x_2} - c\frac{x_1^2 x_3}{x_2}\right) \tag{66}$$

$$y = \xi_1 \tag{67}$$

For a simple choice of the input u to cancel all the nonlinearities in Eq. (66) such as

$$u = (a+b)x_1 - q\frac{x_1}{x_2} + c\frac{x_1^2 x_3}{x_2} + \frac{1}{\theta x_2}v \tag{68}$$

For this selection of the input u, the normal form of the DC motor drive dynamics is linear and described by two linear first order differential equations and a linear state output equation

$$\frac{d\xi_1}{dt} = \xi_2, \frac{d\xi_2}{dt} = v, y = \xi_1 \tag{69}$$

Since the DC motor drive model is linearized, both stabilization and tracking problems will be easily solved, but only if the stability of internal dynamics must be ensured, required to ensure the existence of the function $\phi_1(x) = x_2$, and the transformation $z = T(x)$ to be diffeomorphism [34]. The analysis of the internal stabilization of the DC motor drive model dynamics is performed by checking if the equation

$$\frac{d\eta}{dt} = -b\eta + q - c\frac{\xi_1\xi_2}{\theta\eta} = f_0(\eta, \xi) \tag{70}$$

is asymptotic stable around the origin $\xi = (\xi_1, \xi_2) = (0, 0)$, known also as zero dynamics, given by the following equation.

$f_0(\eta, 0) = 0$, so equivalent for asking that the equation given below is stable around an equilibrium point $(\eta, \xi) = \left(\eta_{ss} = \frac{q}{b}, \xi = 0\right)$.

$$\frac{d\eta}{dt} = -b\eta + q \tag{71}$$

Lemma 1. "The origin of the closed loop system is asymptotic stable if the origin of zero dynamics is asymptotic stable", as is stated in [34].

According to this Lemma, the DC motor drive connected in closed-loop is asymptotic stable only if the origin of its zero dynamics model is asymptotic stable. In other words, the asymptotic stability of zero dynamics guarantees the asymptotic stability of closed loop linearized system.

4.2 Zero dynamics interpretation

As long as $b > 0$, the origin of zero dynamics (71) of the DC motor drive model is exponentially asymptotic stable since the solution of the homogeneous equation (71) is given by:

$$\eta_0(t) = e^{-bt}\eta(0) \tag{72}$$

since $\eta_0(t) \to 0, when\, t \to \infty$, then the origin of zero dynamics is exponentially asymptotic stable, and according to Lemma 1, the origin of the closed-loop system is also asymptotic stable.

Conclusion: If zero dynamics of the system is not asymptotically stable then the linearization of the nonlinear system is not possible to be realized.

In closed loop, the input u (DC motor armature voltage) is defined in the original state variables x_1, x_2, x_3 as

$$u = (a + b)x_1 - q\frac{x_1}{x_2} + c\frac{x_1^2 x_3}{x_2} - \frac{1}{\theta x_2}v, \wedge v = -(k_1\xi_1 + k_2\xi_2) \tag{73}$$

and replacing ξ_1, ξ_2 by $\xi_1 = x_3, \xi_2 = \theta x_1 x_2$, u becomes:

$$u = (a + b)x_1 - q\frac{x_1}{x_2} + c\frac{x_1^2 x_3}{x_2} - \frac{1}{\theta x_2}(k_1 x_3 + k_2\theta x_1 x_2) \tag{74}$$

The Simulink model of the open loop and closed loop of the DC motor drive is shown in **Figure 11**.

The MATLAB Simulink simulations results for the nonlinear DC motor drive (DCMD) connected in open loop are shown in **Figure 12a** and **b** for field current $i_f = x_1$, armature current $i_a = x_2$, and DCMD speed ω=x_3 [rad/s] for a step input voltage test, u = 12 [V].
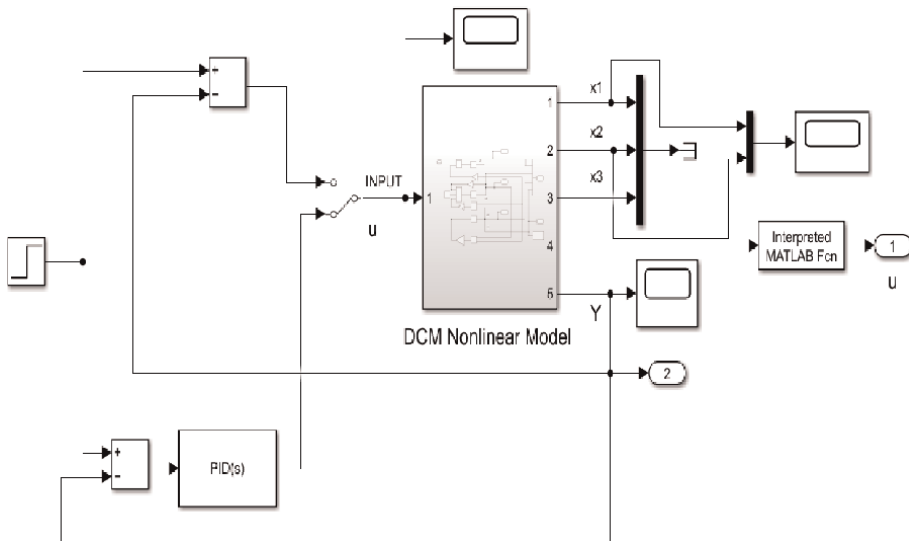
Figure 11.
DCM drive – Simulink nonlinear model, closed-loop control loop and PID control law for reference tracking.

In **Figure 12a** are presented the DCMD field and armature currents and in **Figure 12b** is depictured the DCM speed in rad/s. It is noticeable that the current field remains constant when the DCMD is running and the armature current increases from initial condition value at approximative 1.5 A and then during the steady-state decreases to zero when RPM speed of DCMD is stabilized in steady state to approximate 314 rad/s.

In closed loop for DCMD state feedback linearized whose dynamics is described in Eq. (69) and the new input v is given by

$$v = -K\xi = -k_1\xi_1 - k_2\xi_2 \tag{75}$$

and the values of the coefficients k_1, k_2 are obtained through a pole placement technique that stabilizes the linearized system (69)

$$\begin{bmatrix} k_1 \\ k_2 \end{bmatrix} = place(A_c, B_c, [-2; -5]), A_c = \begin{bmatrix} 0 & 1 \\ 0 & 0 \end{bmatrix}, B_c = \begin{bmatrix} 0 \\ 1 \end{bmatrix}, k_1 = 10, k_2 = 7 \tag{76}$$

The MATLAB simulation results of the DCMD in closed loop canonical form (69) in the new state variables (η, ξ_1, ξ_2) are shown for the evolution of each variable and for actuator effort (v to stabilize these state variables are shown in the **Figure 13a** and **b**.

Figure 13a reveals the evolution of the states during the transient and in steady state, where zeta1 and zeta2 are stabilized to zero, and eta is stabilized to the equilibrium point (close to 1.49, that is $\eta_{ss} = \frac{q}{b}$, thus it validates the zero dynamics result). In **Figure 13b** is presented the actuator effort to stabilize all three variables around the equilibrium point of zero dynamics ($\eta_{ss} = \frac{q}{b} = 1.49, \xi_1 = 0, \xi_2 = 0$).

The MATLAB simulation results for closed loop partial state feedback linearization and state feedback input u given by Eq. (74) are shown in **Figure 14a–c**.

In **Figure 14a** is depicted the DCMD speed stabilized in steady state at equilibrium point of the closed system, similar as for zero dynamics. **Figure 14b** reveals the field and armature currents stabilized at same equilibrium point as for zero dynamics. In **Figure 14c** is visualized the effort of the actuator to keep stabilized the nonlinear

(a)   (b)
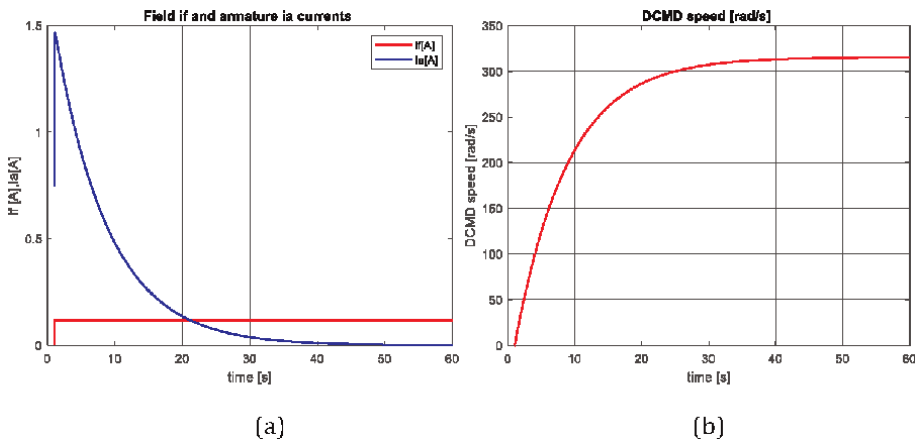
Figure 12.
MATLAB Simulink simulations results: (a) field and armature currents; (b) DCMD speed [rad/s].

(a)   (b)
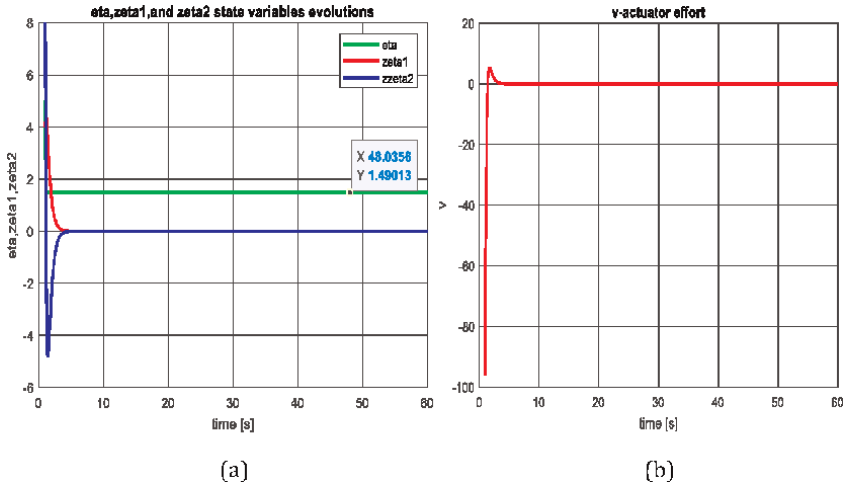
Figure 13.
MATLAB closed-loop simulations for DCMD model in canonical form: (a) the evolution of the new states (eta, zeta1, zeta2); (b) the actuator effort for stabilization.

(a)   (b)

(c)
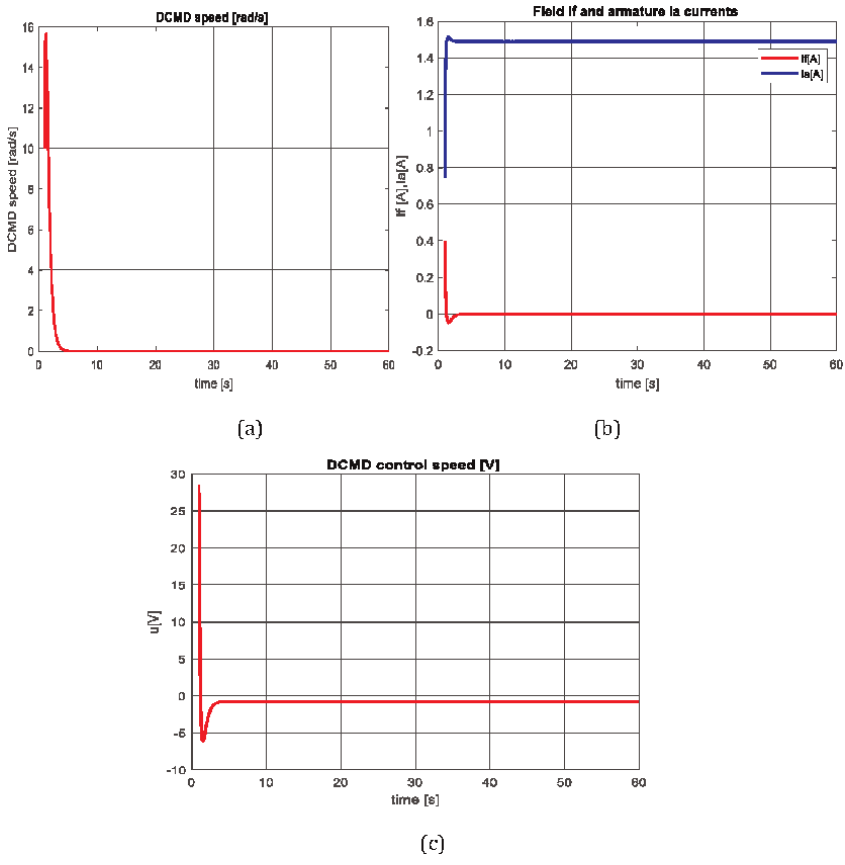
Figure 14.
MATLAB simulation results in closed-loop by feedback linearization; (a) the DCMD speed stabilization; (b) field and armature currents stabilization at equilibrium point; (c) the actuator effort to stabilize the DCMD in steady-state at equilibrium point.

system at an equilibrium point, same as for zero dynamics, therefore the result of Lemma 1 is now validated.

Tracking problem can be solved similar as stabilization but we need to substract from the output the reference input r, such that the error:

$$e(t) = y(t) - r(t) \to 0, \quad \text{when } t \to \infty \tag{77}$$

In **Figure 11** it can be seen both options for reference tracking of the DCM drive speed r = 100 rad/s. First option is an integration of the DCM nonlinear model in a unit output feedback closed loop that compares the output measured value to the desired track reference value r = 100 rad/s. The MATLAB Simulink simulations results are depictured in **Figure 15a** and **c**, as follows, field and armature currents in **Figure 15a**, the DCM Driver speed in rad/s revealed in **Figure 15b**, and the actuator effort is visualized in **Figure 15c**.

The second control law is a PID traditional law for which the MATLAB Simulink simulation results are presented in **Figure 16a** and **d**, with same significance as in


(a)

(b)

(c)
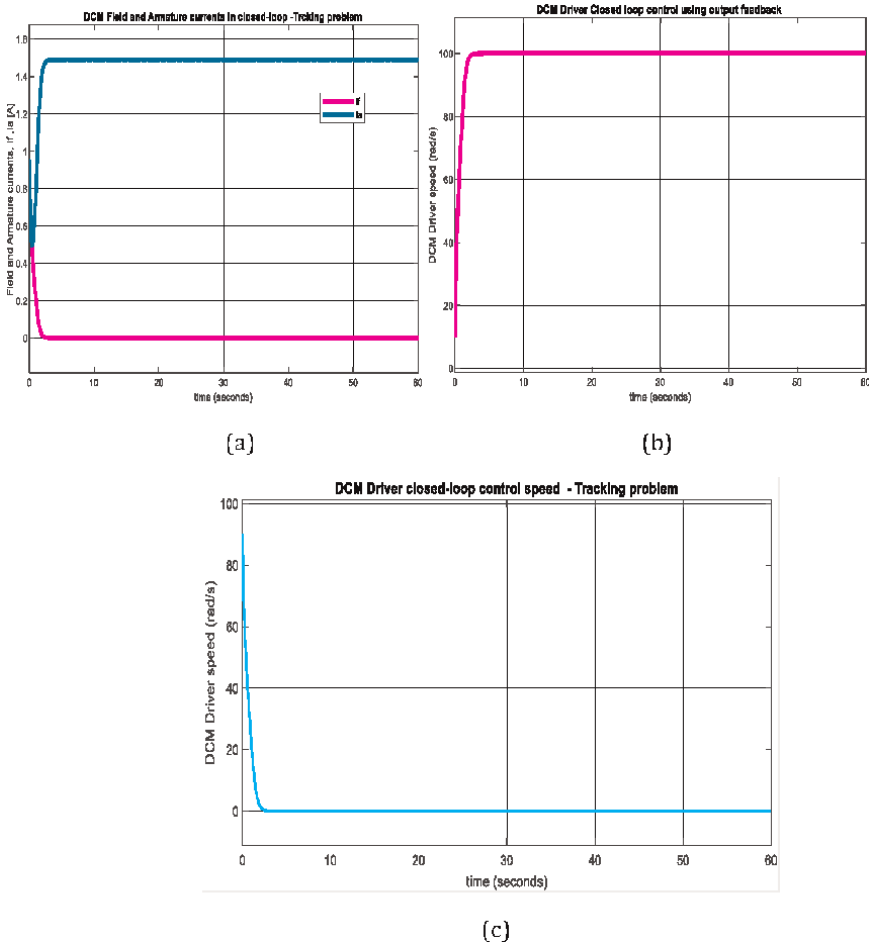
Figure 15.
DCM driver closed-loop control speed – MATLAB Simulink simulation results: (a) field and armature currents; (b) DCM driver tracking speed in rad/s; (c) actuator control effort.

Figures 15a and **c**, and the tuning settings values of PID controller parameters KP, K_I and K_D are shown in **Figure 16d**. Comparing the results obtained by using both closed-loop controls it is worth to notice that for first option the DCM speed is an aperiodic fast response (sharply) but with a big actuator effort, instead the PID controller response is slightly slower and smooth with a smaller actuator effort.

The feedback linearization can be performed also by taking advantage of deep training learning techniques to build intelligent neuro controllers. In MATLAB Simulink the Deep Learning Toolbox includes three interesting block sets to develop intelligent neuro controllers, namely NARMA-L2, Model Predictive and Reference Model. The end of this section is an introduction to nonlinear autoregressive moving average (ARMA), similar to SOC and battery terminal voltage, for which an intelligent NARX neural network estimator was developed in the Section 3. The NARMA-L2 smart controller is a brilliant tool for feedback linearization of nonlinear systems, such as the DCM drive described in this section, designed for use in possible EV applications. This intelligent neuro controller is data-driven, so does not require an accurate

(a)

(b)

(c)

(d)
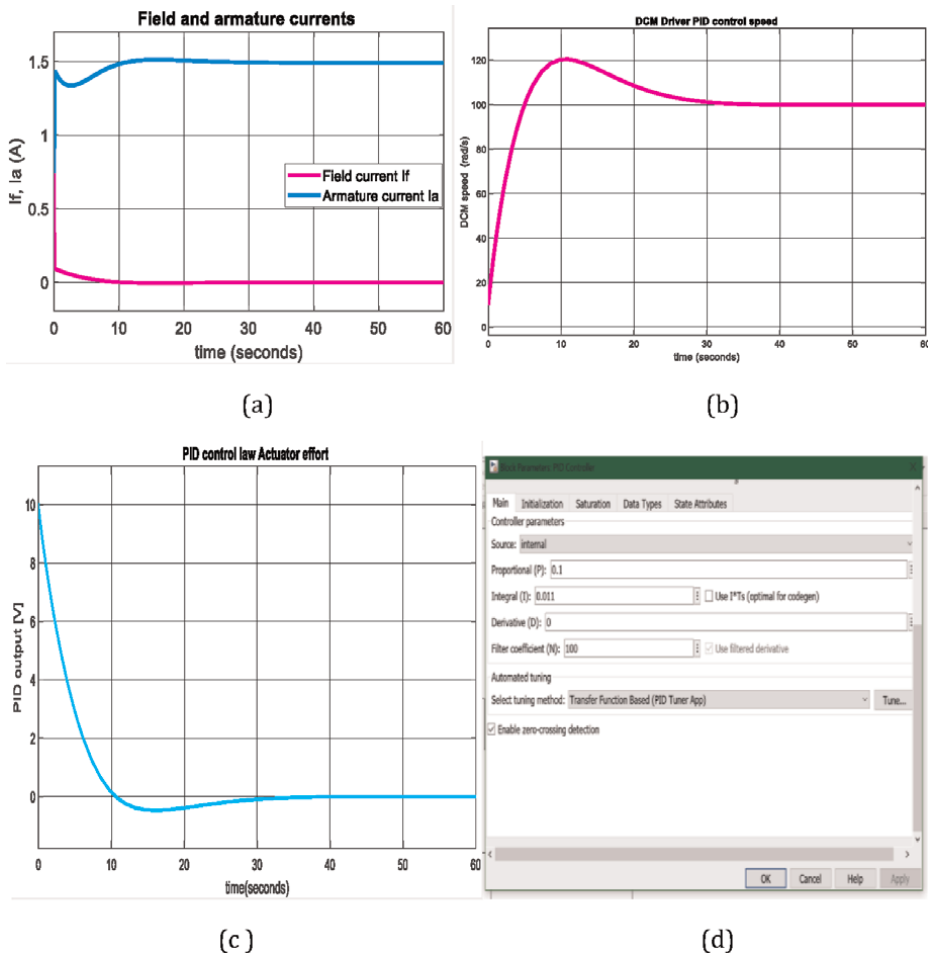
Figure 16.
MATLAB Simulink simulation results for DCM driver tracking problem using a PID control law: (a) field and armature currents; (b) DCM driver speed (rad/s); (c) PID actuator control law effort; (d) PID parameters tuning values settings.
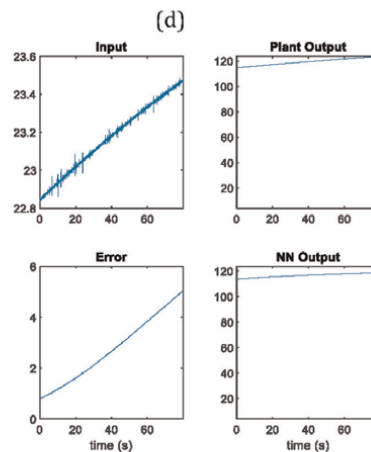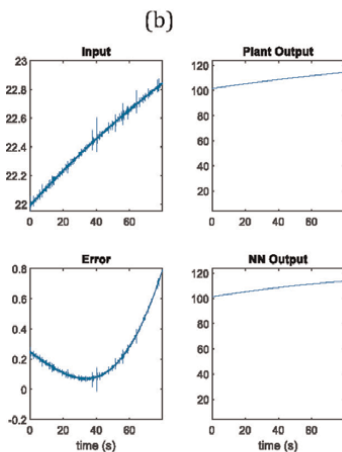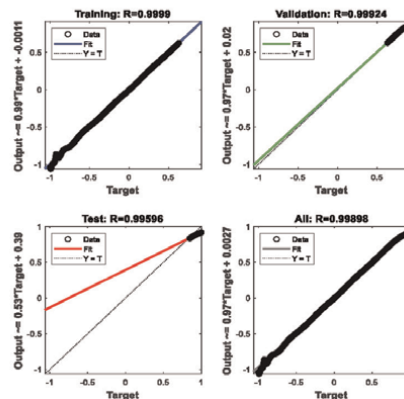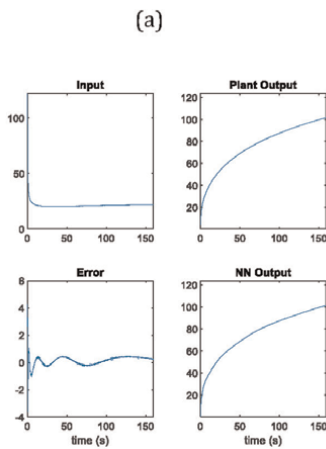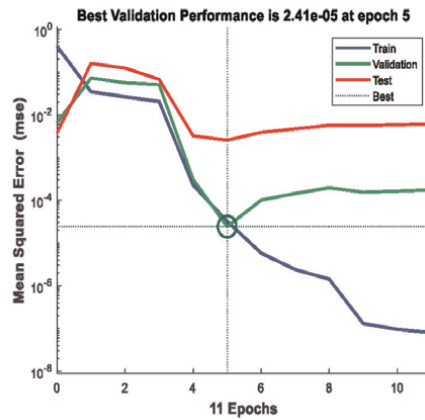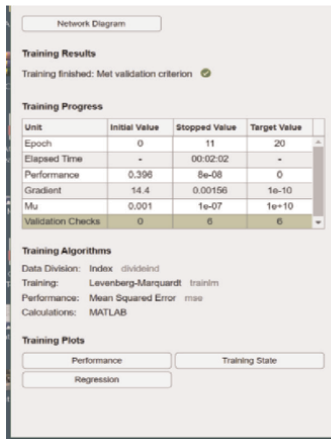
Figure 17.
MATLAB Simulink simulation results during learning step of DCM drive nonlinear model (feedback linearization): (a) process training results; (b) the best validation performance reached at epoch 5; (c) training phase process; (d) regression performance; (e) validation phase process; (f) testing phase process.
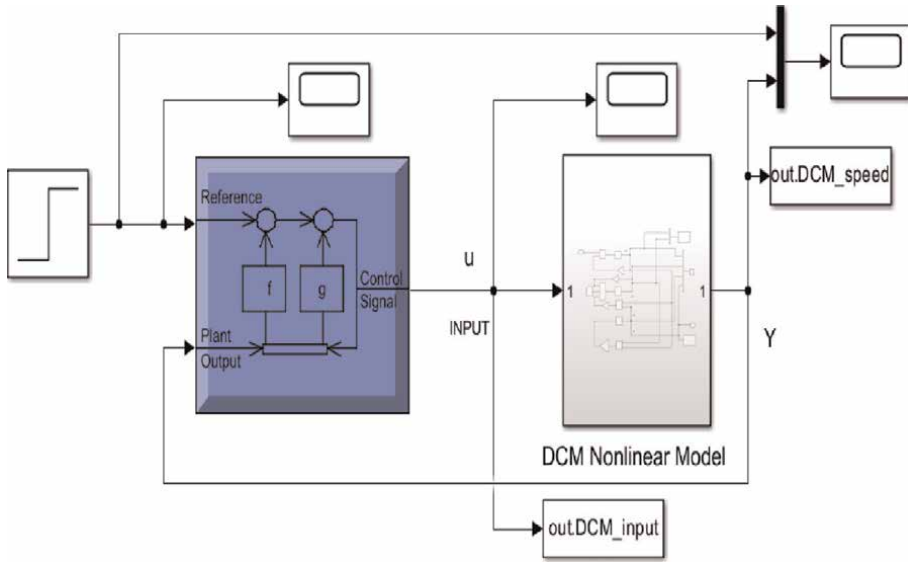
Figure 18.
MATLAB Simulink model of the DCM drive speed control in closed-loop using a NARMA-L2 controller.

model to perform well, and therefore the impact of some modeling imperfections will be significantly attenuated. To design such a controller, two steps must be followed. In the first step, the Deep learning Simulink block is trained separately to learn the nonlinear model, which is to be feedback linearized. In the second step, the trained neural network will be connected to the NARMA-L2 neuro controller to perform a reference tracking problem, similar to nonlinear feedback linearization. So, all the nonlinearities will be canceled in the first step, and in the second step, the controller solve a reference tracking problem. The main reason for finishing this research is to open some exciting research directions in developing intelligent neuro controllers that deal with all types of nonlinearities. Only the first step is solved in this research, i.e., the Simulink neuro controller block learns the nonlinear model of the DCM drive to be connected to the neuro controller for performing the reference tracking problem. The MATLAB Simulink simulation results are presented in **Figure 17a–f**, with the following meaning, training process results in **Figure 17a**, the best validation performance during the training process in **Figure 17b**, training data phase in **Figure 17c**, regression performance in all the stages (training, validation and test), is shown the in **Figure 17d**, validation data phase in **Figure 17e**, and test data phase in **Figure 17f**.

The Simulink model block of NARMA-L2 controller is illustrated in **Figure 18**.

5. Conclusion

The following results are worth highlighting among the authors' main contributions to this book chapter.

- 2RC ECM Li-ion battery model selection, design and implementation, a rigorous performance analysis.

- EKF SOC estimation and terminal voltage prediction design, implementation, and performance analysis in terms of SOC accuracy and robustness.

- An intelligent advanced NARX neural network deep learning SOC estimator, terminal voltage predictor, and curve fitting of nonlinear Li-ion battery characteristics OCV = f(SOC).

- A DCM drive nonlinear model selection with a detailed description of nonlinear linearization techniques such as full and partial state feedback, input-output linearization and advanced intelligent NARMA-L2 neuro-controller. The main issues/challenges problems were revealed, focussing on possible singularities, internal dynamics, zero dynamics, closed loop stabilization and reference tracking problems to be solved.

- Closed-loop DCM drive speed control techniques, such as full state feedback linearization, the closed-loop output unit negative feedback, PID controller, and performance comparison.

All the algorithms' implementation and extensive simulations were conducted on MATLAB Simulink R2023b software platform, a valuable and the strongest implementation tool from the software engineering market, in a beautiful and user-friendly environment. The MATLAB Simulink simulation results proved that the advanced intelligent estimators outperform the traditional ones. For future work, the research continues in the direction of design and implementation of new advanced intelligent learning techniques and neuro controllers such as NARMA-L2, Model Predictive and Model Reference neuro controllers. The energy management performance of the Li-ion battery connection to the DCM drives will be further investigated.

Conflict of interest

The authors declare no conflict of interest.

Author details

Roxana-Elena Tudoroiu[1], Mohammed Zaheeruddin[2], Nicolae Tudoroiu[3*],
Sorin Mihai Radu[1] and Hana Chammas[3]

1 University of Petrosani, Petrosani, Romania

2 Concordia University from Montreal, Montreal, Canada

3 John Abbott College, Sainte-Anne-de-Bellevue, Canada

*Address all correspondence to: ntudoroiu@gmail.com

IntechOpen

References

[1] Xia B, Zheng W, Zhang R, Lao Z, Sun Z. Mint: A novel observer for Lithium-ion battery state of charge estimation in electric vehicles based on a second-order equivalent circuit model. Énergies. 2017;**10**(8):1150. DOI: 10.3390/en10081150. Available from: http://www.mdpi.com/1996-1073/10/8/1150/htm

[2] Young K, Wang C, Wang LY, Strunz K. Electric vehicle battery technologies–chapter 2. In: Garcia-Valle R, Lopes JAP, editors. Electric Vehicle Integration into Modern Power Networks. 1st, 9 and 32 ed. New-York, USA: Springer Link: Springer-Verlag; 2013. pp. 15-26. DOI: 10.1007/978-1-4614-0134-6

[3] Farag M. Lithium-ion batteries. In: Modeling and State of Charge Estimation. Ontario, Canada: McMaster University of Hamilton; 2013. p. 169

[4] Tudoroiu RE, Zaheeruddin M, Radu SM, Tudoroiu N, Martinez LR, Prieto MD, editors. New trends in electrical vehicle powertrains. New Trends Electrical Vehicles in Powertrains. 2019;**4**:55-81. DOI: 10.5772/intechopen.76230.ch4

[5] Plett GL. Extended Kalman filtering for battery management systems of LiPB-based HEV battery packs: Part 2. Modeling and identification. Power Sources. 2004;**134**:262-276. DOI: 10.1016/j.jpowsour.2004.02.032

[6] Zhang R, Xia B, Li B, Cao L, Lai Y, Zheng W, et al. State of the art of Li-ion battery SOC estimation for electrical vehicles. Energies. 2018;**11**:1820

[7] Zhongqiang W, Shang M, Shen D, Qi S. SOC estimation for batteries using MS-AUKF and neural network. Journal

of Renewable and Sustainable Energy. 2019;**11**:024103. DOI: 10.1063/1.5064479

[8] Ali MU, Zafar A, Nengroo SH, Hussain S, Junaid Alvi M, Kim H-J. Towards a smarter battery management system for electric vehicle applications: A critical review of Lithium-ion battery state of charge estimation. Energies. 2019;**12**:446. DOI: 10.3390/en12030446

[9] Alyakhni A, Boulon L, Vinassa J-M, Briat O. A comprehensive review on energy management strategies for electric vehicles considering degradation using aging models. IEEE Access. 2021;**9**:143922-143940. DOI: 10.1109/ACCESS.2021.3120563

[10] Ghaeminezhad N, Monfared M. Charging control strategies for lithium-ion battery packs: Review and recent developments. IET Power Electronics. 2022;**15**:349-367. DOI: 10.1049/pel2.12219

[11] Nuroldayeva G, Serik Y, Adair D, Uzakbaiuly B, Bakenov Z. State of health estimation methods for Lithium-ion batteries. International Journal of Energy Research. 2023;**2023**:21. DOI: 10.1155/2023/4297545

[12] Pang B, Chen L, Dong Z. Data-driven degradation Modeling and SOH prediction of Li-ion batteries. Energies. 2022;**15**:5580. DOI: 10.3390/en15155580

[13] Camargos M, Angelov P. State of health and lifetime prediction of lithium-ion batteries using self-learning incremental models. In: Proceedings of the 7th European Conference of the Prognostics and Health Management Society, Turin, Italy. 2022

[14] Li M, Liu F, Han B, et al. Research on temperature control performance of

battery thermal management system composited with multi-channel parallel liquid cooling and air cooling. Ionics. 2021;**27**:2685-2695. DOI: 10.1007/s11581-021-04033-w

[15] Yuan S, Hongjie W, Yin C. State of charge estimation using the extended Kalman filter for battery management systems based on the ARX battery model. MDPI, Energies Journal. 2013;**6**:444-470. DOI: 10.3390/en6010444

[16] Rzepka B, Bischof S, Blank T. Implementing an extended Kalman filter for SoC estimation of a Li-ion battery with hysteresis: A step-by-step guide. Energies. 2021;**14**:3733. DOI: 10.3390/en14133733

[17] Cheng M, Fang F, Navon IM, Pain C. Ensemble Kalman filter for GAN-ConvLSTM based long lead-time forecasting. Journal of Computational Science. 2023;**69**:102024. DOI: 10.1016/j.jocs.2023.102024

[18] Askari I, Haile MA, Tu X, Fang H. Implicit particle filtering via a Bank of nonlinear Kalman filters. Systems and Control. 2022;**145**:110469. DOI: 10.1016/j.automatica.2022.110469

[19] Namdari A, Samani MA, Durrani TS. Lithium-ion battery prognostics through reinforcement learning based on entropy measures. Algorithms. 2022;**15**:393. DOI: 10.3390/a15110393

[20] Zraibi B, Mansouri M, Okar C. Comparing single and hybrid methods of deep learning for remaining useful life prediction of lithium-ion batteries. In: The 4th International Conference of Computer Science and Renewable Energies (ICCSRE'2021), E3S Web of Conferences, Agadir, Morocco. Vol. 297. July 2021. p. 8. DOI: 10.1051/e3sconf/202129701043

[21] Wang S, Ren P, Takyi-Aninakwa P, Jin S, Fernandez C. A critical review of improved deep convolutional neural network for multi-timescale state prediction of lithium-ion batteries. Energies. 2022;**15**:5053. DOI: 10.3390/en15145053

[22] Cui Z, Dai J, Sun J, Li D, Wang L, Wang K. Hybrid methods using neural network and Kalman filter for the state of charge estimation of lithium-ion battery. Hindawi Mathematical Problems in Engineering. 2022;**2022**:11. DOI: 10.1155/2022/9616124

[23] MathWorks MATLAB Version R2021b on-line Documentation, Neuro-Adaptive Learning and ANFIS. Available from: https://www.mathworks.com/help/fuzzy/neuro-adaptive-learning-and-anfis.html

[24] Konsoulas IS. Adaptive neuro-fuzzy inference systems (ANFIS) library for Simulink MATLAB Central File Exchange. Available from: https://www.mathworks.com/matlabcentral/fileexchange/36098-adaptive-neuro-fuzzy-inference-systems-anfis-library-for-simulink [Accessed: January 19, 2022]

[25] MathWorks MATLAB Version R2021b on-line Documentation, Neuro-Fuzzy Designer. Available from: https://www.mathworks.com/help/fuzzy/neurofuzzydesigner-app.html

[26] Bellali B, Hazzab A, Bousserhane IK, Lefebvre D. A decoupled parameters estimators for in nonlinear systems fault diagnosis by ANFIS. International Journal of Electrical and Computer Engineering (IJECE). 2012;**2**(2):166-174. DOI: 10.11591/ijece.v2i2.221

[27] MathWorks MATLAB Version R2023a on-line Documentation. Shallow neural network time-series prediction and modeling. 2023. https://www.math

works.com/help/deeplearning/gs/ neural-network-time-series-prediction-and-modeling.html [Accessed May 23, 2023]

[28] MathWorks MATLAB Version R2023a on-line Documentation. Multistep Neural Network Prediction. 2023. https://www.mathworks.com/ help/deeplearning/ug/multistep-neural-network-prediction.html [Accessed May 23, 2023]

[29] Tudoroiu N, Zaheeruddin M, Tudoroiu R-E, Radu MS, Chammas H. Intelligent deep learning estimators of a Lithium-ion battery state of charge design and MATLAB implementation-a case study. Vehicles. 2023;**5**:535-564. DOI: 10.3390/vehicles5020030

[30] Tudoroiu N, Zaheeruddin M, Tudoroiu R-E, Radu MS, Chammas H. Investigations on using intelligent learning techniques for anomaly detection and diagnosis in sensors signals in Li-ion battery-case study. Inventions. 2023;**8**:74. DOI: doi.org/10.3390/ inventions8030074

[31] Tiezhou W, Wang M, Xiao Q, Wang X. The SOC estimation of power Li-ion battery based on ANFIS model. Smart Grid and Renewable Energy. 2012;**3**:51-55. DOI: 10.4236/ sgre.2012.31007

[32] Jamlouie MHA. Accuracy Improvement of SOC Estimation IN LITHIUM-Ion Batteries by ANFIS Vs Ann MODELING of Nonlinear Cell Characteristics. Ontario, Canada: Ryerson University; 2018

[33] Ehsani M, Gao Y, Gay SE, Emadi A. Modern electric, hybrid electric, and fuel cell vehicles-fundamentals, theory, and design. In: Power Electronics and Applications Series, Rashid M.H., 2005,

1–419, University of West Florida, Boca Raton, FL. USA

[34] Khalil KH. Nonlinear Systems. 3rd ed. New Jersey, USA: Prentice-Hall; 2002

[35] Willson SS, Mullhaupt P, Bonvin D. Avoiding feedback-linearization singularity using a quotient method – The field-controlled DC motor case. In: 2012 American Control Conference; 27–29 June 2012. Montreal, Canada: IEEE; 2012. pp. 1-7. DOI: 10.1109/ACC.2012. 6315095

[36] Philip DO. Feedback linearization of DC motors. IEEE Transactions on Industrial Electronics. 1991;**8**(6)

[37] MathWorks MATLAB version R2023a. Design NARMA-L2 Neural Controller in Simulink. 2023. Available from: https://www.mathworks.com/he lp/deeplearning/ug/design-narma-l2-ne ural-controller-in-simulink.html [Accessed: May 26, 2023]

[38] Konsoulas I. Recurrent fuzzy neural network (RFNN) library for Simulink MATLAB Central File Exchange. 2022. Available from: https://www.math works.com/matlabcentral/fileexchange/ 43021-recurrent-fuzzy-neural-ne twork-rfnn-library-for-simulink [Accessed: January 19, 2022]

Chapter 2

Load-Sharing Management for Fuel Cell Hybrid Electric Vehicle (FCHEV) Based on Intelligent Controllers and Optimization Algorithms

Mustafa A. Kamoona and Juan Manuel Mauricio

Abstract

This study proposes an intelligent controller for a hydrogen-powered plug-in fuel cell hybrid electric vehicle (FCHEV) that integrates a fuel cell (FC) with two energy storage systems, which are ultracapacitor (UC) and battery (BAT), which results in a high dynamic response along with maintaining efficient use of resources for energy storage. Moreover, this controller works on effectively managing the system power flow to reduce the amount of power needed for the FCHEV. An effective energy management system (EMS) has been developed that utilizes the fuzzy logic controller (FLC) and artificial neural networks (ANNs) to achieve the EMS requirements. Also, the proposed system operates these three power sources at high efficiency with their mechanism performance, meets load power demands efficiently, and uses less hydrogen. Furthermore, the Crow Search Algorithm (CSA) and Particle Swarm Optimization (PSO) methods are utilized to adjust the parameters of the wavelet neural network that is connected to the PI controller, called WNN-PI. The DC-DC converters control the output voltage of the FC and BAT for maintaining the DC-bus voltage constant at 300 volts. The state-of-charge (SOC) for the BAT and UC is also considered in this study. The proposed system is analyzed and evaluated using the MATLAB/Simulink environment, and two vehicle driving cycles were implemented using the ADVISOR Simulator.

Keywords: FCHEV, artificial neural networks, CSA, fuzzy logic controller, PSO

1. Introduction

Nowadays, demand for electric vehicles (EV), as well as hybrid electric vehicles (HEVs), have grown in popularity for environmental reasons. Moreover, there are also several other benefits, such as a decrease in pollution also a cessation of dangerous gas emissions. The internal combustion engine (ICE) is regarded as one of the most widely utilized in transportation services as the primary power for driving automobiles. The ICE is a remarkable achievement in contemporary technology since it offers

a high level of power and has the ability to drive a vehicle over extended distances. Due to the fact that ICE burns petrol, it emits CO_2 and has a number of other drawbacks, including a high degree of complexity, loud noise operation, and entire reliance on a single fuel source.

In recent years, scientists and developers have concentrated on enhancing the performance of EVs [1–3]. HEVs especially are more functional and environmentally friendly than traditional cars [4]. The fuel cell electric vehicle (FCEV) uses hydrogen as fuel and produces only water as emissions. The FC engine has certain disadvantages as well, including a sluggish dynamic response, a high hydrogen cost, and a failure to use the car's regenerative braking power. To address these deficiencies, an FCHEV should be developed by integrating the FC engine with energy-storage devices such as UCs and BATs. The ultracapacitor (UC) has a very rapid dynamic reaction in order to adapt to the vehicle's unexpected load fluctuations. Therefore, the FC output power must be regulated. In addition, throughout the charging and discharging phases, the power flow between the battery, UC, and the load also must be efficiently managed. In order to actively optimize the control system, an energy management system (EMS) is necessary; along with the central control system for each converter, power electronics converters are also necessary to connect the power sources with the loads. Consequently, a lot of publications and investigation papers [5–11], as well as comprehensive review papers [12–14] for studying the importance of energy management for FCHEV.

The objective of this work is to create an intelligent energy management system (EMS) for the FCHEV that utilizes less hydrogen while effectively meeting the load power needs. The main power source of our proposed model plug-in hybrid FCEV is that the FC is meant to give power for steady-state loads only, whereas the UC is responsible for providing the transient power and the BAT is responsible for providing the medium frequency power. Also controlling the DC bus voltage; additionally, the power of the BAT supports the power output of the fuel cell in feeding the load if needed. This possibly be accomplished by providing the FC and BAT switching converters with the proper signals to guarantee that the hybrid FC system is working properly to handle the load dynamics. Also, this work presents two optimization algorithms, which are PSO and CSA.

2. Fuel cell hybrid electric vehicle configurations

Developing EVs has many factors, the most important one is the energy source cost sector. Therefore, researchers are being conducted using different designs of storage energy as well as a control system that aims to reduce the cost of energy storage with consideration of keeping a high level of improving efficiency. Thus, different configurations of EVs have been introduced [15], for example, some classifications of hybrid electric vehicle (HEV) such as series, parallel, and series–parallel. Meanwhile, the plug-in hybrid electric vehicle (PHEV) has the same configuration as HEV but with an extra plug-in port connection to charge from an external source at home or public charge stations. As shown in **Figure 1** the PHEV block diagram.

Overall, electric vehicles can be classified into three basic types, which are battery electric vehicles (BEVs) that use only batteries, fuel cell electric vehicles (FCEVs) that use only fuel cells stack, and hybrid electric vehicles (HEVs) that use a hybrid system. For example, HEVs such as batteries and other energies are called BHEVs or fuel cells stack and other energies are named FCHEVs. Moreover, all HEV types can be plug-in or not.
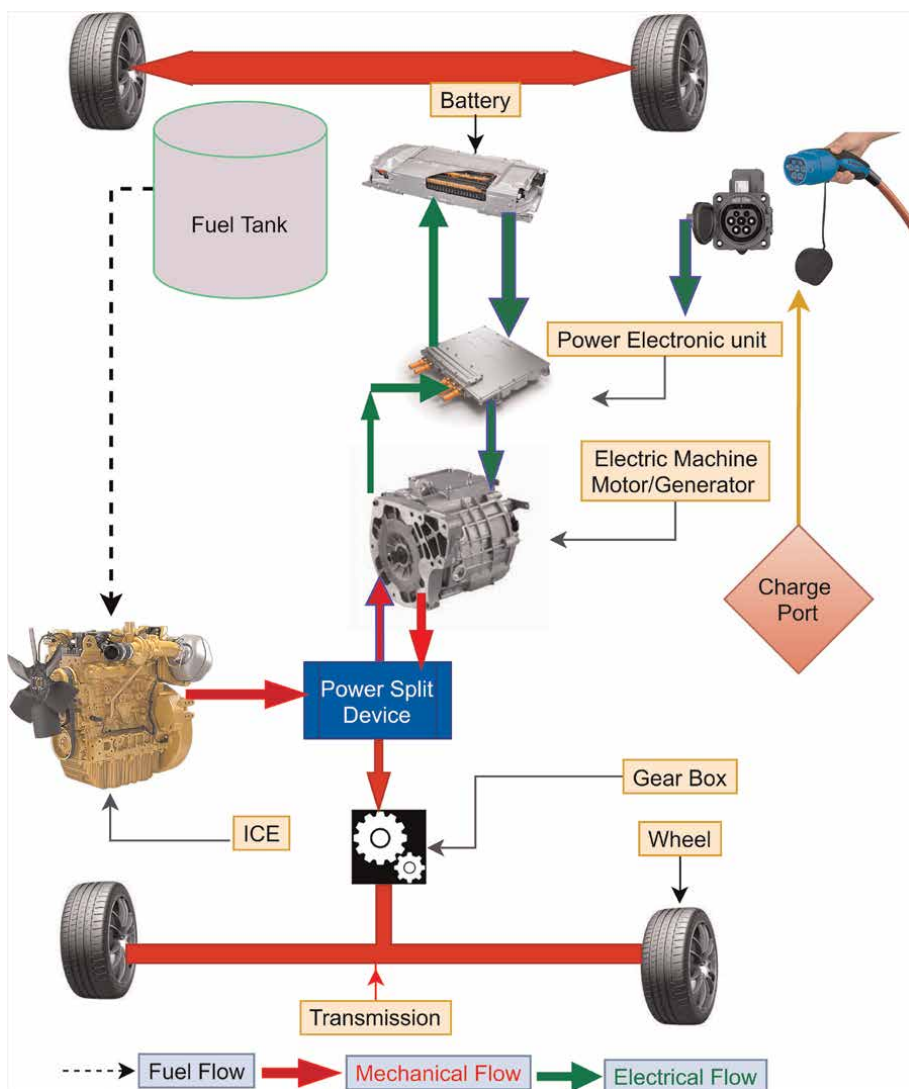
Figure 1.
PHEV block diagram.

The working principle of FCHEV can be summarized and simplified in three steps:

- Two or three powers in FCHEV, which are a fuel cell, battery, and/or ultracapacitor combined; and controlled by an (ex: intelligent control method) for the energy management system (EMS). First starting of the vehicle at very low load driving (low speed) of the FCHEV run by one of the power sources ultracapacitor or battery if the ultracapacitor/battery has sufficient energy to ensure soft starting.

- The FCHEV is run by fuel cells stack individually at normal load driving (normal speed) to drive the vehicle and charge the ultracapacitor/battery; but at
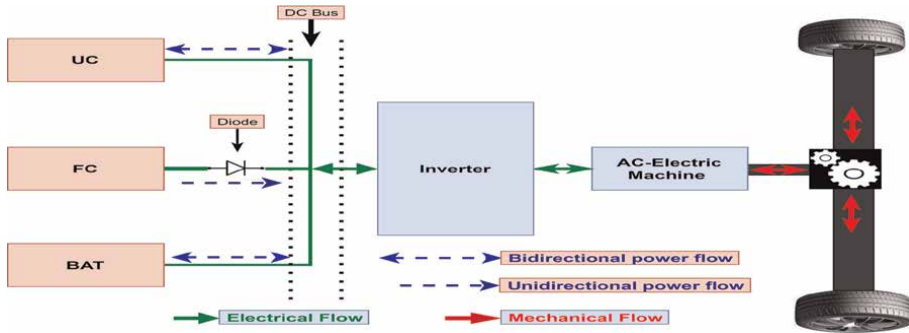
Figure 2.
The fundamental block diagram of the passive connection topology.
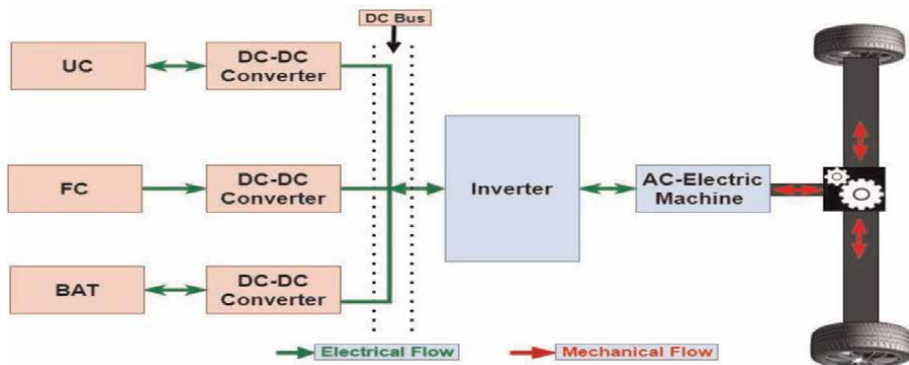
Figure 3.
The fundamental block diagram of the fully active connection topology.

accelerating (high speed), the fuel cells stack and ultracapacitor/battery are combined together to get powerfully driving.

• When deceleration (Brake), the vehicle recovers the kinetic energy of tire friction and converts it into electricity, in order to charge the ultracapacitor/ battery.

Generally, there are three main classification topologies of FCHEVs configuration, which are passive connection, full active connection, and semi-active connection [16]. In the passive configuration, the FC stack, BAT, and UC are directly connected to the DC bus, without employing any electrical power converters, as illustrated in **Figure 2**. The design of the passive connection structure is flexible and simple construction as well as high efficiency, low power losses, and low costs [16]. Meanwhile, this topology structure has disadvantages [16, 17] such as the output voltage of FC, BAT, and UC must be the same. Also, unable to be controlled power sources under the energy management strategy. Moreover, the vehicle weight is high and requires a large FC generator to meet the DC bus voltage.

The fully active configuration uses three DC-DC converters where each one is connected to the DC bus through independent power electronic converters as shown in **Figure 3**. The fully active configuration structure can use the FC generator with a
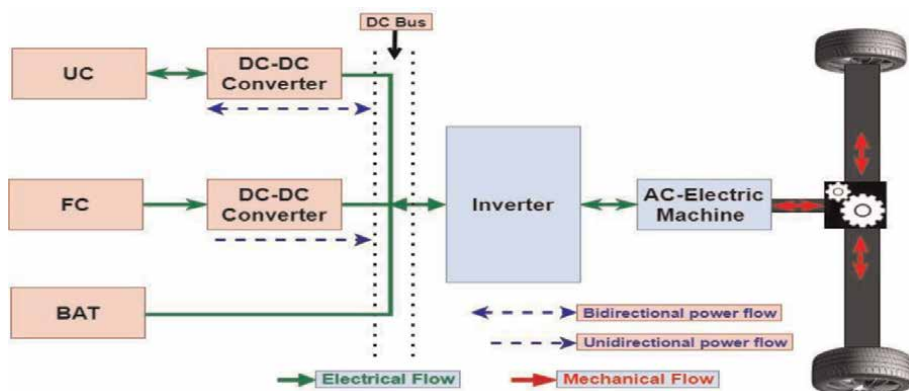
Figure 4.
Semi-active connection topology: BAT links directly to the DC-bus.
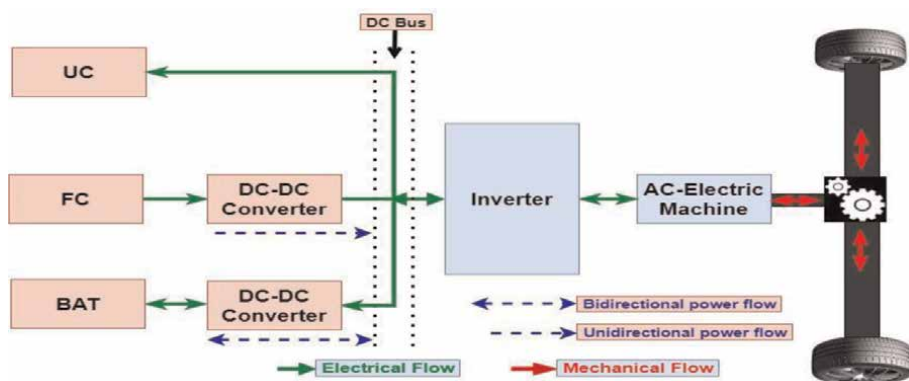
Figure 5.
Semi-active connection topology: UC links directly to the DC-bus.

voltage much less than the DC voltage bus due to combined to boost DC-DC converter; then, this is the main advantage of this topology. Also, the weight of the vehicle in terms of the power sources (FC, BAT, and UC) is smaller than the passive connection. However, the fully active configuration has some drawbacks such as the extra weight of adding three converters, high cost, and high power losses [17].

In order to find the most efficient configuration, the semi-active topology is proposed, which combines and uses the features of the active and the passive connections. Moreover, there are two types of semi-active topology. The first is that the fuel cell is connected to the DC-bus voltage through a unidirectional DC-DC converter, whereas the BAT has a direct link to the DC-bus voltage, and the UC is attached to the DC-bus *via* a bidirectional DC-DC converter, as illustrated in **Figure 4**. The FC is connected to the DC-bus *via* a unidirectional DC-DC converter, although the UC is attached straight to the DC-bus, and the BAT is tied to the DC-bus voltage *via* a bidirectional DC-DC converter, as illustrated in **Figure 5**.

This work aimed at improving the topology of the second type of semi-active topology (see **Figure 5**) *via* the proposed EMS that is designed to achieve that the BAT responds to load power that has low-frequency orders and the UC responds to power

demand that has high-frequency orders since it is connected directly to DC bus. While the FC gives steady-state power, its efficiency is increasing.

3. Power unit converters of FCHEV

Regulation of the DC-bus voltage required DC-DC converters to regulate the voltage as well as adjust the power flow between the power sources of the developed FCHEV system. This work uses two topologies DC-DC converters, as shown in **Figure 6**, for the unidirectional boost converter that is used for the FC generator, and **Figure 7** shows the converter of the BAT, which is a bidirectional buck-boost type.

The waveforms can be averaged over a period of time that is brief in comparison to the system's inherent time constants without appreciably influencing the response [18]. When the basic condition is met, averaging the single-quadrature converter waveforms throughout the switching period is a good approximation. The converter's low-frequency behavior is predicted by the averaged model, which ignores the high-frequency switching harmonics. The single-quadrature converter is modeled by using a conventional transformer-less single-quadrature architecture. Therefore, the pro-posed work uses the average model converter instead of the electronic circuit model,
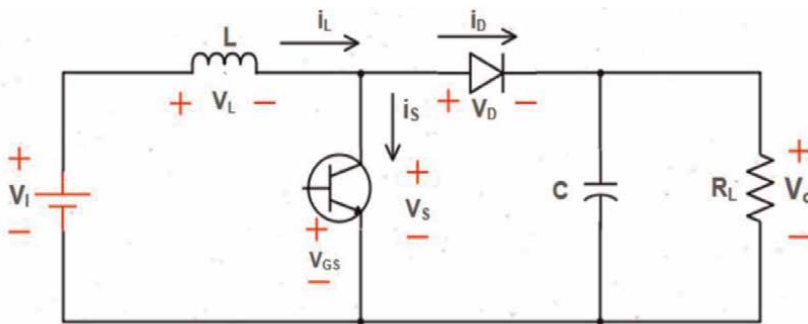
Figure 6.
Circuit diagrams of the unidirectional boost converter.
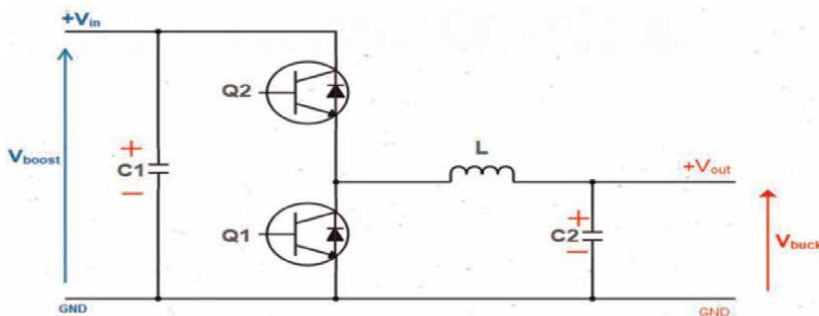
Figure 7.
Circuit diagrams of the bidirectional buck-boost converter.
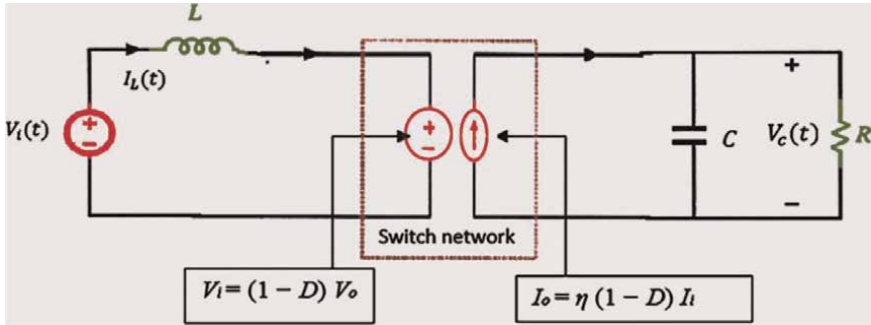
Figure 8.
Equivalent averaged model of single-quadrature DC-DC converter.
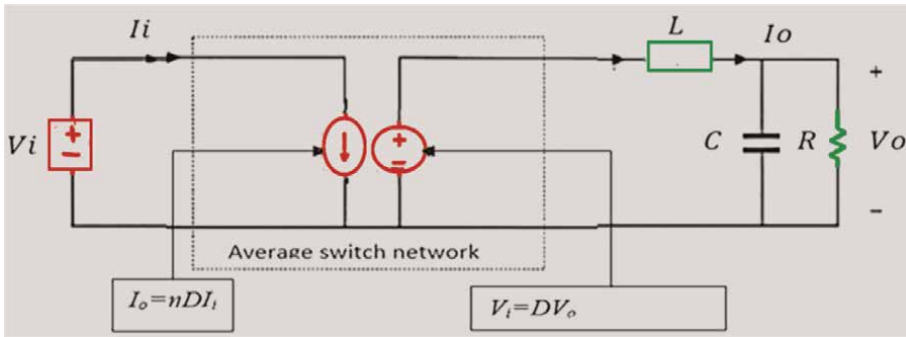
Figure 9.
Average model of two-quadrature converter in the buck mode.

which in return speeds up the simulation time and gets the same results. **Figure 8** illustrates the proposed single-quadrature averaged converter model.

The relationships between the average of currents for the input and output converter are represented as [18]:

$$I_o = \eta \, (1 - D) \, I_i \tag{1}$$

Generally, the efficiency of the converter should be constant. Assumed to be 90% at full load. The relationship between VI and VO can be calculated *via* the voltage second balance across the inductor as shown in Ref. [19]:

$$V_O = \frac{V_i}{1 - D} \tag{2}$$

The two-quadrature converter is directly controlled by the duty cycle signal. The two-quadrant bidirectional outputs can be utilized in either a buck or boost configuration. Two-quadrature DC-DC converter average switch model can be derived based on buck (Charging Mode) and boost (Discharging Mode) operations. **Figure 9** illustrates the proposed two-quadrature averaged converter model.
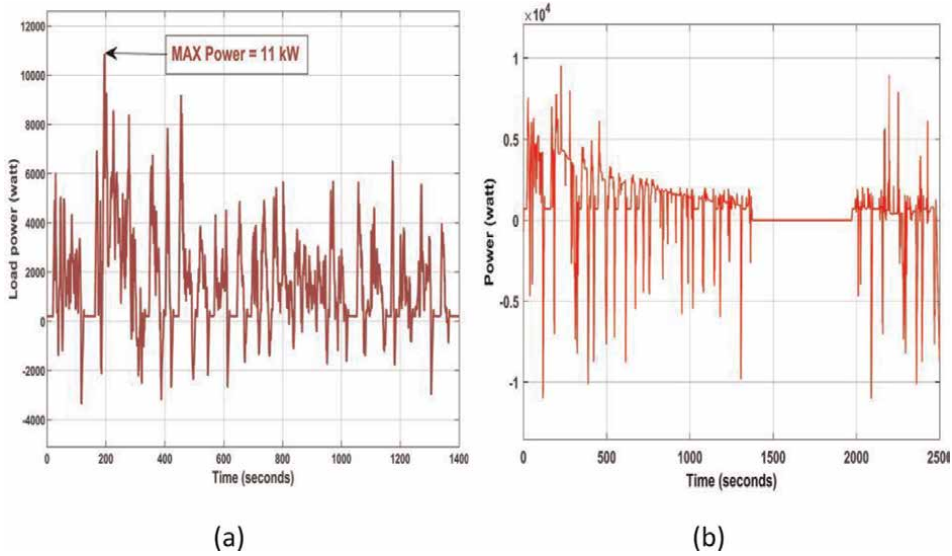
Figure 10.
The power load profile of (a) UDDS and (b) FTP.

In the operation of buck mode, the relationships for V_i and I_o can be obtained as shown below:

$$Vi = DV_o \qquad (3)$$

$$I_o = \eta DI_i \qquad (4)$$

Where D consists of d1 for the boost switch and d2 for the buck switch.

4. Power load driving cycles and power sources parameters

In order to accomplish the design and sizing of the parameters in terms of the power sources for FC, UC, and BAT of the FCHEV; and evaluate the reliability of FC, UC, and BAT power sources when utilized by the proposed EMS. Load profiles are needed; therefore, two driving cycles have been proposed, which are Urban Dynamometer Driving Schedule (UDDS) and Federal Test Procedure (FTP) were acquired by the ADVISOR analysis program. Since UDDS has the worst peak power consumption variations of any of the driving cycle standards, it serves as the primary example for analyzing FCHEV performance. **Figure 10a** and **b** illustrate the power profile of UDDS and FTP, respectively.

On the basis of UDDS driving cycle power profile characteristics, the maximum load power is 11 kW while the average power is 7 kW. As a result, the power requirement for this load has been modeled on a hybrid system that integrates FC, BAT, and UC, which are built by extracting the actual technical specifications of these resources from their datasheets and incorporating them into the Simulink model environment to make system performance outcomes as realistic as feasible in the real world. The following are the power sources:

1. Fuel cell: Hydrogenics 12.5 kW HyPM-HD12 PEMFC; Number of cells is 65; FC datasheet in [20].

2. Battery: Valence Technology U-Charge U1-12XP lithium-ion BAT. The BAT is represented by four series-connected cells. The nominal voltage of each string is 12.6 V. BAT datasheet in [21].

3. Ultracapacitor: Maxwell Boostcap®BCAP1200 UC; the Maxwell 1200F, 2.7 V/cell Boostcap®BCAP1200. 120 cells in series in order to produce 300 volts due to the DC link voltage of the FCHEV system being 300 V and the UC being directly connected to the DC link. UC datasheet in [22].

5. Methodology

The proposed controllers (WNN-PI, and the developed (EMS by FLC and ANNs)) supervise the BAT and FC current boundaries to guarantee proper timing for the charging and discharging of the BAT/UC and no negative current supply to the FC. The BAT current is supplied to a two-quadrature DC-DC converter, whereas the current of the FC is sent to a single-quadrature converter and responds to steady-state load power. Due to the UC capabilities that allow it to react fast to sudden changes in power load and the UC is directly attached to the DC bus, therefore, it is recharged before the BAT recharges. BAT converter is bidirectional and thus capable of utilizing rapid brakes of the vehicle for recharging the BAT. Wavelet methods are used to regulate the BAT converter with wavelet and PI controller identified as WNN-PI, which are tuned online using optimization algorithms (PSO or CSA). The boost converter is used for the FC, which is managed by an EMS with either an FLC or an ANN. The overall objective of the EMS control procedures is to efficiently deliver the required power to the vehicle load power, to control hydrogen consumption as effectively as possible, to increase the responsiveness and run efficiency of the FC, to increase the lifespan of the FC, BAT, and UC, and to minimize the size of the FC stack system, which in return lowers the FC cost.

5.1 Fuzzy and ANN for EMS of FCHEV

First, the FC reference current is managed by the FLC control system. Given that the ANN requires input and output data to be trained. As a result, the FLC method has been used to build the EMS first in order to get the necessary input/output data. Then, the ANNs have been trained after obtaining the necessary data *via* FLC. Keeps the fuel cell power generator output under control and satisfies all the FCHEV requirements for safe and efficient operation. Therefore, to control and achieve an efficient run of FC, consider the output power of the fuel cell in three cases; which are the minimum FC power (Pfc_min) is from zero till reaches 0.49 kW, and the maximum FC power (Pfc_max) is from 1.59 kW till reaches 11 kW, then the optimal FC power output (Pfc_opt) is from 0.5 kW till reach 1.6 kW. The fuel cell reference current is calculated by using a set of Fuzzy If-Then Rules which take into account both the power needed from the FC and the SOC limits for the battery, as illustrated in **Figure 11**, the FLC model in the Simulink environment. Moreover, the developed FLC has been implemented using a trapezoidal memberships function (trapmf).

The neural control system has two inputs, which are the load power and the SOC of the battery. The output of ANNs is the FC reference power. The parameters of the ANNs have been defined as the following:
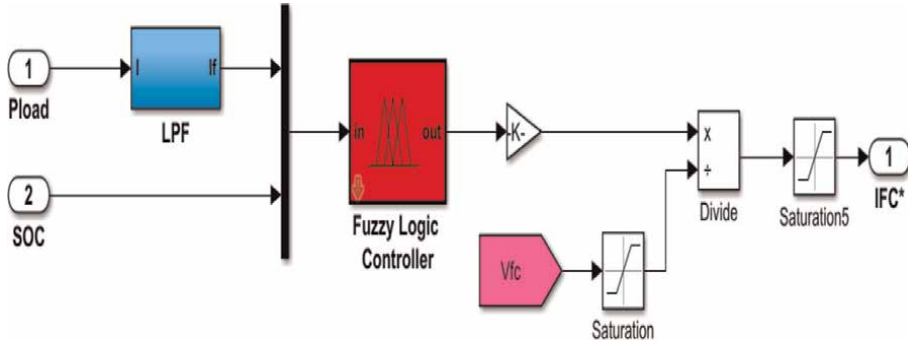
Figure 11.
The EMS model with fuzzy logic control.

1. The network used is "feedforwardnet" training algorithm that used the "Levenberg–Marquardt" method to train the neural network.

2. The number of epochs is 1000 epoch

3. Three hidden layers have been employed, and each layer's neurons are 30, 20, 15, and 10, which are chosen by the trial-and-error theorem.

4. Training goad (MSE) is 10^{-30}

Whereby 15% are used for testing, 15% for validation, and 70% are for training. The codes used to create this network and the network diagram are shown in **Figure 12**.

5.2 Wavelet strategy and optimization algorithm for EMS of FCHEV

The actual DC link voltage is subtracted from the reference DC voltage 300 V to get the error signal, which is then fed to the WNN-PI controller in order to get the BAT current reference, which in return controls the BAT DC-DC converter. The feed-forward wavelet neural network is used in this work (WNN-PI). **Figure 13** shows the Simulink model; the PSO and CSA are used to tune the WNN-PI parameters, which are WNN variables dilation (a's), translation (b's), and weights (w's); PI controller parameters are Ki and Kp.

The fitness function for an optimal value is obtained using the "Integral of Squared Error" (ISE), which is the same function used by both PSO and CSA optimization methods.

$$\text{fitness function} = \ \min(\text{ISE}) \tag{5}$$

$$\text{ISE} = \int e^2(t)dt \tag{6}$$

$$e(j) = D(j) - y(j) \tag{7}$$

Where e(j) is the error that is produced when the desired value D(j) is subtracted from the actual value of the model y(j). Following that, PSO should use
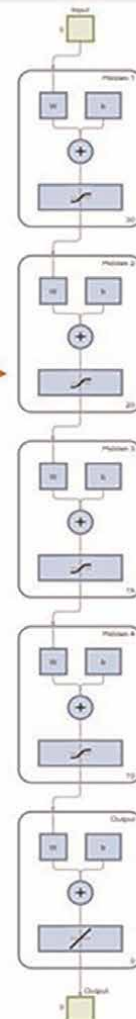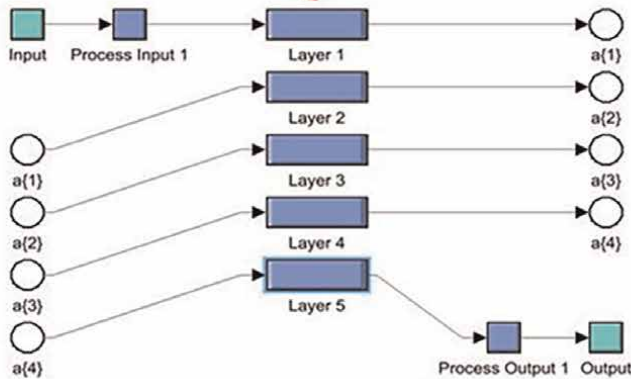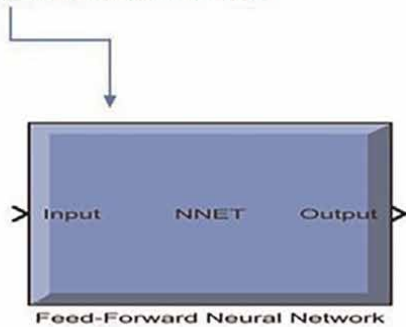
Figure 12.
ANNs codes and network diagram.

Eq. (6) to continuously update each swarm particle's current position xj (m) and velocity vj at (m):

$$v_j^{m+1} = w * v_j^m + c_1 * R_1 * \left(lbest_j - x_j^m \right) + c_2 * R_2 * \left(gbest_j - x_j^m \right) \qquad (8)$$

Applying Eq. (9) to modify the current position:
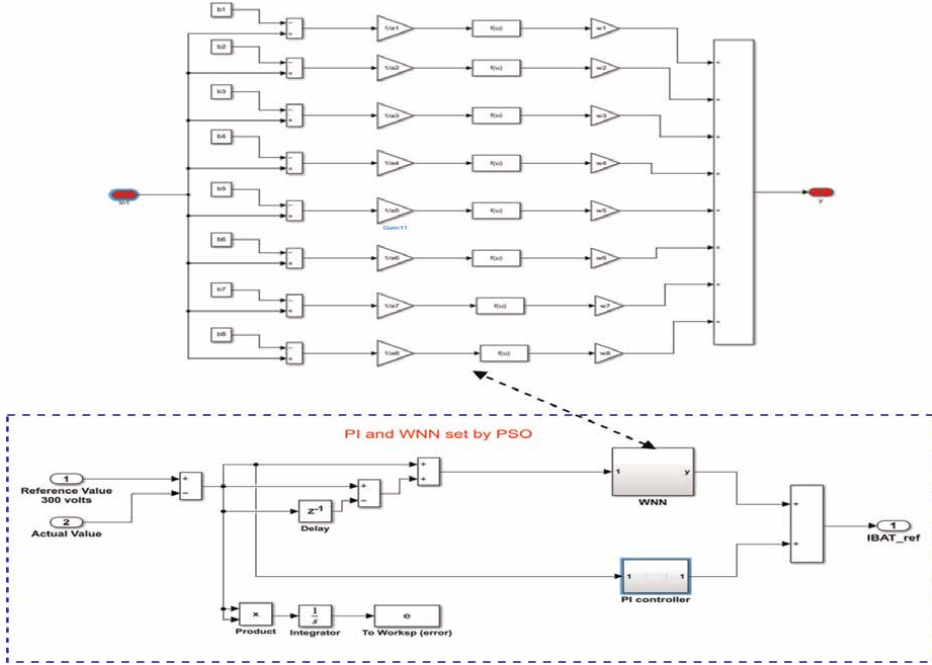
Figure 13.
Battery controller scheme by wavelet and PI in Simulink model.

$$x_j^{m+1} = x_j^m + v_j^{m+1} \tag{9}$$

A generalized wavelet is created by linearly combining a collection of daughter wavelets $\psi_{a,b}$:

$$\psi_{a,b} = \psi\left(\frac{x-b}{a}\right) \tag{10}$$

The wavelet's ultimate output is as follows:

$$y = \sum_{n=1}^{N} w_N \psi_{a_N, b_N} \tag{11}$$

For each crow, the CSA creates a new location in the search space. Assume that crow i follows a crow (for example, crow j) at random to find out where crow j is. Crow i's position update is divided into two circumstances. First, crow j is unaware that crow i is following it. Using Eq. (12), evaluate the fitness function, and choose a random position. Second, crow j detects crow i and follows it, and crow j moves crow i to a random position. Based on Eq. (6) results, Eq. (13) follows [23]:

$$X^{i,itr+1} = \frac{X^{i,itr} + r_i \times fl^{i,itr} \times \left(m^{j,itr} - X^{i,itr}\right) r_j \geq AP^{j,itr}}{\text{a random position otherwise}} \tag{12}$$

Then, using Eq. (13) for updating the memory matrix of each crow based on Eq. (12) [24]:

$$m^{i,itr+1} = \frac{X^{i,itr+1}, f\left(x^{i,itr+1}\right) \text{ is better than } f\left(m^{i,itr}\right)}{x^{i,itr+1} \text{ otherwise}} \qquad (13)$$

The algorithms of PSO and CSA are shown below, respectively:

PSO algorithm: Find optimum values for WNN-PI parameters "

Step 1:	*Initialization PSO*
	*No. of birds **n** = 20, No. **birds_steps** = 10*
	Dimension of the problem (dim)
	WNN-PI = 14
	*PSO parameters **c1** = 1.4 & **c2** = 1.6*
	*Inertia **w** = 0.85*
	> fitness = 0*ones(n,bird_setp);
Step 2:	*Initialize the parameter*
	R1 & R2 = rand(n,dim);
	> current_fitness = 0*ones(n,1);
Step 3:	*Initializing swarm and velocities and position*
	current_position = abs(10*(rand(n,dim)-.6));
	> velocity = .25*randn(n,dim);
	local_best_position = current_position;
Step 4:	*Evaluate initial population*
	> for i = 1:n
	PI = current_position(j,:);
	Set all (a's, b's, w's) and (kp & ki)
	a_{1–4} = PI(_{1–4}); and same for b's, w's and (kp & ki)
Step 5:	*Initialize sim options (Simulink)*
	> Simout = sim('WNN_PI.slx');
	Compute the error
	e = max(V_Actual)-300;
	m = abs(e);
	error = sum(m);
	Fitness Function is F = error
	current_fitness(j) = F;
	end
Step 6:	**Velocity Update**
	> velocity = w *velocity + c1*(R1.*(local_best_position-current_position)) + c2*(R2.*(globl_best_position-current_position));
Step 7:	*Swarm Update*
Step 8:	*Evaluate anew swarm: Back to Step.5:*
Step 9:	*Choose the optimum values and submit them to the Simulink model.*
	> a_{1–4} = globl_best_position(n,_{1–4});

CSA algorithm: Find optimum values for WNN-PI parameters"

Step 1:	*"Optimization Initialization and system definition*
	*No. of Variables **pd** = 14 and No. of Population size **N** = 30*
	*Awareness Probability **AP** = 0.6 and Flight Step **FI** = 2*

Step 2:   *Initialize Function*
                   [x l u] = init(N,pd); % Function for initialization, l = 0; u = 300; %
                   Lower and upper bounds
Step 3:   *Generate Random Position*
                          num = ceil(N*rand(1,N));
Step 4:   >   *Compute the error*
                   function **ft = fitness(FI,N,pd)** % Function for fitness evaluation
                   simout = sim('WNN_PI.slx');
                   m = abs(e); error = sum(m); F = error; ft(i) = F;
Step 5:   >   for i = **1:N**
                   tmax = 300; % Maximum number of iterations (itermax)
                   ft = fitness; % fitness evaluation
Step 6:   *Evaluate Memory Initialization*
        >   **fit_mem = ft;** % Fitness of memory positions
        >   if **rand > AP**
        >   **xnew(i,:) = x(i,:) + FI*rand*(mem(num(i),:)-x(i,:));**
                   % Generation of a new position for crow I (state 2)
                     else
                     > for j = **1:pd**
        >   **xnew(i,j) = l-(l-u)*rand;** % Generation of a new position for crow i
                   (state 2)
                     end
                     end
                     end
Step 7:   *Evaluate Fitness Function and Update new error*
        >   **F = xnew;**
                     ft = fitness;
Step 8:   *Update new Position and the Memory*
        >   for i = **1:N** % Update position and memory
                     if **xnew(i,:) > =l & xnew(i,:) < =u**
                     ft = fitness; % Function for fitness evaluation
                     mem = x; % Memory initialization
                     fit_mem = ft; % Fitness of memory positions
                     x(i,:) = xnew(i,:); % Update position
                       if **ft(i) < fit_mem(i)**
                       mem(i,:) = xnew(i,:); % Update memory
                     fit_mem(i) = ft(i);
                       end
                     end
                   end
              ffit(t) = min(fit_mem); % Best value until iteration t
                min(fit_mem);
                 end
Step 9:   *Evaluate fitness function: Back to Step.5:*
        >   **ngbest = find(fit_mem== min(fit_mem));**
Step 10:   *Select the optimum values and send them to Simulink.*
        >   **g_best = mem(ngbest(1),:);**
   >   **a$_{1–4}$ = g_best_position($_{1–4}$);"**

6. Simulation results and discussions

This section summarizes the simulation results for AI EMS, which was evaluated over two drive cycles (UDDS and FTP) with two alternative control approaches. The first is FC control by FLC, while the second is FC control by ANNs. WNN-PI controls the BAT, which is adjusted *via* PSO and CSA. The results reveal that FC controlling by ANNs is superior to FLC due to ANNs are a predictable system, resulting in more efficiency than FLC, particularly when utilized in the FTP drive cycle. Moreover, the ANNs offered optimal flow of power among power sources and FCHEV load. Furthermore, WNN-PI has superior tuning by PSO than CSA since CSA has sluggish speed convergence and readily falls into the local optimum [23–25]. **Figure 14** illustrates the DC-bus voltage under UDDS driving cycle load profile.

It is observed that the fluctuation of the DC-Bus voltage by PSO is less than the voltage fluctuation of CSA due to that PSO tuned the parameters of the WNN-PI more precisely than CSA. By modifying the duty cycle for the buck and boost converters of the BAT and for the boost mode of the FC converter, the voltage of the DC-bus was preserved at an acceptable level. Also, observed that all of the converters' duty cycle values by PSO are more stable, where all are below 90% which is an acceptable percent as illustrated in **Figure 15** the duty cycle of the BAT in boost mode, and as per in **Figure 16** the buck mode, while the FC converter as shown in **Figure 17**.

The duty cycles for the converters were successfully given by PSO and CSA. However, the findings indicate that PSO is more effective than CSA in terms of the DC-Bus voltage and duty cycles of the converters for the FC and the BAT during the UDDS even during the FTP driving cycle. Also, the ANN is more effective than FLC. Therefore, the remainder results of the proposed model have been carried out based on PSO and ANN. Whereby, the power of the FC, BAT, and UC during UDDS cycle are illustrated in **Figures 18**–**20**, respectively. Additionally, the power of the FC, BAT, and UC during FTP cycle are illustrated in **Figure 21**–**23**, respectively.

The proposed control approach properly satisfies the AI EMS of FCHEV needs under the load power profile of UDDS and FTP driving cycles as well as the charging/recharging requirements of the BAT and UC, as illustrated in **Figure 24**. The FC power is also steady-state during the demand of load power and does not react to rapid
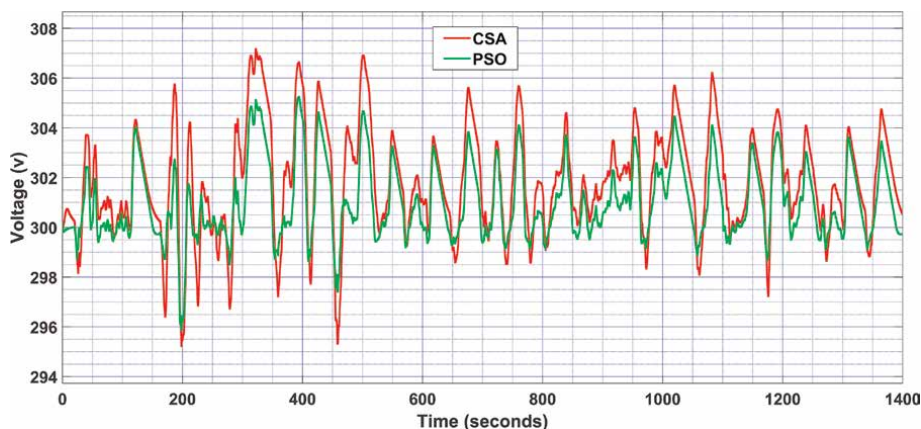
Figure 14.
DC-bus voltage during USSD cycle.
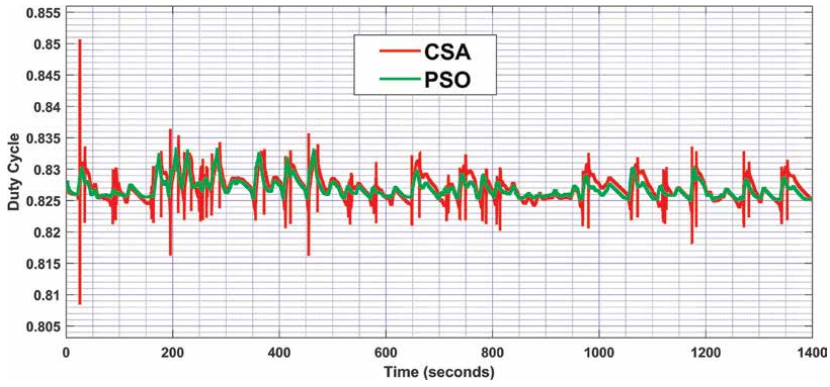
Figure 15.
Duty cycle BAT converter in boost mode during UDDS cycle.
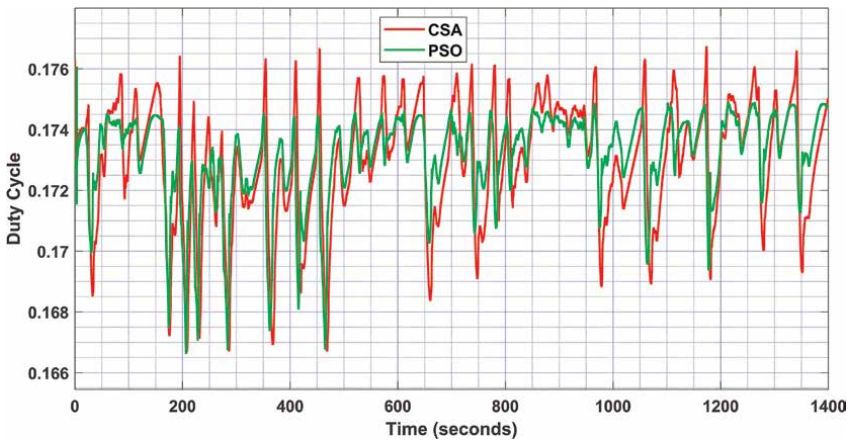
Figure 16.
Duty cycle of BAT converter in buck mode during UDDS cycle.
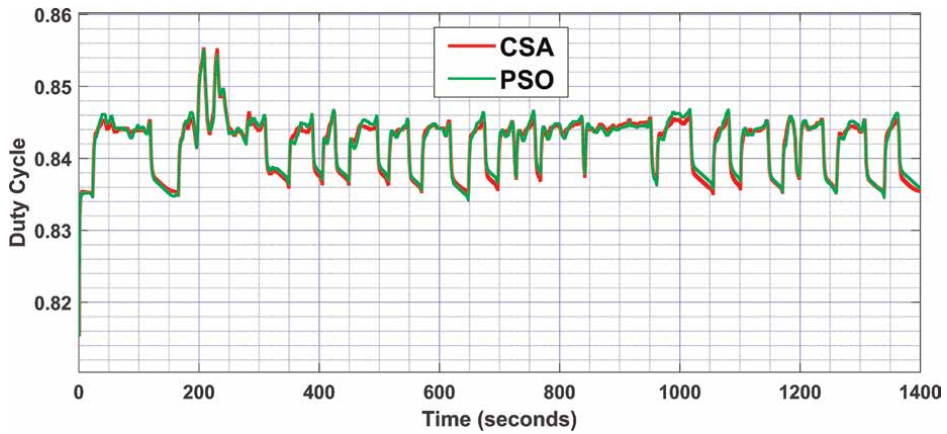
Figure 17.
Duty cycle of FC during UDDS cycle.
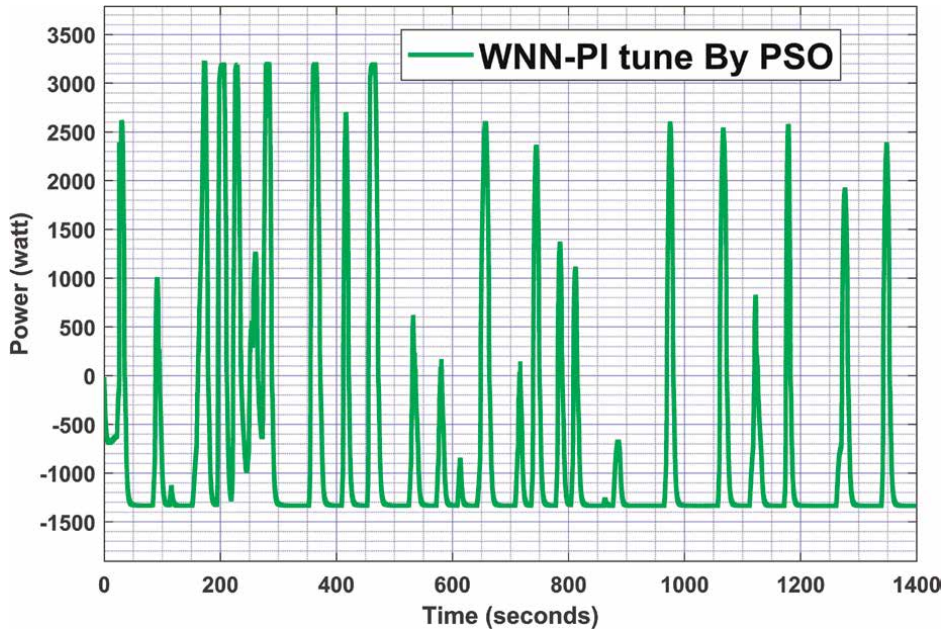
Figure 18.
BAT power during UDDS cycle.
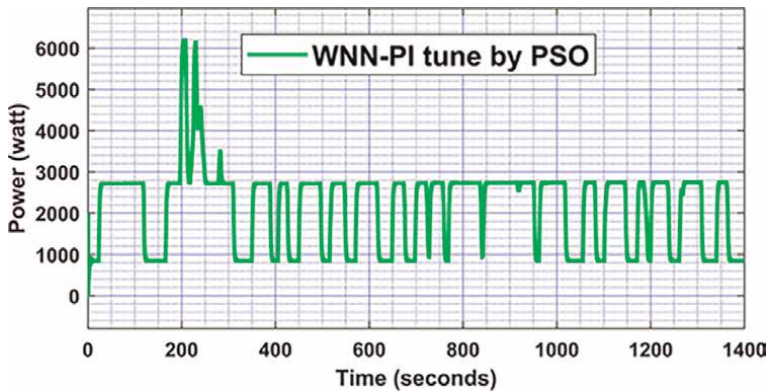
Figure 19.
FC power during UDDS cycle.

fluctuations of the power load; whereas the BAT delivers a medium-frequency power to the power load, then it supports the FC to cover the power for the remaining load needed; and the UC power delivers high-frequency power to the power load to overcome abrupt load fluctuations. The power resources (FC, BAT, and UC) accomplished the optimal power flow for the FCHEV, which in turn makes the BAT and UC function safely and extend their lifespans as well as decreasing H2 (Hydrogen) use.

The plug-in FC hybrid electric vehicle analysis and evaluation in this study were carried out under two vehicle driving cycles using the Advanced Vehicle Simulator (ADVISOR) and the MATLAB/Simulink 2022b (64bit) environment
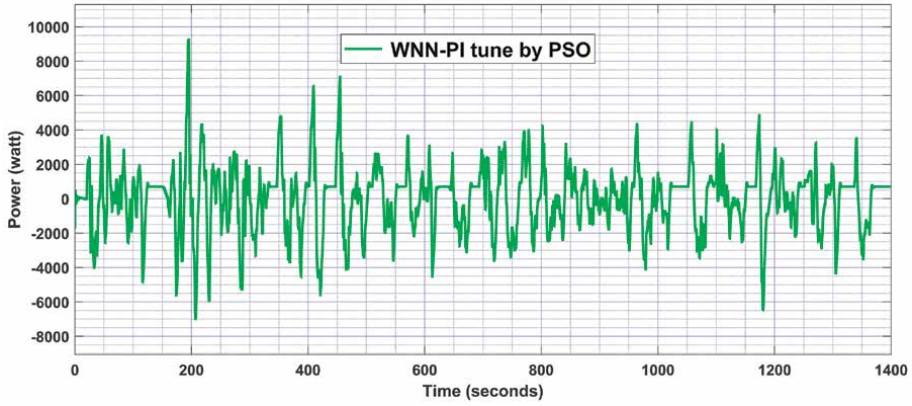
Figure 20.
UC power during UDDS cycle.
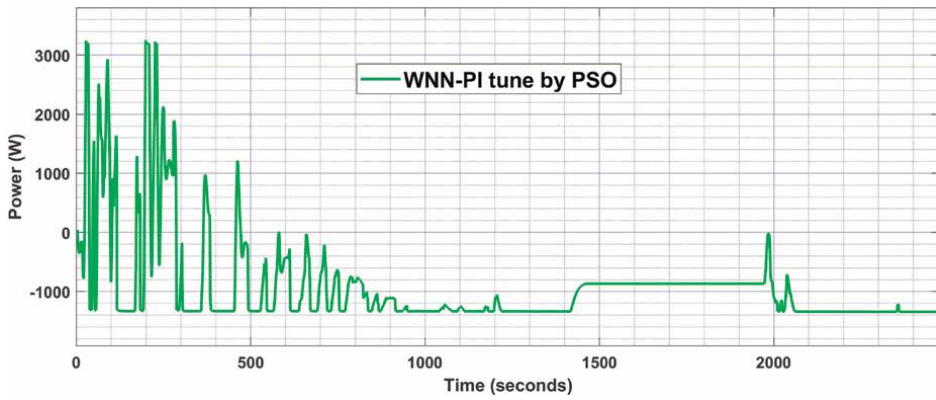
Figure 21.
BAT power during FTP cycle.
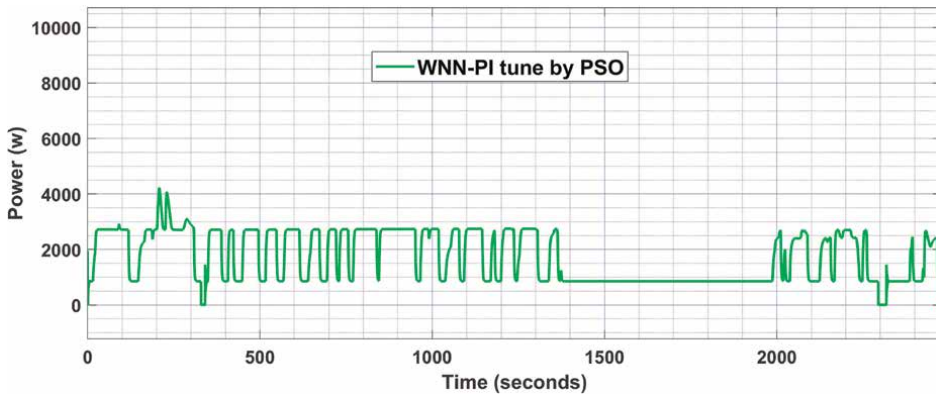
Figure 22.
FC power during FTP cycle.
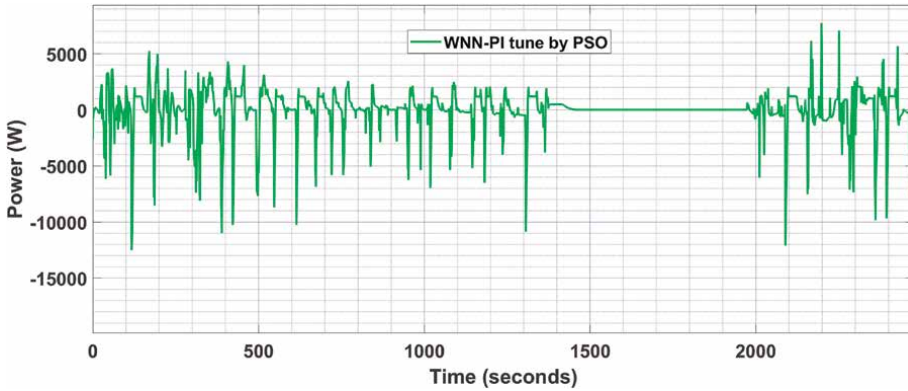
Figure 23.
UC power during FTP cycle.
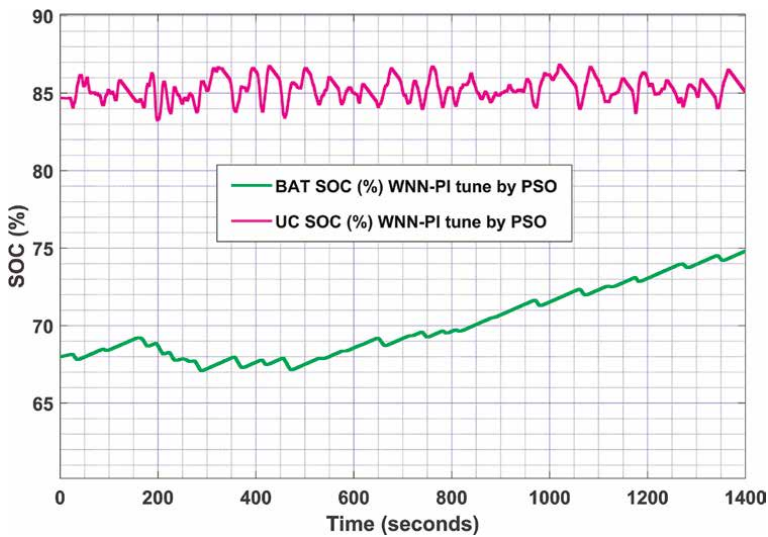
Figure 24.
BAT and UC state of charge during UDDS cycle.

based on the proposed AI EMS structure and optimization algorithm. **Figure 25** illustrates the proposed Simulink model for a compact car with a maximum load of 11 kW.

7. Conclusion

An energy management system that manages a hybrid plug-in FCEV is presented by this study as a combined intelligent controller system. The objective of this study was to develop the next generation of an EMS system employing a combination of fuel cells, ultracapacitors, and batteries in order to reduce the fuel consumption of the FCHEV powertrain and improve the system's efficiency. In the design system, the created EMS scheme took into account the characteristics of FC, UC, and BAT. Also,
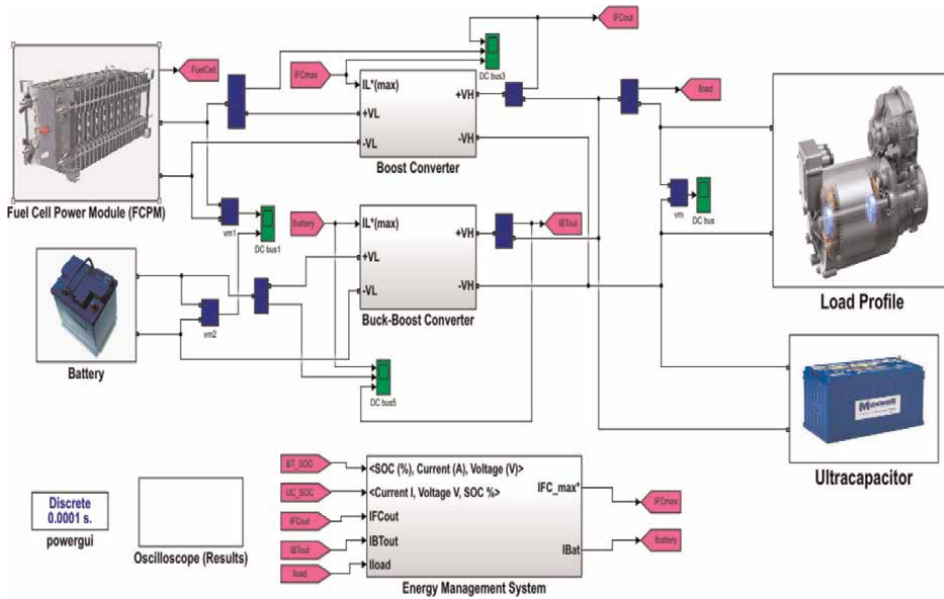
Figure 25.
The proposed Simulink model.

the proposed EMS considers the dynamic responsiveness of the power sources. FLC and ANN have been used with WNN-PI that is tuned *via* two optimization algorithms, which are PSO and CSA. The most significant findings of this work are as follows:

- The National Renewable Energy Laboratory's ADVISOR software was used to construct acceleration and grading test processes for analyzing hybrid vehicle dynamic properties and determining their electrical load power profile. The software was used to extract two varieties of load power profiles (UDDS and FTP), which were used to simulate FCHEV and evaluate the effectiveness of the proposed intelligent EMS.

- The FC, BAT, and UC are modeled using datasheets from their respective manufacturers. As a result, the characteristics of the power sources have been developed as close to their real-world characteristics.

- The power converters were modeled using the average modeling approach. Average models use less time to simulate a system than the switching model.

- The proposed model guarantees that the BAT provides specified energy with a safe run for the BAT, extends its lifespan, as well as not reposed to high load power variations. Moreover, the FC output power responds only to the steady-state power load, which in turn ensures that the FC works efficiently. Whereas UC has the first response to unexpected load fluctuations.

- WNN-PI has superior tuning by PSO than CSA. Whereby, the findings indicate that PSO is more effective than CSA in terms of the DC-Bus voltage and duty cycles of the converters for the FC and the BAT

Author details

Mustafa A. Kamoona* and Juan Manuel Mauricio
University of Seville, Seville, Spain

*Address all correspondence to: mustafazzasim@gmial.com

IntechOpen

References

[1] Vignesh S, Bhateshvar YK, Agrewale MR, Vora KC. Comprehensive Design of Small Electric Vehicle for Powertrain Optimization for Optimum Range with Weight and Size Reduction: Planning of Hybrid Renewable Energy Systems, Electric Vehicles and Microgrid: Modeling, Control and Optimization. Singapore: Springer Nature Singapore; 2022. pp. 443-486

[2] Venkatasatish R, Dhanamjayulu C. Reinforcement learning based energy management systems and hydrogen refuelling stations for fuel cell electric vehicles: An overview. International Journal of Hydrogen Energy. 2022; **47**(64):27646-27670

[3] Pramuanjaroenkij A, Kakaç S. The fuel cell electric vehicles: The highlight review. International Journal of Hydrogen Energy. 2023;**48**(25): 9401-9425

[4] Gao DW, Mi C, Emadi A. Modeling and simulation of electric and hybrid vehicles. Proceedings of the IEEE. 2007; **95**(4):729-745

[5] Fazhan T, Zhu L, Zhumu F, Si P, Sun L. Frequency decoupling-based energy management strategy for fuel cell/battery/ultracapacitor hybrid vehicle using fuzzy control method. IEEE Access. 2020;**8**:166491-166502

[6] Kamoona MA, Kivanc OC, Ahmed OA. Intelligent energy management system evaluation of hybrid electric vehicle based on recurrent wavelet neural network and PSO algorithm. International Journal of Intelligent Engineering & Systems. 2023;**6**:1

[7] Hu X, Liu S, Song K, Gao Y, Zhang T. Novel fuzzy control energy management strategy for fuel cell hybrid electric vehicles considering state of health. Energies. 2021;**14**(20):6481

[8] Gharibeh HF, Yazdankhah AS, Azizian MR, Farrokhifar M. Online energy management strategy for fuel cell hybrid electric vehicles with installed PV on roof. IEEE Transactions on Industry Applications. 2021;**57**(3):2859-2869

[9] Kamoona M, Kivanc OC, Ahmed OA. Intelligent energy management system for hybrid electric vehicle based on optimization wavelet neural network by PSO algorithm. In: International Conference on Computing and Information Technology. Cham: Springer International Publishing; 2022. pp. 558-573

[10] Li H, Zhou Y, Gualous H, Chaoui H, Boulon L. Optimal cost minimization strategy for fuel cell hybrid electric vehicles based on decision-making framework. IEEE Transactions on Industrial Informatics. 2020;**17**(4): 2388-2399

[11] Sun H, Zhumu F, Tao F, Zhu L, Si P. Data-driven reinforcement-learning-based hierarchical energy management strategy for fuel cell/battery/ultracapacitor hybrid electric vehicles. Journal of Power Sources. 2020;**455**: 227964

[12] Lü X, Yinbo W, Lian J, Zhang Y, Chen C, Wang P, et al. Energy management of hybrid electric vehicles: A review of energy optimization of fuel cell hybrid power system based on genetic algorithm. Energy Conversion and Management. 2020;**205**:112474

[13] Teng T, Zhang X, Dong H, Xue Q. A comprehensive review of energy management optimization strategies for

fuel cell passenger vehicle. International Journal of Hydrogen Energy. 2020; **45**(39):20293-20303

[14] İnci M, Büyük M, Demir MH, İlbey G. A review and research on fuel cell electric vehicles: Topologies, power electronic converters, energy management methods, technical challenges, marketing and future aspects. Renewable and Sustainable Energy Reviews. 2021;**137**: 110648

[15] Tran D-D, Vafaeipour M, El Baghdadi M, Barrero R, Van Mierlo J, Hegazy O. Thorough state-of-the-art analysis of electric and hybrid vehicle powertrains: Topologies and integrated energy management strategies. Renewable and Sustainable Energy Reviews. 2020;**119**:109596

[16] Gao L, Dougal RA, Shengyi L. Active power sharing in hybrid battery/ capacitor power sources. In: Eighteenth Annual IEEE Applied Power Electronics Conference and Exposition, APEC'03. 2003. Vol. 1. Miami Beach, FL, USA: IEEE; 2003

[17] Chen Y-S, Lin S-M, Hong B-S. Experimental study on a passive fuel cell/battery hybrid power system. Energies. 2013;**6**(12): 6413-6422

[18] Erickson RW, Maksimoic D. Fundamentals of Power Electronics. 2nd ed. Norwell, MA, USA: Kluwer Academic Publishers; 2004

[19] Javad M, Ali A, Ali E, Daniel JS. Power electronic circuits and controls. USA: CRC Press, LLC; 2002

[20] HyPM-HD12 PEMFC Datasheet. Available from: https://silo.tips/ download/hypm-fuel-cell-power-modules [Accessed: August 07, 2023]

[21] U-Charge U1-12XP Lithium-ion Battery Datasheet. Available from: https://www.celltech.se/fileadmin/user_ upload/Celltech/Products/Litium_ladd ningsbara/Valence_Modules/XP_Mod ule_Datasheet.pdf [Accessed: August 07, 2023]

[22] Maxwell Boostcap®BCAP1200 UC Datasheet. Available from: https://www. datasheetarchive.com/pdf/download.ph p?id=692d2c8a33a1c020f38f0ee5addb 244b9a3475&type=M&term=BCAP1200 [Accessed: August 07, 2023]

[23] Askarzadeh A. A novel metaheuristic method for solving constrained engineering optimization problems: Crow search algorithm. Computers and Structures. 2016;**169**:1-12. DOI: 10.1016/ j.compstruc.2016.03.001

[24] Cheng Q, Huang H, Chen M. A novel crow search algorithm based on improved flower pollination. Mathematical Problems in Engineering. 2021;**2021**:1-26. DOI: 10.1155/2021/ 1048879

[25] Meraihi Y, Gabis AB, Ramdane-Cherif A, Acheli D. A comprehensive survey of crow search algorithm and its applications. Artificial Intelligence Review. 2021;**54**(4):2669-2716. DOI: 10.1007/s10462-020-09911-9

Chapter 3

Battery State of Charge Management for an Electric Vehicle Traction System

Ahmed Sayed Abdelaal Abdelaziz

Abstract

This chapter introduces a battery state of charge (SOC) management technique designed for an electric vehicle traction system that incorporates an indirect field-oriented induction motor drive. The primary goal of this technique is to restrict the change in battery SOC from exceeding a maximum limit, by compensating for the motor speed tracking performance. It employs a fuzzy-tuned model predictive controller (FMPC), where a fuzzy logic controller (FLC) adjusts the input weight in the objective function to ensure that the change in battery SOC does not exceed the maximum permitted value while regulating the motor speed. The various components of the EV traction system are thoroughly modeled, and simulations are conducted using MATLAB/Simulink 2018b. The simulation results, carried out using the New European Drive Cycle (NEDC), verify that the technique limits the change in SOC while controlling the motor speed. This approach offers the advantage of maintaining precise control over the battery bank SOC, which distinguishes it from conventional speed regulators.

1. Introduction

One of the primary concerns associated with electric vehicles (EVs) pertains to their limited operational range. Additionally, the shortage of charging infrastructure and the extended charging duration remain significant challenges. In addressing these challenges, this chapter aims to shed light on a range of battery energy management (BEM) strategies outlined in existing literature while also introducing an innovative technique that holds promise for the EV market.

Regarding EVs, the BEM strategies can be segregated into two categories [1]. The first category involves the development of rules before initiating the system. Those rules dictate the behavior of the system during operation. Strategies falling within the second category are distinguished by their cost function and require an optimization technique to achieve the system's objective. In the literature, the first category of strategies involves the use of a fuzzy logic controller (FLC) for managing multiple

power sources such as combustion engines, ultra-capacitors, and batteries [2]. An FLC allocates power demand among these sources to maximize each source's efficiency. In an alternative approach, an FLC is designed to consider battery SOC, input reference speed, and commanded vehicle acceleration to determine the battery's power output, albeit with a trade-off of sacrificing a certain degree of motor performance to achieve battery energy conservation [3]. In the works [4], an advanced energy management system was developed. This system oversees both the torque signal and the SOC of the battery, subsequently generating the electric throttle signal to control the motor's speed. Additionally, in Suhail et al.'s study [5], a neural FLC was introduced for efficient management of regenerative braking in a hybrid EV. This controller continuously monitors the engine's speed and power, while accurately calculating the necessary torque for the given situation [5]. When the delivered power surpasses the required amount, the regenerative braking system initiates the process of charging the battery bank using the surplus power generated by the engine [5].

Among the strategies in the second category, dynamic programming (DP) is the most frequently employed optimization technique due to its ability to settle on the optimal solution [6]. In order to reduce the computational complexity, alternative approaches, such as coupling convex programming with a model predictive controller (MPC), can achieve a sub-optimal solution. Furthermore, the equivalent consumption and minimization strategy (ECMS) also obtained a sub-optimal solution [6].

The MPC-based BEM techniques primarily focus on solving receding horizon algorithms, predicting velocity profiles, and generating SOC reference trajectories. An adaptive ECMS (A-ECMS), and a fuzzy adaptive ECMS (Fuzzy A-ECMS) were compared [6]. They improve upon the original ECMS by dynamically estimating the optimal equivalent factor online, in contrast to the static value set by the user in ECMS. They continuously evaluate the current battery SOC against the desired SOC and adjust the optimal equivalent factor accordingly to minimize errors. The Fuzzy A-ECMS technique showed more robustness to various driving conditions as compared to the A-ECMS technique. In Ref. [7], an FLC monitors changes in the battery's first and second derivative of SOC and generates an input weight R for the MPC cost function. When sudden high acceleration occurs, an increase in R prompts the MPC to restrict the EV's acceleration to a safe level, minimizing battery energy consumption. In Ref. [8] a synthesized velocity profile prediction method is utilized to obtain driving velocity profiles. DP was then used to calculate optimal battery SOC trajectory and constraints at various set points [9]. These set points are then integrated into an MPC, which controls the maximum battery power output to track the optimal battery SOC at each set point. In Ref. [10], the road gradient was used in conjunction with an MPC, to generate a velocity profile for the vehicle. The MPC accelerated the vehicle when traveling up the road slope and decelerated the vehicle when traveling down the road slope. This was done prior to the occurrence of the road slope. Consequently, the power requirement from the battery was reduced. Furthermore, Zhao et al. [11] combined the wavelet neural network with the MPC to generate the reference SOC trajectory over a prediction horizon. This technique utilized particle swarm optimization to aid the wavelet neural network in generating the global SOC trajectory, which was used as a reference in the MPC. Furthermore, Chen et al. [12] adapted a long short-term memory velocity predictor. It gauged the vehicle's speed and power demand of the vehicle. Subsequently, an MPC strategically allocates load power between an ultra-capacitor and a battery through a DC-DC converter. This was carefully structured to guarantee that they operated at their highest efficiency and to minimize the overall power dissipation.

Inspired by the techniques discussed in Refs. [6, 7], this chapter introduces a novel SOC tracking method capable of restricting the maximum change in SOC at the cost of speed-tracking performance degradation. The chapter's scope focuses on designing and testing this technique through simulation and excludes the method for obtaining the SOC reference trajectory. The test results suggest that the proposed SOC tracking method successfully regulates the SOC degradation, and maintains it at the desired SOC reference. The testing was performed on the New European Drive Cycle (NEDC), and the average of the magnitude of the deviation from the SOC reference was found to be 0.00095 for the proposed SOC tracking technique compared to the 0.0037 obtained by the A-ECMS and the 0.0019 obtained by the Fuzzy A-ECMS techniques [6].

This chapter comprises five sections, with the introduction as the first section. Section 2 introduces the SOC tracking technique. Section 3 describes the EV traction system components and controllers. Section 4 presents the simulation methodology and results, and finally, Section 5 concludes the chapter.

2. Description of the state of charge tracking technique

Among the BEM strategies explored in Ref. [7], the fuzzy-tuned model predictive controller (FMPC) technique stands out as having broader potential applications within the EV traction system. It offers the possibility of fine-tuning the approach to achieve a similar outcome to the Fuzzy A-ECMS strategy detailed in Ref. [6], particularly in terms of SOC tracking. However, before delving into these adjustments, it is essential to grasp the fundamental workings of the FMPC technique and gain a comprehensive understanding of the overall system.

2.1 Fuzzy-tuned model predictive controller

Figure 1 illustrates a flowchart detailing the FMPC BEM technique, as discussed in Ref. [7]. The primary aim of this approach is to mitigate variations in the speed regulating current signal, denoted as i_{sq}^*, to address abrupt accelerations. These rapid speed increases are reflected in sudden surges in battery bank current, leading to a rapid decline in battery bank SOC over a short period. This not only reduces the battery's runtime but also contributes to a shorter battery lifespan [7].

To counteract these issues, the technique monitors the battery bank current and estimates the SOC. The rate of change of SOC, denoted by the first derivative of SOC, is obtained by taking the difference between the current sample of SOC and the preceding SOC sample. Furthermore, the second derivative in SOC is obtained by taking the difference between the current and preceding sample for the change in SOC. Those variables are processed by the FLC and G_{MPC} gain. The final result is the parameter R that impacts the MPC objective function. This parameter is used to penalize variations in i_{sq}^*. Additionally, the technique incorporates motor speed and drive cycle information into the MPC block. The chosen drive cycles are the NEDC drive cycle, representing a smooth driving behavior, and the US06 drive cycle, representing an aggressive driving behavior [7]. These drive cycles provide a comprehensive assessment of the FMPC BEM technique's ability to regulate speed across a range of driving habits. The MPC, equipped with the estimated model of the EV traction system, solves the cost function, which has been adjusted with the input
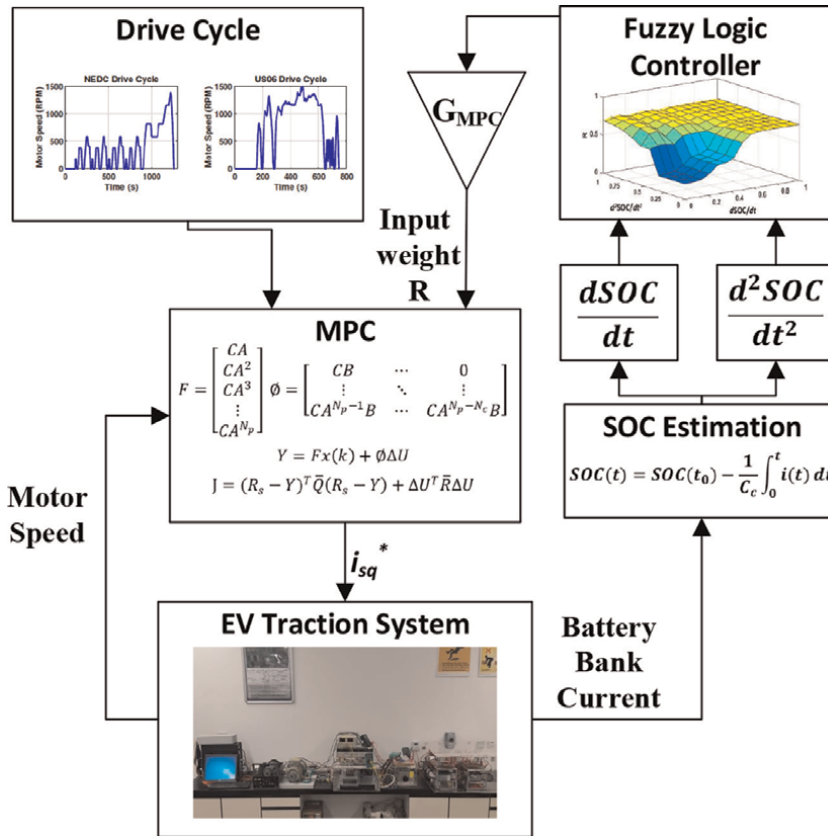
Figure 1.
Flowchart for the FMPC BEM technique [7].

weight R, using a receding horizon algorithm. The resulting i_{sq}^* signal effectively regulates motor speed while suppressing abrupt acceleration patterns. This design assists in preventing abrupt surges in battery current during acceleration and enables a smoother transition to the steady-state value of the battery bank's discharge current.

2.2 Proposed modification for the state of charge tracking

For the SOC tracking to be effective, it is crucial for the input weight R to adapt based on the error between the battery bank SOC and the reference SOC. **Figure 2** presents the flowchart outlining the SOC tracking approach. This method utilizes an MPC for speed regulation, while an FLC assesses the difference between the SOC reference trajectory and the actual battery SOC. Subsequently, it generates an input weight R that constrains the MPC's speed regulating signal, i_{sq}^*. This approach possesses the capability to tightly constrain the motor tracking performance to an extensive degree by closely adhering to the SOC reference trajectory. The effectiveness of this scheme was evaluated through simulation, with testing conducted using the NEDC drive cycle. Subsequent sections will detail the design of the EV traction system components and the Simulink model employed in this study.
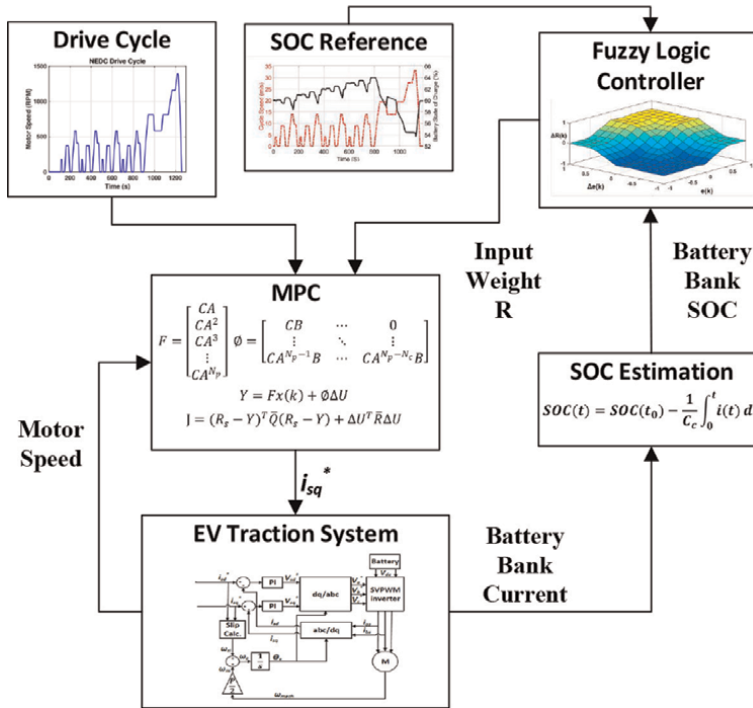
Figure 2.
Flowchart for the proposed SOC tracking technique.

3. Component modeling for an electric vehicle traction system

3.1 Lithium-ion battery bank model

3.1.1 Chen and Mora's model

The Chen and Mora (CM) circuit model is a comprehensive representation that captures the dynamic attributes of the battery's terminal voltage, and variations in battery parameters concerning SOC, and has undergone extensive experimentation over the last decade [13]. **Figure 3** depicts the CM equivalent circuit battery model
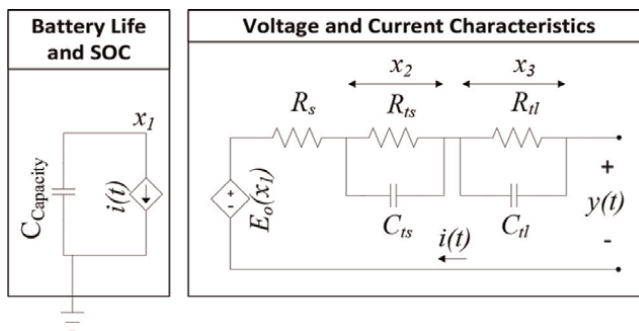
Figure 3.
CM lithium-ion equivalent battery circuit model.

utilized in this study. The left section of the circuit represents the variation in battery SOC due to the fluctuations in battery current. On the other hand, the variations in battery terminal voltage in response to the battery current are shown on the right. In this model, the state variable x_1 represents the battery's SOC, while x_2 corresponds to the voltage across $R_{ts}\|C_{ts}$, and x_3 corresponds to voltage across $R_{tl}\|C_{tl}$. The parallel combination $R_{ts}\|C_{ts}$ characterizes the short-term terminal voltage dynamics in response to fluctuations in discharge current, while the parallel combination $R_{tl}\|C_{tl}$ characterizes the long-term terminal voltage dynamics in response to variations in discharge current [13]. Eqs. (1)–(4) describe the CM equivalent circuit model [13].

$$\dot{x}_1(t) = -\frac{1}{C_C}i(t), \quad C_C = 3600Cf_1f_2f_3 \tag{1}$$

$$\dot{x}_2(t) = -\frac{x_2(t)}{R_{ts}(x_1)C_{ts}(x_1)} + \frac{i(t)}{C_{ts}(x_1)} \tag{2}$$

$$\dot{x}_3(t) = -\frac{x_3(t)}{R_{tl}(x_1)C_{tl}(x_1)} + \frac{i(t)}{C_{tl}(x_1)} \tag{3}$$

$$y = E_o(x_1) - x_2(t) - x_3(t) - i(t)R_s(x_1) \tag{4}$$

In this model, the SOC, denoted as x_1, varies within the range of $[0, 1]$. The states x_2 and x_3 are positive while the battery is discharging, and their sign depends on whether the battery is charging or discharging. Eq. (1) contains the parameter C which represents the capacity in ampere-hours (A.h). Furthermore, the impact of temperature on battery performance, the number of charging and discharging cycles, and the effect of self-discharging are taken into account through the factors f_1, f_2, and f_3. They are set to 1 in this work. Eq. (4) depicts the states x_2 and x_3 and their impact on the terminal voltage y. In addition, the impact of the battery's series resistance is taken care of by multiplying $i(t)$ and R_s then subtracting the product from the open-circuit voltage E_o. Eqs. (5)–(10) define the variables R_s, C_{tl}, R_{tl}, C_{ts}, R_{ts}, and E_o [13].

$$E_o(x_1) = -a_1e^{-a_2x_1} + a_3 + a_4x_1 - a_5x_1^2 + a_6x_1^3 \tag{5}$$

$$R_{ts}(x_1) = a_7e^{-a_8x_1} + a_9 \tag{6}$$

$$R_{tl}(x_1) = a_{10}e^{-a_{11}x_1} + a_{12} \tag{7}$$

$$C_{ts}(x_1) = -a_{13}e^{-a_{14}x_1} + a_{15} \tag{8}$$

$$C_{tl}(x_1) = -a_{16}e^{-a_{17}x_1} + a_{18} \tag{9}$$

$$R_s(x_1) = a_{19}e^{-a_{20}x_1} + a_{21} \tag{10}$$

The lithium battery's E_o curve was recorded through the technique described in Ref. [13]. Furthermore, MATLAB was employed to determine the variables a_1 through a_6 in Eq. (5). The remaining parameters of the lithium-ion battery model, as specified in Eqs. (6)–(9), are acquired using the APE technique [13]. The R_s constants a_{19} through a_{21} can be obtained by fitting Eq. (10) with curve $R_s(x_1(t))$ versus $x_1(t)$ [13]. The values for parameter a_1 through a_{21} are provided in Table 4 in Ref. [7].

3.1.2 SOC estimation by coulomb counting

The SOC illustrates the available capacity as a percentage of the rated capacity [13]. The mathematical formulation for the Coulomb counting (CC) method is shown in Eq. (11).

$$SOC(t) = SOC(t_o) - \frac{1}{C_c} \int_0^t i(t)dt \tag{11}$$

The starting SOC is denoted by $SOC(t_o)$, while the parameter C_c stands for the capacity of the battery, calculated according to Eq. (1). The variable $i(t)$ signifies the discharge current, with positive values indicating discharging and negative values signifying charging.

3.2 Description of the controllers

3.2.1 Model predictive controller

The model predictive control (MPC) technique utilizes the system's model to calculate the desired control signal required which will lead the system toward the required value. Before formulating the equations for the MPC, we need to select the prediction horizon, denoted as N_p, which signifies how many samples into the future the controller can forecast. The second variable is the control horizon, represented as N_c. It indicates the number of control variables that can be manipulated, with the condition that N_p must be greater than or equal to N_c.

Consider a system in which the output at a particular sampling instant, denoted as k, is not directly influenced by the control signal. This system can be described using the discrete-time state-space model as shown in Eqs. (12) and (13).

$$x_m(k+1) = A_m x_m(k) + B_m u(k) \tag{12}$$

$$y(k) = C_m x_m(k) \tag{13}$$

Eqs. (14) and (15) define the difference between the current and previous values of the control signal, denoted as Δu, and the state variable Δx_m.

$$\Delta u(k) = u(k) - u(k-1) \tag{14}$$

$$\Delta x_m(k) = x_m(k) - x_m(k-1) \tag{15}$$

We can formulate Eqs. (16) and (17) by merging Eqs. (12)–(15)

$$\Delta x_m(k+1) = A_m \Delta x_m(k) + B_m \Delta u(k) \tag{16}$$

$$\begin{aligned} y(k+1) &= y(k) + C_m \Delta x_m(k+1) \\ &= y(k) + C_m A_m \Delta x_m(k) + C_m B_m \Delta u(k) \end{aligned} \tag{17}$$

Eqs. (16) and (17) can be employed to construct the augmented state-space model of the system as depicted in Eqs. (18) and (19).

$$x(k+1) = Ax(k) + B\Delta u(k) \tag{18}$$

$$y(k) = Cx(k) \tag{19}$$

where $x(k) = \begin{bmatrix} \Delta x_m(k) \\ y(k) \end{bmatrix}$, $A = \begin{bmatrix} A_m & 0_m^T \\ C_m A_m & 1 \end{bmatrix}$, $B = \begin{bmatrix} B_m \\ C_m B_m \end{bmatrix}$, $C = [0_m \ 1]$.

and the empty spaces in the matrix are filled by the zero matrix $0_m = [0, 0, \cdots 0]$.

At instant k, Eq. (20) describes the system states for future samples. This is obtained by expanding $x(k + 1)$ in Eq. (18).

$$
\begin{aligned}
x(k + 1|k) \quad &= Ax(k) + B\Delta u(k) \\
&\vdots \\
x(k + N_p|k) \quad &= A^{N_p}x(k) + A^{N_p-1}B\Delta u(k) + \cdots + \\
&\quad A^{N_p - N_c}B\Delta u(k + N_c - 1)
\end{aligned}
\tag{20}
$$

Likewise, Eq. (21) can be derived by expanding $y(k + 1)$ in Eq. (19).

$$
\begin{aligned}
y(k + 1|k) \quad &= CAx(k) + CB\Delta u(k) \\
&\vdots \\
y(k + N_p|k) \quad &= CA^{N_p}x(k) + CA^{N_p-1}B\Delta u(k) + \cdots + \\
&\quad CA^{N_p - N_c}B\Delta u(k + N_c - 1)
\end{aligned}
\tag{21}
$$

Eqs. (22) and (23) describe the matrix ΔU, with length N_c, containing the changes in the control signal starting with instant k. Meanwhile, the matrix Y, with length N_p, describes the predicted output for the system.

$$
\Delta U = [\Delta u(k) \ \Delta u(k + 1) \ \cdots \Delta u(k + N_c - 1)]^T
\tag{22}
$$

$$
Y = \left[y(k + 1|k) \ y(k + 2|k) \ \ldots \ y(k + N_p|k)\right]^T
\tag{23}
$$

Merging Eqs. (20)–(23) yields Eq. (24).

$$
Y = Fx(k) + \Phi\Delta U(k)
\tag{24}
$$

where $F = \begin{bmatrix} CA \\ CA^2 \\ \vdots \\ CA^{N_p} \end{bmatrix}$ and $\Phi = \begin{bmatrix} CB & 0 & \cdots & 0 \\ CAB & CB & \cdots & 0 \\ \vdots & \vdots & \ddots & \vdots \\ CA^{N_p-1}B & CA^{N_p-2}B & \cdots & CA^{N_p-N_c}B \end{bmatrix}$.

The vector containing the reference signal of the system has a length of N_p and is defined by Eq. (25).

$$
R_s^T = [1 \ 1\cdots 1 \ 1]r(k)
\tag{25}
$$

Eq. (26) contains the cost function J.

$$
J = (R_s - Y)^T\overline{Q}(R_s - Y) + \Delta U^T\overline{R}\Delta U
\tag{26}
$$

where $\overline{R}$ is an $N_c \times N_c$ input weight matrix, and $\overline{Q}$ is an $N_c \times N_c$ output weight matrix. The specific values of these weight matrices can be adjusted depending on the system's operational requirements. The ratio of the input weight R to the output weight Q serves to penalize variations in the control signal during the system's

operation. In this work, Q was kept at 1, while the modification was performed on R while the system was running. Eq. (27) can be obtained by expanding Eq. (26).

$$J = (R_s - Fx(k))^T(R_s - Fx(k)) \tag{27}$$

The partial derivative with respect to ΔU is taken and equated to zero yielding Eqs. (28) and (29).

$$\frac{\partial J}{\partial \Delta U} = -2\Phi^T(R_s - Fx(k)) + 2(\Phi^T\Phi + \overline{R})\Delta U \tag{28}$$

$$\frac{\partial J}{\partial \Delta U} = 0 \rightarrow \Delta U = (\Phi^T\Phi + \overline{R})^{-1}\Phi^T(R_s - Fx(k)) \tag{29}$$

The element $\Delta u(k)$ is obtained from matrix ΔU and is used to update $u(k-1)$. This results in the updated control signal $u(k)$.

3.2.2 Fuzzy logic controller

The architecture of the fuzzy logic controller (FLC) is illustrated in **Figure 4**. This FLC generates the change in the input weight at time instant k, denoted by $\Delta R(k)$. It monitors the error $e(k)$ and changes in error $\Delta e(k)$ of the battery SOC, denoted by $SOC_{battery}(k)$, and the SOC reference, denoted by $SOC_{reference}(k)$. Furthermore, **Figure 4** depicts the three stages that the signal passes through before the controller issues a command. The fuzzifier generates linguistic variables from the given signal. Next, the inference mechanism correlates the linguistic variables with the rule base and then produces a linguistic output. Finally, the defuzzifier creates the control signal from the linguistic outputs. The change in the weight $\Delta R(k)$ is produced by the FLC and is added to the current value $R(k-1)$ to form $R(k)$.

The surface representing the fuzzy inference system is depicted in **Figure 5**. When the values of $e(k)$ and $\Delta e(k)$ lie within $[0.5, 1]$, the resultant $\Delta R(k)$ is positive, indicating a large increase in the input weight. Conversely, when $e(k)$ and $\Delta e(k)$ are between $[-1, -0.5]$, there is a significant drop in $\Delta R(k)$. When $e(k)$ and $\Delta e(k)$ fall between $[-0.5, 0.5]$, the magnitude $\Delta R(k)$ depends on their point of intersection with the surface. A minor increase or decrease in $\Delta R(k)$ is applied until $e(k)$ and $\Delta e(k)$ approach zero.

3.3 Induction motor drive

Eqs. (30)–(35) describe the induction motor (IM) model in the synchronously rotating dq-coordinate system [7].
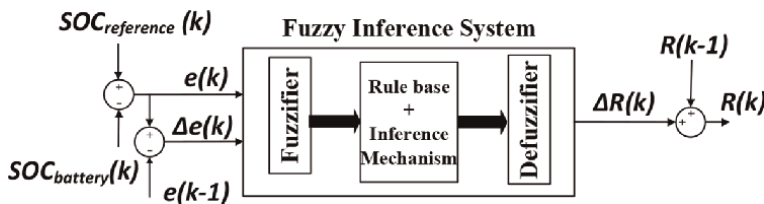
Figure 4.
Fuzzy logic controller block diagram.
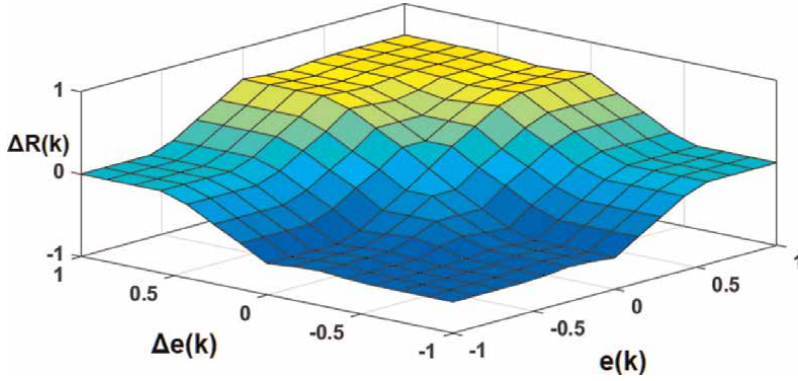
Figure 5.
Fuzzy logic controller surface.

$$V_{sd} = R_s i_{sd} + \frac{d\lambda_{sd}}{dt} - \omega_e \lambda_{sq} \qquad (30)$$

$$V_{sq} = R_s i_{sq} + \frac{d\lambda_{sq}}{dt} - \omega_e \lambda_{sd} \qquad (31)$$

$$V_{rd} = R_r i_{rd} + \frac{d\lambda_{rd}}{dt} - \omega_{sl} \lambda_{rq} \qquad (32)$$

$$V_{rq} = R_r i_{rq} + \frac{d\lambda_{rq}}{dt} - \omega_{sl} \lambda_{rd} \qquad (33)$$

$$T_{em} = \frac{3p}{2} \frac{L_m}{L_r} \left(\lambda_{rq} i_{rd} - \lambda_{rd} i_{rq} \right) \qquad (34)$$

$$\frac{d\omega_m}{dt} = \frac{1}{J} (T_{em} - T_L - B\omega_m) \qquad (35)$$

The variables V, i, and λ correspond to the voltages, currents, and fluxes, where the dq coordinate system components for the rotor are denoted by subscript r, and the stator is denoted by subscript s. The variables T_L, T_{em}, B, and J are the load torque, motor torque, coefficient of friction, and motor inertia. While R_s is the the stator resistance and R_r is the rotor resistance. Additionally, ω_m, ω_e, and ω_{sl} denote the rotor speed, the speed at which the d-axis is rotating, and the speed at which the rotor axis is rotating, respectively. Furthermore, ω_e was intentionally set equated to $\omega_{sync} = 2\pi f$ which represents the synchronous speed.

The electrical coupling equations are represented by Eqs. (30)–(34), and Eq. (35) represents the mechanical coupling equation of the induction machine. Eq. (36) illustrates the relationship between the dq-fluxes and the dq-currents in matrix form.

$$\begin{bmatrix} \lambda_{sd} \\ \lambda_{sq} \\ \lambda_{rd} \\ \lambda_{rq} \end{bmatrix} = \begin{bmatrix} L_s & 0 & L_m & 0 \\ 0 & L_s & 0 & L_m \\ L_m & 0 & L_r & 0 \\ 0 & L_m & 0 & L_r \end{bmatrix} \begin{bmatrix} i_{sd} \\ i_{sq} \\ i_{rd} \\ i_{rq} \end{bmatrix} \qquad (36)$$

Eqs. (37) and (38) represent the conversion matrices used in the system. The variables are converted to the dq coordinate system components, manipulated, then transformed back to abc components.

$$\begin{bmatrix} i_{sd} \\ i_{sq} \end{bmatrix} = \sqrt{\frac{2}{3}} \begin{bmatrix} \cos(\theta_e) & \cos\left(\theta_e - \frac{2\pi}{3}\right) & \cos\left(\theta_e - \frac{4\pi}{3}\right) \\ -\sin(\theta_e) & -\sin\left(\theta_e - \frac{2\pi}{3}\right) & -\sin\left(\theta_e - \frac{4\pi}{3}\right) \end{bmatrix} \begin{bmatrix} i_a \\ i_b \\ i_c \end{bmatrix} \tag{37}$$

$$\begin{bmatrix} i_a \\ i_b \\ i_c \end{bmatrix} = \sqrt{\frac{2}{3}} \begin{bmatrix} \cos(\theta_e) & -\sin(\theta_e) \\ \cos\left(\theta_e + \frac{4\pi}{3}\right) & -\sin\left(\theta_e + \frac{4\pi}{3}\right) \\ \cos\left(\theta_e + \frac{2\pi}{3}\right) & -\sin\left(\theta_e + \frac{2\pi}{3}\right) \end{bmatrix} \begin{bmatrix} i_{sd} \\ i_{sq} \end{bmatrix} \tag{38}$$

where θ_e represents the angle that the d-axis makes with the stationary axis [7].

3.3.1 Indirect field-oriented control (IFO)

To perform indirect field-orientation (IFO) we fix λ_{rq} to zero. Therefore, we can obtain Eq. (39) by combining Eqs. (32) and (36). This rotor flux is calculated using Eq. (39). In addition, Eq. (33) merged with Eq. (36), will result in Eq. (40) [7]. Eq. (40) serves the purpose of calculating the rotor slip.

$$\lambda_{rd} = L_m i_{sd} \tag{39}$$

$$\omega_{sl} = \frac{L_m}{\tau_r} \frac{i_{sq}}{\lambda_{rd}} \tag{40}$$

where τ_r is the rotor time constant.

The state-space representation of the IFO IM drive can be derived by combining Eqs. (34) and (36), resulting in

$$T_{em} = \frac{3p}{2} \frac{L_m}{L_r} \left(\lambda_{rd} i_{sq}\right) \tag{41}$$

A relationship governing the speed ω_m and the current i_{sq} can be obtained by combining Eqs. (35) and (41).

$$\frac{d\omega_m}{dt} = \frac{1}{J} \left(\frac{3p}{2} \frac{L_m}{L_r} \left(\lambda_{rd} i_{sq}\right) - T_L - B\omega_m \right) \tag{42}$$

Under a specific load T_L, differentiating Eq. (42) results in

$$\frac{d^2\omega_m}{dt^2} = -\frac{B}{J} \frac{d\omega_m}{dt} + \frac{3p}{2} \frac{L_m}{L_r} \frac{\lambda_{rd}}{J} \frac{di_{sq}}{dt} \tag{43}$$

The state-space representation of the IFO IM drive is provided in Eqs. (44) and (45) [7].

$$\begin{bmatrix} \ddot{\omega}_m \\ \dot{\omega}_m \end{bmatrix} = \begin{bmatrix} -\frac{B}{J} & 0 \\ 1 & 0 \end{bmatrix} \begin{bmatrix} \dot{\omega}_m \\ \omega_m \end{bmatrix} + \begin{bmatrix} \frac{3p}{2} \frac{L_m}{L_r} \frac{\lambda_{rd}}{J} \\ 0 \end{bmatrix} \frac{di_{sq}}{dt} \tag{44}$$
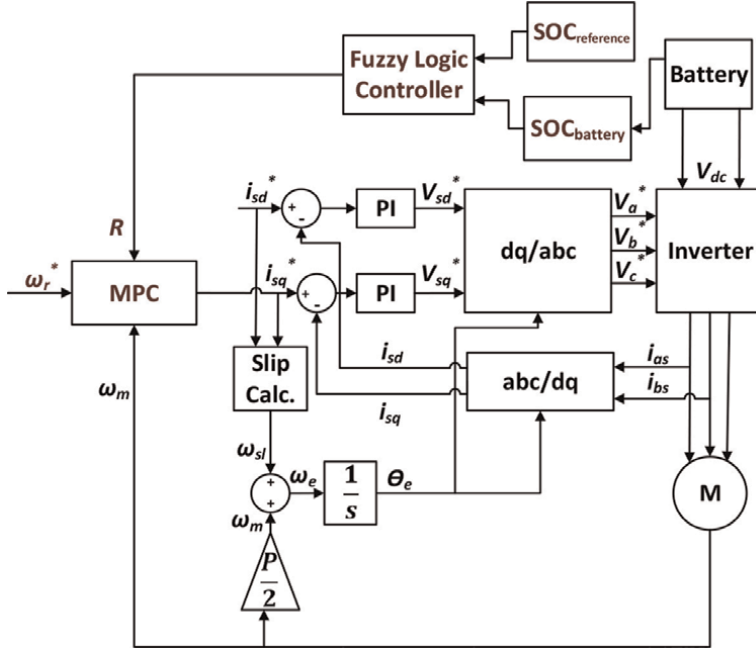
Figure 6.
IFO IM drive with SOC tracking.

$$\omega_m = \begin{bmatrix} 0 & 1 \end{bmatrix} \begin{bmatrix} \dot{\omega}_m \\ \omega_m \end{bmatrix} \tag{45}$$

The comprehensive EV traction system, encompassing the IFO IM drive, the battery bank, and the SOC tracking scheme is illustrated in **Figure 6**. The battery bank current is used to estimate the battery SOC, and an FLC compares the battery bank SOC and reference SOC, then generates an input weight R for the MPC objective function. The outer controller loop comprising the input weight R, the MPC, and the motor speed ω_m is responsible for generating the reference i_{sq}^* current. The d-axis current i_{sd}^* and q-axis current i_{sq}^* are responsible for regulating the flux and torque of the induction motor, respectively. The "Slip Calc." block carries out rotor flux estimation using Eq. (39) and subsequently calculates the slip using Eq. (40). Moreover, PI controllers for the inner current loops ensure that the stator q and d component currents are tracking the reference q and d component currents, respectively. The q and d component voltages are generated from the inner PI controllers and converted to the reference *abc* component sinusoidal voltages used to produce the inverter gating signals.

4. Simulation results

4.1 Testing methodology

4.1.1 Drive cycle description

A driving cycle consists of data points that represent the velocity of a real-life vehicle measured over time. The New European Drive Cycle (NEDC) consists of both

urban and extra-urban driving stages. It is a combination of straight acceleration and constant speed periods, and it is depicted in **Figure 7**. The urban driving cycle lasts for 800 seconds, starting at second 11 and ending at second 785. It consists of three constant speed peaks, and they are repeated four times as shown in the rectangle. The constant speed peaks are arranged in ascending order with the peaks occurring at 187, 400, 625, and 437 RPM, respectively. The extra-urban driving stage spans 370 seconds, beginning at second 800 and concluding at second 1170. The speed peaks occur at 625, 875, 1250, and 1500 RPM.

4.1.2 Simulink model description

Figure 8 shows the Simulink model for the EV traction system used in this work. A 580 V lithium-ion battery bank with a capacity of 4000 mAh provides the required voltage and power for the EV traction system. The inverter produces the required voltage and frequency to control the speed of the IM. Furthermore, the IM ratings were 0.5 kW, 415 V, and 50 Hz. The references in the system are the red block representing the reference motor d-axis current i_{sd}^*, the drive cycle reference block, and the SOC reference block. The slip frequency estimation block estimates the rotor flux and slip using Eqs. (39) and (40), respectively. The battery bank SOC estimation is performed using Eq. (11), and the SOC is sent to the FLC. The FLC compares the
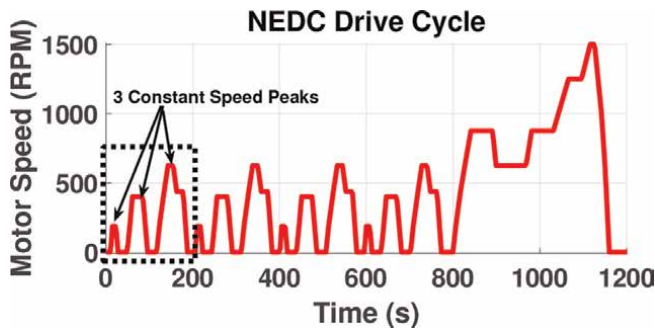
Figure 7.
NEDC drive cycle.
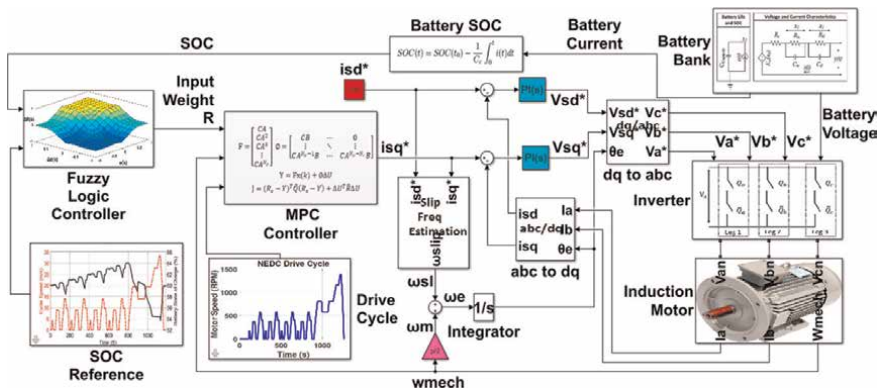
Figure 8.
MATLAB/Simulink model for the EV traction system with SOC tracking.

battery SOC with the reference SOC and generates the R for the MPC cost function. The MPC generates the speed-regulating signal i_{sq}^* while giving consideration to the reference SOC. The motor dq currents are regulated by the inner PI controllers. While the dq voltages are converted to the reference abc sinusoidal voltages V_a^*, V_b^*, and V_c^* that are used by the inverter to generate the required voltages for the motor. The simulation sampling time is 10 kHz.

4.1.3 State of charge reference

The scope of this work focused on devising a technique to regulate the SOC of the EV traction system rather than producing an SOC reference signal. Therefore, the SOC reference signal used in this work is just a limitation to the maximum change in SOC. **Figure 9a** shows the SOC deterioration over the NEDC drive cycle. The rate of change of SOC, denoted by ΔSOC, is obtained by taking the difference between the current and previous sample for the SOC signal. **Figure 9b** illustrates the inverted version of the ΔSOC over-the-NEDC drive cycle, and is used as the primary evaluation metric for the SOC tracking technique. The inverted ΔSOC will be referred to as ΔSOC for simplicity.

The ΔSOC graph is divided into five regions as shown in **Figure 10**. The regions are classified as follows:

- Region 1: Represents the urban stage of the NEDC drive cycle, and is characterized by steady acceleration, deceleration, and constant speed. No limitations are set on the ΔSOC. This region represents the impact of the motor current on the ΔSOC when the motor performance is unrestricted. It also acts as the reference point for generating the maximum permitted ΔSOC value for regions 2 through 4. The peak values for the ΔSOC occur at 0.15, 0.19, and 0.255 Coulombs.

- Region 2: Represents the urban stage of the NEDC drive cycle, and is characterized by steady acceleration, deceleration, and constant speed. The ΔSOC is restricted to 90% of its original value. The maximum permitted ΔSOC value is obtained by multiplying the ΔSOC of region 1 by 90%. The maximum permitted ΔSOC value is shown by the 3 red bars in region 2.
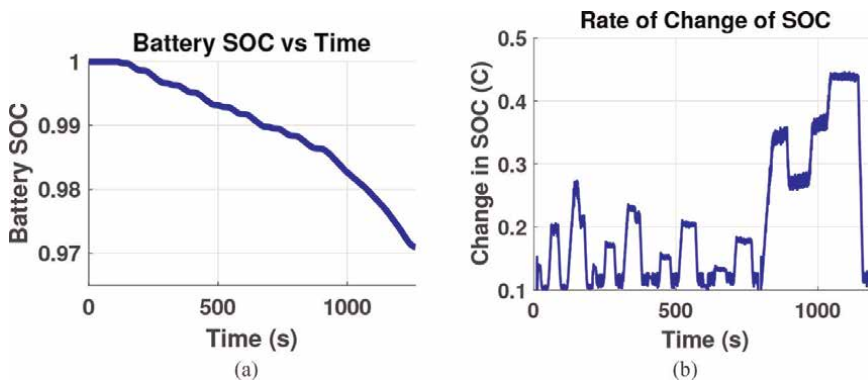
Figure 9.
Battery bank (a) SOC decay (b) inverted ΔSOC with the SOC tracking technique.
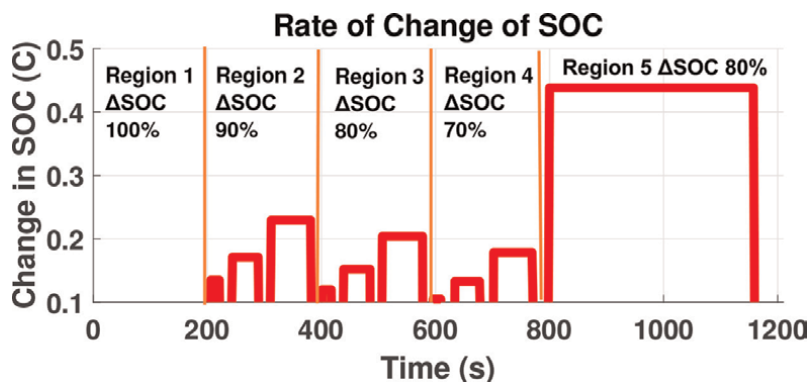
Figure 10.
Battery bank maximum permitted ΔSOC values on regions 2 through 5.

- Region 3: Represents the urban stage of the NEDC drive cycle, and is characterized by steady acceleration, deceleration, and constant speed. The ΔSOC is restricted to 80% of its original value. The maximum permitted ΔSOC value is obtained by multiplying the ΔSOC of region 1 by 80%. The maximum permitted ΔSOC value is shown by the 3 red bars in region 3.

- Region 4: Represents the urban stage of the NEDC drive cycle, and is characterized by steady acceleration, deceleration, and constant speed. The ΔSOC is restricted to 70% of its original value. The maximum permitted ΔSOC value is obtained by multiplying the ΔSOC of region 1 by 70%. The maximum permitted ΔSOC value is shown by the 3 red bars in region 4.

- Region 5: Represents the extra-urban stage of the NEDC drive cycle, and is distinguished by its high speed. The ΔSOC is restricted to 80% of the ΔSOC when the motor is running at 1500 *RPM* (0.55 Coulombs). The maximum permitted ΔSOC value is shown by the red bar in region 5.

4.2 Test results

Figure 11 overlaps the ΔSOC readings with the predefined maximum permitted values. Region 1 serves as an example of what the ΔSOC values in regions 2 through 4 would have been if the SOC tracking scheme had not enforced maximum permitted ΔSOC values. Regions 2 through 4 clearly demonstrate that the ΔSOC was constrained and prevented from exceeding the established maximum permitted value, confirming the effectiveness of the SOC tracking method. Additionally, in region 5, we observe that when the ΔSOC remained below the maximum permitted value, it was allowed to adapt freely. However, once the ΔSOC began to rise, beyond the 1000-second mark, it was capped at the maximum permitted value. Moreover, during these capping periods, the magnitude of the error ΔSOC was recorded and the average was obtained. **Figure 12** displays the average of the absolute value of the error during the capping periods. The absolute average error for the capping periods varies between $[0.00052, \ 0.0013]$ and the average for the complete NEDC drive cycle is 0.00095. This result is comparable to the ECMS, A-ECMS, and Fuzzy A-ECMS techniques which yielded 0.0003, 0.0037, and 0.0019 deviations off the reference SOC while testing on the NEDC drive cycle.
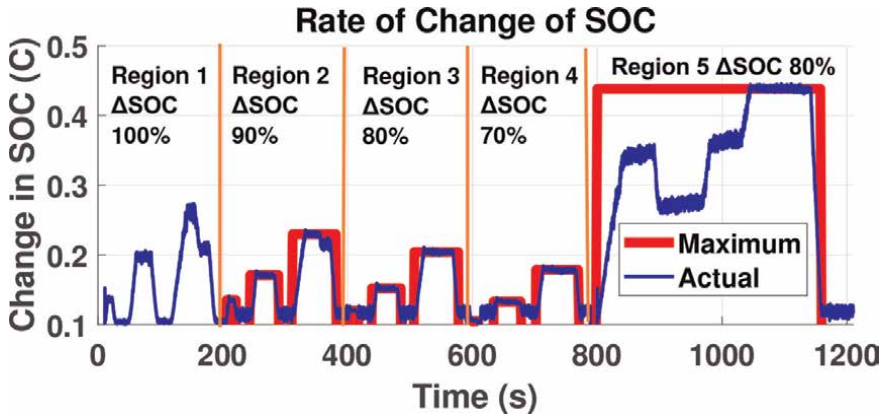
Figure 11.
Battery bank ΔSOC and maximum permitted ΔSOC values with the SOC tracking technique.
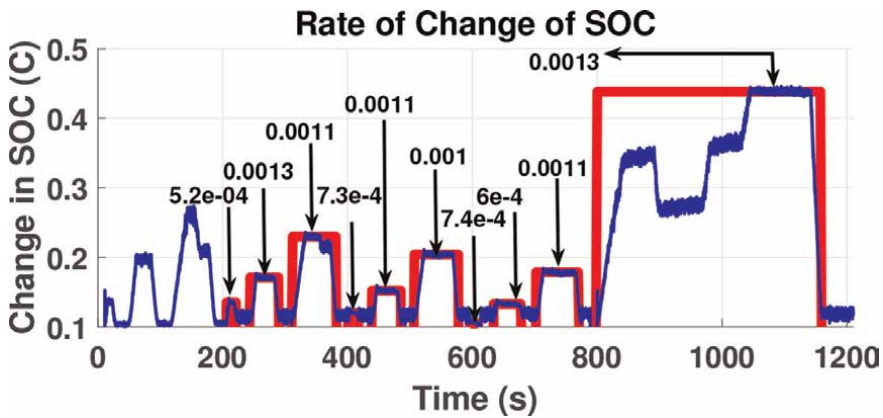
Figure 12.
ΔSOC absolute average error at the maximum permitted ΔSOC values with the SOC tracking technique.

Figure 13 illustrates the response of the motor's speed during the NEDC drive cycle. In region 1, it is evident that the unrestricted SOC tracker technique adeptly regulates the motor's speed. However, as we move into regions 2 through 4 (where the maximum permitted ΔSOC values range from 90 to 70%), we observe a noticeable decline in the motor's speed tracking performance. The more stringent the ΔSOC constraint, the larger the drop in the motor's speed-tracking performance. Consequently, in region 4, we witness a substantial deterioration in motor speed tracking performance compared to regions 2 and 3. Moving to region 5, we note that before the 1000-second mark, the ΔSOC remained below its maximum permitted value, allowing for effective regulation of the motor speed. Conversely, after the 1000-second mark, the ΔSOC reached its maximum permitted value and was held at that boundary, resulting in a decline in speed tracking performance.

Figure 14 presents the fluctuation in the input weight parameter, denoted as R throughout the NEDC drive cycle. It is important to note that the input weight R plays a direct role in determining the generation of the motor speed-regulating current i_{sq}^*, which was discussed in the previous section. Specifically, as the value of R increases, it imposes a more significant constraint on i_{sq}^*. Since i_{sq}^* directly influences the motor
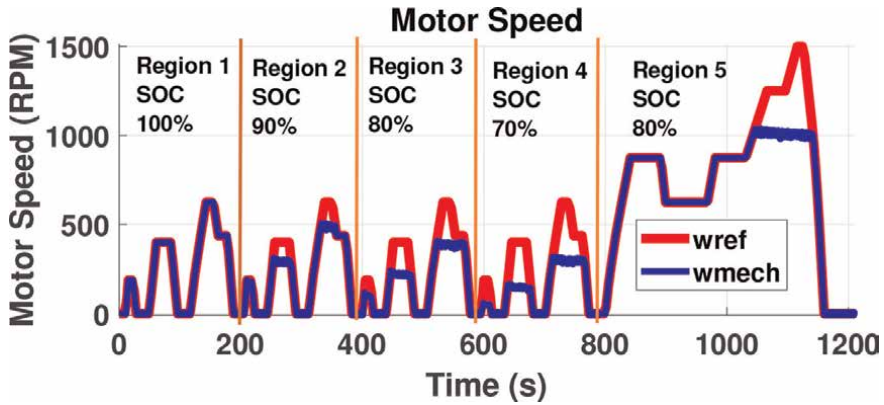
Figure 13.
Motor speed response with the SOC tracking technique.
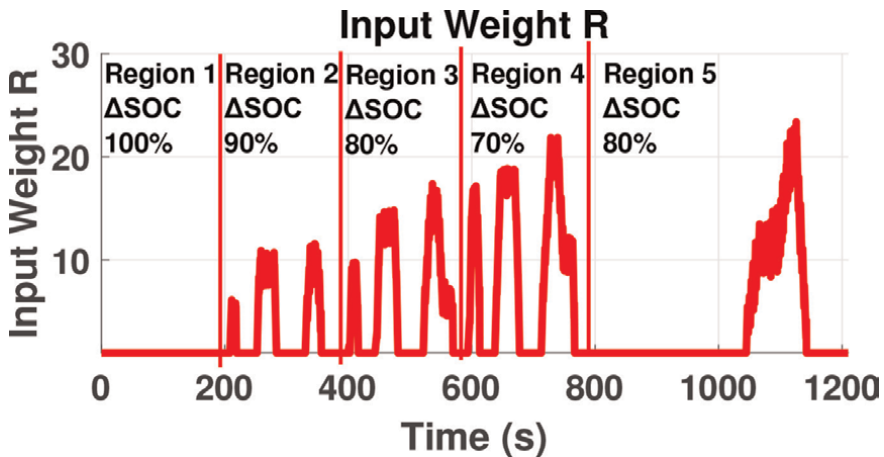
Figure 14.
Input weight R with the SOC tracking technique.

current, a lower i_{sq}^* results in drawing less current from the battery bank, eventually leading to a reduced ΔSOC.

From the previous statement, it is apparent that enforcing a stricter limit on ΔSOC necessitates a higher value for R. This becomes evident when comparing the values of R in regions 2 through 4, which have the same speed reference. As ΔSOC constraints become more stringent (from 90 to 70% maximum permitted ΔSOC), the value of R increases correspondingly.

Furthermore, an increase in the reference speed demands a higher value for i_{sq}^*, consequently increasing the ΔSOC value. If there is a maximum permitted ΔSOC value, then the input weight R must rise in tandem with the increasing reference speed to restrict i_{sq}^* further, and thereby maintain the ΔSOC at the maximum permitted value. This phenomenon is observable when examining region 5. Before the 1000-second mark, the ΔSOC value below the maximum permitted value, R remained at the minimum level. However, after the 1000-second mark, as the ΔSOC value reached

the maximum permitted value, the input weight R increased in line with the reference speed signal to uphold the ΔSOC at its maximum permitted value.

5. Conclusions

This chapter introduces a method for tracking the state of charge (SOC) using a fuzzy-tuned model predictive controller. The mathematical models for the components of an electric vehicle traction system were developed and tested on Simulink. The simulation was conducted using the New European Drive Cycle, during which the motor speed and battery SOC were continuously monitored. The outcomes of the simulation demonstrate the effectiveness of the SOC tracking technique in regulating motor speed when there are no SOC restrictions. Furthermore, it successfully maintains the battery SOC within the defined maximum permitted value, albeit with some trade-offs in motor speed tracking performance. The absolute average deviation from the reference for the SOC tracking technique was lower than the Fuzzy A-ECMS, and A-ECMS techniques which yielded 0.00095, 0.0019, and 0.0037, respectively. However, the ECMS technique with a fixed optimal equivalent factor had the lowest deviation of 0.0003. In other words, there is still room for improvement in the SOC tracking technique. Furthermore, the robustness of the technique on different driving behaviors is yet to be tested. In summary, the simulation results provide substantial evidence supporting the effectiveness of the SOC tracking technique.

Future research directions include:

- Testing the robustness of the technique on an aggressive drive cycle such as the US06 drive cycle.

- Testing the effectiveness of the technique on a reference SOC instead of a fixed rate of change of SOC.

- Incorporating the i_{sd} current in the MPC objective function, and monitoring the impact on the absolute average deviation from the reference SOC.

Abbreviations

EV	electric vehicle
BEM	battery energy management
SOC	state of charge
DP	dynamic programming
MPC	model predictive controller
FLC	fuzzy logic controller
FMPC	fuzzy model predictive controller
ECMS	equivalent consumption minimization strategy
A-ECMS	adaptive equivalent consumption minimization strategy
Fuzzy A-ECMS	fuzzy adaptive equivalent consumption minimization strategy
CM	Chen and Mora
CC	Coulomb counting
IM	induction motor

IFO	indirect field orientation
PI	Proportional-integral controller
NEDC	New European drive cycle

Author details

Ahmed Sayed Abdelaal Abdelaziz
Department of Electrical Engineering, American University of Sharjah, Sharjah,
United Arab Emirates

*Address all correspondence to: b00060280@alumni.aus.edu

IntechOpen

References

[1] Jianjun H, Xiao F, Mei B, Lin Z, Chunyun F. Optimal energy efficient control of pure electric vehicle power system based on dynamic traffic information flow. IEEE Transactions on Transportation Electrification. 2022; **8**(1):510-526

[2] Li SG, Sharkh SM, Walsh FC, Zhang C-N. Energy and battery management of a plug-in series hybrid electric vehicle using fuzzy logic. IEEE Transactions on Vehicular Technology. 2011;**60**(8):3571-3585

[3] Galdi V, Piccolo A, Siano P. A fuzzy based safe power management algorithm for energy storage systems in electric vehicles. In: 2006 IEEE Vehicle Power and Propulsion Conference. Windsor, UK: IEEE; Sep. 2006. pp. 1-6

[4] Phan D, Bab-Hadiashar A, Fayyazi M, Hoseinnezhad R, Jazar RN, Khayyam H. Interval type 2 fuzzy logic control for energy management of hybrid electric autonomous vehicles. IEEE Transactions on Intelligent Vehicles. 2021;**6**(2): 210-220

[5] Suhail M, Akhtar I, Kirmani S, Jameel M. Development of progressive fuzzy logic and ANFIS control for energy management of plug-in hybrid electric vehicle. IEEE Access. 2021;**9**:62219-62231

[6] Wang S, Huang X, López JM, Xiangyang X, Dong P. Fuzzy adaptive-equivalent consumption minimization strategy for a parallel hybrid electric vehicle. IEEE Access. 2019;**7**: 133290-133303

[7] Abdelaal AS, Mukhopadhyay S, Rehman H. Battery energy management techniques for an electric vehicle traction system. IEEE Access. 2022;**10**: 84015-84037

[8] Zhang Y, Chu L, Ding Y, Nan X, Guo C, Zicheng F, et al. A hierarchical energy management strategy based on model predictive control for plug-in hybrid electric vehicles. IEEE Access. 2019;**7**:81612-81629

[9] Zhang C, Vahidi A, Pisu P, Li X, Tennant K. Role of terrain preview in energy management of hybrid electric vehicles. IEEE Transactions on Vehicular Technology. 2009;**59**(3):1139-1147

[10] Wang X, Park S, Han K. Energy-efficient speed planner for connected and automated electric vehicles on sloped roads. IEEE Access. 2022;**10**: 34654-34664

[11] Zhao N, Zhang F, Yang Y, Coskun S, Lin X, Xiaosong H. Dynamic traffic prediction-based energy management of connected plug-in hybrid electric vehicles with long short-term state of charge planning. IEEE Transactions on Vehicular Technology. 2023;**72**(5): 5833-5846

[12] Chen H, Xiong R, Lin C, Shen W. Model predictive control based real-time energy management for hybrid energy storage system. CSEE Journal of Power and Energy Systems. 2021;**7**(4):862-874

[13] Mukhopadhyay S, Usman HM, Rehman H. Real time Li-ion battery bank parameters estimation via universal adaptive stabilization. IEEE Open Journal of Control Systems. 2022;**1**: 268-293

Nonlinear Robust Control of Trajectory-Following for Autonomous Ground Electric Vehicles

Xianjian Jin and Qikang Wang

Abstract

This chapter proposes a nonlinear robust H-infinity control approach to enhance the trajectory-following capabilities of autonomous ground electric vehicles (AGEV). Given the inherent influence of driving maneuvers and road conditions on vehicle trajectory dynamics, the primary objective is to address the control challenges associated with trajectory-following, including parametric uncertainties, system nonlinearities, and external disturbance. Firstly, taking into account parameter uncertainties associated with the tire's physical limits, the system dynamics of the AGEV and its uncertain vehicle trajectory-following system are modeled and constructed. Subsequently, an augmented system for control-oriented vehicle trajectory-following is developed. Finally, the design of the nonlinear robust H-infinity controller (NRC) for the vehicle trajectory-following system is carried out, which is designed based on the H-infinity performance index and incorporates nonlinear compensation to meet the requirements of the AGEV system. The controller design involves solving a set of linear matrix inequalities derived from quadratic H-infinity performance and Lyapunov stability. To validate the efficacy of the proposed controller, simulations are conducted using a high-fidelity CarSim® full-vehicle model in scenarios involving double lane change and serpentine maneuvers. The simulation results demonstrate that the proposed NRC outperforms both the linear quadratic regulator (LQR) controller and the robust H-infinity controller (RHC) in terms of vehicle trajectory-following performance.

Keywords: autonomous vehicles, electric vehicles, trajectory-following, robust control, nonlinear control

1. Introduction

In recent years, the emergence of AGEV has attracted significant attention from the experts and scholars [1, 2]. AGEV technology offers notable benefits such as reducing traffic congestion, minimizing air pollution, and enhancing road safety. One key area of research focus is the application of active front steering (AFS) as a chassis active control technology for AGEV steering systems. AFS employs adaptive steering

gear ratio to improve vehicle stability and active safety. The integration of AFS systems in AGEV provides substantial advantages in terms of driver safety, handling flexibility, and trajectory-following performance for AGEV [3]. The inherent features of AFS, including its rapid response and precise execution, contribute to enhanced active safety and superior trajectory-following performance for AGEV [4, 5].

Extensive researches have been conducted in the literatures on the trajectory-following control of AGEV with AFS system [6–12]. For achieving trajectory-following for AGEV with the AFS system, a controller utilizing the Kalman filter with multi-rate is designed to account for the motor control period and the sampling time of the camera [6]. To address the challenges of the control distribution between steering and the control system for AGEV, a model predictive control (MPC) method is proposed in Ref. [7], which reallocates the braking and steering control based on tire force to precisely follow the desired trajectory. Aiming to enhance steering stability for AGEV, a variable steering ratio AFS controller is developed in Ref. [8], it establishes a mapping between vehicle velocity and steering wheel angle. Based on the linearization of the vehicle's model, the vehicle front steering angle is gained by the AFS system to follow the desired trajectory on slippery roads [9]. Moreover, the advanced steering capabilities of the AFS system have proven valuable in other application areas related to trajectory-following control [10–12].

Despite the success achieved in trajectory-following, there remain challenges in handling system nonlinearity, external disturbances, and uncertain model parameters [13, 14]. For example, researchers have employed various control strategies. Nonlinear model predictive control (NMPC) has been utilized to solve the system nonlinearity and ensure feasibility and convergence [15]. A combination of sliding mode and observer technique is applied to estimate model errors and disturbances for enhancing the system's stability [16]. In the context of Markov jump cyber-physical systems, an adaptive sliding mode control (SMC) framework is proposed to handle safety issues arising from actuator failures and external attacks [17]. For uncertain challenges of robotic arm systems, a switchable neural networks-based SMC framework has been developed to accurately track motion trajectories, which can provide real time control to enhance the stability of the trajectory-following control system by adaptive algorithm [18]. An adaptive fuzzy controller (FC) is developed to address the challenge nonlinear trajectory-following system, and the stability of system is guaranteed by Lyapunov method [19]. Some extensions of FC can be obtained from Refs. [20, 21]. Furthermore, active disturbance rejection control is employed to dynamically estimate and offset unmodeled system dynamics and unpredictable external disturbances, it enhances the stability of vehicle trajectory-following system [22]. Speed MPC strategies are proposed to achieve accurate trajectory-following for AGEV [23]. In the milling system, the optimal control and time delay techniques are used to suppress chatter by adaptive extreme value algorithm [24]. To handle the problems of parameter jump in complex nonlinear systems, an adaptive control method with multi-model switching is presented. The least squares technique and some lemmas are also utilized to develop an adaptive control law [25]. For dealing with the system disturbances, a novel optimal control based on iterative techniques is proposed in [26], and it provides the conditions of system asymptotic stability and the *H*-infinity control. An output feedback-based global adaptive control strategy is proposed to handle system nonlinear time-varying parameters [27]. Moreover, robust control strategies have also been implemented in trajectory-following control, providing benefits in addressing the challenges of system nonlinearity, parameter variation, and external disturbance [28].

Therefore, this chapter develops a novel nonlinear robust control framework for AGEV to address the challenges associated with trajectory-following control, including system nonlinearities, uncertain parameter, and disturbances. Firstly, the dynamics of the AGEV and the trajectory-following system are formulated. Subsequently, taking into account the *H*-infinity performance criterion, nonlinear system compensation, and aim of the trajectory-following, a nonlinear robust controller for trajectory-following is designed. Then, the robustness and effectiveness of the nonlinear robust controller is validated through MATLAB/Simulink/Carsim Co-simulation platform under two scenes. The following sections are structured as follows: Section 2 introduces vehicle trajectory-following modeling. Section 3 outlines the design of the nonlinear robust controller. Section 4 analyzes and discusses the simulation outcomes, and Section 5 presents the conclusions.

2. Vehicle trajectory-following model

The primary focus of the chapter revolves the trajectory-following problem for AGEV. It is assumed that the suspension is a rigid structure, and under normal driving conditions, the slip angle tends to be small. For facilitating the analysis of vehicle actual motion, the bicycle model is selected:

$$m\left(\dot{v}_x - v_y\dot{\varphi}\right) = F_{fy}\sin\delta_f + F_{fx}\cos\delta_f + F_{rx} \tag{1}$$

$$m(\ddot{y} + v_x\dot{\varphi}) = F_{fy}\cos\delta_f + F_{fx}\sin\delta_f + F_{ry} \tag{2}$$

$$I_z\ddot{\varphi} = l_f\left(F_{fy}\cos\delta_f + F_{fx}\sin\delta_f\right) - l_rF_{ry} \tag{3}$$

This model incorporates variables such as mass m, yaw angle φ, lateral velocity v_x and longitudinal velocity v_y, lateral tire forces F_{iy}, longitudinal tire forces F_{ix}, moment of inertia I_z. Specifically, F_y can be expressed:

$$F_y = f_y(\alpha, F_z, s_r, \mu) \tag{4}$$

The computation of α is:

$$\alpha = \tan^{-1}\left(\frac{v_{wy}}{v_{wx}}\right) \tag{5}$$

$$\begin{cases} v_{wfx} = v_x\cos\delta_f + \left(v_y + l_f\dot{\varphi}\right)\sin\delta_f \\ v_{wrx} = v_x\cos\delta_f + \left(v_y - l_r\dot{\varphi}\right)\sin\delta_f \end{cases} \tag{6}$$

$$\begin{cases} v_{wfy} = v_x\cos\delta_f - \left(v_y + l_f\dot{\varphi}\right)\sin\delta_f \\ v_{wry} = v_x\cos\delta_f - \left(v_y - l_r\dot{\varphi}\right)\sin\delta_f \end{cases} \tag{7}$$

s_r is defined as follows:

$$s_r = \begin{cases} 1 - \dfrac{v_{wx}}{rw_w}(rw_w \neq 0, rw_w > v_{wx}) \\ \dfrac{rw_w}{v_{wx}} - 1(v_{wx} \neq 0, rw_w < v_{wx}) \end{cases} \tag{8}$$

where the tire's radius and angular velocity are represented by r and w_w, respectively. F_Z is given by the following equation:

$$\begin{cases} F_{Zfl,Zfr} = \dfrac{l_r mg}{2(l_r + l_f)} \mp \Delta F_1 + \Delta F_2 \\[3mm] F_{Zrl,Zrr} = \dfrac{l_f mg}{2(l_r + l_f)} \mp \Delta F_2 + \Delta F_1 \end{cases} \tag{9}$$

ΔF_1 and ΔF_2 are calculated using specific equations:

$$\begin{cases} \Delta F_1 = \dfrac{m(\dot{v}_x - v_y w)h_{cog}}{2(l_r + l_f)} \\[3mm] \Delta F_2 = \dfrac{m(\dot{v}_x - v_y w)h_{cog}}{2L_h} + \dfrac{gm_s h_s}{2L_h}\left(\dfrac{h_{cog}\xi}{g} - \sin\xi\right) \end{cases} \tag{10}$$

Under the assumption that α is small under driving conditions, the tire forces can be simplified:

$$F_{iy} = N_{\alpha i}\alpha_i, (i = f, r) \tag{11}$$

where $N_{\alpha i}$ is the cornering stiffness. Slip angle α_i can be gained:

$$\alpha_f = \delta_f - \frac{v_y + l_f\dot{\varphi}}{v_x}, \alpha_r = -\frac{v_y + l_r\dot{\varphi}}{v_x} \tag{12}$$

Taking into account the small front wheel angle, we can approximate $\cos\delta_f \approx 1$ and $\sin\delta_f \approx 0$. Additionally, we assume AGEV only moves in the horizontal plane, and it neglects the influence of other effects. Consequently, based on Eqs. (11) and (12), Eqs. (2) and (3) can be rewritten:

$$\ddot{y} = -\frac{N_{\alpha f} + N_{\alpha f}}{mv_x}\dot{y} - \left(\frac{l_f N_{\alpha f} - l_r N_{\alpha f}}{mv_x} + v_x\right)\dot{\varphi} + w_2 \tag{13}$$

$$\ddot{\varphi} = -\frac{l_f N_{\alpha f} - l_r N_{\alpha f}}{I_z v_x}\dot{y} - \frac{l_f^2 N_{\alpha f} + l_r^2 N_{\alpha f}}{I_z v_x}\dot{\varphi} + w_4 \tag{14}$$

where w_2 and w_4 represent the model state error.

During the trajectory-following process of the AGEV, it is crucial to consider state information of the vehicle. **Figure 1** depicts the diagram illustrating the trajectory-following process of the AGEV. The current and expected yaw angles are represented by φ and φ_r, respectively. Furthermore, the derivatives of y_e and φ_e can be expressed:

$$\dot{y}_e = v_y - v_x\varphi_e \tag{15}$$

$$\dot{\varphi}_e = \dot{\varphi} - \dot{\varphi}_r = \dot{\varphi} - \chi\dot{s} \tag{16}$$

The derivative information of s can be expressed as:

$$\dot{s} = v_x + v_y\varphi_e \tag{17}$$
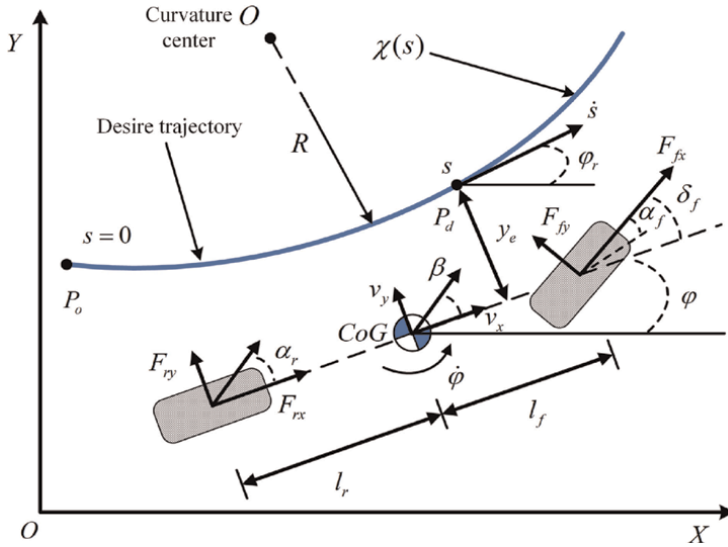
Figure 1.
The diagram illustrating the trajectory-following process of the AGEV.

$$\ddot{s} = \dot{v}_x + \dot{v}_y \varphi_e + v_y \dot{\varphi}_e \tag{18}$$

By utilizing Eqs. (15)–(18), the derivatives of y_e and φ_e are transformed into Eqs. (19) and (20), respectively.

$$\ddot{y}_e = \dot{v}_y - \dot{v}_x \varphi_e - v_x \dot{\varphi}_e \tag{19}$$

$$\ddot{\varphi}_e = \dot{\zeta} - \dot{\chi}\dot{s} - \chi\ddot{s} \tag{20}$$

The vehicle dynamics mentioned can be reformulated into a state space representation:

$$\dot{x} = Ax + Bu + B_w w \tag{21}$$

$$x = \begin{bmatrix} y_e \\ \dot{y}_e \\ \varphi_e \\ \dot{\varphi}_e \end{bmatrix}, A = \begin{bmatrix} 0 & 1 & 0 & 0 \\ 0 & -\dfrac{N_{af} + N_{ar}}{mv_x} & \dfrac{N_{af} + N_{ar}}{m} & -\dfrac{l_f N_{af} - l_r N_{ar}}{mv_x} \\ 0 & 0 & 0 & 1 \\ 0 & -\dfrac{l_f N_{af} - l_r N_{ar}}{I_z v_x} & \dfrac{l_f N_{af} - l_r N_{ar}}{I_z} & -\dfrac{l_f^2 N_{af} + l_r^2 N_{ar}}{I_z v_x} \end{bmatrix}, B_w = \begin{bmatrix} 0 \\ 1 \\ 0 \\ 1 \end{bmatrix}^T$$

$$B = \begin{bmatrix} 0 & \dfrac{N_{af}}{m} & 0 & \dfrac{l_f N_{af}}{I_z} \end{bmatrix}^T$$

The correlation between front wheel angle δ_f and steering wheel angle δ_a can be represented:

$$\delta_a = \tau_f \delta_f \tag{22}$$

where τ_f is the gear ratio.

As AGEV navigate through complex and dynamic road conditions, N_i ($i = af, ar$) vary and remain within certain bounds. This variation can be addressed in the following manner:

$$N_i = \overline{N}_i + n_i \tilde{N}_i, |n_i| < 1 (i = af, ar) \tag{23}$$

$$\overline{N}_{az} = \frac{N_{az\,min} + N_{az\,max}}{2} (z = f, r) \tag{24}$$

$$\tilde{N}_{az} = \frac{N_{az\,max} - N_{az\,min}}{2} (z = f, r) \tag{25}$$

The maximum and minimum values of N_i ($i = af, ar$) are denoted as N_{imax} and N_{imin}, respectively. The time-varying parameters n_i of the system satisfy the condition $|n_i| \le 1 (i = af, ar)$.

The system model (21) can be modified as follows:

$$\dot{x} = A_d x + B_d u + B_w w \tag{26}$$

The arguments in the equation have the following significance:

$$A_d = \overline{A}_d + \Delta A, B_d = \overline{B}_d + \Delta B, [\Delta A \quad \Delta B] = H_d F_d [E_A \quad E_B], |F_d| \le 1 \overline{A}_d =$$

$$\begin{bmatrix} 0 & 1 & 0 & 0 \\ 0 & -\dfrac{\overline{N}_{af} + \overline{N}_{ar}}{mv_x} & \dfrac{\overline{N}_{af} + \overline{N}_{ar}}{m} & -\dfrac{l_f \overline{N}_{af} - l_r \overline{N}_{ar}}{I_z} \\ 0 & 0 & 0 & 1 \\ 0 & -\dfrac{l_f \overline{N}_{af} - l_r \overline{N}_{ar}}{I_z v_x} & \dfrac{l_f \overline{N}_{af} - l_r \overline{N}_{ar}}{I_z} & -\dfrac{l_f^2 \overline{N}_{af} + l_r^2 \overline{N}_{ar}}{I_z v_x} \end{bmatrix}, \overline{B}_d = \begin{bmatrix} 0 \\ \dfrac{\overline{N}_{af}}{m} \\ 0 \\ \dfrac{l_f \overline{N}_{af}}{I_z} \end{bmatrix}$$

$$E_A = \begin{bmatrix} 0 & -\dfrac{1}{mv_x} & \dfrac{1}{m} & -\dfrac{l_f}{mv_x} \\ 0 & -\dfrac{1}{mv_x} & \dfrac{1}{m} & \dfrac{l_r}{mv_x} \\ 0 & -\dfrac{l_f}{I_z v_x} & \dfrac{l_f}{I_z} & -\dfrac{l_f^2}{I_z v_x} \\ 0 & \dfrac{l_r}{I_z v_x} & -\dfrac{l_r}{I_z} & -\dfrac{l_r^2}{I_z v_x} \end{bmatrix}, H_d = \begin{bmatrix} 0 & 0 & 0 & 0 \\ \tilde{N}_{af} & \tilde{N}_{ar} & 0 & 0 \\ 0 & 0 & 0 & 0 \\ 0 & 0 & \tilde{N}_{af} & \tilde{N}_{ar} \end{bmatrix}, E_B = \begin{bmatrix} \dfrac{1}{m} \\ 0 \\ \dfrac{l_f}{I_z} \\ 0 \end{bmatrix}$$

3. The design of nonlinear robust controller

3.1 Robust feedback control design

To achieve the desired trajectory tracking, an error function is defined and a robust linear feedback gain is designed as follows:

$$J_s = \int_0^\infty q_1 y_e^2 + q_2 \dot{y}_e^2 + q_3 \varphi_e^2 + q_4 \dot{\varphi}_e^2 + q_4 \delta^2 dt \tag{27}$$

where the letter symbols in the equation hold the following meanings:

$$y_e = y_a - y_d, \dot{y}_e = v_y - v_x \varphi_e, \varphi_e = \varphi - \varphi_r, \dot{\varphi}_e = \dot{\varphi} - \chi \dot{s}$$

The equation presented above can be expressed as follows:

$$
\begin{aligned}
J &= \int_0^\infty \left[\left(\overline{C}_1 x + \overline{D}_{11} w \right)^T U \left(\overline{C}_1 x + \overline{D}_{11} w \right) + u^T V u \right] dt \\
&= \int_0^\infty \left[\left(U^{\frac{1}{2}} \overline{C}_1 x + U^{\frac{1}{2}} \overline{D}_{11} w \right)^T \left(U^{\frac{1}{2}} \overline{C}_1 x + U^{\frac{1}{2}} \overline{D}_{11} w \right) + \int_0^\infty \left(V^{\frac{1}{2}} u \right)^T \left(V^{\frac{1}{2}} u \right) dt \right.
\end{aligned}
\tag{28}
$$

The arguments in the equation hold the following significance:

$$
\overline{C}_1 = \begin{bmatrix} 1 & 0 & 0 & 0 \\ 0 & 1 & 0 & 0 \\ 0 & 0 & 1 & 0 \\ 0 & 0 & 0 & 1 \end{bmatrix}, \overline{D}_{11} = 1, U = \begin{bmatrix} q_1 & 0 & 0 & 0 \\ 0 & q_2 & 0 & 0 \\ 0 & 0 & q_3 & 0 \\ 0 & 0 & 0 & q_4 \end{bmatrix} 0, V = q_5
$$

The control output z can be obtained:

$$z = C_1 x + D_{11} w + D_{12} u \tag{29}$$

where:

$$
C_1 = \begin{bmatrix} U^{\frac{1}{2}} \overline{C}_1 \\ 0 \end{bmatrix}, D_{11} = \begin{bmatrix} U^{\frac{1}{2}} \overline{D}_{11} \\ 0 \end{bmatrix}, D_{12} = \begin{bmatrix} 0 \\ V^{\frac{1}{2}} \end{bmatrix}
$$

The error cost function J is related to the control output z in the following manner:

$$J = \|z\|_2^2 \tag{30}$$

By utilizing the aforementioned system model (26) and the control output of the system (29), the problem of trajectory-following can be reformulated as a standard H-infinity control problem.

$$
\begin{cases} \dot{x} = A_d x + B_w w + B_d u \\ z = C_1 x + D_{11} w + D_{12} u \end{cases}
\tag{31}
$$

In accordance with H_∞ control theory, the aim of this trajectory-following system is to devise a controller $u_L = Kx$ that satisfy the requirements of trajectory-following for AGEV.

By utilizing Eq. (31) and the state feedback controller $u_L = Kx$, it can derive the vehicle trajectory-following system.

$$
\begin{cases} \dot{x} = A_s x + B_s w \\ z = C_s x + D_s w \end{cases}
\tag{32}
$$

where:

$$A_s = \overline{A}_d + \overline{B}_d K + H_d F_d (E_A + E_B K), B_s = B_w, C_s = C_1 + D_{12} K, D_s = D_{11}$$

Within this investigation, w is regarded as an external disturbance affecting the system. The representation of the system's transfer function (32) can be formulated as follows:

$$T(s) = C_s(sI - A_s)B_s + D_s \tag{33}$$

$w(t)$ and $z(t)$ are presented:

$$\|\Xi\|_2^2 = \int_0^{+\infty} \Xi^T(t)\Xi(t)dt, \Xi = w, z \tag{34}$$

The definition of the H-infinity norm is given by:

$$\|T(s)\|_\infty = \sup_{w \neq 0} \frac{\|z\|_2}{\|w\|_2} \tag{35}$$

In other words, the H-infinity norm represents system maximum singular value. The object of the H-infinity is to find K that satisfies the desired following performance while constraining the impact of disturbances on the output to a specific level. Hence, the subsequent H-infinity performance index is chosen:

$$\frac{\int_0^\infty z^T(t)z(t)dt}{\gamma^2} < \int_0^\infty w^T(t)w(t)dt \tag{36}$$

In order to demonstrate the stability and H_∞ performance of the system (33), several lemmas will be presented.

Lemma 1 [14, 21]: Given matrix $P = \begin{bmatrix} P_{11} & P_{12} \\ P_{21} & P_{22} \end{bmatrix}$, where $P = P^T$, the conditions (37)–(39) are equivalent:

$$P < 0 \tag{37}$$
$$P_{11} < 0, P_{22} - P_{12}^T P_{11-1} P_{12} < 0 \tag{38}$$
$$P_{22} < 0, P_{11} - P_{12} P_{22-1} P_{12}^T < 0 \tag{39}$$

Lemma 2 [26, 27]: Let F be an appropriately dimensioned matrix such that $P = P^T$. Suppose M and N are symmetric real matrices, and $F^T F \leq 1$. Under these conditions, the following inequality holds:

$$P + MFN + N^T F^T M^T < 0 \tag{40}$$

The existence of a positive value $\alpha > 0$ satisfying the following inequality is both sufficient and necessary conditions:

$$P + \alpha M M^T + \alpha^{-1} N^T N < 0 \tag{41}$$

The H-infinity control gain K for trajectory-following system (33) can be obtained by applying the developed Theorem 1.

Theorem 1: In order to ensure both the stability and H_∞ performance of the system, certain conditions need to be satisfied. These conditions involve the existence of symmetric matrices $Y > 0$, $X > 0$, and positive values γ and η, which satisfy the inequality (42). Furthermore, there should exist a H_∞ control gain K for the system that fulfills the following equation.

$$
\begin{bmatrix}
syms\left(\overline{A}_d Y + \overline{B}_d X\right) & B_w & \Upsilon_1 & \varepsilon H_d & \Upsilon_2 \\
* & -\gamma I & D_{11}^T & 0 & 0 \\
* & * & -\gamma I & 0 & 0 \\
* & * & * & -\eta I & 0 \\
* & * & * & * & -\eta I
\end{bmatrix} < 0 \qquad (42)
$$

where:

$$
syms(*) = * + *^T, \Upsilon_1 = YC_1^T + X^T D_{12}^T, \Upsilon_2 = YE_A^T + X^T E_B^T
$$

Proof: The condition of stability and H_∞ performance for system (32) is that there exists a symmetric matrix $U > 0$ and value γ that satisfies:

$$
\begin{bmatrix}
UA_s + A_s^T U & UB_s & C_s^T \\
* & -\gamma I & D_s^T \\
* & * & -\gamma I
\end{bmatrix} < 0 \qquad (43)
$$

Inequation (43) can be written:

$$
\begin{bmatrix}
syms\left(U\left(\overline{A}_d + \overline{B}_d K\right) + U H_d F_d (E_A + E_B K)\right) & UB_w & \left(C_1 + D_{12}K\right)^T \\
* & -\gamma I & D_{11} T \\
* & * & -\gamma I
\end{bmatrix} < 0 \qquad (44)
$$

Inequation (44) further rewrite:

$$
\begin{bmatrix}
syms\left(U\left(\overline{A}_d + \overline{B}_d K\right)\right) & UB_w & C_s^T \\
* & -\gamma I & D_{11}^T \\
* & * & -\gamma I
\end{bmatrix}
+
\begin{bmatrix}
syms(U H_d F_d (E_A + E_B K)) & 0 & 0 \\
* & 0 & 0 \\
* & * & 0
\end{bmatrix} < 0
$$

$$(45)$$

Inequation (45) is equivalent to:

$$
\begin{bmatrix}
syms\left(U\left(\overline{A}_d + \overline{B}_d K\right)\right) & UB_w & C_s^T \\
* & -\gamma I & D_{11}^T \\
* & * & -\gamma I
\end{bmatrix}
+
\begin{bmatrix}
U H_d \\
0 \\
0
\end{bmatrix}
F_d \begin{bmatrix} (E_A + E_B K) & 0 & 0 \end{bmatrix}
$$

$$
+
\begin{bmatrix}
(E_A + E_B K)^T \\
0 \\
0
\end{bmatrix}
F_d^T \begin{bmatrix} (U H_d)^T & 0 & 0 \end{bmatrix} < 0
$$

$$(46)$$

Assume that:

$$\overline{H}_d = [\, UH_d \quad 0 \quad 0\,]^T, \overline{F}_d = F_d \tag{47}$$

$$\overline{E}_{AB} = [\,(E_A + E_B K) \quad 0 \quad 0\,] \tag{48}$$

$$\varpi = \begin{bmatrix} syms\left(U\left(\overline{A}_d + \overline{B}_d K\right)\right) & UB_w & C_{cl}^T \\ * & -\gamma I & D_{11}T \\ * & * & -\gamma I \end{bmatrix} \tag{49}$$

Inequation (46) can be written as the following conditions:

$$\varpi + \overline{H}_d \overline{F}_d \overline{E}_{AB} + \overline{E}_{AB}^T \overline{F}_d^T \overline{H}_d^T < 0 \tag{50}$$

Based on lemma 2, there exists $\eta > 0$ satisfy:

$$\varpi + \eta \overline{H}_d \overline{H}_d^T + \eta^{-1} \overline{E}_{AB} \overline{E}_{AB}^T < 0 \tag{51}$$

Inequation (51) can be gained from Lemma 1.

$$\begin{bmatrix} \varpi & \overline{H}_d & \overline{E}_{AB}^T \\ * & -\eta^{-1}I & 0 \\ * & * & -\eta I \end{bmatrix} < 0 \tag{52}$$

Expand the inequality (52), according to the property of linear matrix inequality and diag$\{U^{-1}, I, I, \eta, I\}$. Let $Y = U^{-1}$, $KY = X$, Theorem 1 can be obtained.

3.2 Nonlinear robust control design

Subsequently, in order to enhance system's rapid response and minimize over-shoot, the design of the nonlinear compensation feedback control part will be formulated as follows:

$$u_{nla} = \rho(r, h)B^T Q x \tag{53}$$

Here, the nonlinear compensation function $\rho(r, h)$ is introduced, and it depends on the error state x, the reference value r and actual value h. Q can be obtained:

$$A_s^T Q + Q A_s + W = 0 \tag{54}$$

$$W = 100^l \cdot I \tag{55}$$

where l is adjustable value.
The nonlinear compensation part is as follows:

$$\rho(r, h) = -\beta \frac{1}{1 - e^{-1}} \left(e^{-\alpha \left| 1 - \frac{h - h_0}{r - h_0} \right|} - e^{-1} \right) \tag{56}$$

where α and β are positive adjustable parameters.

By integrating the linear part and the nonlinear part, the actuator's output is ultimately derived in the subsequent expression (57). The utilization of linear feedback part facilitates swifter system response within the trajectory-following, while concurrently, the nonlinear compensation part attains stable output and diminishes system overshoot.

$$u_{final} = Kx + \rho(r,h)B^T Qx \tag{57}$$

Based on the aforementioned nonlinear compensation part, and taking into account the saturation of the system's actuator output, the nonlinear robust control system model can be reformulated in the subsequent manner.

$$\begin{cases} \dot{x} = A_d x + B_w w + B_d sat\left(u_{final}\right) \\ z = C_1 x + D_{11} w + D_{12} sat\left(u_{final}\right) \end{cases} \tag{58}$$

$$sat\left(u_{final}\right) = \begin{cases} u_{\max}, & u_{final} > u_{\max} \\ Kx + \rho(r,h)B^T Qx, & |u_{final}| < u_{\max} \\ -u_{\max}, & u_{final} < -u_{\max} \end{cases} \tag{59}$$

Taking into account the saturation of the front wheel angle, the actual expression for the nonlinear compensation can be represented as follows:

$$u_{nla} = sat(u) - Kx \tag{60}$$

Based on the aforementioned conditions, the expression for u_{nla} can be formulated as follows.

$$0 < |u_{nla}| < \rho(r,h)B^T Qx \tag{61}$$

Subsequently, the impact of the nonlinear compensation on H-infinity performance and stability of the system will be demonstrated.

Proof: The Lyapunov functional V is defined as follows:

$$V = x^T Sx \tag{62}$$

$$\begin{aligned} \dot{V} &= \dot{x}^T Sx + x^T S\dot{x} = \left(\overline{A}x + \overline{R}x + B_w w\right)^T Sx + x^T S\left(\overline{A}x + \overline{R}x + B_w w\right) \\ &= x^T \overline{A}^T Sx + x^T \overline{R}^T Sx + w^T B_w^T Sx + x^T S\overline{A}x + x^T S\overline{R}x + x^T SB_w w \\ &= x^T \left(\overline{A}^T S + S\overline{A}\right)x + x^T \left(\overline{R}^T S + S\overline{R}\right)x + w^T B_w^T Sx + x^T SB_w w \end{aligned} \tag{63}$$

where:

$$\overline{A} = A_d + B_d K, \overline{R} = B_d u_{nla}$$

When $w = 0$:

$$\dot{V} = x^T \left(\overline{A}^T S + S\overline{A}\right)x + x^T \left(\overline{R}^T S + S\overline{R}\right)x \tag{64}$$

Assuming that:

$$V_1 = x^T \left(\overline{A}^T S + S\overline{A} \right) x \tag{65}$$

It can be inferred that $V_1 > 0$.
Assuming that

$$V_2 = x^T \left(\overline{R}^T S + S\overline{R} \right) x = 2x^T SB \left(sat \left(Kx + \rho B^T Sx \right) - Kx \right) = 2m (sat(n + \rho m) - n) \tag{66}$$

where:

$$m = x^T SB, n = Kx$$

When actuator output is not saturated:

$$|sat(n + \rho m)| < u_{max} \tag{67}$$

At this time:

$$V_2 = 2m (sat(n + \rho m) - n) = 2\rho m^2 < = 0 \tag{68}$$

Therefore:

$$\dot{V} = V_1 + V_2 = x^T \left(\overline{A}^T S + S\overline{A} \right) x + 2m(sat(n + \rho m) - n) < = x^T \left(\overline{A}^T S + S\overline{A} \right) x < 0 \tag{69}$$

When actuator output is saturated:

$$|sat(n + \rho m)| \geq u_{max} \tag{70}$$

Suppose that j is saturated and $\rho m = 0$, the system is asymptotically stable.
When j is not subjected to saturation, the output can take on the following two forms:

$$\begin{cases} m < 0, sat(n + \rho m) - n \geq 0, & When \ n + \rho m \geq u_{max} \ and \ n > 0 \\ m > 0, sat(n + \rho m) - n \leq 0, & When \ n + \rho m \leq -u_{max} \ and \ n < 0 \end{cases} \tag{71}$$

It can be observed from the inequality condition (71): $V_2 = 2m(sat(n + \rho m) - n) < = 0$ (72)
Thus:

$$\dot{V} = V_1 + V_2 = x^T \left(\overline{A}^T S + S\overline{A} \right) x + 2m(sat(n + \rho m) - n) < = x^T \left(\overline{A}^T S + S\overline{A} \right) x < 0 \tag{72}$$

Thus, the system with a nonlinear compensation function is asymptotically stable without interference.

Next, the stability and *H*-infinity performance of the system with a nonlinear compensation function under external disturbances will be demonstrated.

Let initially establish a cost function J_f:

$$J_f = \dot{V} + z^T z - \gamma^2 w^T w \tag{73}$$

Since the system exhibits asymptotic stability, then if the *H*-infinity satisfies the following inequality:

$$\|z\|^2 < \gamma^2 \|w\|^2 \tag{74}$$

Then, inequality (76) exists

$$J_f = \dot{V} + z^T z - \gamma^2 w^T w < 0 \tag{75}$$

The above inequality (76) can be further rewritten:

$$J_f = \begin{bmatrix} x \\ w \end{bmatrix}^T \left(\begin{bmatrix} \overline{A}^T S + S\overline{A} + 2S\overline{R} & SB_w \\ * & 0 \end{bmatrix} + \begin{bmatrix} C^T C & C^T D \\ * & D^T D \end{bmatrix} + \begin{bmatrix} 0 & 0 \\ * & \gamma^2 \end{bmatrix} \right) \begin{bmatrix} x \\ w \end{bmatrix} \tag{76}$$

Based on inequality (77) and the characteristics of quadratic form, it can establish the following inequality:

$$\Psi = \begin{bmatrix} \overline{A}^T S + S\overline{A} + 2S\overline{R} & SB_w \\ * & 0 \end{bmatrix} + \begin{bmatrix} C^T C & C^T D \\ * & D^T D \end{bmatrix} + \begin{bmatrix} 0 & 0 \\ * & \gamma^2 \end{bmatrix} \tag{77}$$

Based on Lemma 1:

$$\Psi = \begin{bmatrix} \overline{A}^T S + S\overline{A} + 2S\overline{R} & SB_w & C^T \\ * & \gamma^2 I & D^T \\ * & * & -I \end{bmatrix} \tag{78}$$

Let *U* = *S,* Eq. (79) is negative from Theorem 1, inequality (66), (68), and (72). Thus, the stability and *H*-infinity performance of system with nonlinear compensation function is proved.

4. Simulation and analysis

This section simulates and validates the proposed nonlinear robust H-infinity state-feedback controller on the MATLAB/Simulink-Carsim®. The simulation framework is implemented using MATLAB/Simulink, while the high-fidelity dynamics model for AGEV trajectory-following is provided by CarSim® software. **Figure 2** illustrates the simulation flowchart, and **Table 1** defines the key parameters of AGEV.

The simulation scenarios include double lane change (DLC) road and serpentine road scenes, with a constant forward speed of 54 km/h. These road scenes are chosen to evaluate the controller's robust following ability and steady-state response
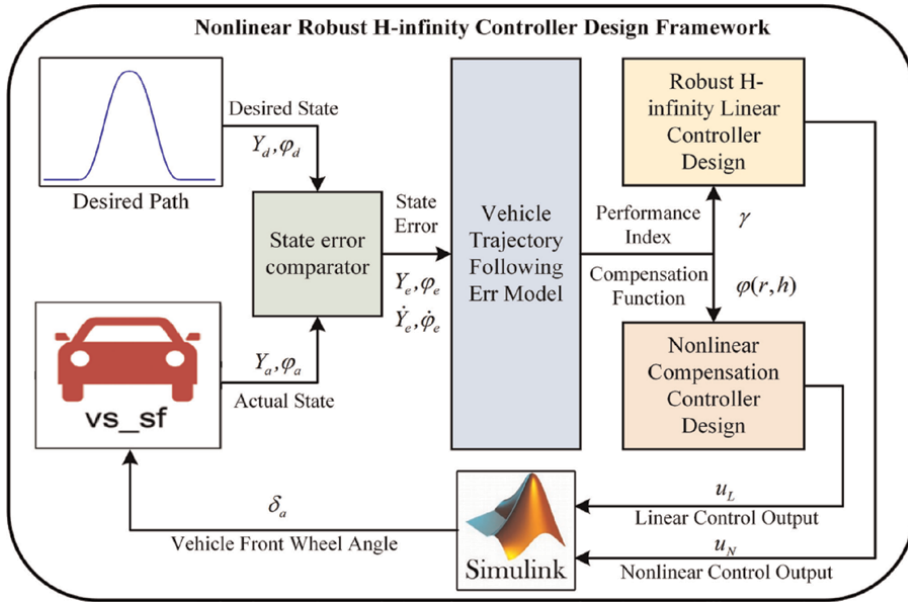
Figure 2.
*Flowchart of system simulation framework.*

| Parameter	Scale	Unit	Parameter	Scale	Unit
m	1413	kg	I_z	1536.7	$kg{\cdot}m^2$
N_{af}	[97,996,119,772]	N/rad	N_{ar}	[79,351,96,985]	N/rad
l_f	1.015	m	l_z	0.54	m
l_r	1.895	m	r	0.325	m

Table 1.
The key parameters of the vehicle.

performance. For comparison purposes, the performance of the proposed controller is also compared with that of the LQR and RHC controllers.

4.1 Double lane change scene

The simulation results for double lane change (DLC) are presented in **Figures 3–9**, depicting global trajectories, lateral errors, road curvature, front wheel angle, yaw, yaw error, linear angle, and nonlinear compensation part. **Figures 3** and **4** show the global trajectories and lateral errors obtained from three controllers during DLC scenario. All three controllers exhibit satisfactory tracking performance. The maximum of the lateral error for LQR controller is approximately 0.4 m, while for the RHC controller it is around 0.24 m. Notably, the NRC controller achieves a smaller maximum lateral error compared to the other two controllers, indicating its superior tracking performance. Furthermore, **Figure 3** demonstrates that NRC maintains exceptional system response within the range of 45 to 55 meters, further it highlights NRC has ability to enhance the transient performance of the system.
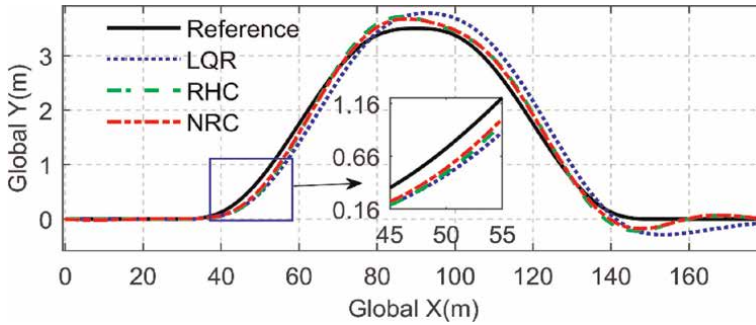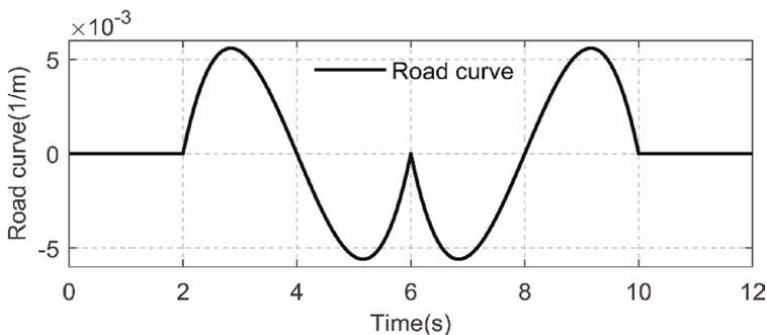
Figure 3.
*Global trajectories of three controllers under DLC scene.*
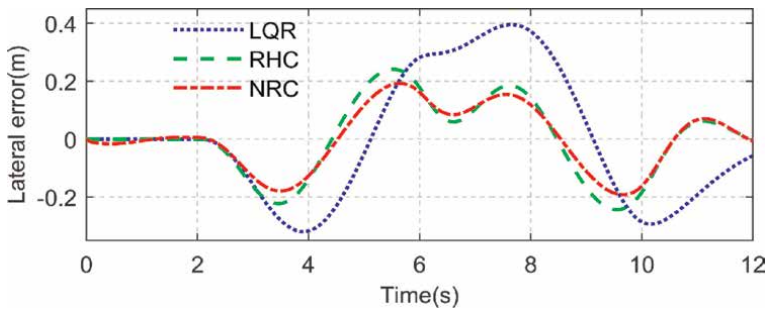
Figure 4.
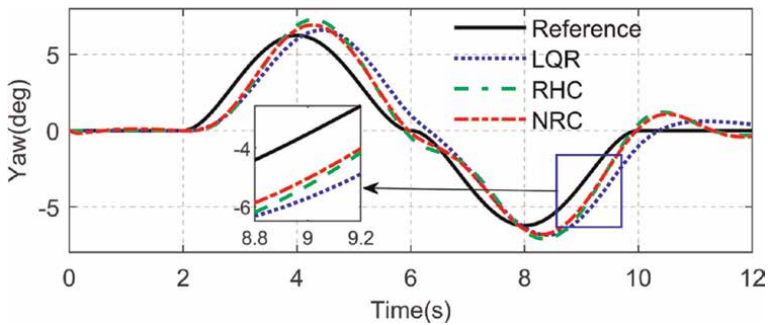*Lateral errors of three controllers under DLC scene.*

The road curvature and front wheel angle for AGEV during DLC scene are illustrated in **Figures 5** and **6**. **Figure 6** indicates that the front wheel angle of the NRC controller consistently falls between that of the LQR and RHC controllers. It is attributed to the fact that a too small front wheel angle would result in a slow system response, while a too large front wheel angle would lead to significant overshoot. The NRC controller incorporates a linear feedback part to enhance the system response and a nonlinear compensation part to mitigate excessive overshoot. As a result, the NRC controller demonstrates excellent trajectory-following capabilities.
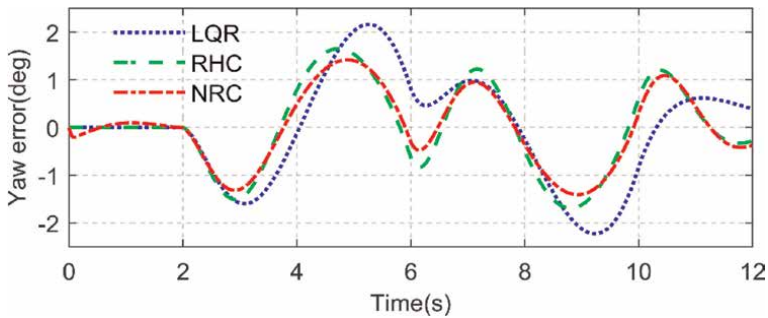

Figure 5.
Curvature of road under DLC scene.
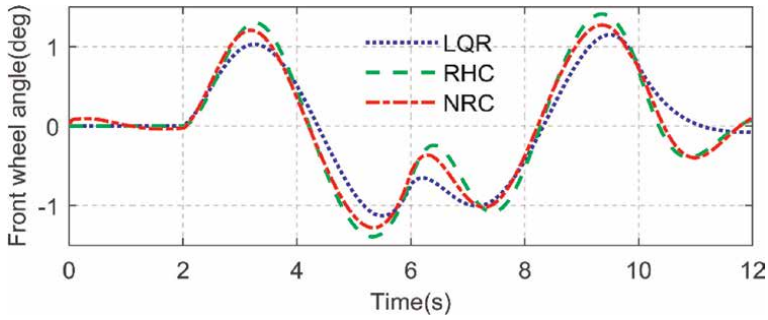
Figure 6.
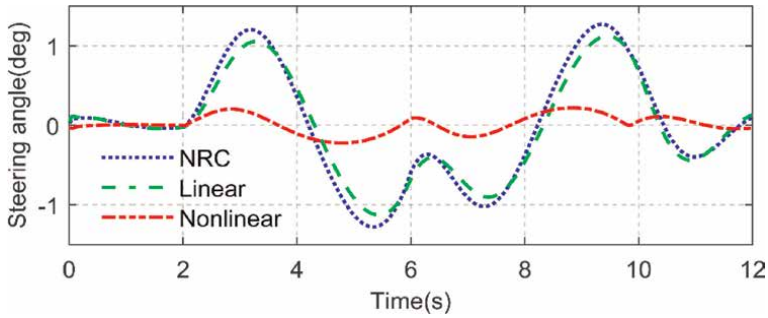*Front wheel angle of three controllers under DLC scene.*

Figure 7.
Yaw of three controllers under DLC scene.

Figure 8.
Yaw error of three controllers under DLC scene.

Figures 7 and **8** depict the yaw and yaw error of the NRC controller, and the NRC controller exhibits smaller yaw error and excellent trajectory-following capabilities compared to the RHC and LQR controllers. The angle of the linear feedback and nonlinear compensation of the NRC controller are illustrated in **Figure 9**. Notably, while the lateral error is smaller, the system nonlinear part of the NRC controller is significant. Conversely, as the vehicle lateral error increases, the system nonlinear part gradually decreases. It aligns with the design intention of the NRC controller, wherein the system exhibits fast response under increasing error scenes and small overshoot when the error is minimal.
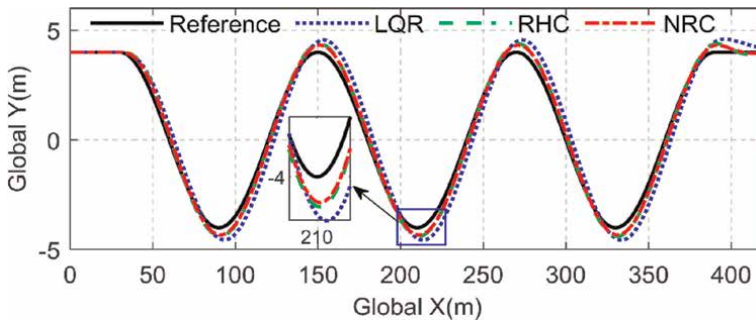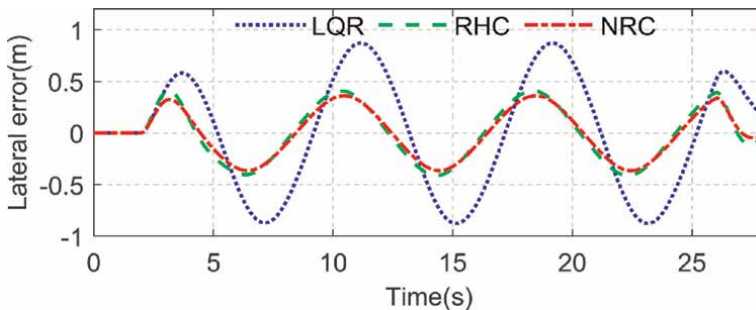
Figure 9.
Steering angle of NRC under DLC scene.

4.2 Serpentine scene

Figures 10 and **11** illustrate the global trajectories and lateral errors during serpentine tracking. It can be observed that the NRC controller exhibits smaller maximum lateral errors compared to the LQR and RHC controllers. Furthermore, the NRC controller demonstrates higher response speed and superior transient performance in comparison with the other two controllers. These findings indicate that the NRC controller outperforms the LQR and RHC controllers in terms of tracking performance on serpentine roads.

Figure 10.
Global trajectories of three controllers under serpentine scene.

Figure 11.
Lateral errors of three controllers under serpentine scene.

Figures 12 and **13** present the road curvature and front wheel angle of the serpentine scene. The maximum of serpentine road curvature is approximately $0.01(1/m)$. Similar to the DLC scene, the front wheel angle value of the NRC lies within the range of the LQR and RHC controllers. The inclusion of nonlinear compensation enables NRC to demonstrate stable trajectory-following capability.

In **Figures 14** and **15**, it can be observed that NRC responds quickly with minimal yaw error when tracking a trajectory with large curvature. This results in low yaw error and ensures stable tracking performance. **Figure 16** illustrates the angle of linear and nonlinear feedback of NRC under the serpentine scene. The value of the nonlinear
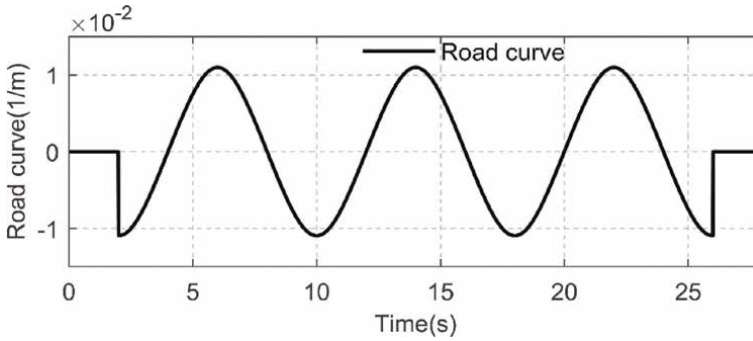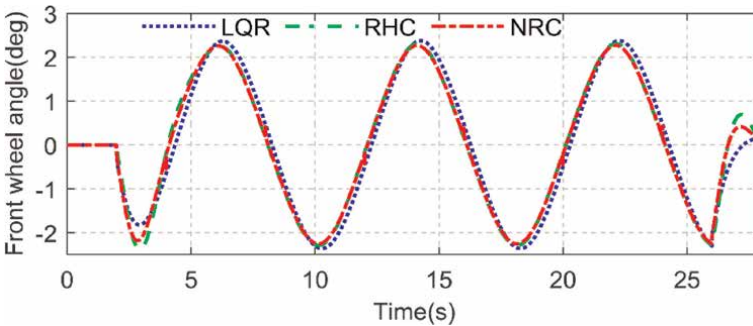

Figure 12.
Curvature of road under serpentine scene.

Figure 13.
Front wheel angle of three controllers under serpentine scene.
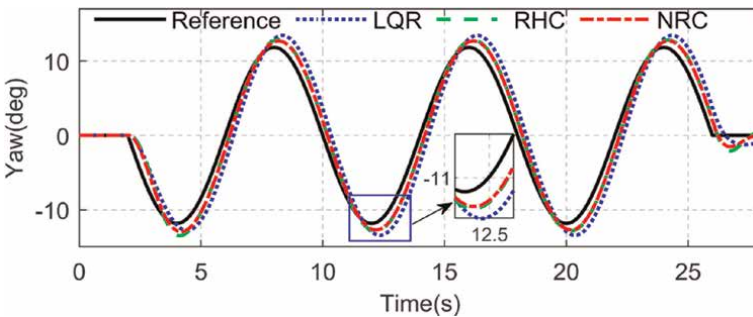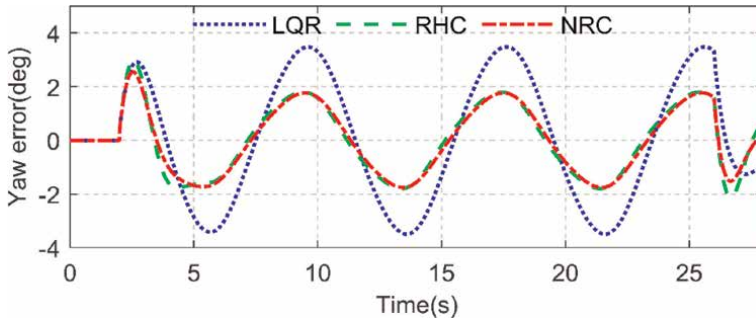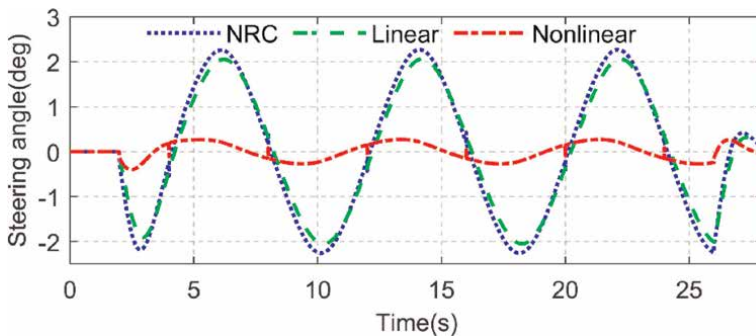

Figure 14.
Yaw of three controllers under serpentine scene.

Figure 15.
Yaw error of three controllers under serpentine scene.

Figure 16.
Steering angle of NRC under serpentine scene.

compensation function aligns with the trend of linear feedback, and it contributes to enhanced system response speed and trajectory tracking accuracy.

The mean absolute lateral error (MAE), maximum lateral error (ME), and root-mean-square lateral error (RMSE) are used to quantitatively analyze the trajectory-following performance of NRC, and the RHC and LQR controllers are utilized as comparative test.

Table 2 presents the values of ME, MAE, RMSE, RI, and RII for the lateral displacement in both DLC and serpentine scenes. The data clearly indicate NRC achieves smaller ME, MAE, and RMSE compared to LQR and RHC in both scenarios.

Scene	Index(y_e)	LQR(m)	RHC(m)	NRC(m)	RI	RII
DLC	ME	0.395	0.244	0.193	51.30%	20.96%
	MAE	0.178	0.102	0.087	51.12%	14.49%
	RMSE	0.220	0.131	0.108	50.95%	17.69%
Serpentine	ME	0.876	0.413	0.365	58.40%	11.64%
	MAE	0.472	0.224	0.196	58.36%	12.42%
	RMSE	0.552	0.264	0.232	57.94%	12.08%

Notes: RI = (LQR- NRC)/LQR, RII = (RHC - NRC)/RHC.

Table 2.
Quantitatively analyze of lateral error under two scenes.

The larger errors observed in the DLC scene can be attributed to the significant lateral displacement in this scenario, which lead to greater trajectory-following errors. In terms of performance improvement, NRC demonstrates an overall enhancement of over 50% compared to LQR in the DLC scene, and over 57% improvement in the serpentine scene. Additionally, under the DLC scene, NRC exhibits a 20.96% higher ME than RHC, which indicates its faster system response in trajectory-following with large model state errors. Furthermore, the MAE of NRC is approximately 14.49% in the DLC scene, which is higher than RHC, it highlights its smaller errors compared to RHC. Overall, the proposed controller outperforms RHC and LQR by offering advantages such as fast response speed and reduced overshoot.

5. Conclusion

To enhance the precision of trajectory-following, speed of system response, and suppression of overshoot in the control system for AGEV equipped with AFS system, we propose a novel NRC strategy. Initially, we establish the system dynamics of AGEV and its vehicle trajectory-following control system with dynamic error. By applying Lyapunov stability theory, we ultimately design the nonlinear robust *H*-infinity controller for the AGEV trajectory-following system. The proposed controller is solved by using a set of linear matrix inequalities. The efficacy of the proposed controller is validated by utilizing MATLAB/Simulink and Carsim® software. The simulation results demonstrate that the proposed controller has efficient trajectory-following performance compared to RHC and LQR.

Conflict of interest

The authors declare no conflict of interest.

Author details

Xianjian Jin[1,2]* and Qikang Wang[1]

1 School of Mechatronic Engineering and Automation, Shanghai University, Shanghai, China

2 Shanghai Key Laboratory of Intelligent Manufacturing and Robotics, Shanghai University, Shanghai, China

*Address all correspondence to: jinxianjian@yeah.net

IntechOpen

References

[1] Deng H, Zhao Y, Nguyen AT, Huang C. Fault-tolerant predictive control with deep-reinforcement-learning-based torque distribution for four in-wheel motor drive electric vehicles. IEEE/ASME Transactions on Mechatronics. 2023;**28**(2):668-680. DOI: 10.1109/TMECH.2022.3233705

[2] Yassine A, Hossain MS, Muhammad G, Guizani M. Double auction mechanisms for dynamic autonomous electric vehicles energy trading. IEEE Transactions on Vehicular Technology. 2019;**68**(8):7466-7476. DOI: 10.1109/TVT.2019.2920531

[3] Barari A, Saraygord AS, Liang X. Coordinated control for path-following of an autonomous four in-wheel motor drive electric vehicle. Proceedings of the Institution of Mechanical Engineers, Part C: Journal of Mechanical Engineering Science. 2022;**236**(11):6335-6346. DOI: 10.1177/09544062211064797

[4] Gözü M, Ozkan B, Emirler MT. Disturbance observer based active independent front steering control for improving vehicle yaw stability and tire utilization. International Journal of Automotive Technology. 2022;**23**(3): 841-854. DOI: 10.1007/s12239-022-0075-1

[5] Mousavinejad E, Han QL, Yang F, Zhu Y, Vlacic L. Integrated control of ground vehicles dynamics via advanced terminal sliding mode control. Vehicle System Dynamics. 2017;**55**(2):268-294. DOI: 10.1080/00423114.2016.1256489

[6] Wang Y, Nguyen B, Fujimoto H, Hori Y. Multirate estimation and control of body slip angle for electric vehicles based on onboard vision system. IEEE Transactions on Industrial Electronics.

2014;**61**:1133-1143. DOI: 10.1109/TIE.2013.2271596

[7] Wang G, Liu Y, Li S, Tian Y, Zhang N, Cui G. New integrated vehicle stability control of active front steering and electronic stability control considering tire force reserve capability. IEEE Transactions on Vehicular Technology. 2021;**70**:2181-2195. DOI: 10.1109/TVT.2021.3056560

[8] Cho J, Huh K. Active front steering for driver's steering comfort and vehicle driving stability. International Journal of Automotive Technology. 2019;**20**: 589-596. DOI: 10.1007/s12239-019-0056-1

[9] Falcone P, Borrelli F, Asgari J, Tseng H, Hrovat D. Predictive active steering control for autonomous vehicle systems. IEEE Transactions on Control Systems Technology. 2007;**15**:566-580. DOI: 10.1109/TCST.2007.894653

[10] Soltani A, Azadi S, Jazar RN. Integrated control of braking and steering systems to improve vehicle stability based on optimal wheel slip ratio estimation. Journal of the Brazilian Society of Mechanical Sciences and Engineering. 2022;**44**(3):102. DOI: 10.1007/s40430-022-03420-2

[11] Hladio A, Nielsen C, Wang D. Path following for a class of mechanical systems. IEEE Transactions on Control Systems Technology. 2012;**21**(6): 2380-2390. DOI: 10.1109/TCST.2012.2223470

[12] Ahmadian N, Khosravi A, Sarhadi P. Driver assistant yaw stability control via integration of AFS and DYC. Vehicle system dynamics. 2022;**60**(5): 1742-1762. DOI: 10.1080/00423114.2021.1879390

[13] Ghaffari V. Optimal tuning of composite nonlinear feedback control in time-delay nonlinear systems. Journal of the Franklin Institute. 2020;**357**(2): 1331-1356. DOI: 10.1016/j. jfranklin.2019.12.024

[14] Mobayen S. Robust tracking controller for multivariable delayed systems with input saturation via composite nonlinear feedback. Nonlinear Dynamics. 2014;**76**(1):827-838. DOI: 10.1007/s11071-013-1172-5

[15] Yu S, Li X, Chen H, Allgöwer F. Nonlinear model predictive control for path following problems. International Journal of Robust and Nonlinear Control. 2015;**25**(8):1168-1182. DOI: 10.1002/ rnc.3133

[16] Chen J, Shuai Z, Zhang H, Zhao W. Path following control of autonomous four-wheel-independent-drive electric vehicles via second-order sliding mode and nonlinear disturbance observer techniques. IEEE Transactions on Industrial Electronics. 2020;**68**(3): 2460-2469. DOI: 10.1109/ TIE.2020.2973879

[17] Liu Z, Chen X, Yu J. Adaptive sliding mode security control for stochastic markov jump cyber-physical nonlinear systems subject to actuator failures and randomly occurring injection attacks. IEEE Transactions on Industrial Informatics. 2022;**19**(3):3155-3165. DOI: 10.1109/TII.2022.3181274

[18] Zhao X, Liu Z, Jiang B, Gao C. Switched controller design for robotic manipulator via neural network-based sliding mode approach. IEEE Transactions on Circuits and Systems II: Express Briefs. 2023;**70**(2):561-565. DOI: 10.1109/TCSII.2022.3169475

[19] Xu B, Sun F, Pan Y, Chen B. Disturbance observer based composite learning fuzzy control of nonlinear systems with unknown dead zone. IEEE Transactions on Systems, Man, and Cybernetics: Systems. 2016;**47**(8): 1854-1862. DOI: 10.1109/ TSMC.2016.2562502

[20] Cao H, Song X, Zhao S, Bao S, Huang Z. An optimal model-based trajectory-following architecture synthesising the lateral adaptive preview strategy and longitudinal velocity planning for highly automated vehicle. Vehicle System Dynamics. 2017;**55**(8): 1143-1188. DOI: 10.1080/ 00423114.2017.1305114

[21] Cervantes J, Yu W, Salazar S, Chairez I. Takagi–Sugeno dynamic neuro-fuzzy controller of uncertain nonlinear systems. IEEE Transactions on Fuzzy Systems. 2016;**25**(6):1601-1615. DOI: 10.1109/TFUZZ.2016.2612697

[22] Wu Y, Wang L, Zhang J, Li F. Path following control of autonomous ground vehicle based on nonsingular terminal sliding mode and active disturbance rejection control. IEEE Transactions on Vehicular Technology. 2019;**68**(7): 6379-6390. DOI: 10.1109/ TVT.2019.2916982

[23] Ding T, Zhang Y, Ma G, Cao Z, Zhao X, Tao B. Trajectory tracking of redundantly actuated mobile robot by MPC velocity control under steering strategy constraint. Mechatronics. 2022; **84**:102779. DOI: 10.1016/j. mechatronics.2022.102779

[24] Moradi H, Vossoughi G, Movahhedy MR, Salarieh H. Suppression of nonlinear regenerative chatter in milling process via robust optimal control. Journal of Process Control. 2013;**23**(5):631-648. DOI: 10.1016/j.jprocont.2013.02.006

[25] Fu Y, Li B, Fu J. Multi-model adaptive switching control of a nonlinear

system and its applications in a smelting process of fused magnesia. Journal of Process Control. 2022;**115**:67-76. DOI: 10.1016/j.jprocont.2022.04.009

[26] Fahmy SFF, Banks SP. Robust *H*-infinity control of uncertain nonlinear dynamical systems via linear time-varying approximations. Nonlinear Analysis: Theory, Methods & Applications. 2005;**63**(5–7):2315-2327. DOI: 10.1016/j.na.2005.03.030

[27] Ju G, Wu Y, Sun W. Adaptive output feedback asymptotic stabilization of nonholonomic systems with uncertainties. Nonlinear Analysis: Theory, Methods and Applications. 2009;**71**(11):5106-5117. DOI: 10.1016/j.na.2009.03.088

[28] Li SE, Gao F, Li K, Wang LY, You K, Cao D. Robust longitudinal control of multi-vehicle systems-a distributed H-infinity method. IEEE Transactions on Intelligent Transportation Systems. 2017;**19**(9):2779-2788. DOI: 10.1109/TITS.2017.2760910

Dynamics Modeling and Characteristics Analysis of Distributed Drive Electric Vehicles

Jinhao Liang, Tong Shen, Ruiqi Fang and Faan Wang

Abstract

Due to the short transmission chain, compact structure, and the feature of quick and accurate torque generation, distributed drive electric vehicle (DDEV) has attracted many researchers from academia and industry. The significantly redundant execution characteristic of four independently driven in-wheel motors also provides more potential to guarantee the vehicle dynamics performance. Moreover, the unique torque vector control of DDEV generates the direct yaw moment control mode. It has been proven to be effective to modify the vehicle steering characteristics. Through a reasonable torque vector allocation strategy, the energy-saving can also be realized. This chapter will introduce the distributed drive electric vehicle from the viewpoint of the dynamics modeling, stability performance analysis, and energy-saving strategy.

Keywords: distributed drive electric vehicle, vehicle system dynamics, torque vector control, stability performance analysis, energy-saving

1. Introduction

Electric vehicles (EVs) have been regarded as one of the effective green transportation in urban traffic due to the zero-emission [1–3]. As a novel chassis structure, distributed drive electric vehicles (DDEVs) choose in-wheel motors as their actuators [4], which is believed to be a promising electric vehicle architecture [5]. DDEVs with multiple powertrains can provide more control schemes through different torque-vector allocation methods. Such could make full use of the tire force limitation to enhance the vehicle handling stability while improving energy efficiency. However, the limited driving range becomes an important factor that restricts the development of EVs in the industry. Extensive research has focused on how to develop the advanced battery technologies, such as the higher energy-density [6] and superfast charging method [7]. Additionally, improving the work efficiency of in-wheel motors can also be an effective approach to reduce the energy consumption. Thanks to the independently controllable motors of DDEVs, it can be achieved by reasonable torque-vector allocation. It should be noted that the yaw motion control generated by the differential torque inputs between left and right wheels may bring about the vehicle instability. Therefore, it would be an interesting study on how to design a

torque-vector allocation framework to realize the energy-saving of DDEVs while enhancing the vehicle handling stability.

The vehicle stability control during lateral motion has been a topic of interest in vehicle dynamics control for many years. One of the intuitive approaches to determining stability is the stability region-based method. This method defines the stability region using various vehicle states as indexes, and then identifies the areas in phase planes that correspond to vehicle instability. While several studies have explored the stability regions of centralized drive vehicles (CDVs), few have explored the same for DDEVs. Wang et al. [8] investigated the impact of driving modes on vehicle stability, and Liu et al. [9] studied the effects of driving-steering coupling on lateral stability. However, both studies failed to consider the effects of DYC on stability. Like steering angle, DYC has the potential to significantly alter the flow pattern of vehicle lateral dynamics, leading to changes in the stability regions for different DYC values. Therefore, further research is needed to better understand the effects of DYC on vehicle stability.

There are several methods available to estimate a vehicle's stability region, which can be categorized as either numerical or analytical. Numerical methods use a mesh on the phase plane to determine the convergence of grid points, and include cell-to-cell mapping, Lyapunov exponent [10], and ARC length methods [11]. However, these methods tend to be time-consuming despite their high accuracy. Analytical methods, on the other hand, aim to find a function to estimate the stability region, with Lyapunov's second method being a common approach. Unfortunately, this method is often too conservative. Although some attempts have been made to address this issue, the estimation remains conservative. The Sum of Squares Programming (SOSP) method is a polynomial programming technique that can systematically search for the Lyapunov function. By setting constraints on the SOSP, the optimization of the Lyapunov function can be converted into a convex semi-definite program [12], which ensures both complexity and accuracy. Therefore, this study adopted the SOSP method to find the maximal Lyapunov function for stability region estimation.

Furthermore, a reasonable torque vector control can also realize the energy-saving. The in-wheel motors can work in a high-efficiency zone through the torque allocation and reduce the energy consumption. Related research has been conducted. Reference [13] proposes an offline optimization procedure to replace the traditional motor-efficiency mapping method. The simulation results demonstrate that the proposed controller can reduce the motor power loss under different driving conditions while improving the computational efficiency in real applications. Chen et al. [14] discuss and compare the energy-saving results with different energy-efficient control alloca-tion (EECA) schemes. The simulation and experiment results show that Karush-Kuhn-Tuckert (KKT)-based EECA method consumes the least energy, which also has less computational burden [15]. Analytical solutions are derived in [16] for the torque allocation strategy, which aims to reduce the energy loss on the basis of satisfying the total torque demands. Compared with another two allocation methods, the proposed strategy can achieve both energy-saving and computational efficiency.

The vehicle stability control combined with energy-saving is commonly designed through the hierarchical structure. The upper layer includes the total torque inputs and yaw-moment according to the control objectives of longitudinal speed and lateral stability, respectively. The lower layer allocates the torque considering the energy-efficiency. In [17], the top layer develops a DYC to continuously work and guarantee the cornering stability in extreme conditions. The bottom layer designs a switch-rule based on the friction ellipse constraint to judge the control priority for energy-saving and handling stability during the torque allocation. Hua et al. [18] present a

hierarchical structure to realize a trade-off between multi-objectives. The higher motion layer aims to generate the desired total torque and yaw moment based on the sliding mode controller. The lower allocation layer uses model predictive control to optimize the motor efficiency. However, the studies in [19–21] show that the vehicle yaw moment control has the potential for improving energy-efficiency of EVs. The inappropriate yaw-moment control may lead to extra energy consumption. To this end, this work introduces a relaxation factor in the lower layer (i.e. yaw-moment control layer), which aims to reduce the energy consumption of the excessive yaw motion control when the vehicle has enough safety space. The phase plane [1] is adopted to bound the vehicle stability space and designed as a constraint in the MPC controller. The main contributions of this chapter are shown as follows:

1. This study quantifies the stability region of DDEVs using the SOSP technique, expressing stability regions as analytical Lyapunov functions. The results show that DDEVs has a broader stability region than CDVs. An LMI-based mode decision theorem is developed to determine the boundaries of the drive stability regions. This approach constrains control inputs to a safe region based on the concept of drive stability region.

2. A dual LTV-MPC-based hierarchical control framework is constructed to ensure both energy-saving and stability performance of DDEVs. Specifically, it decouples the torque vector control for the motor efficiency optimization and vehicle yaw motion stability control in different control layers. To reduce the energy consumption caused by the excessive direct yaw motion control, a relaxation factor is introduced to balance different control objectives by evaluating the vehicle stability performance in the $\beta - \gamma$ phase plane.

To further prove the energy-saving performance of the proposed controller (PC), the conventional linear model predictive control method (LMPC), and the average torque (AT) allocation method are set as the comparison.

The comparative results with different performance indices are shown in **Figure 1**. Specifically, the control indices including the energy consumption $\Delta_1 = \sum_{\eta=1}^{\Gamma} \frac{1}{E_{\max}\Gamma}|E_\eta|$, the vehicle speed tracking performance $\Delta_2 = \sum_{\eta=1}^{\Gamma} \frac{1}{e_{v,\max}\Gamma}|e_{v,\eta}|$, and the tire slip ratio $\Delta_3 = \sum_{\eta=1}^{\Gamma} \frac{1}{\lambda_{t,\max}\Gamma}|\lambda_{t,\eta}|$ are defined, where E_η, $e_{v,\eta}$, and $\lambda_{t,\eta}$ denote
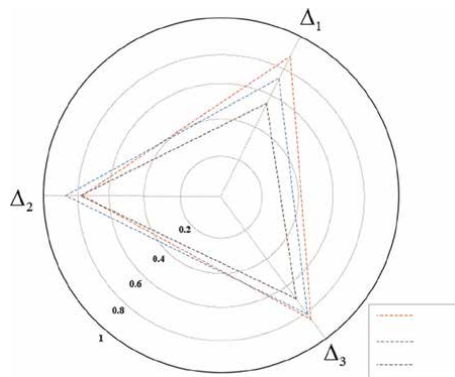
Figure 1.
The performance indices with different control strategies.

the energy consumption, the speed tracking error, and the sum of absolute value of tire longitudinal slip ratio at each sampling time, respectively. Γ is the total test time. E_{max}, $e_{v,max}$, and $\lambda_{t,max}$ correspond to the maximum absolute value. From the results, the proposed controller behaves better to balance different control objectives compared with other methods. On the basis of guaranteeing the driver's longitudinal speed control intention, the energy-saving control and longitudinal stability performance can be significantly enhanced.

2. The lateral stability region of DDEV for state constraint

2.1 DDEV dynamic model

DDEV with wheel-side or hub motor drive have great advantages in energy saving and emission reduction. Wheel-side or Hub motors operate with low noise, high peak efficiency and high load capacity, and also attract much research attention because of their independently controllable torque and fast and accurate torque response, which can effectively improve the vehicle handling stability and safety. Moreover, the DDEV can also realize the differential steering of the vehicle by independently controlling the drive torque difference between the left and right front wheels. It can serve both as a backup system for steering by wire and as the sole steering system of the vehicle, and the latter can further simplify the vehicle structure. DDEV offers flexible chassis layout options, unconstrained by the design limitations of conventional mechanical transmission, and can leverage the benefits of various drive modes.

A DDEV model with front-wheel steering is established [22, 23]. Ignoring the pitch and roll motions, the vehicle has three planar degrees of freedom for longitudinal motion, lateral motion, and yaw motion. A schematic of the vehicle model is shown in **Figure 2**. According to the principle of balance of forces and moment, the vehicle model in the longitudinal, lateral, and yaw directions can be expressed as:

$$\begin{cases} \dot{V}_x = V_y\gamma + \dfrac{1}{m}\left[(F_{x1}+F_{x2})\cos\delta + F_{x3} + F_{x4} - (F_{y1}+F_{y2})\sin\delta\right] \\[2mm] \dot{V}_y = -V_x\gamma + \dfrac{1}{m}\left[(F_{y1}+F_{y2})\cos\delta_f + (F_{y3}+F_{y4})\right] \\[2mm] \dot{\gamma} = \dfrac{1}{I_z}\left[(F_{y1}+F_{y2})\cos\delta_f - l_r(F_{y3}+F_{y4})\right] + \dfrac{1}{I_z}M_c \end{cases} \tag{1}$$
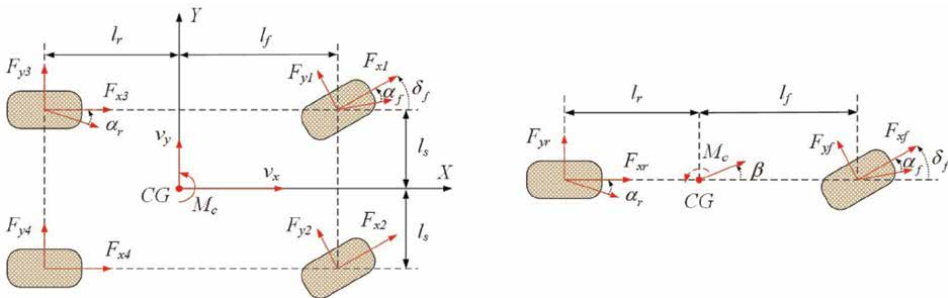
Figure 2.
Schematic diagram of a vehicle planar motion model.

The external yaw moment M_c is generated with the longitudinal tire force difference between the left and right wheels.

$$M_c = \left(F_{x1}\cos \delta_f + F_{x3}\right)t_w - \left(F_{x2}\cos \delta_f + F_{x4}\right)t_w \tag{2}$$

When the tire slip angles are small, the front and rear lateral forces can be modeled as:

$$F_{y1} + F_{y2} = C_f\alpha_f, F_{y3} + F_{y4} = C_r\alpha_r \tag{3}$$

And then the tire slip angles can be expressed as:

$$\begin{cases} \alpha_f = \delta_f - \dfrac{V_y + \gamma l_f}{V_x} \\[2mm] \alpha_r = \dfrac{\gamma l_r - V_y}{V_x} \end{cases} \tag{4}$$

The rotational dynamics of each wheel can be represented by

$$J_{wi}\dot{w}_i = -R_e F_{xi} + T_{wi} \tag{5}$$

And then the longitudinal tire force at each tire can be rewritten as:

$$F_{xi} = \frac{1}{R_e}\left(T_{wi} - J_{wi}\dot{w}_i\right) \tag{6}$$

In summary, the overall vehicle model (1) can be rewritten as:

$$\begin{cases} \dot{V}_x = V_y\gamma + \dfrac{1}{mR_e}(u_1 + u_2) + d_1 \\[3mm] \dot{V}_y = -\dfrac{(C_f + C_r)V_y}{mV_x} + \left(\dfrac{C_r l_r - C_f l_f}{mV_x} - V_x\right)\gamma + \dfrac{C_f}{m}u_3 + d_2 \\[3mm] \dot{\gamma} = \dfrac{(C_r l_r - C_f l_f)V_y - \left(C_f l_f^2 + C_r l_r^2\right)\gamma}{I_z V_x} + \dfrac{C_f l_f}{I_z}u_3 + \dfrac{l_s}{I_z R_{\text{eff}}}(u_1 - u_2) + d_3 \end{cases} \tag{7}$$

where u_1 and u_2 represent the total motor torque values in the vehicle longitudinal direction on the left and right sides of the vehicle, respectively. u_3 represents the front wheel steering angle.

$$\begin{cases} u_1 = T_{w1}\cos \delta + T_{w3} \\ u_2 = T_{w2}\cos \delta + T_{w4} \\ u_3 = \delta \end{cases} \tag{8}$$

$$\begin{cases} d_1 = \dfrac{1}{m}\left(F_{y1} + F_{y2}\right)\sin \delta + \dfrac{1}{mR_e}\left(J_{w1}\dot{w}_1\cos \delta + J_{w2}\dot{w}_2\cos \delta + J_{w3}\dot{w}_3 + J_{w4}\dot{w}_4\right) \\[3mm] d_2 = \dfrac{1}{m}\left(F_{y1} + F_{y2}\right)(\cos \delta - 1) \\[3mm] d_3 = \dfrac{l_f}{I_z}\left(F_{y1} + F_{y2}\right)(\cos \delta - 1) + \dfrac{l_s}{I_z R_e}\left(J_{w1}\dot{w}_1\cos \delta - J_{w2}\dot{w}_2\cos \delta + J_{w3}\dot{w}_3 - J_{w4}\dot{w}_4\right) \end{cases} \tag{9}$$

2.2 Rational polynomial based DDEV model

To accurately estimate the stability region, a nonlinear tire model is necessary as the fixed cornering stiffness used in the tire model is insufficient for extreme conditions. Here, we propose to use a rational polynomial function to fit the tire force curve. We define the nominal lateral tire force in Eq. (10) without loss of generality.

$$f_y(\alpha_i) = \frac{p_1 \alpha_i^3 + p_2 \alpha_i}{q_1 \alpha_i^4 + q_2 \alpha_i^2 + q_3} \tag{10}$$

We choose an odd function for the tire model 10 to cover both positive and negative tire forces. By incorporating the vertical load F_z and friction coefficient μ into the model, we derive a rational polynomial tire model expressed as Eq. (11).

$$F_{yi} = \frac{F_{zi} \mu_i \left(p_1 (\alpha_i/\mu_i)^3 + p_2 (\alpha_i/\mu_i) \right)}{q_1 (\alpha_i/\mu_i)^4 + q_2 (\alpha_i/\mu_i)^2 + q_3} \tag{11}$$

After conducting experiments with a 6000 N vertical load, **Figure 3** was produced to display the corresponding test data. A least-squares algorithm was then utilized to fit the polynomial coefficients in Eq. (11). Then, the rational polynomial tire model (11) will be employed in the dynamic model of DDEV. For the convenience of deduction, Eq. (11) is recorded as

$$F_{yi} = n_i(\alpha_i)/d_i(\alpha_i), (i = f, r) \tag{12}$$

According to the kinematic characteristic, the tire slip angle α can be represented by the vehicle state variables.
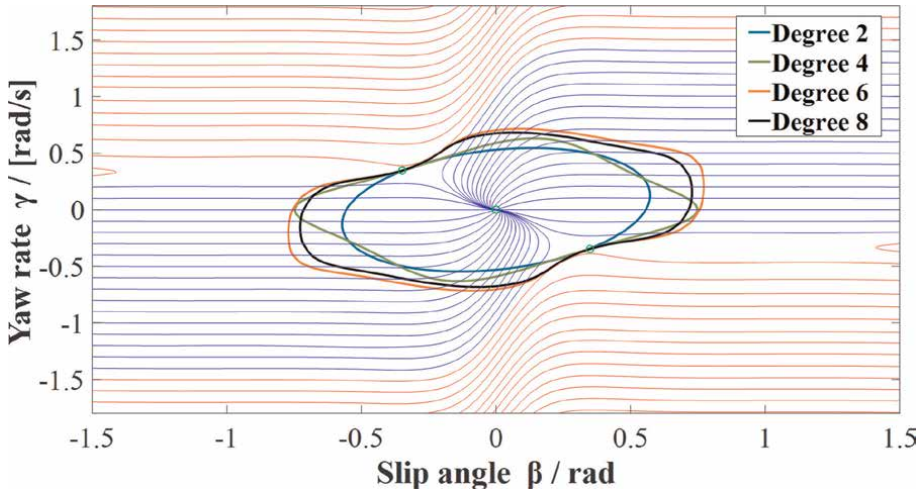
Figure 3.
Stability region estimation of different degrees.

$$\begin{cases} \alpha_f = \delta_f - \beta - \dfrac{l_f}{V_x}\gamma \\[2ex] \alpha_r = \dfrac{l_r}{V_x}\gamma - \beta \end{cases} \tag{13}$$
$$s.t. \quad \beta = V_y/V_x$$

The lateral dynamic model of DDEV can be transformed into the standard state space form (14). This results in the rational polynomial dynamic model for stability region estimation.

$$\dot{x} = f(x,u) = \frac{N(x,u)}{D(x,u)} \tag{14}$$

2.3 Basic principles of SOSP

The Lyapunov method is commonly utilized to estimate the stability region by seeking the maximal Lyapunov function that approaches the RoA boundary. Although systematic methods for searching the Lyapunov function are scarce, the stability region estimation can be converted into a convex optimization problem by SOSP when dealing with Lyapunov functions in polynomial form. This section introduces the fundamental principles of SOSP.

2.3.1 Sum of Squares Programming

Definition 1 Consider a polynomial function $p(x)$, $p(x)$ with n real variables and m degrees. $p(x)$ is called sum of squares (SOS) if there exist polynomials $f_i(x)$ such that

$$p(x) = \sum_{i=1} f_i^2(x) \tag{15}$$

Lemma 1 (Quadratic form of polynomial.) For a polynomial $p(x)$, there definitely exist a symmetric matrix Q such that

$$p(x) = z^T(x)Qz(x) \tag{16}$$

where $z(x)$ is a vector of all monomials of degree less than or equal to $\frac{m}{2}$. Commonly, the matrix Q is not unique. The matrix space of Q could be represented as a function of λ_i (17).

$$Q(\lambda) = Q_0 + \sum_{i=1}^{N} \lambda_i M_i \tag{17}$$

Lemma 2 (Sum of Squares Programming.) For a polynomial $p_i(x)$ is SOS if and only if there exist $\lambda_i, i = 1, \ldots, N$ such that

$$Q(\lambda) = Q_0 + \sum_{i=1}^{N} \lambda_i M_i \geq 0 \tag{18}$$
$$s.t. p(x) = z^T(x)Q(\lambda)z(x)$$

It is worth noting that Lemma 2 can be formulated as a linear matrix inequality (LMI) feasibility problem. Moreover, the sum-of-squares (SOS) property of a polynomial is equivalent to the SDP of the corresponding matrix Q. Therefore, the SDP approach provides an effective way to solve the SOSP problem.

2.3.2 Generalized S-procedure

The stability region estimation is usually concerned with causality of multiple inequalities. For the convenience of solving, it should be integrated as a single LMI.

Lemma 3 (Generalized S-procedure.) Consider a series of polynomials $p(x)$, $i = 0, \dots, m$ such that

$$p_0(x) \geq 0$$
$$s.t.x \in D \tag{19}$$

where D is domain of x represented as:

$$p_1(x) \geq 0, \dots, p_m(x) \geq 0 \tag{20}$$

The inequality (19) hold if there exist $q_i(x), i = 1, \dots, m$ such that

$$p_0(x) - \sum_{i=1}^{m} q_i(x)p_i(x) \geq 0$$
$$s.t.x \in R^n \tag{21}$$

2.4 Stability region estimation and analysis

Lemma 4 (Invariant subset of RoA.) Consider a function V and $\gamma > 0$. Region $\Omega_{V,\gamma}$ is defined as $\{x \in R^n : V(x) \leq \gamma\}$. If conditions in (22) holds, $\Omega_{V,\gamma}$ is an invariant subset of RoA.

$$\Omega_{V,\gamma} \text{ is bounded}$$
$$V(0) = 0, V(x) > 0 (\forall x \in R^n)$$
$$\Omega_{V,\gamma} \backslash \{0\} \subset \{x \in R^n : \nabla V(x)f(x) \leq 0\} \tag{22}$$

To construct an SOSP problem, the Lyapunov function V should be restricted as a polynomial form. Besides, formula ③ can be converted to a SOSP problem according to generalized S-procedure. Except of this, Lemma 4 is not sufficient to find the maximal Lyapunov function. Thus, we set a shape function $s(x)$ to expand the stability region of DDEV (23). By maximize β, V tends to approach the maximal Lyapunov function.

$$\max \beta : \{x \in R|s(x) < \beta\} \subset \Omega_{V,\gamma} \tag{23}$$

Theorem 1 For the nonlinear dynamic system, the stability region $\Omega_{V,\gamma}$ can be found by finding $V, q_1, q_1 \in \sum_{n,m} [x]$ and positive $\gamma > 0$ that maximize β such that

$$\max \beta$$
$$\begin{cases} V(x) - \varphi_1(x) \in \sum[x] \\ q_1(x)(s - \beta) - (V - \gamma) \in \sum[x] \\ -\nabla_x VN - D\varphi_2(x) + Dq_2(x)(V - \gamma) \in \sum[x] \end{cases} \tag{24}$$

The degree of Lyapunov function V has a huge impact on the estimation of stability region. To select the appropriate degree of V, we compare the stability regions with different degrees on the phase plane. **Figure 3** shows the stability regions of different degrees.

Figure 3 illustrates the phase trajectories near the equilibrium point of straight-running, where the blue lines represent the region of attraction (RoA) and the remaining area indicates instability. Generally, the stability region expands as the degree increases. However, the RoA of the two-degree V only approaches the boundary of yaw rate due to the ellipse shape, which cannot accurately describe the margin of slip angle. In contrast, the six and eight degree V significantly increase the stability region in all directions and better capture the RoA feature around the equilibrium. Given the computational complexity, we opt for the six-degree V to estimate the stability region of DDEV.

2.4.1 Impact of longitudinal velocity and road adhesion

During straight-running conditions, steering angle and DYC control inputs are both set to zero. Longitudinal velocity V_x and road adhesion coefficient μ are two primary factors that influence lateral stability. To explore their effects on the stability region, we varied V_x and μ and plotted the estimated stability regions in phase portraits, as shown in **Figures 4–7**. Our results indicate that as V_x increases, the stability region in the yaw rate direction tends to shrink, which is consistent with the view that high-speed steering can cause vehicle instability. Similarly, when μ decreases, not only does the available yaw rate reduce, but the stability region in the slip angle direction also sharply decreases due to the restriction of tire adhesion margin from low road friction. As a consequence, the maximum wheel slip angle decreases, leading to a reduction in body slip angle. However, at higher speeds, the tire adhesion margin remains constant, and can still supply sufficient tire force for the vehicle's lateral motion. These findings suggest that stability control in low road friction conditions may pose a greater challenge than in high-speed running. With
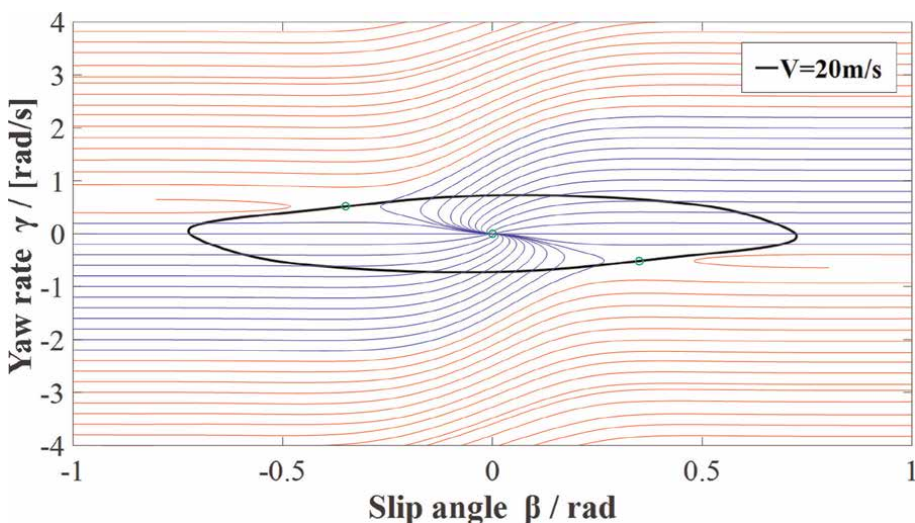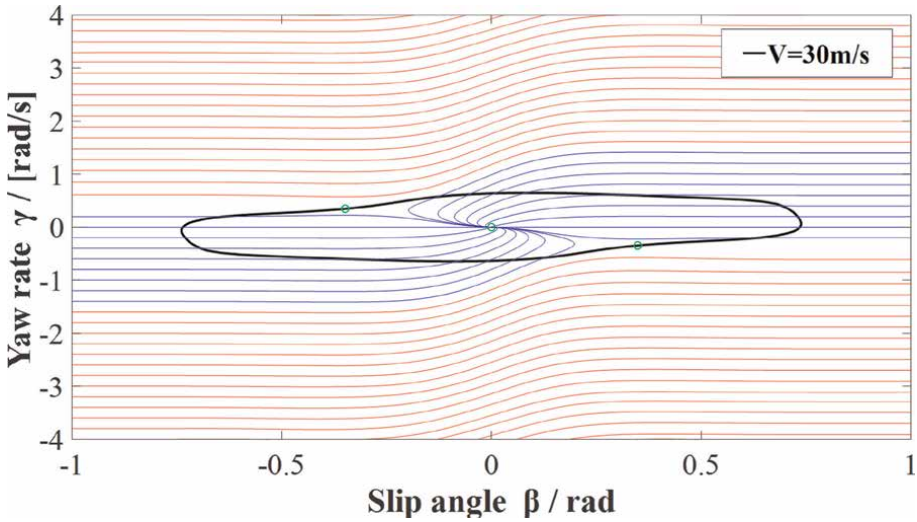

Figure 4.
$V_x = 20m/s \ (\mu = 1)$.

Figure 5.
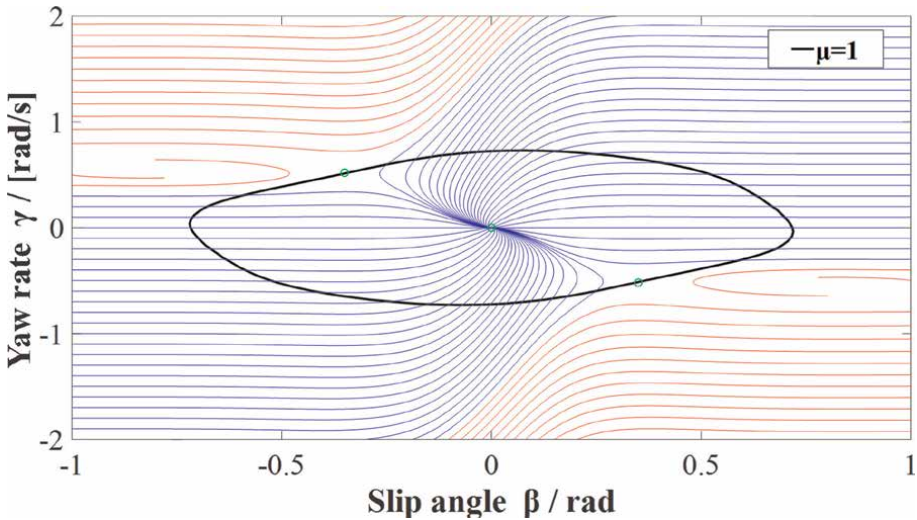$V_x = 30m/s$ ($\mu = 1$).

Figure 6.
$\mu = 1$ ($V_x = 20m/s$).

these insights, we can better understand the factors influencing lateral stability, and design more effective control strategies for safer vehicle operation.

2.4.2 Impact of steering angle and DYC

Compared to straight-running conditions, the estimation of cornering conditions is more complex due to the non-zero control inputs δ_f and M_z, which cause the equilibrium to shift away from the origin. To apply Theorem 2, we must first solve for the new equilibrium and then substitute the state variables to transform the equilibrium to the origin, enabling the estimation of the stability region for cornering conditions.
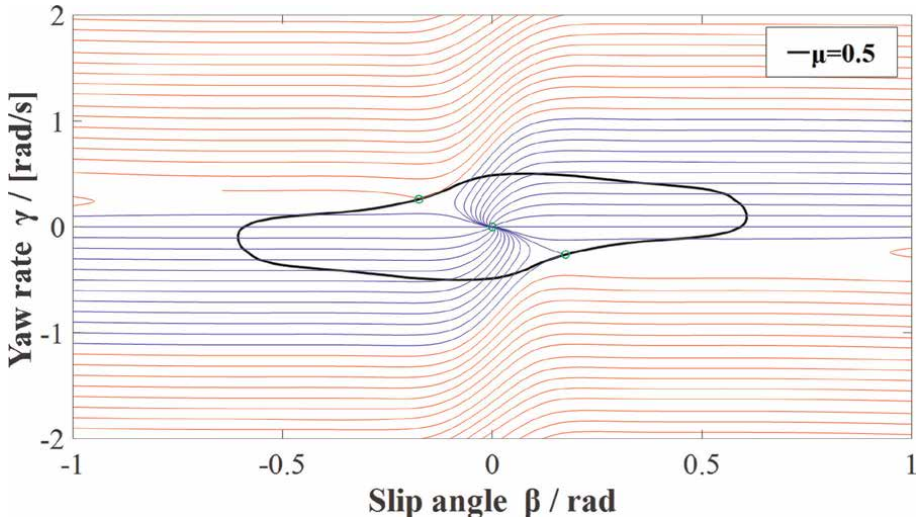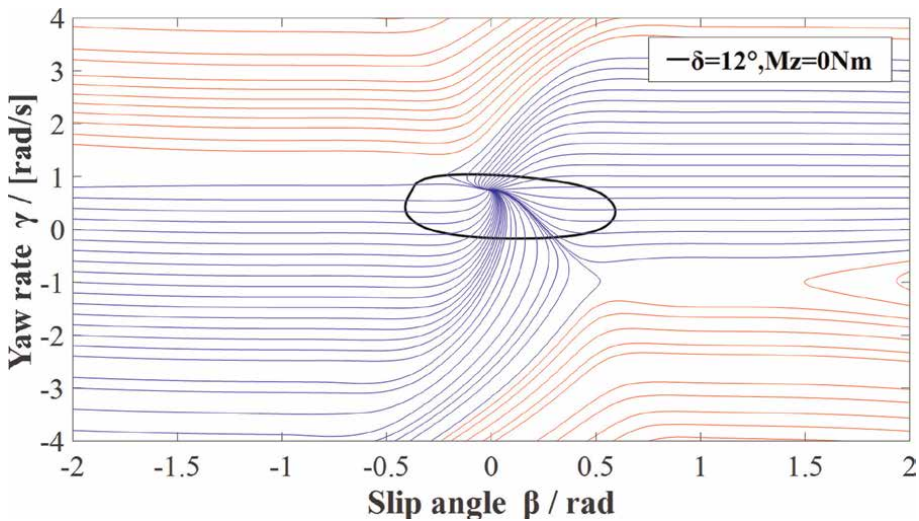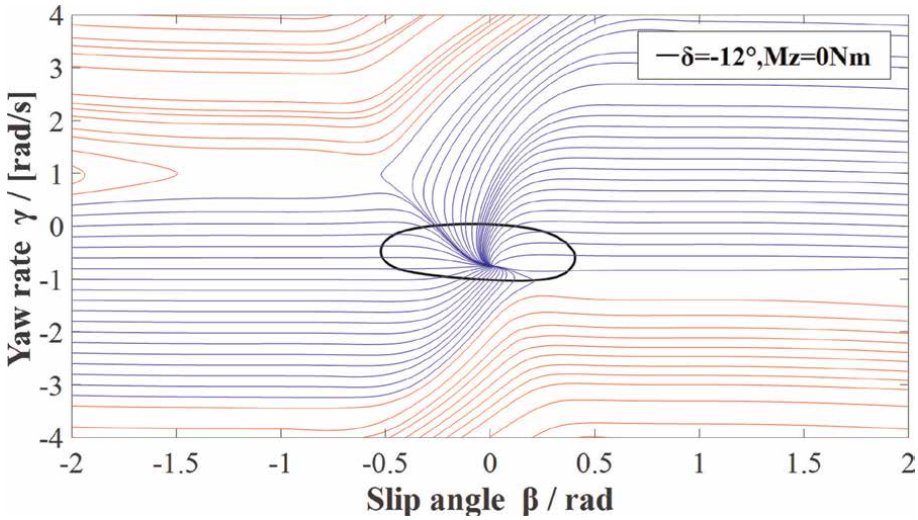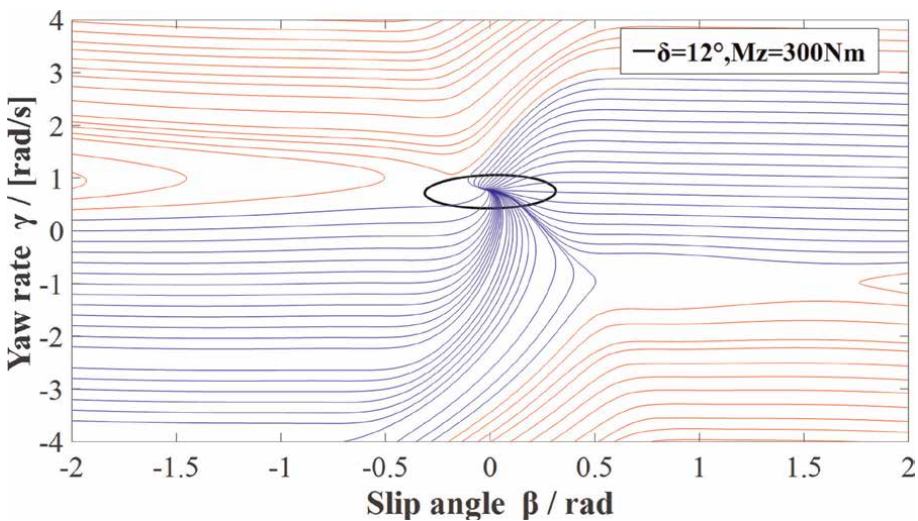
Figure 7.
$\mu = 0.5$ ($V_x = 20m/s$).

Figure 8.
$M_z = 0\ nm$ ($\delta = 12°$).

For the CDV, the only control input is the steering angle. **Figures 8** and **9** illustrate the stability regions for a steering angle of $\pm12°$, showing that the stability region in the yaw rate direction shrinks in the same direction as the steering angle. This suggests that further increases in steering angle may result in vehicle instability. Furthermore, the stability region for cornering conditions is much narrower than that for straight-running, making the vehicle more susceptible to external disturbances. These findings highlight the importance of understanding the effects of control inputs on vehicle stability and developing effective control strategies to ensure safe and stable operation.

Figure 9.
$M_z = 0\ nm\ (\delta = -12°)$.

To improve lateral stability, DDEV generates DYC by distributing torque unbalance, affecting the vehicle's lateral dynamics. However, DYC cannot be arbitrarily imposed. To investigate the impact of DYC on the stability region, we apply different values of M_z in the same or opposite directions of the steering angle, as shown in **Figures 10** and **11**. For left-turning conditions, a 300 Nm M_z significantly reduces the stability region of the yaw rate. However, an opposite -800 Nm M_z greatly expands the stability region. Compared to 0 and 300 Nm M_z, a much higher available yaw rate is achievable with an opposite DYC, allowing the vehicle to withstand greater yaw motion. Thus, we conclude that DDEV can enhance lateral stability by applying an opposite DYC. Simulations in the next section will confirm this hypothesis (**Figures 12** and **13**).
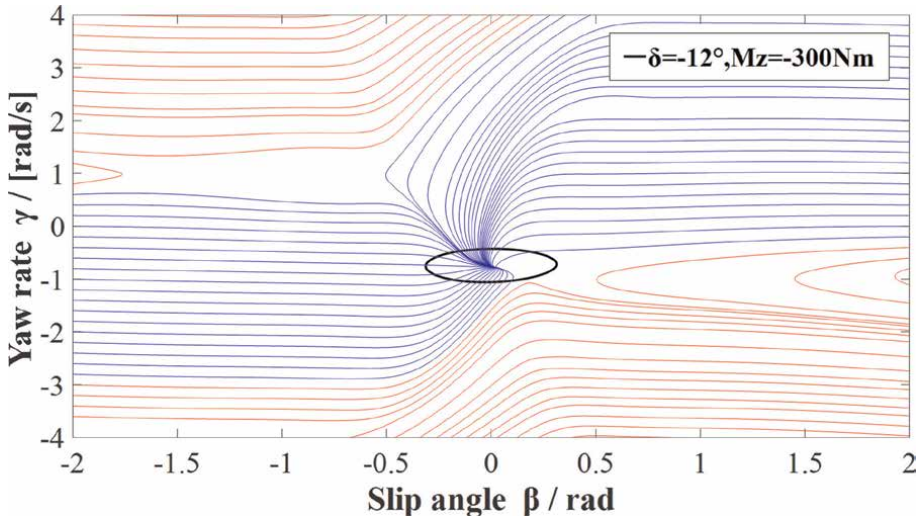

Figure 10.
$M_z = 300\ nm\ (\delta = 12°)$.

Figure 11.
$M_z = -300\ nm\ (\delta = -12°)$.

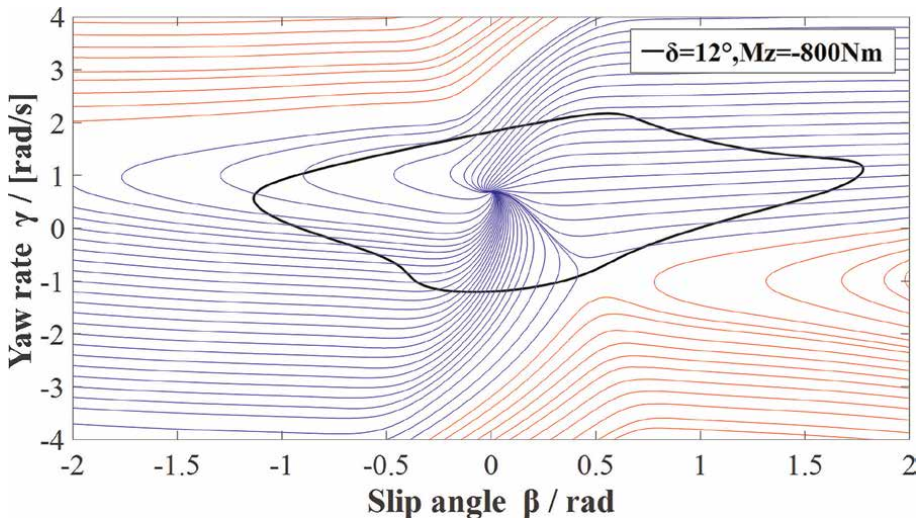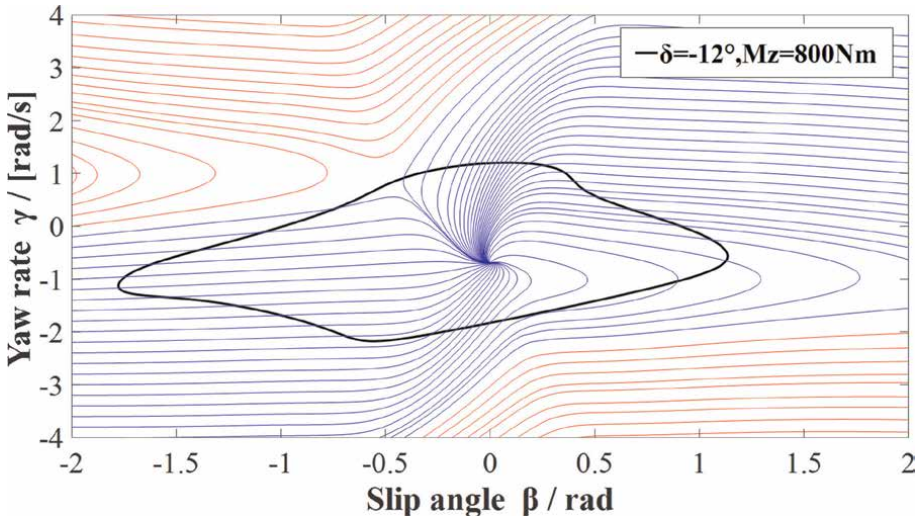**Figure 12.**
$M_z = -800\ nm\ (\delta = 12°)$.

3. The drive stability region of DDEV for control constraint

3.1 The definition of drive stability region

In a hierarchical DYC control scheme, the lateral stability controller at the high level calculates the efficient DYC M_{zopt}, while the driver's actions provide the total traction force Fxall. To transform F_{xall} and M_{zopt} into four-wheel torques, a rational distribution algorithm is necessary. A number of approaches consider F_{xall} and M_{zopt} as a strict constraint and employ optimization techniques to solve the problem. However, the excessive values of F_{xopt} and M_{zopt} could surpass the adhesion limit during

Figure 13.
$M_z = 800\ nm\ (\delta = -12°)$.

handling limit. The difficulty of distribution control lies in whether to satisfy F_{xall} and M_{zopt} or only satisfy one of them. Here we divide them into several situations. By taking the traction force and DYC as the two axes of a plane, we can divide the plane into different areas and make reasonable inferences. First, there is a maximum region $D_{max\,1}$ in which both F_{xall} and M_{zopt} can be fulfilled without sacrificing stability. Second, if we disregard the F_x requirement, we can obtain a larger region $D_{max\,2}$ where M_{zopt} can be met without losing stability. For the areas beyond $D_{max\,2}$, it is not possible to fully comply with either F_{xall} or M_{zopt} without compromising stability. As F_{xall} and M_{zopt} are linked to the driver's maneuvers, these feasible regions are referred to as drive stability regions. **Figure 14** provides an intuitive depiction of the drive stability region. According to the different drive stability regions, we obtain the definition of three Torque distribution Methods (TDMS).
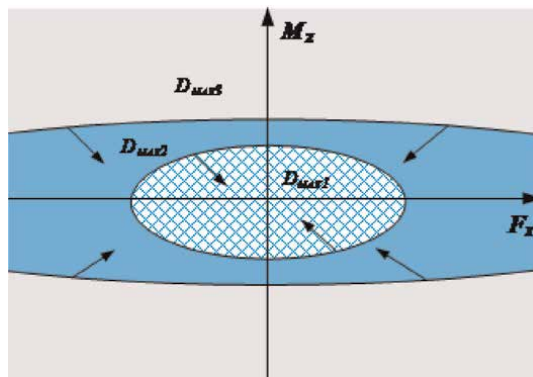
Figure 14.
The schematic diagram of drive stability region.

3.2 The construction of drive stability region

In order to estimate the drive stability region, a suitable vehicle dynamic model is required. As the drive stability region is related to the longitudinal and lateral dynamics of the vehicle, a three-degree-of-freedom vehicle plane motion model is developed for analysis.

$$\begin{cases} m\left(\dot{v}_x - \gamma V_y\right) = F_{xfl} + F_{xfr} + F_{xrl} + F_{xrr} \\ m\left(\dot{v}_y + \gamma V_x\right) = F_{yfl} + F_{yfr} + F_{yrl} + F_{yrr} \\ I_z\dot{\gamma} = l_f\left(F_{yfl} + F_{yfr}\right) - l_r\left(F_{yrl} + F_{yrr}\right) + t_w\left(F_{xfr} - F_{xfl} + F_{xrr} - F_{xrl}\right)/2 \end{cases} \tag{25}$$

where $t_w\left(F_{xfr} - F_{xfl} + F_{xrr} - F_{xrl}\right)/2$ is the actual DYC M_{zc}. As the longitudinal tire force increases, the lateral tire force decreases. The maximum longitudinal and lateral tire force envelope forms an ellipse known as the tire adhesion ellipse. This adhesion ellipse is utilized to establish the drive stability region, which is presented in Eq. (26).

$$\left(\frac{F_{xij}}{\mu_x}\right)^2 + \left(\frac{F_{yij}}{\mu_y}\right)^2 \leq F_{zij}{}^2 \tag{26}$$

Certainly, the lateral and vertical tire force mentioned in Eq. (25) cannot be directly obtained and must be estimated using the three-freedom vehicle plane model. Accounting for load transfer, the vertical tire force can be calculated using Eq. (27), where h_g represents the height of the center of mass and W is the wheelbase.

$$\begin{aligned} F_{zfl} &= \frac{mgl_r}{2L} - \frac{m\dot{v}_xh_g}{2L} - \frac{m\dot{v}_yh_gl_r}{t_wL} & F_{zfr} &= \frac{mgl_r}{2L} - \frac{m\dot{v}_xh_g}{2L} + \frac{m\dot{v}_yh_gl_r}{t_wL} \\ F_{zrl} &= \frac{mgl_f}{2L} + \frac{m\dot{v}_xh_g}{2L} - \frac{m\dot{v}_yh_gl_f}{t_wL} & F_{zrr} &= \frac{mgl_f}{2L} + \frac{m\dot{v}_xh_g}{2L} + \frac{m\dot{v}_yh_gl_f}{t_wL} \end{aligned} \tag{27}$$

The front and rear lateral tire force is represented as:

$$\begin{cases} F_{yf} = F_{yfl} + F_{yfr} = \left(l_rm\left(\dot{v}_y + \gamma V_x\right) + I_z\dot{\gamma} + M_{zc}\right)/L \\ F_{yr} = F_{yrl} + F_{yrr} = \left(l_fm\left(\dot{v}_y + \gamma V_x\right) - I_z\dot{\gamma} - M_{zc}\right)/L \end{cases} \tag{28}$$

Here, we assume that the lateral force transfer is similar to the vertical force transfer, and define the load transfer coefficients as follows.

$$\begin{aligned} k_{fl} &= F_{zfl}/\left(F_{zfl} + F_{zfr}\right) & k_{fr} &= F_{zfr}/\left(F_{zfl} + F_{zfr}\right) \\ k_{rl} &= F_{zrl}/\left(F_{zrl} + F_{zrr}\right) & k_{rr} &= F_{zrr}/\left(F_{zrl} + F_{zrr}\right) \end{aligned} \tag{29}$$

Combined with Eq. (28), the lateral tire force of each wheel can be calculated, which is represented in Eq. (30).

$$\begin{cases} F_{yfi} = k_{fi}\left(l_rm\left(\dot{v}_y + \gamma V_x\right) + I_z\dot{\gamma} + M_{zc}\right)/L \\ F_{yri} = k_{ri}\left(l_fm\left(\dot{v}_y + \gamma V_x\right) - I_z\dot{\gamma} - M_{zc}\right)/L \end{cases} \tag{30}$$

The longitudinal and lateral tire forces can be estimated using the state variables of the DDEV model. With this information, a linear matrix inequality-based mode decision theorem is formulated below.

Lemma 5 (LMI based conditions of TDM 1) TDM 1 is satisfied for the current vehicle condition, given the total traction force Fxall and optimal DYC M_{zopt}, if and only if the linear matrix inequality (LMI) shown in Eq. (27) is solvable, where $X = \begin{bmatrix} F_{xall} & M_{zopt} \end{bmatrix}^T, j = l, r.$

$$A_{m1}X \geq b_{m1}$$

$$s.t. A_{m1} = \begin{bmatrix} -\dfrac{1}{2} & \dfrac{1}{2} & -\dfrac{1}{2} & \dfrac{1}{2} \\ 1 & -\dfrac{1}{t_w} & -1 & \dfrac{1}{t_w} \end{bmatrix}^T$$

$$b_{m1} = \begin{bmatrix} -A_{fl} - A_{rl} & -A_{rl} - A_{fl} & -A_{fr} - A_{rr} & -A_{rr} - A_{fr} \end{bmatrix}^T \tag{31}$$

$$A_{fj} = \sqrt{\left(\mu_x F_{zfj}\right)^2 - \left(k_{fj}\mu_x\left(l_r m\left(\dot{v}_y + \gamma V_x\right) + I_z\dot{\gamma} + M_{zc}\right)/\mu_y L\right)^2}$$

$$A_{rj} = \sqrt{\left(\mu_x F_{zrj}\right)^2 - \left(k_{rj}\mu_x\left(l_f m\left(\dot{v}_y + \gamma V_x\right) - I_z\dot{\gamma} - M_{zc}\right)/\mu_y L\right)^2}$$

Lemma 6 (LMI based conditions of TDM 2)

$$A_{m2}X \geq b_{m2}$$

$$s.t. \ A_{m2} = \begin{bmatrix} -\dfrac{2}{t_w} & \dfrac{2}{t_w} \end{bmatrix}^T \tag{32}$$

$$b_{m2} = \begin{bmatrix} -3A_{fl} - 3A_{fr} - A_{rl} - A_{rr} & -3A_{fl} - 3A_{fr} - A_{rl} - A_{rr} \end{bmatrix}^T$$

Lemma 7 (LMI based conditions of TDM 3) For the given total traction force F_{xall} and optimal DYC M_{zopt}, TDM3 is satisfied, if and only if (24) and (25) is unsolvable (**Figures 15–20**).
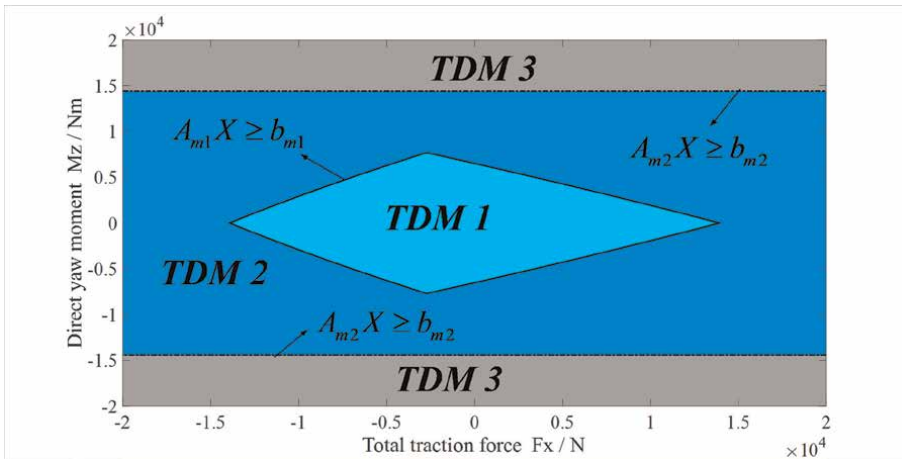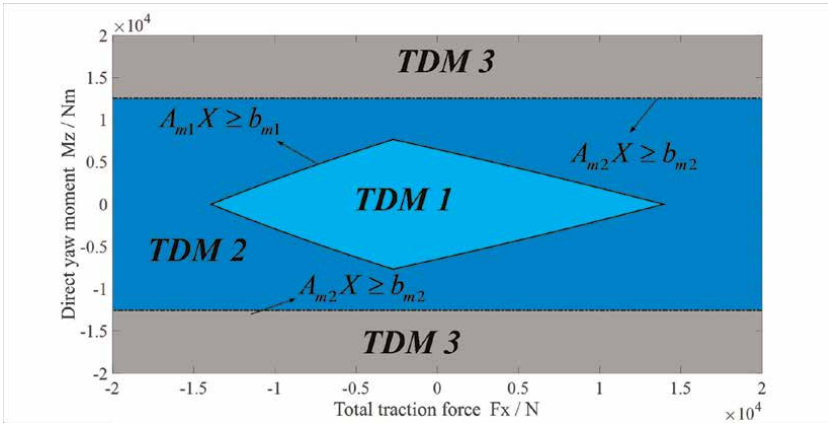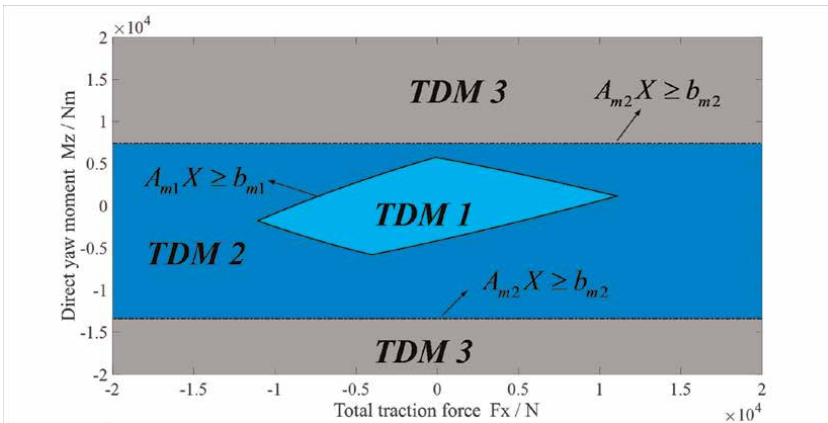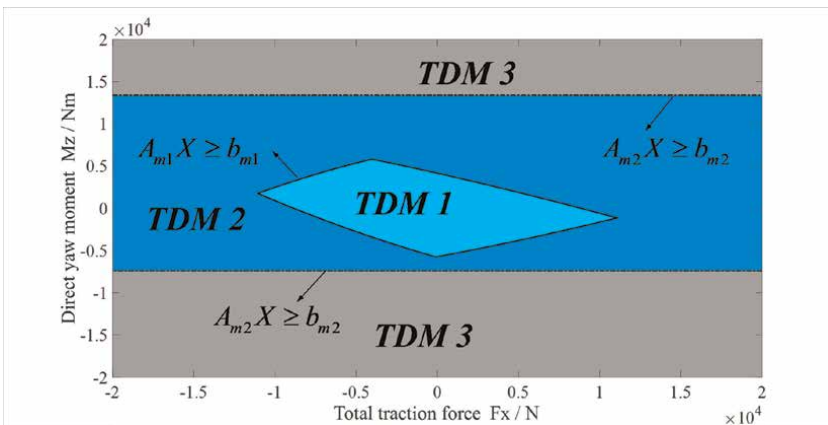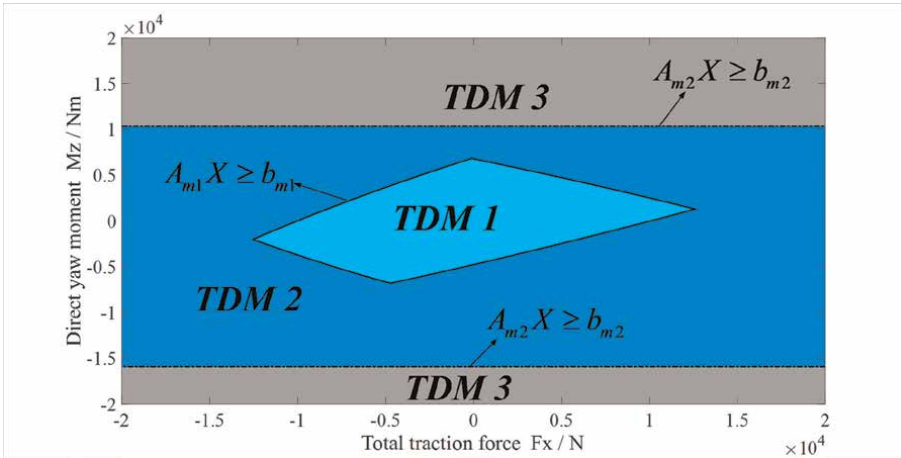

Figure 15.
Static.

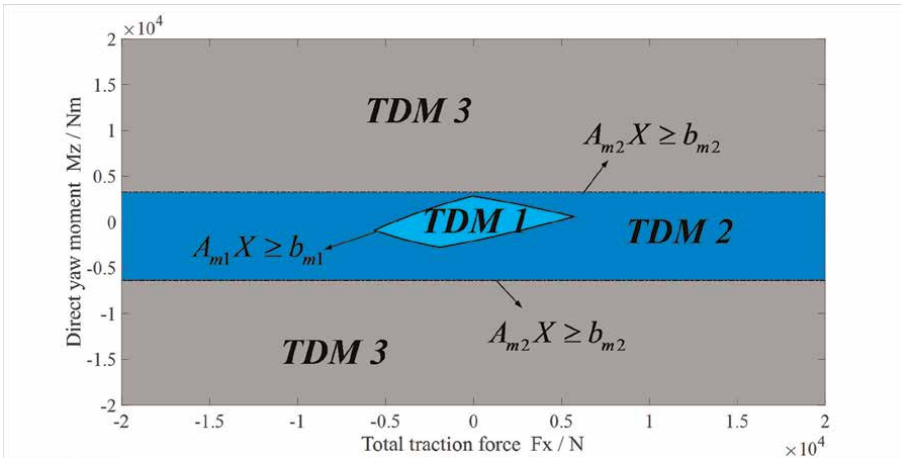**Figure 16.**
Acceleration.

Figure 17.
Turn left.

Figure 18.
Turn right.

125

Figure 19.
High friction.

Figure 20.
Low friction.

Thus far, we have developed three TDMs, each with its own set of boundaries (**Figures 17–20**). These boundaries can be plotted in a two-dimensional plane with F_x (total traction force) and M_{zopt} (optimal DYC) as the horizontal and vertical axes, respectively. The drive stability region for each TDM is denoted by $D_i (i = 1,2,3)$. It is important to note that the shape of these regions varies depending on the specific vehicle and road parameters. **Figure 8** displays the drive stability regions for different conditions.

It can be observed that TDM 1 is characterized by a quadrilateral shape with curved edges, while TDM 2 is represented by a band shape. Compared to the static condition, the TDM 2 region under acceleration is slightly narrower, indicating a reduction in available DYC. During left turns, TDM 1 tends to tilt towards the left side, and the upper boundary of TDM 2 is significantly reduced due to the saturated lateral tire force. This suggests the need for DYC in the opposite direction to ensure vehicle stability. On low-friction roads, both TDM 1 and TDM 2 regions are much narrower, indicating a decrease in available M_{zopt} and F_{xall}.

4. Energy-saving oriented torque allocation strategy of distributed drive electric vehicles

4.1 The overall control framework

The four independently driven in-wheel motors endow more potential to enhance the multi-performance control requirement of distributed drive electric vehicles. The hierarchical control scheme can balance the multi-objectives through the layered control methods while simplifying the system complexity. Hence, this section introduces a dual MPC (model predictive control)-based hierarchical scheme to ensure energy conservation and stability control. The control framework details in **Figure 21**.

In the upper layer, the total torque inputs are generated according to the driver's speed control requirement. Then using the energy-efficiency map obtained from the dynamometer, the optimal torque inputs are distributed to the front and rear axles. Such design can realize the energy saving through guaranteeing the in-wheel motors work in a high-efficiency zone.

In the lower layer, the additional direct yaw moment control is generated by the differential torque inputs of left and right in-wheel motors, which aims to ensure vehicle handling stability. Considering that the additional torque inputs would degrade the energy-saving performance, a relaxation factor is designed to prevent excessive control inputs based on guaranteeing the vehicle safety. Note that $\beta - \gamma$ phase plane is used to represent the vehicle stability margins.

4.2 The upper layer torque allocation strategy

This section allocates the torque inputs to the front and rear axles according to the motor efficiency map as shown in **Figure 22**. This is a PD18 RAM in-wheel motor. The design principle is to enable the in-wheel motors to work in a high-efficiency zone. Meanwhile, the system scheme should also take the vehicle longitudinal stability performance into account. Here, we build the wheel dynamics model to represent the rotational motion with the torque control inputs.
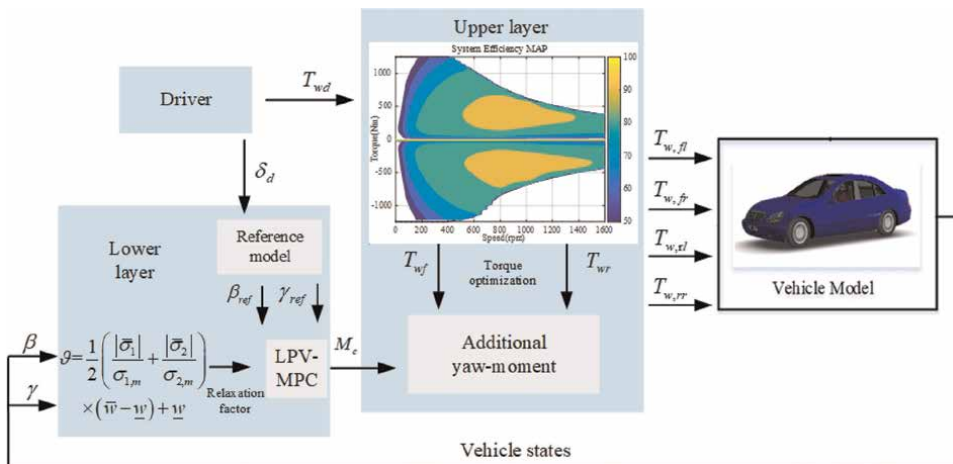
Figure 21.
Overall diagram of the proposed control strategy.

4.2.1 Wheel dynamics model

Through lumping the left and right wheels to the axle, the vehicle longitudinal motion can be represented as follows considering the tire slip ratio.

$$J_w \dot{w}_i = T_{wi} - R_e F_{xi} \tag{33}$$

$$F_{xi} = k_i \lambda_{wi}, \lambda_{wi} = \frac{w_i R_e - V_{xi,w}}{V_{xi,w}}, (i = f, r) \tag{34}$$

Combining Eq. (33) and Eq. (34), the tire rotational motion can be expressed by

$$\dot{\lambda}_{wi} = -\frac{R_e^2}{J_{wi} V_{xi,w}} k_i \lambda_{wi} + \frac{R_e}{J_{wi} V_{xi,w}} T_{wi} \tag{35}$$

where $V_{xi,w}$ and w_i are the longitudinal speed and angular speed of wheel i, respectively. R_e and J_w represent rolling radius and inertia moment around y axis of the wheel, respectively. k_i and $\lambda_w i$ donate the tire longitudinal stiffness and slip ratio, respectively. T_{wi} and F_{xi} represent the torque input and tire longitudinal force, respectively. Then the state space equation of the wheel motion is given by

$$\dot{x} = Ax + Bu \tag{36}$$

where $x = \lambda_{wi}$, $u = T_{wi}$, $A = -\frac{R_e^2}{J_{wi} V_{xi,w}} k_i$, $B = \frac{R_e}{J_{wi} V_{xi,w}}$.

4.2.2 Energy-saving controller design

The LTV-MPC (linear time varying model predictive control) is employed to handle the uncertain model parameter of longitudinal velocity. The Eq. (36) is required to be discrete first in the predictive controller. The ΔT is the sampling time. Then the discrete equation is expressed as

$$x(k+1) = A'x(k) + B'u(k) \tag{37}$$

where $A' = e^{A\Delta T}$, $B' = \int_{k\Delta T}^{(k+1)\Delta T} e^{A[(k+1)\Delta T - t]} B dt$. The vehicle state and torque control input at time k are represented by $x(k)$ and $u(k)$, respectively. It should be noted that in the LTV-MPC design, $V_{xi,w}$ in the parameter matrices is updating at different sampling time. The LTV-MPC can guarantee the model accuracy, thereby avoiding the invalid direct yaw moment control inputs.

In the upper layer of the torque allocation strategy, the driver's longitudinal velocity control requirement is satisfied first by the total torque control input. Here, a PI controller is employed to describe the driver longitudinal speed-tracking intention. Hence, the total in-wheel motor torque input is calculated by

$$T_{wd} = K_P e_v + K_I \int e_v dt \tag{38}$$

where e_v denotes the speed-tracking deviation. K_i and K_p represent the integral and proportional coefficients. Then the following cost function is designed to realize the total torque control.

$$J_1 = \sum_{t=1}^{N_p} \rho \left(2T_{wf}(t+k|k) + 2T_{wr}(t+k|k) - T_{wd}(k)\right)^2 \qquad (39)$$

where $T_{w,\min} \leq T_{wi} \leq T_{w,\max}$. $T_{w,\max}$ and $T_{w,\min}$ are the admitted maximal and minimal torque control inputs, respectively. T_{wf} and T_{wr} represent the torque control inputs of front and rear in-wheel motors. ρ and N_p denote the weight coefficient and predictive horizon, respectively. Note that the predictive horizon is equal to the control horizon in this paper. Next, the energy-saving control has a priority in the upper layer. The specific method is to guarantee a higher efficiency zone for the motors. Hence, we establish a mapping function between the vehicle speed and energy efficiency. Based on the motor efficiency map in **Figure 22**, The most energy-efficient torque control at the current speed is selected as the reference value $T_{wi,r}(i = f, r)$ to optimize the control inputs. Then the obtained optimal torque inputs of front and rear axles are evenly distributed to the left and right in-wheel motors. Moreover, the optimization objective of a smaller tire slip ratio is also added to the cost function and expressed by

$$J_2 = \sum_{t=1}^{N_p} \left(J_2^1 + J_2^2\right) \qquad (40)$$

$$J_2^1 = \sum_{t=1}^{N_p} \left[\hbar_1\left(T_{wf}(k+t|k) - T_{wf,r}(k)\right)^2 + \hbar_2\left(T_{wr}(k+t|k) - T_{wr,r}(k)\right)^2\right] \qquad (41)$$

$$J_2^2 = \sum_{t=1}^{N_p} \left(\alpha_1 \lambda_{wf}^2(k+t|k) + \alpha_2 \lambda_{wr}^2(k+t|k)\right) \qquad (42)$$

where α_1, α_2, $\hbar_1$, and $\hbar_2$ are the weighting coefficients. Considering the vehicle longitudinal stability, the front axle has a priority to satisfy the high-efficiency zone. When approaching the tire force limitation, a small slip of the rear wheel would lead
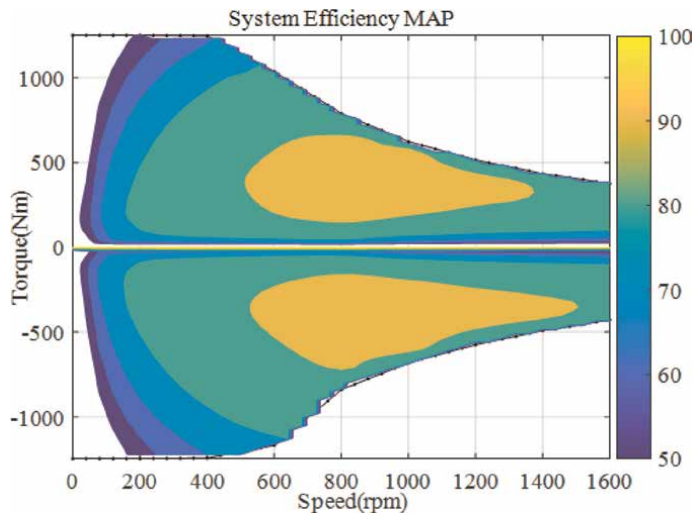
Figure 22.
The upper layer torque allocation strategy.

to the vehicle instability. Therefore, $\hbar_1$ is endowed with a higher value. Furthermore, to ensure the driver's longitudinal control intention, a logical judgment is also added. If the optimized torque of the rear wheel is not consistent with the driver's control intention, the control inputs are set as 0. Through combing Eq. (39)-Eq. (42), the control objective function is represented by

$$J = J_1 + J_2 \qquad (43)$$

4.3 The lower layer of direct yaw moment control strategy

The lower layer develops the direct yaw moment control (DYC) to enhance the vehicle handling stability based on the differential torque control inputs of left and right in-wheel motors. To improve the energy efficiency, the relaxation factor is introduced to prevent the excessive yaw moment control inputs. Here, the $\beta - \gamma$ phase plane is used to represent the vehicle stability region.

4.3.1 The vehicle dynamics modeling

A two degree-of-freedom (2-DoF) vehicle model is adopted to describe the vehicle lateral dynamics characteristics. Assuming that the vehicle runs with a small yaw angle and steering input, the vehicle model is expressed as

$$
\begin{aligned}
mV_x(\dot{\beta} + \dot{\varphi}) &= F_{yf} + F_{yr} \\
I_z\dot{\gamma} &= l_f F_{yf} - l_r F_{yr} + M_c
\end{aligned}
\qquad (44)
$$

where I_z is the vehicle inertia moment of the yaw motion. l_f and l_r represent the distances from the front and rear axles to the vehicle gravity, respectively. β and ϕ denote the vehicle sideslip angle and yaw angle, respectively. $\gamma = \dot{\varphi}$, $F_{yi} = 2C_i\alpha_i$. γ represents the vehicle yaw rate. The tire slip angle α_i generates the lateral force F_{yi}. M_c is the additional direct yaw moment control input.

The tire slip is further written as

$$
\begin{cases}
\alpha_f = \delta_f - \dfrac{l_f\gamma}{V_x} - \beta \\[2mm]
\alpha_r = \dfrac{l_r\gamma}{V_x} - \beta
\end{cases}
\qquad (45)
$$

where δ_f is the driver steering input. Through combing Eq. (44) and Eq. (45), we can obtain

$$\dot{\xi} = \overline{A}\xi + \overline{B}\nu + \overline{C}\delta_f \qquad (46)$$

where $\xi = [\beta, \gamma]^T$, $\overline{A} = \begin{bmatrix} -\dfrac{C_f + C_r}{mV_x} & \dfrac{C_r l_r - C_f l_f}{mV_x^2} - 1 \\[3mm] \dfrac{C_r l_r - C_f l_f}{I_z} & -\dfrac{C_f l_f^2 + C_r l_r^2}{I_z V_x} \end{bmatrix}$, $\overline{B} = [0\,1/I_z]^T$, $\overline{C} = \left[\dfrac{2C_f}{mV_x}\, \dfrac{2C_f l_f}{I_z}\right]^T$,

$\nu = M_c$.

To facilitate the MPC design, the vehicle lateral dynamics model is discrete as follows.

$$\xi(k+1) = \overline{A}' \xi(k) + \overline{B}' \nu(k) + \overline{C}' \delta_f \tag{47}$$

The system matrices are obtained by

$$\overline{A}' = e^{\overline{A}\Delta T}, \overline{B}' = \int_{k\Delta T}^{(k+1)\Delta T} e^{\overline{A}[(k+1)\Delta T - t]}\overline{B}dt, \overline{C}' = \int_{k\Delta T}^{(k+1)\Delta T} e^{\overline{A}[(k+1)\Delta T - t]}\overline{C}dt \tag{48}$$

Due to the uncertain model parameter of vehicle longitudinal velocity, the LTV-MPC is also adopted in the lower layer.

4.3.2 The vehicle yaw motion control design

For the vehicle yaw motion control, the sideslip angle and yaw rate are treated as important indices to represent the handling stability performance. In this paper, the steady yaw rate response and small value of sideslip angle are used as the reference value. Hence, the reference yaw motion can be represented by

$$\begin{cases} \beta_{ref} = 0 \\ \gamma_{ref} = \dfrac{V_x}{l_f + l_r + \dfrac{mV_x^2(C_r l_r - C_f l_f)}{2C_f C_r(l_f + l_r)}}\delta_f \end{cases} \tag{49}$$

The cost function for the MPC design can be expressed as

$$\overline{J} = \sum_{t=1}^{N_p}\left[\lambda_1\left(\beta(t+k|k) - \beta_{ref}(k)\right)^2 + \lambda_2\left(\gamma(t+k|k) - \gamma_{ref}(k)\right)^2 + \lambda_3\nu^2\right] \tag{50}$$

$$|\Theta_1\gamma - \Theta_2\beta| \le \sigma_1 \tag{51}$$

$$|\Phi_1\gamma - \Phi_2\beta| \le \sigma_2 \tag{52}$$

where $M_{\min} \le M_c \le M_{max}$. M_{max} and M_{min} represent the admitted maximal and minimal yaw moment control input, respectively. λ_1, λ_2, and λ_3 denote the weighting coefficients.

The Eq. (51) and Eq. (52) is widely used as the envelop control to describe the vehicle stability margin [1]. However, as shown in **Figure 23**, the direct yaw moment control input would also have an effect on the vehicle stability performance. Hence, in this work, the slack factors Φ_1 and Φ_2 in Eq. (53) and Eq. (54) are introduced to permit the vehicle runs out of the traditional stability boundaries to some extent.

$$|\Theta_1\gamma - \Theta_2\beta| \le \sigma_1 + \Psi_1 \tag{53}$$

$$|\Phi_1\gamma - \Phi_2\beta| \le \sigma_2 + \Psi_2 \tag{54}$$

Furthermore, considering that the yaw moment control input would also have an effect on the energy saving performance, a small DYC control should be given when
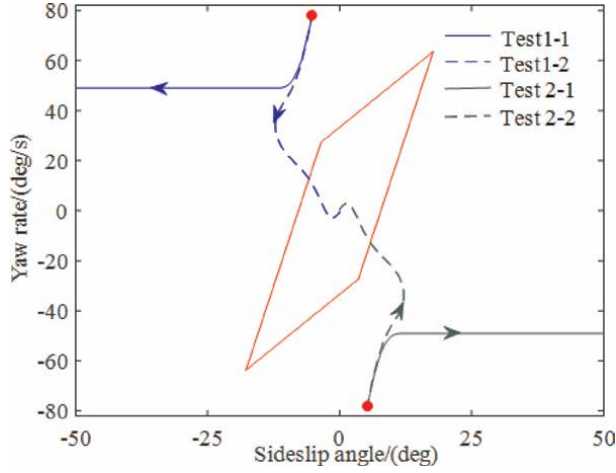
Figure 23.
Effect of yaw-moment control on the vehicle stability region.

the vehicle has enough stability region. Therefore, a relaxation factor ϑ is adopted to dynamically adjust the weighting coefficients λ_1 and λ_2. Here, the relaxation factor ϑ can be calculated by

$$\vartheta = \frac{1}{2}\left(\frac{|\overline{\sigma}_1|}{\sigma_{1,m}} + \frac{|\overline{\sigma}_2|}{\sigma_{2,m}}\right) \times (\overline{w} - \underline{w}) + \underline{w} \tag{55}$$

where $\underline{w} = 0.5, \overline{w}, \sigma_{i,m} = \sigma_i + \Psi_i (i = 1, 2)$. Then the weighting coefficients are rewritten as

$$\overline{\lambda}_1 = \vartheta\lambda_1, \overline{\lambda}_2 = \vartheta\lambda_2 \tag{56}$$

Then the optimal direct yaw moment control inputs are evenly allocated to the left and right in-wheel motors. The total torque inputs for each in-wheel motor are represented by

$$\begin{cases} T_{w,fl} = T_{w,f} - \dfrac{M_c}{t_w}R_e \\[2mm] T_{w,fr} = T_{w,f} + \dfrac{M_c}{t_w}R_e \\[2mm] T_{w,rl} = T_{w,r} \\[1mm] T_{w,rr} = T_{w,r} \end{cases} \tag{57}$$

4.4 Test results

Here, as shown in **Figure 24**, the hardware-in-the-loop test is conducted to verify the control effect. A high-fidelity distributed drive electric vehicle built by the commercial software Carsim is embedded into the PXI, which provides a real-time
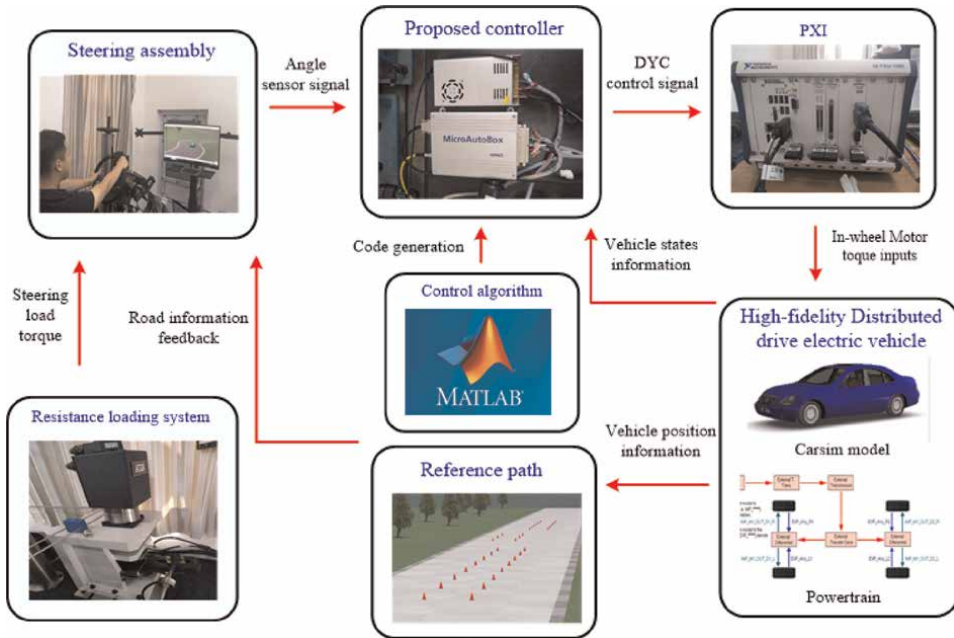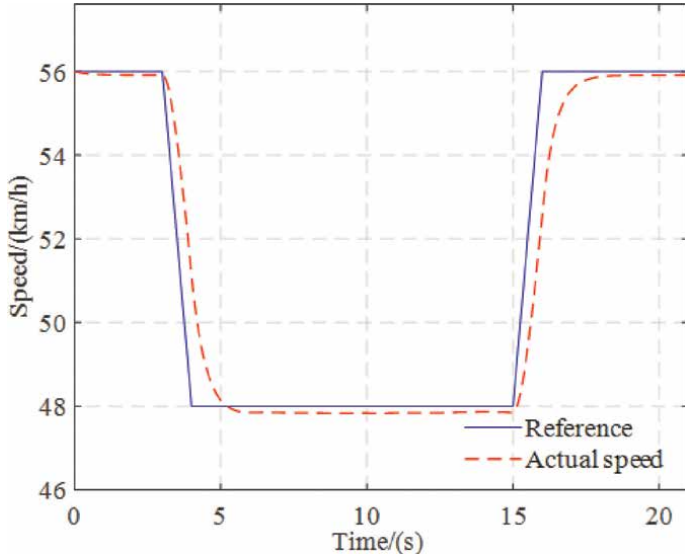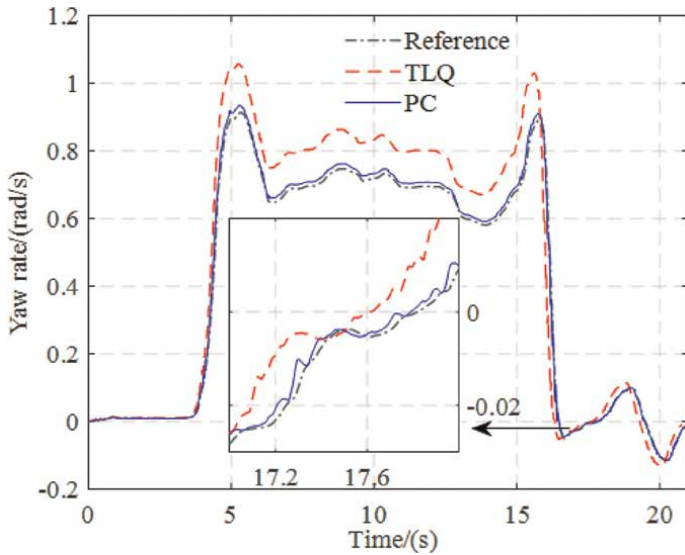
Figure 24.
HIL bench test.

simulator. The control strategy is downloaded in the calculation platform dSPACE by the code generation technology. The calculated torque inputs are sent to the PXI through the CAN bus. The DDEV model will execute the control command. Then the vehicle states are regarded as the feedback signal and transmitted to the dSPACE to calculate the optimal control inputs. The driver steering behavior is obtained by the driving simulator. The U-turn maneuver is selected as the test condition in the HIL test. In addition, to demonstrate the proposed method (PC), the traditional torque allocation combined linear quadratic regulator (TLQ) and the proposed controller without the relaxation factor (WRF) are set as the comparative tests. The traditional torque allocation method can be represented by

$$T_{w,fl} = T_{w,fr} = \frac{l_r}{l_f + l_r} \frac{T_{wd}}{2}, T_{w,rl} = T_{w,rr} = \frac{l_f}{l_f + l_r} \frac{T_{wd}}{2} \qquad (58)$$

Considering the limitation of the tire force, **Figure 25** shows the reference vehicle speed. The proposed method behaves with good performance to track the desired speed. The vehicle lateral dynamics response is shown in **Figures 26** and **27**. It can be seen that the proposed method can significantly guarantee the vehicle reference yaw rate tracking performance compared with the TLQ method, while reducing the sideslip angle. Owing to the superiority to handle the uncertain model parameter, the proposed method is effective to enhance vehicle handling stability under the large-curvature road driving condition. However, the tracking error of the TLQ method is a little large. In addition, as observed from the vehicle $\beta - \gamma$ phase
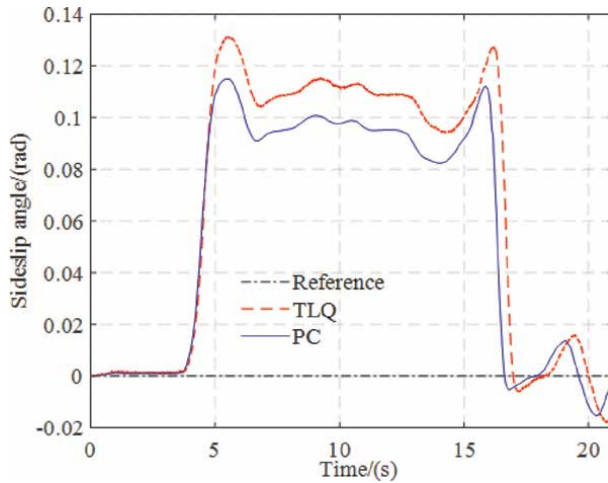
Figure 25.
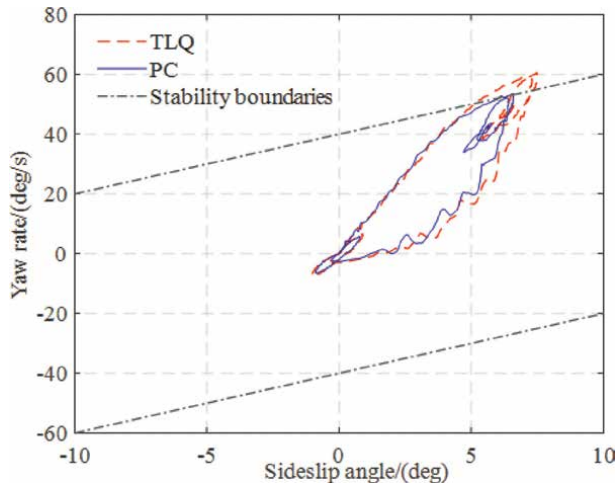*Vehicle speed tracking performance.*

Figure 26.
Vehicle yaw rate.

plane in **Figure 28**, the proposed method can guarantee a more safe state by the DYC control. In contrast, the vehicle runs out of the stability margins with the TLQ method. It also proves the proposed method works to balance the multi-performance control.
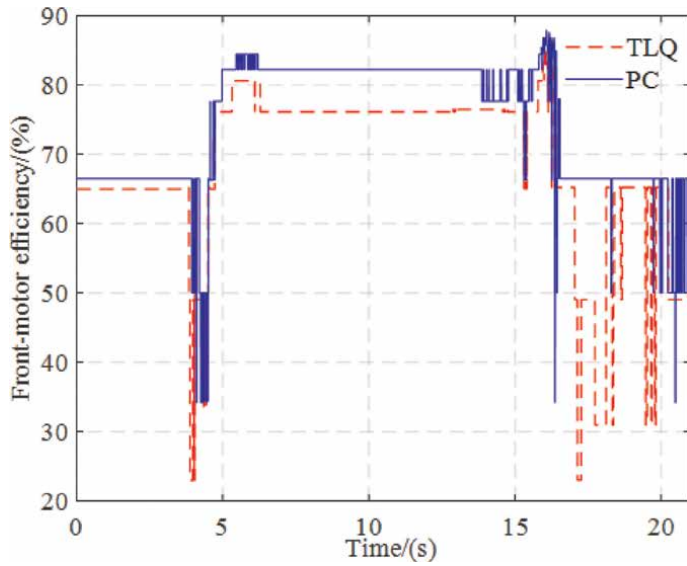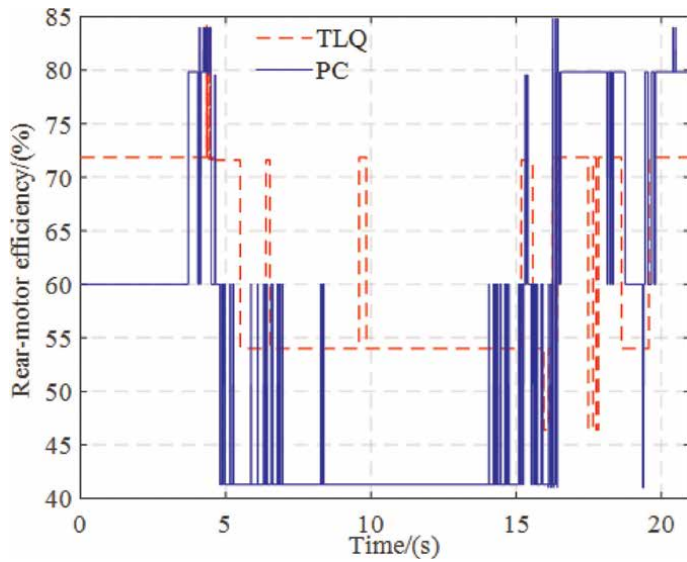
Figure 27.
Vehicle sideslip angle.

Figure 28.
Vehicle yaw motion phase plane.

Figures 29 and **30** show the efficiency of front and rear in-wheel motors, respectively. It is clear that the efficiency of the front in-wheel motor with the proposed method is better than that of the rear in-wheel motor. This is because when allocating the torque inputs, the proposed method is first to guarantee the high-efficiency work zone for front in-wheel motors. Hence, the efficiency of the rear in-wheel motor with the proposed method is worse than that of the TLQ method. However, from the power consumption in **Figure 31**, the proposed method still performs better to ensure the energy-saving performance compared with the TLQ method. However, the test results also demonstrate the proposed controller can be effective to guarantee the prescribed performance. Due to the existence of the disturbance during the HIL tests, there would have some fluctuation in test results. However, the test results also

Figure 29.
Vehicle speed tracking performance.

Figure 30.
Vehicle yaw rate.

demonstrate the proposed controller can be effective to guarantee the prescribed performance. From **Table 1**, the proposed method can reduce energy consumption by 3.18% and 10.02% compared to the WRF method and e TLQ method, respectively.

Furthermore, the feasibility of the proposed energy-saving control method has been proved in the HIL test. This indicates that the proposed controller has great potential to improve the comprehensive performance of the vehicle. In the future, we would concentrate on more efficient ways of energy-saving optimization problems.

TLQ	WRF	PC
43.1107	40.0642	38.7917

Table 1.
Energy consumption/(kJ).
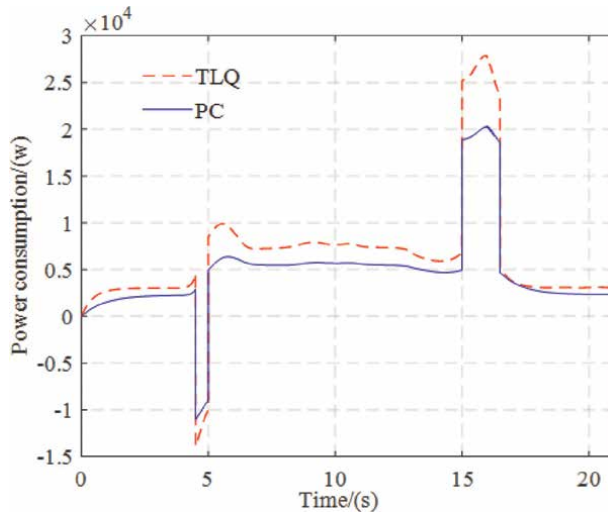
Figure 31.
Vehicle sideslip angle.
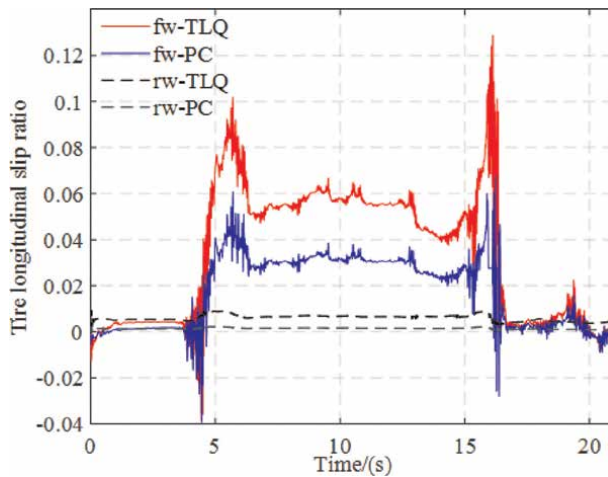
Figure 32.
Vehicle yaw motion phase plane.

The proposed strategy can not only be limited to the distributed drive electric vehicles. Meanwhile, the emergency collision avoidance condition would be also considered. In addition, from **Figure 32**, the tire longitudinal slip ratio with the proposed method is significantly smaller than that of the TLQ method. This demonstrates the proposed method can also improve the vehicle longitudinal stability. The test results

verify the proposed method can be effective to improve the energy-saving performance based on guaranteeing the vehicle stability.

5. Conclusions

This chapter introduces the distributed drive electric vehicle from the viewpoint of the dynamics modeling, stability performance analysis, and energy-saving strategy. The conventional modeling method of DDEVs is detailed first. Then, the stability region of DDEVs is estimated by establishing a rational polynomial-based DDEV model and adopting the SOSP technique to find the maximal Lyapunov function for estimation. The resulting stability regions with different parameters are presented, and comparison shows that the additional DYC has an expanding effect on the stability region. This suggests that DDEVs have greater potential in terms of stability and safety compared to centralized drive vehicles. Finally, a torque vector control framework for DDEVs is proposed in this paper to reduce the energy-consumption on the basis of maintaining the vehicle stability. The LTV-MPC-based hierarchical strategy is adopted to realize the parallel control of energy-saving and handling stability. A relaxation factor is introduced to reduce the energy consumption caused by additional direct-yaw-moment control input through evaluating the vehicle stability performance.

The proposed stability analysis method also has some issues to solve, in which the developed mode decision theorem and division of drive stability regions are mainly based on the tire adhesion ellipse theorem. However, the nonlinearity of the vehicle dynamics model also has an influence on the stability performance. In future research, theorems of body stability including $\gamma - \beta$ phase diagram and $g - g$ diagram will be considered in the torque distribution method design.

Furthermore, the feasibility of the proposed energy-saving control method has been proved in the HIL test. This indicates that the proposed controller has great potential to improve the comprehensive performance of the vehicle. In the future, we would concentrate on more efficient ways of energy-saving optimization problems. The proposed strategy can not only be limited to the distributed drive electric vehicles. Meanwhile, the emergency collision avoidance condition would be also considered.

Abbreviations

DDEV	distributed drive electric vehicle
EV	electric vehicle
CDV	centralized drive vehicle
DYC	direct yaw moment control
LTV-MPC	linear time varying model predictive control
SOSP	Sum of Squares Programming
EECA	energy-efficient control allocation
KKT	Karush-Kuhn-Tuckert
SOS	sum of squares
LMI	linear matrix inequality
RoA	region of attraction

TDMS   three Torque distribution Methods
MPC   model predictive control
2-DoF   two degree-of-freedom
TLQ   torque allocation combined linear quadratic regulator
WRF   without the relaxation factor
PC   proposed controller
LMPC   linear model predictive control
AT   average torque

Author details

Jinhao Liang[1†], Tong Shen[2†], Ruiqi Fang[2†] and Faan Wang[3*†]

1 The Department of Civil and Environmental Engineering, National University of Singapore, Singapore

2 The School of Mechanical Engineering, Southeast University, Nanjing, China

3 The Faculty of Modern Agricultural Engineering, Kunming University of Science and Technology, Kunming, China

*Address all correspondence to: wfa@kust.edu.cn

† These authors contributed equally.

IntechOpen

References

[1] Liang J, Feng J, Fang Z, Lu Y, Yin G, Mao X, et al. An energy-oriented torque-vector control framework for distributed drive electric vehicles. IEEE Transactions on Transportation Electrification. DOI: 10.1109/TTE.2022.3231933

[2] Hu X, Murgovski N, Johannesson L, Egardt B. Energy efficiency analysis of a series plug-in hybrid electric bus with different energy management strategies and battery sizes. Applied Energy. 2013;**111**:1001-1009. DOI: 10.1016/j.apenergy.2013.06.056

[3] Spanoudakis P, Tsourveloudis N, Doitsidis L, Karapidakis E. Experimental research of transmissions on electric vehicles energy consumption. Energies. 2019;**12**(3):388. DOI: 10.3390/en12030388

[4] Xiong L, Teng GW, Yu ZP, Zhang WX, Feng Y. Novel stability control strategy for distributed drive electric vehicle based on driver operation intention. The International Journal of Automotive Technology. 2016;**17**(4):651-663. DOI: 10.1007/s12239-016-0064-3

[5] Jin XJ, Yin G, Chen N. Gain-scheduled robust control for lateral stability of four-wheel-independent-drive electric vehicles via linear parameter-varying technique. Mechatronics. 2015;**30**:286-296. DOI: 10.1016/j.mechatronics.2014.12.008

[6] Manzetti S, Mariasiu F. Electric vehicle battery technologies: From present state to future systems. Renewable and Sustainable Energy Reviews. 2015;**51**:1004-1012. DOI: 10.1016/j.rser.2015.07.010

[7] Elma O. A dynamic charging strategy with hybrid fast charging station for electric vehicles. Energy. 2020;**202**:117680. DOI: 10.1016/j.energy.2020.117680

[8] Zhang H, Wang J. Vehicle lateral dynamics control through AFS/DYC and robust gain-scheduling approach. IEEE Transactions on Vehicular Technology. 2016;**65**(1):489-494. DOI: 10.1109/TVT.2015.2391184

[9] Qu T, Chen H, Cao D, Guo H, Gao B. Switching-based stochastic model predictive control approach for modeling driver steering skill. IEEE Transactions on Intelligent Transportation Systems. 2015;**16**(1):365-375. DOI: 10.1109/TITS.2014.2334623

[10] Wang Z, Montanaro U, Fallah S, Sorniotti A, Lenzo B. A gain scheduled robust linear quadratic regulator for vehicle direct yaw moment control. Mechatronics. 2018;**51**:31-45. DOI: 10.1016/j.mechatronics.2018.01.013

[11] Liang J, Lu Y, Yin G, Fang Z, Zhuang W, Ren Y, et al. A distributed integrated control architecture of AFS and DYC based on MAS for distributed drive electric vehicles. IEEE Transactions on Vehicular Technology. 2021;**70**(6):5565-5577. DOI: 10.1109/TVT.2021.3076105

[12] Huang Y, Chen Y. Integrated AFS and ARS control based on estimated vehicle lateral stability regions. In: 2018 Annual American Control Conference (ACC). Milwaukee, WI, USA: IEEE; 2018. pp. 5516-5521. DOI: 10.23919/ACC.2018.8431174

[13] Pennycott A, De Novellis L, Sabbatini A, Gruber P, Sorniotti A.

Reducing the motor power losses of a four-wheel drive, fully electric vehicle via wheel torque allocation. Proceedings of the Institution of Mechanical Engineers, Part D: Journal of Automobile Engineering. 2014;**228**(7):830-839. DOI: 10.1177/0954407013516106

[14] Chen Y, Wang J. Design and experimental evaluations on energy efficient control allocation methods for Overactuated electric vehicles: Longitudinal motion case. IEEE/ASME Transactions on Mechatronics. 2014;**19**(2):538-548. DOI: 10.1109/TMECH.2013.2249591

[15] Zhang X, Göhlich D, Zheng W. Karush–Kuhn–Tuckert based global optimization algorithm design for solving stability torque allocation of distributed drive electric vehicles. Journal of the Franklin Institute. 2017;**354**(18):8134-8155. DOI: 10.1016/j.jfranklin.2017.10.005

[16] Lenzo B, De Filippis G, Dizqah AM, Sorniotti A, Gruber P, Fallah S, et al. Torque distribution strategies for energy-efficient electric vehicles with multiple drivetrains. Journal of Dynamic Systems, Measurement, and Control. 2017;**139**(12):121004. DOI: 10.1115/1.4037003

[17] Zhai L, Hou R, Sun T, Kavuma S. Continuous steering stability control based on an energy-saving torque distribution algorithm for a four in-wheel-motor independent-drive electric vehicle. Energies. 2018;**11**(2):350. DOI: 10.3390/en11020350

[18] Hua M, Chen G, Zhang B, Huang Y. A hierarchical energy efficiency optimization control strategy for distributed drive electric vehicles. Proceedings of the Institution of Mechanical Engineering, Part D: Journal of Automobile Engineering. 2019;**233**(3):

605-621. DOI: 10.1177/0954407017751788

[19] Kobayashi T, Katsuyama E, Sugiura H, Ono E, Yamamoto M. Efficient direct yaw moment control: Tyre slip power loss minimisation for four-independent wheel drive vehicle. Vehicle System Dynamics. 2018;**56**(5):719-733. DOI: 10.1080/00423114.2017.1330483

[20] Kobayashi T, Katsuyama E, Sugiura H, Ono E, Yamamoto M. Direct yaw moment control and power consumption of in-wheel motor vehicle in steady-state turning. Vehicle System Dynamics. 2017;**55**(1):104-120. DOI: 10.1080/00423114.2016.1246737

[21] Parra A, Tavernini D, Gruber P, Sorniotti A, Zubizarreta A, Pérez J. On nonlinear model predictive control for energy-efficient torque-vectoring. IEEE Transactions on Vehicular Technology. 2021;**70**(1):173-188. DOI: 10.1109/TVT.2020.3022022

[22] Wang R, Zhang H, Wang J. Linear parameter-varying controller Design for Four-Wheel Independently Actuated Electric Ground Vehicles with Active Steering Systems. IEEE Transactions on Control Systems Technology. 2014;**22**(4):1281-1296. DOI: 10.1109/TCST.2013.2278237

[23] Wang R, Wang J. Fault-tolerant control with active fault diagnosis for four-wheel independently driven electric ground vehicles. IEEE Transactions on Vehicular Technology. 2011;**60**(9):4276-4287. DOI: 10.1109/TVT.2011.2172822

Chapter 6

Hybrid Energy Storage Systems in Electric Vehicle Applications

Federico Ibanez

Abstract

This chapter presents hybrid energy storage systems for electric vehicles. It briefly reviews the different electrochemical energy storage technologies, highlighting their pros and cons. After that, the reason for hybridization appears: one device can be used for delivering high power and another one for having high energy density, thus large autonomy. Different energy storage devices should be interconnected in a way that guarantees the proper and safe operation of the vehicle and achieves some benefits in comparison with the single device storage system source. The chapter shows different topologies for interconnecting electrochemical technologies: passive, semi-active, and full-active, clarifying their benefits and drawbacks. The chapter concludes with a case study, an electric motorcycle, which is ridded using an urban profile. There, the hybridization was performed to extend its cycle life.

Keywords: hybrid energy storage systems, DC/DC power converters, batteries, supercapacitors, lifecycle, electric vehicles, multiport topologies

1. Introduction

Electrical vehicles require energy and power for achieving large autonomy and fast reaction. Currently, there are several types of electric cars in the market using different types of technologies such as Lithium-ion [1], NaS [2] and NiMH (particularly in hybrid vehicles such as Toyota Prius [3]). However, in case of full electric vehicle, Lithium-ion technology is used widely in automobiles, scooters, motorcycles, and busses [4]. It is known that the aging of a battery and its capacity is dependent on the type of use such as the current profile and the depth of discharge [5]. The deeper the battery is discharged and the higher the currents are, the smaller is the number of cycles for the battery. Thus, combining batteries with other energy sources, which can tolerate high currents, deep discharges, and high number of cycles, can reduce the use of the battery in "non-favorable" conditions. Thus, the combination of a supercapacitor (SC) with a battery can lead to longer cycle life of the battery [6].

However, to achieve this goal, a control system needs to select which source of energy should be used in real time. Thus, high complexity is added in the energy storage system (ESS). For that purpose, some DC/DC converter topologies are used with a controller that selects the energy source for each instant [4, 7]. To understand

the advantages of hybrid energy storage systems (HESS), it is important to review the available energy sources.

2. Review of energy sources

There are many technologies for storing energy, most of them in an electrochemical way. Different technologies have different characteristics such as available power density, energy density, number of cycles, temperature range, calendar aging, and others. One of the most common diagrams for comparing energy storage technologies is the specific energy versus specific power plot, see **Figure 1** [8]. There, different technologies are presented in a two-axis plot that clearly shows which technology is more useful for delivering power and which one is better for storing energy. Therefore, combining a high energy density technology with a high power density technology, an energy storage system that fits well in an electric vehicle can be achieved.

In addition to those important indexes, the number of cycles is also important. In general, we can mention four main groups of storage technologies: electrochemical, electrostatic, electric double layer technology, and mechanical. There are also other types of storage technologies such as hydrogen fuel cells [9] and magnetic superconductors [10], but these are not covered in this chapter.
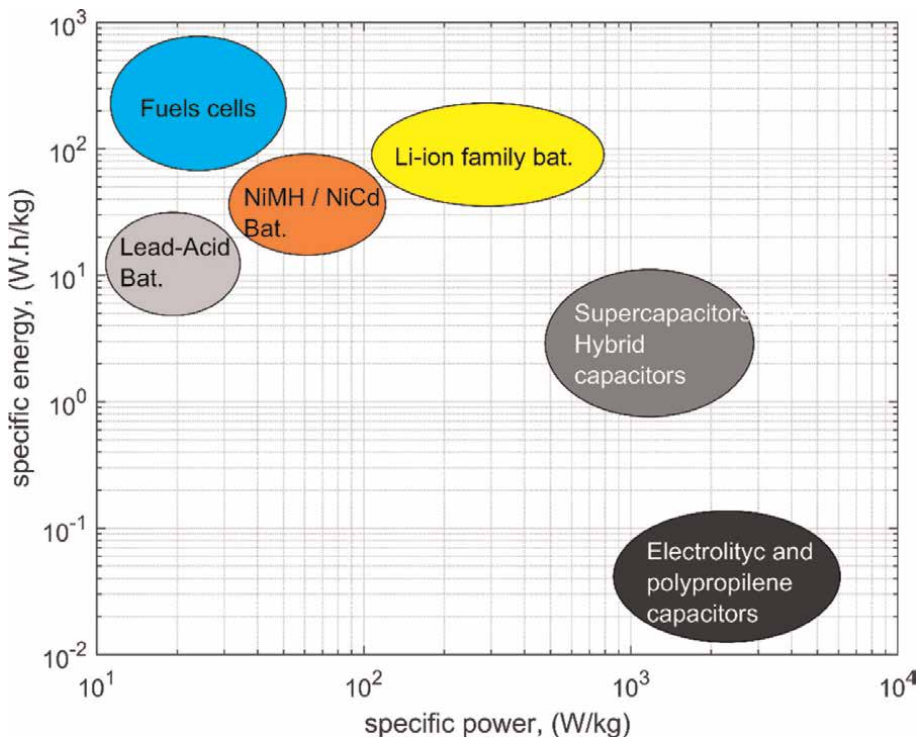
Figure 1.
Specific energy vs. specific power for different storage techniques [8].

2.1 Electrostatic technologies

From **Figure 1**, notice that the devices that can deliver the highest specific power are the electrostatic devices; their limit is their internal resistances. Electrostatic devices include electrolytic capacitors, polyester, and polypropylene capacitors [11]. However the energy density is quite low. The number of cycles is very high and the temperature range as well. Commonly, electrolytic capacitors are used in power electronics for voltage sags in grid-connected power supplies; thus, the output power is not compromised during a temporary energy interruption in the milliseconds range. Polyester and polypropylene capacitors have much smaller internal resistance, so they can deal with higher powers, but the specific energy is extremely low; their use is in the micro to milliseconds range, usually inside power electronic converters [12].

2.2 Electrical double layer capacitors

The next solution is a hybrid between a "capacitor" and an electrochemical cell, the electrical double layer capacitor, supercapacitor, or ultracapacitor. This device has a notable bigger energy density and can deliver high power; two mechanisms can work inside the device, electrostatic and electrochemical processes. Depending on the manufacturer and the applications, one or the other process is dominant. Another advantage is that the number of cycles is much bigger than the traditional electrochemical cells. Manufacturers mention more than 1,000,000 cycles.

Supercapacitors can be understood as an electrochemical cell in which the redox reactions are not present. The cell has two electrodes, an electrolyte and a separator. There is not mass transfer between the electrodes and the electrolyte; thus, only a charge distribution appears. That charge distribution can be considered as a parallel plate capacitor in which one plate is the electrode and the other is the electrolyte. The "dielectric" is the distance between the electrolyte and the electrode. It is very small; this is why it creates a huge capacitance [13]. In addition, the porosity of the electrodes creates a huge specific area, which also maximizes the capacitance effect. The huge capacitance appears in the interface between one electrode and one electrolyte; thus, the full device has two huge capacitors in series. The separator allows the flow of ions and avoids the short circuit between the electrodes.

These devices have impressive capacitances, commercially available around 3500F, but as the distance between plates is very small, the maximum voltage of the device is small as well. For aqueous electrolyte, it is around 1 V, and for organic electrolytes, it can reach around 3.5 V. As the mechanism to store energy remains electrostatic, the number of cycles is still very high.

In addition to the electrostatic effect, there are other supercapacitors that also have faradic processes (redox reactions and other types of reactions), and due to that, they can achieve even a higher capacitance. However, by including this process, the number of cycles is reduced. This type of supercapacitors is sometimes called hybrid supercapacitors.

2.3 Electrochemical technologies

In this group, we can mention Lithium-ion, NiCd, Lead-acid, NiMH, NaS, and other electrochemical technologies that store their energy based on redox reactions. This group has high energy density, moderate number of cycles (a few thousands, depending on the specific design and use), and moderate temperature range. As an

Technology	Voltage (V)	Energy density (Wh/dm^3)	Power density (kW/dm^3)
Lead-acid	2.0	50–80 [14, 15]	10–400
NiCd	1.2	60–150 [16]	150–300
NiMH	1.2	220–250 [17]	~900
Li-ion	4.1	200–500 [18]	500–2000
NaS	2.0	150–250 [14, 18]	150–230

Table 1.
Electrochemical technologies for electric vehicles.

example, **Table 1** shows some of the general characteristics of the most common technologies [19].

2.4 Other technologies

Regarding other ways of storing energy, mechanical storage devices were used in the past for massive storage. The most popular devices are: flywheels [20], which store energy in a kinetic fashion; compressed air energy storage (CAES); which storage energy by compressing and releasing the air; and water pumps, which store potential energy. Another technology is the redox flow batteries [21], which can be use of long periods of time, but its energy density is much lower than Lithium-ion batteries. All of these technologies are not suitable for vehicles, and they are mostly applicable in the electric grid.

Hydrogen fuel cells are also an interesting energy storage system that can fit in the electric vehicle technology and can be hybridized using an auxiliary energy storage such as lithium-ion or supercapacitors.

3. Hybrid energy storage systems (HESS)

There are several reasons for using a hybrid energy storage system instead of a single technology storage system (here, Battery Energy Storage System, BESS). All of them are related to the power sharing between a device that mainly stores energy and a device that mainly delivers power. There are several main benefits of power sharing:

- If the energy storage device (battery) delivers less instantaneous power (or current), the temperature is kept in safe operation area, which extends lifetime.

- If the energy storage device (battery) delivers less power (or current), it is expected that the extracted energy is larger. The less demanded power, the higher amount of energy that can be extracted from the battery. The device behaves more efficiently.

- Using an external device that can deliver more power, a new power limit can be achieved, higher than the one of the single energy storage device.

Therefore, with the aim of reducing the stress in the main battery, an auxiliary energy source is added, which creates an hybrid energy storage system (HESS). Thus,

high currents can be shared, and the battery use is reduced, with the corresponding increase in life cycle.

3.1 Main topologies

Different topologies exist in order to connect two or more energy sources. They can be defined in terms of three main groups:

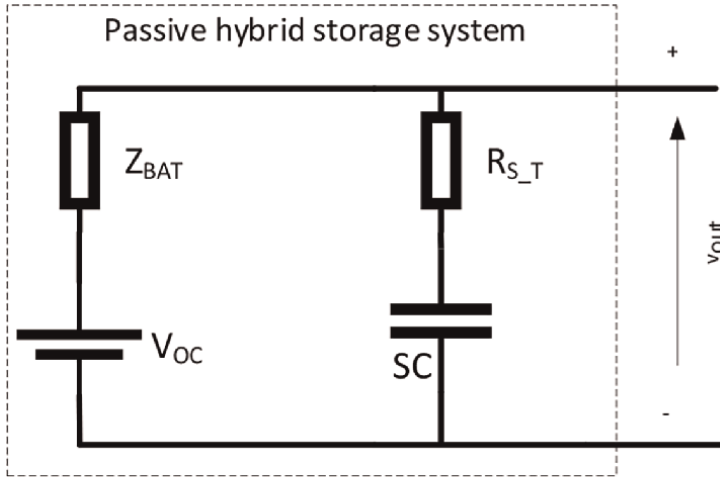- passive HESS

- semi-active HESS

- full-active HESS.

In the **passive HESS topology**, SCs and batteries are in parallel and connected directly to the load. It is a simple and low-cost topology, but the SCs' contribution is poor [7]. The SC delivers energy only if its terminal voltage varies. Therefore, connecting the SC in parallel to the battery limits the voltage variations, thus the contribution is limited. This topology has been used for transient suppression under high current pulses [22]. The circuit topology is shown in **Figure 2a**.

Semi-active HESS topologies allow one of the energy storage devices, the battery or the SC-stack, to be controlled through a DC/DC converter, while the other storage device is directly connected to the load without any control [23].

On the one hand, if the SC-stack is the device under control (**SC-HESS**), the DC/DC converter should deliver high power and be fast enough to react to power pulses [24]. Otherwise, the battery would have to respond to the load, and no advantage would be obtained from the HESS. As a benefit, if the battery is connected directly to the motor drive, the voltage in the output port of the SC-HESS is almost constant because the battery voltage profile is quite flat. Lithium-ion batteries in particular have a very flat profile if the depth of discharge is lower than 70%. The circuit topology is shown in **Figure 2b**.

On the other hand, if the battery is the device under control (**B-HESS**), which is the topology shown in **Figure 2c**, the SCs have a direct connection to the motor drive, so they can react very quickly. The current from the battery can be controlled in order to keep the SCs charged while the battery has a smooth discharging profile, independent of the load profile [25]. Thus, the battery is protected. The main disadvantage is that the motor drive voltage (or SC-stack voltage) is not constant. This is because the SCs' voltage is proportional to the stored electric charge and it changes as the current flows to the load. In order to allow the SCs to interact with the load and to deliver or absorb current, a voltage variation in the HESS output port must be allowed. The bigger the voltage variation, the bigger the current contribution from the SCs.

The full-active HESS solves the drawbacks of both semi-active topologies. Two main topologies exist: (a) parallel DC/DC converters topology [26] and (b) multiport DC/DC converters [27, 28] as shown in **Figure 2d** and **e**, where both the battery and the SCs are connected through a DC/DC converter to an output DC link that is connected to the load [25]. The SC-stack uses its entire operating voltage range; no high power pulses are demanded from the battery because its current is well controlled, and the DC link voltage can be correctly regulated through the DC/DC converters. However, the system is much more complex and efficiency is expected to be lower because the power is transferred always through DC/DC converters.
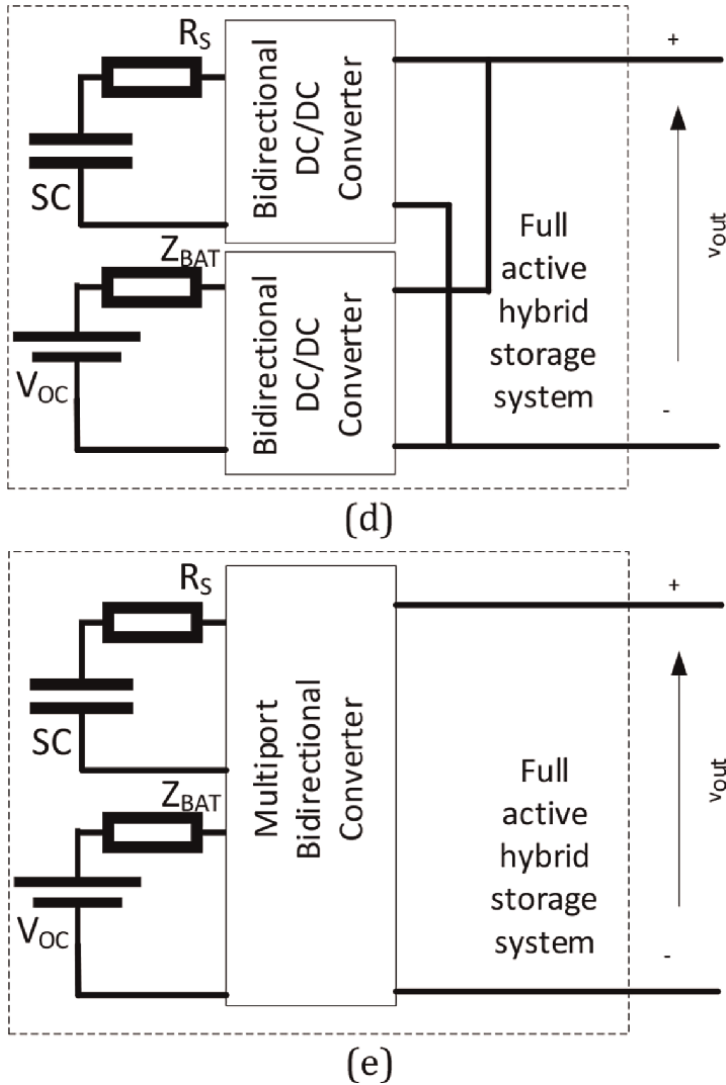
(a)
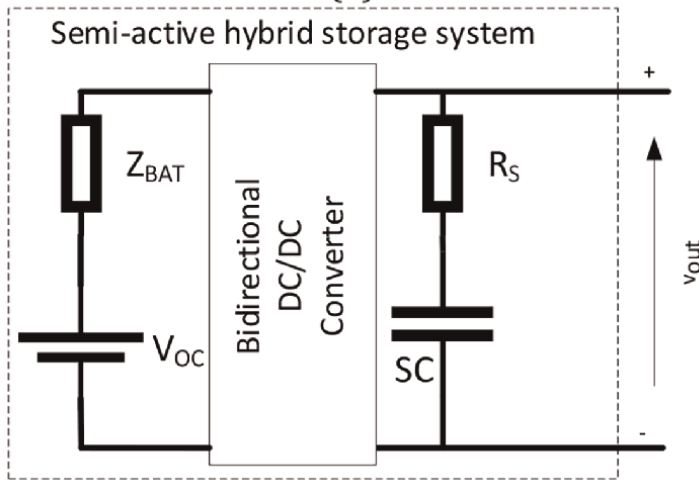
(b)
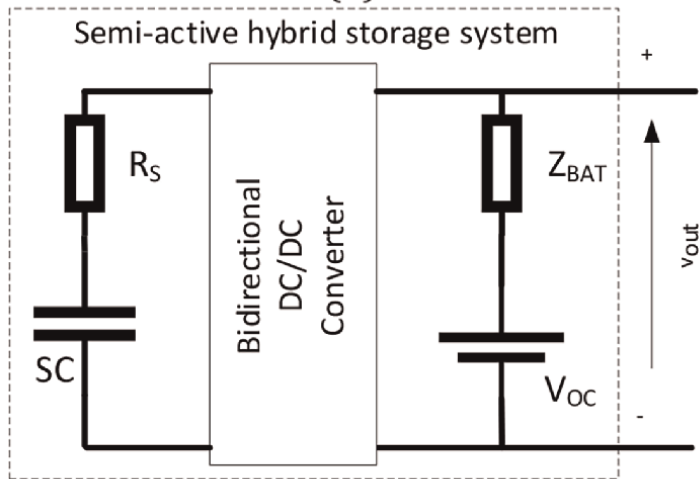
(c)

Figure 2.
Topologies of hybrid energy storage systems: (a) passive, (b) B-HESS semi-active, (c) SC-HESS semi-active, (d) full-active using multiple DC/DC converters, (e) full-active using multiport converters.

Semi-active and full-active systems are the most studied HESSs because they control the power that is delivered to the load and the SCs have a higher impact on the storage system compared to the passive topology. They are mainly used in photovoltaic, grid, and electric vehicle applications [24–26]. HESSs have been used for extending the power transfer capabilities of EV propulsion systems [25].

4. Case study: electro motorcycle

As an example of hybrid energy storage system for electric vehicle applications, a combination between supercapacitors and batteries is detailed in this section. The aim

is to extend the battery lifetime by delivering high power using supercapacitors while the main battery is delivering the mean power.

HESSs have been used for extending the power transfer capabilities of EV propulsion systems [13, 19]. In [14] a control algorithm for a full-active HESS is proposed in which either the battery or the SC-stack is selected as energy source according to the frequency spectrum of the demanding current. A more detailed analysis was performed in [9], where the control algorithm also considers the extreme cases when the SCs are out of energy. As a result, these works presented an improvement in the power response capability of the system and a reduction in the current peaks demanded from the battery.

## 4.1 Aging, thermal, and electric model for the battery

For understanding how the battery lifetime can be extended, aging models have been introduced in the past. Among aging models for batteries, [29] presents a degradation model that considers the depth of discharge in cycles and temperature. The model is based on crack propagation theory [30]. It predicts the capacity reduction and proposes an equivalent electric model that is, modified according to the age of the battery, so it combines the prediction in capacity reduction (Ah) with electric equivalent circuit. The model, without considering the calendar aging, is:

$$\Delta L = k_{co}.N_e.e^{\frac{\sigma_{SoC}-1}{k_{ex}}.\frac{T_N}{T_a}}.e^{k_{soc}\frac{\overline{SoC}-0.5}{0.25}}.e^{k_T\frac{\frac{T-T_a}{T_a}}{T_N}}.(1-L_0) \tag{1}$$

where L is the capacity reduction starting from 0 to 0.2 C when the battery capacity (C) is reduced 20%, which is normally considered as the end of the life time, and L_0 is the initial capacity degradation (L_0 = 1-C_0) during the time interval where ΔL is been computed. K_{co}, k_{ex}, k_{soc}, and k_T are the parameters of the model and need to be fitted using data. $\overline{SoC}$ and σ_{SoC} are the average and normalized standard deviation of the state of charge in the interval. For example, $\sigma_{SoC} = 1$ and $\overline{SoC} = 0.5$ are the values for a time interval that includes a full charge-discharge cycle. N_e is the number of equivalent full charge-discharge cycles during the time interval. T, T_a, and T_N are the battery temperature, ambient temperature, and nominal temperature (298 K) in K. Using (1), the battery capacity degradation, L, can be calculated at any moment: L = L_0 + ΔL.

This model expresses that the aging depends on the number of equal cycles, the previous aging (1-L_0), depth of discharge within a cycle, and temperature. However, for the hybrid energy storage system, the main control parameter is the battery current, particularly, how smooth the discharge current is. This means that what the ratio between RMS and average value is during the cycle. The smaller is the ratio, the smoother is the current.

Unfortunately, this ratio is not explicitly shown in the model. This ratio affects the battery temperature, T, and then, the temperature has an impact in the aging. In order to understand the impact, a relation between the internal temperature of the cell and the RMS/average ratio is needed. A simple model is used as shown in **Figure 3a** and **b** shows the electric circuit. The thermal model is as simple as possible: a thermal capacitance, related to the materials and battery size, and a thermal resistance, which allows the battery to extract the heat. The electric circuit is also simplified as the main goal is not to accurately predict the output, but to estimate the losses.
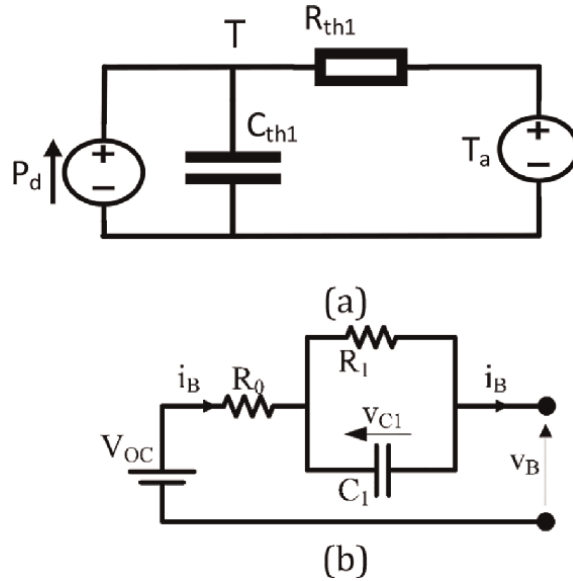
Figure 3.
(a) Thermal and (b) electrical equivalent circuits.
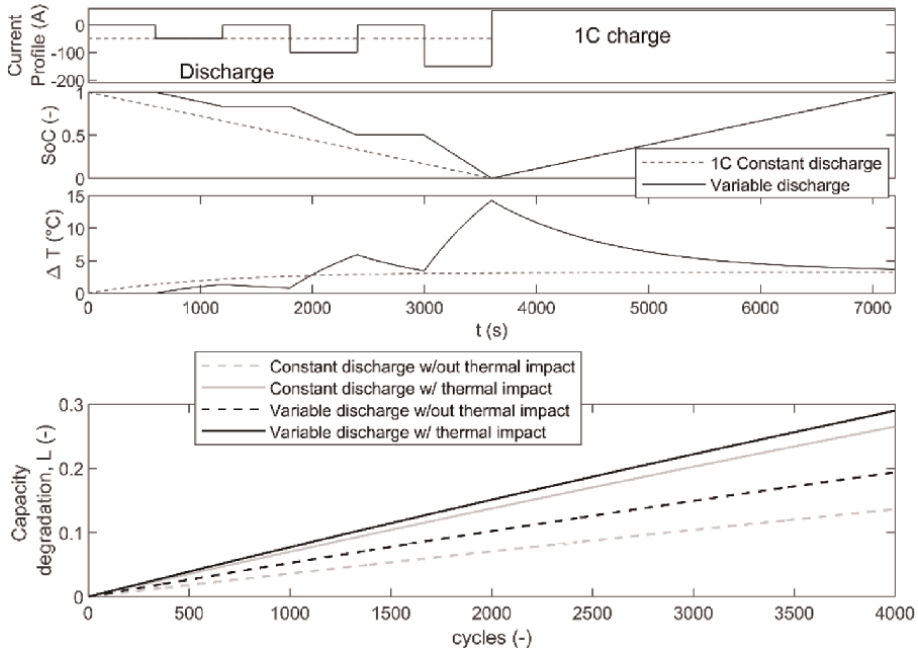
Figure 4.
Example of impact of the temperature in battery capacity degradation.

Figure 4 shows two types of discharge-charge cycle and the temperature effect of it. The constant discharge-discharge cycle has a notable less impact in the temperature although both of them discharge at 1C rate. The variable discharge-charge cycle has a

higher temperature impact, which is reflected in the aging. The aging plot at the end of the figure shows the effect of cycling both constant and variable cycles, considering and neglecting the temperature effect. In both cases, the temperature effect notably increases the degradation of the battery, and the variable discharge process achieves the maximum degradation. In addition, the figure also presents the effect of the degradation only because of the depth of discharge and the current. These parameters also play an important role in the degradation of the battery.

4.2 Motorcycle description, battery current profile with and without HESS

Figure 5 shows the main diagram of the electric motorcycle traction system. In the example, the main characteristics are: in-wheel 5 kW brushless motor, a total weight of 200 kg, a 70 V 50 Ah battery, and a motor drive that can work in the 60 to 100 V range. The battery consists of 22 Lithium-ion 50 Ah cells (LiFePO4) in series.

In the BESS case (only batteries), the battery is connected directly to the motor drive and delivers the current demanded by the motor. For this case study, we propose the use of B-HESS case (**Figure 2b**); the battery is connected through a DC/DC converter to a SC-stack, and both then connect to the motor drive. The semi-active B-HESS was selected because:

1. Passive topologies are robust but cannot take full advantage of the SCs because the power sharing is controlled based on their own internal impedances, so no real-time control.

2. Full-active topologies are attractive, but size, cost, and complexity are above a scooter design and price.

3. Semi-active topologies offer two variants: with SC-HESS, the converter should tolerate SC currents, which can be much larger than the battery currents, so it will be more expensive, bulkier, and heavier. On the contrary, B-HESS is a good trade-off between control, complexity, and cost and allows the full control of the battery current, which is important for keeping the temperature within the safe operational area while still delivering high power.

Therefore, B-HESS was selected.

In this configuration, the SC-stack voltage is allowed to fluctuate between 60 and 100 V, in order to transfer energy to the motor drive. The motor drive is a traditional
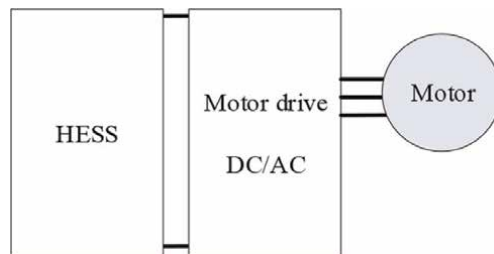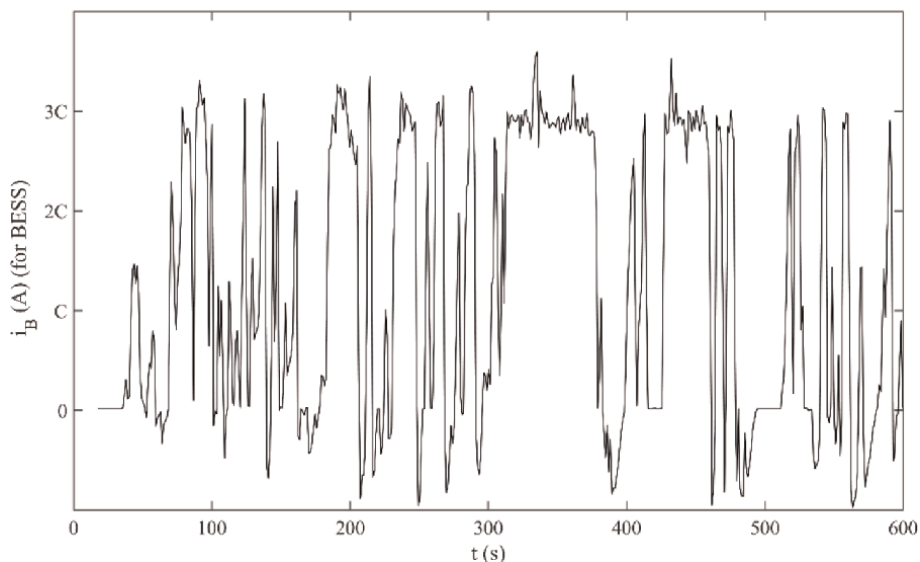

Figure 5.
Motorcycle traction system.

voltage source inverter, which can tolerate that voltage variation. However, if a wider input voltage is needed, other inverters must be used, such as a Z-source converter [31].

The current that the motor drive demands from the battery is shown in **Figure 6**. Notice that the currents peaks achieve 3C for this particular battery 150A and there is a notable variation in the current from zero to the maximum value. However, by using the B-HESS (**Figure 2b**) and using the converter as a low pass filter, the high frequency currents can be delivered by the supercapacitors (SCs) and the average current by the Lithium-ion battery. **Figure 7** shows the profile of the current in the battery using B-HESS. B-HESS consisted of the same battery, a bidirectional half-bridge converter [7], and a set of 33 SC in series as a SC-stack 3 V-3000F. Notice that the high frequency currents are delivered by the SCs, while the main current is delivered by the battery. Also, notice that for long pulses, the supercapacitors cannot deliver the power, so in that case, the battery is the one that is delivering the power. Therefore, if the SCs are exhausted, the battery still provides the energy. This allows a robust performance.

4.3 Aging estimation

Finally, both the BESS discharging current profile from **Figure 6** and the B-HESS discharging current profiles from **Figure 7** were cycled using a 1C-constant charging profile for more than 300 cycles. The results are shown in **Figure 8** for the only battery case (BESS) and in **Figure 9** for the B-HESS case. The rise in the temperature is slightly higher in the BESS case, but the main effect is the current variation, which is much softer in the B-HESS. For both cases, the presented aging model were used with the same parameters. It predicts that the degradation achieves 10% of capacity loss for 900 cycles in the BESS mode; however, for the B-HESS, the capacity loss is 8%. This means around 20% of life cycle extension. In addition, the real battery capacity was
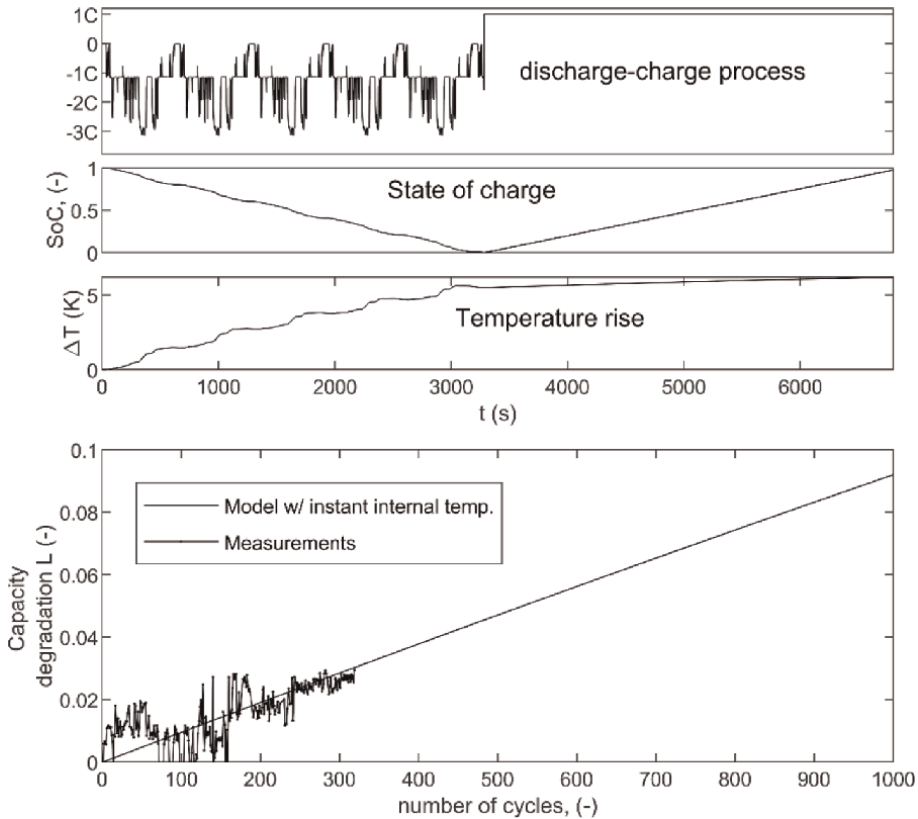
Figure 6.
Battery discharging profiles for an urban ride in a scooter using only BESS.
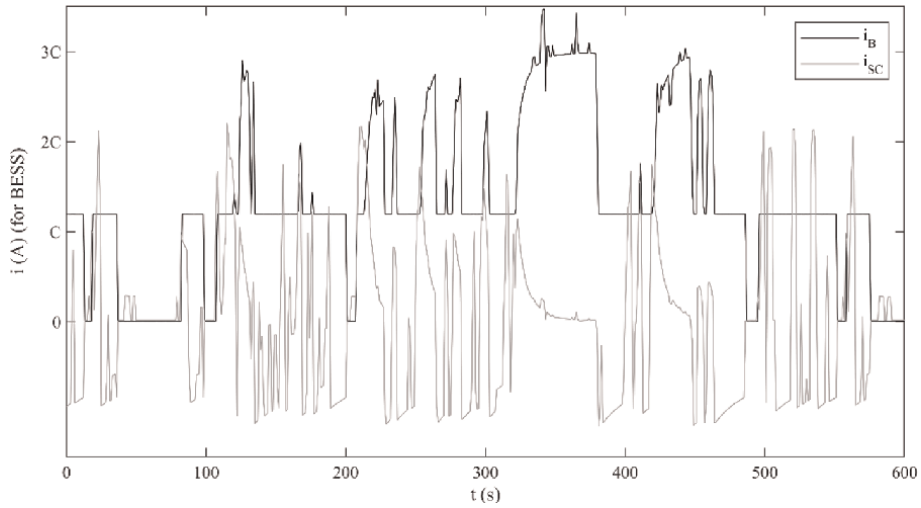
Figure 7.
Battery and SC discharging profiles for an urban ride in a scooter using B-HESS.
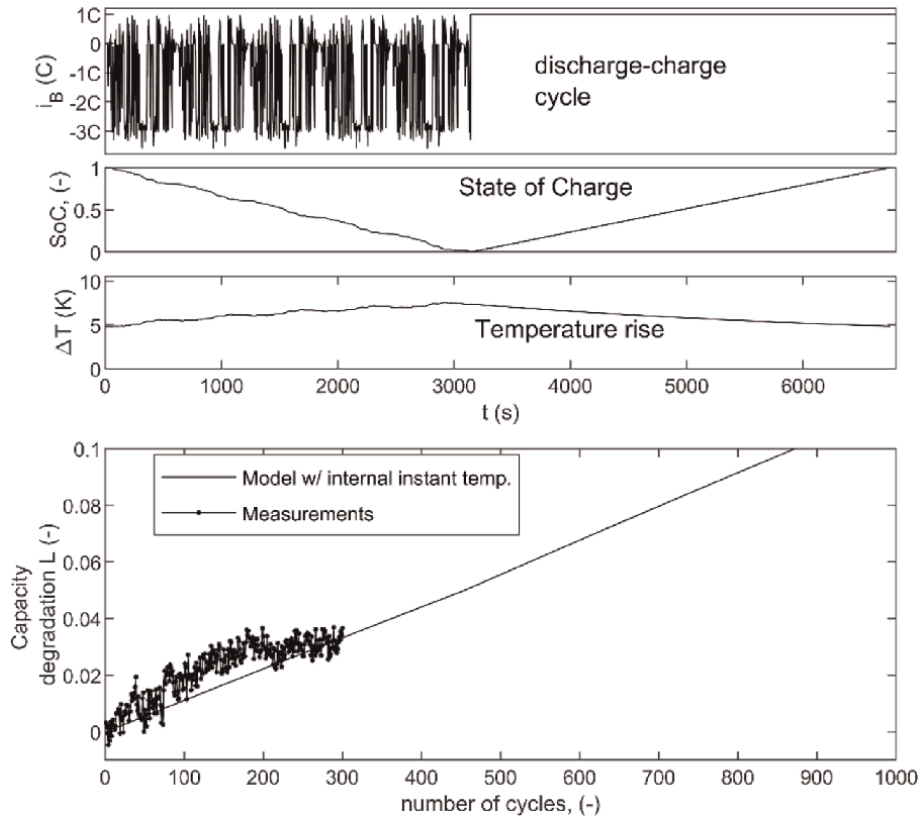
Figure 8.
Degradation test in only battery case, BESS.

Figure 9.
Degradation test in B-HESS case.

measured in each cycle, and the results of the first 300 cycles are in concordance with the proposal.

As a future work, a complete analysis reaching the end of the life should be performed for several cells and several profiles. Unfortunately, these tests are very time demanding, so the validations are limited but express are big potential in life cycle increase using HESS technologies.

5. Conclusion

This chapter briefly describes the technologies for storage energy and from that extracts the idea of combining two different technologies in order to have high power available and high energy density. It suggests that a good combination for this is an HESS with supercapacitors and batteries. For that, several topologies are mentioned: passive, semi-active, and full-active, with their own advantages and disadvantages. The most attractive topologies are semi-active and full-active, due to the flexibility that they offer.

Using HESS, combining SC and batteries, current stress and temperature of the battery can be reduced. These two aspects affect the life cycle of the battery, so the

chapter also presents an aging model that helps to quantify their effect on the battery life cycle.

Finally, the chapter shows a practical case study, in which the energy storage system of an urban scooter is replaced by an HESS. The study clearly shows how the current in the battery becomes smoother and how this impacts the temperature and the capacity degradation. This is shown using the aging model and experimental validation.

Acknowledgements

Author details

Federico Ibanez
Skolkovo Institute of Science and Technology, Moscow, Russia

*Address all correspondence to: fm.ibanez@skoltech.ru

IntechOpen

References

[1] Macharia VM, Garg VK, Kumar D. A review of electric vehicle technology: Architectures, battery technology and its management system, relevant standards, application of artificial intelligence, cyber security, and interoperability challenges. IET Electrical Systems in Transportation. 2023;**2023**:e12083. DOI: 10.1049/els2.12083

[2] Veneri O, Migliardini F, Capasso C, Corbo P. ZEBRA battery based propulsion system for urban bus applications: Preliminary laboratory tests. In: Proceedings of the IEEE 2012 Electrical Systems for Aircraft, Railway and Ship Propulsion. Bologna, Italy: IEEE; 2012. pp. 1-6. DOI: 10.1109/ESARS.2012.6387489

[3] Sayed K. Zero-voltage soft-switching DC–DC converter-based charger for LV battery in hybrid electric vehicles. IET Power Electronics. 2019;**12**:3389-3396. DOI: 10.1049/iet-pel.2019.0147

[4] Meishner F, Uwe Sauer D. Technical and economic comparison of different electric bus concepts based on actual demonstrations in European cities. IET Electrical Systems in Transportation. 2020;**10**:144-153. DOI: 10.1049/iet-est.2019.0014

[5] Wang J, Liu P, Hicks-Garner J, et al. Cycle-life model for graphite-LiFePO$_4$ cells. Journal of Power Sources. 2011;**196**(8):3942-3948

[6] Ibanez FM, Ahmed T, Idrisov I, Gutierrez JS. An impedance based modeling towards the aging prediction of lithium-ion battery for EV applications. In: Proceedings of the IEEE 2019 8th International Conference on Renewable Energy Research and Applications (ICRERA). Brasov, Romania: IEEE; 2019.

pp. 146-151. DOI: 10.1109/ICRERA47325.2019.8996568

[7] Ibanez FM, Beizama Florez AM, Gutiérrez S, Echeverrría JM. Extending the autonomy of a battery for electric motorcycles. IEEE Transactions on Vehicular Technology. 2019;**68**(4):3294-3305. DOI: 10.1109/TVT.2019.2896901

[8] Ottorino V, Capasso C, Patalano S. Experimental study on the performance of a ZEBRA battery based propulsion system for urban commercial vehicles. Applied Energy. 2017;**185**:2005-2018. DOI: 10.1016/j.apenergy.2016.01.124

[9] Mat ZBA, Madya YBK, Hassan SHBA, Talik NAB. Proton exchange membrane (PEM) and solid oxide (SOFC) fuel cell based vehicles-A review. In: Proceedings of the 2017 2nd IEEE International Conference on Intelligent Transportation Engineering (ICITE). Singapore: IEEE; 2017. pp. 123-126. DOI: 10.1109/ICITE.2017.8056893

[10] Breeze P. Chapter 5 – Superconducting magnetic energy storage. In: Power System Energy Storage Technologies. Academic Press; 2018. pp. 47-52. DOI: 10.1016/B978-0-12-812902-9.00005-5

[11] Torki J, Joubert C, Sari A. Electrolytic capacitor: Properties and operation. Journal of Energy Storage. 2023;**58**:106330. DOI: 10.1016/j.est.2022.106330

[12] Arokia Nathan LP, Hemamalini R, Jeremiah RJR, Partheeban P. Review of condition monitoring methods for capacitors used in power converters. Microelectronics Reliability. 2023;**145**:115003. DOI: 10.1016/j.microrel.2023.115003

[13] Martin Ibanez F, Idrisov I, Martin F, Rujas A. Design balancing systems for supercapacitors based on their stochastic model. IEEE Transactions on Energy Conversion. 2020;**35**(2): 733-745. DOI: 10.1109/TEC.2020. 2968364

[14] Rohit AK, Rangnekar S. An overview of energy storage and its importance in Indian renewable energysector: Part II—Energy storage applications, benefits and market potential. Journal of Energy Storage. 2017;**13**:447-456. DOI: 10.1016/ j.est.2017.07.012

[15] Chen H, Cong TN, Yang W, Tan C, Li Y, Ding Y. Progress in electrical energy storage system: A critical review. Progress in Natural Science. 2009;**19**: 291-312. DOI: 10.1016/j.pnsc.2008. 07.014

[16] Das CK, Bass O, Kothapalli G, Mahmoud TS, Habibi D. Overview of energy storage systems indistribution networks: Placement, sizing, operation, and power quality. Renewable and Sustainable Energy Reviews. 2018;**91**: 1205-1230. DOI: 10.1016/j.rser.2018. 03.068

[17] Beard KW, Reddy TB, editors. Linden's Handbook of Batteries. 5th ed. Chichester: McGraw-Hill; 2019

[18] Aneke M, Wang M. Energy storage technologies and real life applications—A state of the art review. Applied Energy. 2016;**179**:350-377. DOI: 10.1016/ j.apenergy.2016.06.097

[19] Behabtu HA, Messagie M, Coosemans T, Berecibar M, Anlay Fante K, Kebede AA, et al. A review of energy storage technologies' application potentials in renewable energy sources grid integration. Sustainability. 2020;**12**: 10511. DOI: 10.3390/su122410511

[20] Li X, Palazzolo A. A review of flywheel energy storage systems: State of the art and opportunities. Journal of Energy Storage. 2022;**46**:103576. DOI: 10.1016/j.est.2021.103576

[21] Bogdanov S, Pugach M, Parsegov S, Vlasov V, Ibanez FM, Stevenson KJ, et al. Dynamic modeling of vanadium redox flow batteries: Practical approaches, their applications and limitations. Journal of Energy Storage. 2023;**57**: 106191. DOI: 10.1016/j.est.2022.106191

[22] Liu H, Wang Z, Cheng J, Maly D. Improvement on the cold cranking capacity of commercial vehicle by using Supercapacitor and Lead-acid battery hybrid. IEEE Transactions on Vehicular Technology. 2009;**58**(3):1097-1105

[23] Song Z, Hofmann H, Li J, et al. A comparison study of different semiactive hybrid energy storage system topologies for electric vehicles. Journal of Power Sources. 2015;**274**:400-411

[24] Kollmeyer P et al. Optimal performance of a full scale li-ion battery and li-ion capacitor hybrid energy storage system for a plug-in hybrid vehicle. In: IEEE Energy Conversion Congress and Exposition (ECCE). Vol. 2017. Cincinnati, OH: IEEE; 2017. pp. 572-577

[25] Ostadi A, Kazerani M. A comparative analysis of optimal sizing of battery-only, ultracapacitor-only, and battery-Ultracapacitor hybrid energy storage systems for a city bus. IEEE Transactions on Vehicular Technology. 2015;**64**(10): 4449-4460

[26] Jing W, Hung Lai C, Wong SHW, Wong MLD. Battery-supercapacitor hybrid energy storage system in standalone DC microgrids: A review. IET Renewable Power Generation. Mar 2017; **11**(4):461-469

[27] Shubnaya A, Ibanez FM, Rodriguez
Cortes P. Compensating measurement
delays in decoupling blocks of dq control
technique for multiple active bridge
converter. In: IEEE Proceedings of
IECON 2022 – 48th Annual Conference
of the IEEE Industrial Electronics
Society. Brussels, Belgium: IEEE;
2022. pp. 1-6. DOI: 10.1109/
IECON49645.2022.9968388

[28] Davalos Hernandez F,
Samanbakhsh R, Mohammadi P,
Ibanez FM. A dual-input high-gain
bidirectional DC/DC converter for
hybrid energy storage systems in DC
grid applications. IEEE Access. 2021;**9**:
164006-164016. DOI: 10.1109/
ACCESS.2021.3132896

[29] Millner A. Modeling lithium ion
battery degradation in electric vehicles.
In: Proceeding of 2010 IEEE Conference
on Innovative Technologies for an
Efficient and Reliable Electricity Supply.
Waltham, MA: IEEE; 2010. pp. 349-356.
DOI: 10.1109/CITRES.2010.5619782

[30] Zhurkov SN. Kinetic concept of
strength of solids. International Journal
of Fracture Mechanics. 1965;**1**:311-323

[31] Florez-Tapia A, Ibanez FM, Vadillo J,
Elosegui I, Echeverria JM. Small signal
modeling and transient analysis of a
trans quasi-Z-source inverter. Electric
Power Systems Research. 2017;**144**:52-62

Edited by Nicolae Tudoroiu

Clean and efficient transportation in countries around the world is only possible if governments and scientists focus on stimulating and supporting the electric vehicle industry by developing and deploying the most advanced Li-ion battery technologies. Recently, several improvements have been made in the direction of operational safety, the elimination of explosion hazards, and the mitigation of chemical toxicity. The state of charge of an electric vehicle battery is an essential internal parameter that plays a vital role in utilizing the battery's energy efficiency, operating safely in various realistic conditions and environments, and extending the battery's life. Also, automated systems are integrated into the architecture of electrical vehicles, allowing for technology, machinery, or systems to perform tasks or processes with minimal human intervention. Automation in electric vehicles involves the integration of advanced technologies to enhance the driving experience, improve safety, optimize energy efficiency, and facilitate the transition to sustainable transportation. The key aspects of automation in electric vehicles are advanced driver assistance, self-driving capabilities, battery and energy management, and safety and collision avoidance. This book provides a comprehensive overview of electric and hybrid electric vehicles, exploring their design, the modeling of Li-ion battery management systems, state-of-charge estimation algorithms, and the most used electric motors. It also discusses new trends in electric vehicle automation as well as different control strategies.

IntechOpen